

INTERFACIAL ELECTRON TRANSFER AT SENSITIZED NANOCRYSTALLINE TiO<sub>2</sub>  
ELECTROLYTE INTERFACES: INFLUENCE OF SURFACE ELECTRIC FIELDS AND  
LEWIS-ACIDIC CATIONS

Timothy J. Barr

A dissertation submitted to the faculty at the University of North Carolina at Chapel Hill in  
partial fulfillment of the requirements for the degree of Doctor of Philosophy in the  
Department of Chemistry.

Chapel Hill  
2017

Approved by:

Gerald J. Meyer

Cynthia Schauer

Wei You

James Cahoon

Joanna Atkin

©2017  
Timothy J. Barr  
ALL RIGHTS RESERVED

## ABSTRACT

Timothy J. Barr: Interfacial Electron Transfer at Sensitized Nanocrystalline TiO<sub>2</sub> Electrolyte Interfaces: Influence of Surface Electric Fields and Lewis-Acidic Cations  
(Under the direction of Gerald J. Meyer)

Interfacial electron transfer reactions facilitate charge separation and recombination in dye-sensitized solar cells (DSSCs). Understanding what controls these electron transfer reactions is necessary to develop efficient DSSCs. Gerischer proposed a theory for interfacial electron transfer where the rate constant was related to the energetic overlap between the donor and acceptor states. The present work focuses on understanding how the composition of the CH<sub>3</sub>CN electrolyte influenced this overlap. It was found that the identity of the electrolyte cation tuned the energetic position of TiO<sub>2</sub> electron acceptor states, similar to how pH influences the flatband potential of bulk semiconductors in aqueous electrolytes. For example, the onset for absorption changes, that were attributed to electrons in the TiO<sub>2</sub> thin film, were ~0.5 V more positive in Mg<sup>2+</sup> containing electrolyte than TBA<sup>+</sup>, where TBA<sup>+</sup> is tetrabutylammonium. Similar studies performed on mesoporous, nanocrystalline SnO<sub>2</sub> thin films reported a similar cation dependence, but also found evidence for electrons that did not absorb in the visible region that were termed ‘phantom electrons.’

Electron injection is known to generate surface electric fields on the order of 2 MV/cm. The rearrangement of cations in response to surface electric fields, termed screening, was investigated. It was found that magnitude of the electric field and the screening dynamics were dependent on the identity of the electrolyte cation. The rate of

charge recombination to the anionic iodide/triiodide redox mediator correlated with the screening ability of the cation, and was initially thought to control charge recombination. However, it was difficult to determine whether electron diffusion or driving force were also cation dependent.

Therefore, a in-lab built apparatus, termed STRiVE, was constructed that could disentangle the influence electron diffusion, driving force, and electric fields had on charge recombination. It was found that electron diffusion was independent of the electrolyte cation. Furthermore, charge recombination displayed the same cation-sensitivity using both anionic and cationic redox mediators, indicating electric fields did not cause the cation-dependence of charge recombination. Instead, it was found that the electrolyte cation tuned the energetic position of the  $\text{TiO}_2$  acceptor states and modulated the driving force for charge recombination.

To my family, thank you for all your love and support.

## ACKNOWLEDGEMENS

I would like to thank those who have supported me in my studies and helped shape who I am today. For my wife, Keri, who has provided years of support and encouragement. She has gently pushed be to broaden my perspective through trips to Europe and even managed to open my pallet to exotic foods, such as tilapia and lobster. I attribute much of my emotional growth for the past 10 years to her positive influence. To my parents, who have helped guide me throughout my life. They taught me how to put my best foot forward and commit to what I want. My determination and work ethic can be traced back to them. To my advisor, Jerry, who has been as an outstanding mentor and helped shape my scientific career. He always encouraged us to ‘follow our nose’ and explore what we were interested in. The phrase ‘living the dream’ seems suitable.

I am also grateful to my fellow graduate students and post-docs in the lab. Having a friendly and enjoyable working environment is not a guarantee in graduate school. I have been quite happy with the friendly and open nature in this research group. Even in the absence of a mandatory Bandido’s Wednesday, the group has managed find precious seconds between running experiments, analyzing data, and writing up results to stay friendly and share (strictly) scientific thoughts with one another. I have no doubt this lab demeanor will continue for years to come.

## TABLE OF CONTENTS

LIST OF FIGURES .....	x
LIST OF TABLES .....	xx
LIST OF SCHEMES.....	xxi
LIST OF EQUATIONS .....	xxii
CHAPTER 1: INTRODUCTION.....	1
1.1 The case for solar energy .....	1
1.2 The dye-sensitized solar cell.....	4
1.3 Description of the electronic states in TiO <sub>2</sub> .....	7
1.4 Influence of electrolyte cations.....	12
1.5 Interfacial electric fields .....	16
1.6 Charge transport and recombination in DSSCs: .....	25
REFERENCES .....	31
CHAPTER 2: ELECTRIC FIELDS AND CHARGE SCREENING IN DYE SENSITIZED MESOPOROUS NANOCRYSTALLINE TiO <sub>2</sub> THIN FILMS .....	38
2.1 Introduction.....	38
2.2 Experimental.....	41
2.3 Results.....	44
2.4 Discussion.....	55

2.5 Conclusion .....	65
REFERENCES .....	67
<b>CHAPTER 3: ELECTRIC FIELDS CONTROL <math>\text{TiO}_2(\text{e}^-)+\text{I}_3^- \rightarrow \text{CHARGE}</math></b> <b>RECOMBINATION IN DYE-SENSITIZED SOLAR CELLS .....</b>	<b>72</b>
3.1 Introduction.....	72
3.2 Results and Discussion .....	73
REFERENCES .....	81
<b>CHAPTER 4: ELECTROLYTE CATION CONTROLS DRIVING FORCE</b> <b>FOR CHARGE RECOMBINATION IN DYE-SENSITIZED SOLAR CELLS .....</b>	<b>83</b>
4.1 Introduction.....	83
4.2 Experimental .....	87
4.3 Results.....	90
4.4 Discussion.....	95
4.5 Conclusions.....	105
REFERENCES .....	106
<b>CHAPTER 5: CHARGE RECTIFICATION AT MOLECULAR-</b> <b>NANOCRYSTALLINE <math>\text{TiO}_2</math> INTERFACES: OVERLAP OPTIMIZATION</b> <b>TO PROMOTE VECTORIAL ELECTRON TRANSFER .....</b>	<b>111</b>
5.1 Introduction.....	111
5.2 Experimental .....	114
5.3 Results and Discussion .....	118
5.4 Conclusions.....	133

REFERENCES .....	134
CHAPTER 6: PHANTOM ELECTRONS IN MESOPOROUS NANOCRYSTALLINE SnO <sub>2</sub> THIN FILMS WITH CATION DEPENDENT REDUCTION ONSETS .....	137
6.1 Introduction.....	137
6.2 Experimental.....	140
6.3 Results.....	142
6.4 Discussion.....	151
6.5 Conclusions.....	160
REFERENCES .....	162
CHAPTER 7: STRiVE DESCRIPTION AND OPERATION .....	167
7.1 Introduction.....	167
7.2 Hardware Description .....	169
7.3 Software Description and Typical Operation .....	175
REFERENCES .....	196
APPENDIX.....	197

## LIST OF FIGURES

<p>Figure 1.01. (A) Solar irradiance measured on the Earth’s surface (terrestrial, black) compared to an ideal blackbody emitter at 5778 K (red). (B) Theoretical power output of a 100 % efficient solar cell absorbing all photons of higher energy than the cutoff value. The maximum power is termed the ‘ideal cutoff.’ .....</p>	4
<p>Figure 1.02. Schematic diagram of a DSSC .....</p>	6
<p>Figure 1.03. Theoretical energetic dependence of the density of states, <math>N(E)</math>, for a bulk semiconductor (left) and the experimentally observed density of states for mesoporous thin films of ~20 nm diameter <math>\text{TiO}_2</math> nanocrystallites (right). .....</p>	10
<p>Figure 1.04. Comparison of strong (left, <math>\text{Li}^+</math> containing electrolyte) and weak (right, <math>\text{TBA}^+</math> containing electrolyte) energetic overlap between the electron donors, <math>W(E)</math>, and acceptors, <math>g(E)</math>, during charge injection into nanocrystalline <math>\text{TiO}_2</math>. The area in gray represents regions of favorable energetic overlap. ....</p>	14
<p>Figure 1.05. Influence of charge density (left) and energetic position (right) of the <math>\text{TiO}_2</math> density of states on open circuit voltage (<math>V_{\text{OC}}</math>, double sided arrows). The <math>V_{\text{OC}}</math> value can be increased by adding more charge carriers to the film or by increasing the energetic position of the <math>\text{TiO}_2</math> acceptor states. ....</p>	16
<p>Figure 1.06. (A) Jablonski-type diagram depicting the ground and excited state energies for molecules aligned antiparallel (blue) orthogonal (green) and parallel (red) to the electric field, <math>F_{\text{ext}}</math>. Note the transition energy for the orthogonal transition is identical to the ground state transition energy. (B) UV/Vis spectra of an arbitrary transition in the presence of an electric field (gray). Also shown are the individual contributions for molecules oriented parallel (red), orthogonal (green) and antiparallel (blue) to the electric field. ....</p>	18
<p>Figure 2.01. Steady-state UV–vis absorbance (A) and photoluminescence (B) spectra of <math>\text{Ru}(\text{dtb})_2(\text{dcb})/\text{TiO}_2</math> in neat acetonitrile and in the presence of 100 mM metal perchlorate electrolyte. ....</p>	45
<p>Figure 2.02. Absorbance as a function of the charge extracted from un-sensitized <math>\text{TiO}_2</math> thin films immersed in 100 mM metal perchlorate acetonitrile solutions. The black line indicates the best fit to the data which yields a molar extinction coefficient of <math>930 \pm 50 \text{ M}^{-1}\text{cm}^{-1}</math>. ....</p>	47
<p>Figure 2.03. Spectra of a potentiostatically controlled <math>\text{Ru}(\text{dtb})_2(\text{dcb})/\text{TiO}_2</math> film in 100 mM <math>\text{LiClO}_4</math> acetonitrile solution (A) and after subtraction of the long-wavelength <math>\text{TiO}_2(e^-)</math> absorption (B). The difference spectra for the data shown in A and B are given in C and D, respectively. The insets in A and B indicate the electric field strength calculated by two different analyses. The spectra in</p>	

dark blue were recorded at +150 mV and spectra recorded at more negative potentials (up to -750 mV) are indicated in red. The arrows indicate the direction of change with increased negative applied potential. ....	49
Figure 2.04. Electric field experienced by Ru(dtb) <sub>2</sub> (dcb)/TiO <sub>2</sub> in acetonitrile solutions containing 100 mM Li <sup>+</sup> , Na <sup>+</sup> , Mg <sup>2+</sup> , or Ca <sup>2+</sup> as a function of (A) the applied potential and (B) the number of TiO <sub>2</sub> (e <sup>-</sup> )s on a per particle basis. ....	51
Figure 2.05. Transient absorption spectra obtained 2.5 μs after pulsed 532 nm excitation of Ru(dtb) <sub>2</sub> (dcb)/TiO <sub>2</sub> in acetonitrile electrolyte solutions containing 100 mM of the indicated perchlorate salts and 250 mM tetra- <i>n</i> -butylammonium iodide. ....	52
Figure 2.06. Single-wavelength transient absorption kinetic data of Ru(dtb) <sub>2</sub> (dcb)/TiO <sub>2</sub> in acetonitrile electrolyte solutions containing 100 mM of the indicated perchlorate salts with 250 mM tetra- <i>n</i> -butylammonium iodide observed at the maximum of the Stark effect bleach, ~500–510 nm.....	54
Figure 2.07. Density of states obtained from spectroelectrochemical measurements of Ru(dtb) <sub>2</sub> (dcb)/TiO <sub>2</sub> sensitized thin films in 100 mM acetonitrile electrolytes of the indicated perchlorate salts. ....	59
Figure 3.01. Visible absorbance spectra of a Ru(dtb) <sub>2</sub> (dcb)/TiO <sub>2</sub> thin film immersed in acetonitrile in the absence (gray) or presence of 100 mM LiI (black), 100 mM NaI (red), 50 mM MgI <sub>2</sub> (blue), and 50 mM CaI <sub>2</sub> (green). ....	74
Figure 3.02. Absorbance change of Ru(dtb) <sub>2</sub> (dcb)/TiO <sub>2</sub> thin films measured (A) under conditions of approximately 20 TiO <sub>2</sub> (e <sup>-</sup> )s per TiO <sub>2</sub> nanoparticle electrochemically generated in 100 mM solutions of NaClO <sub>4</sub> (red), LiClO <sub>4</sub> (black), Mg(ClO <sub>4</sub> ) <sub>2</sub> (blue), and Ca(ClO <sub>4</sub> ) <sub>2</sub> (green) and (B) 2.5 μs after pulsed 532 nm light excitation in 100 mM NaI (red, circles) and 50 mM CaI <sub>2</sub> (green, triangles) acetonitrile solutions. ....	75
Figure 3.03. Absorption changes that correspond to TiO <sub>2</sub> (e <sup>-</sup> ) + I <sub>3</sub> <sup>-</sup> → charge recombination measured in 100 mM LiClO <sub>4</sub> (black), NaClO <sub>4</sub> (red), Mg(ClO <sub>4</sub> ) <sub>2</sub> (blue), and mM Ca(ClO <sub>4</sub> ) <sub>2</sub> (green) acetonitrile solutions with 250 mM TBAI. Overlaid on the data are fits to the KWW function with β = 0.45. The inset shows a plot of the recombination rate constant versus the electric field. ....	77
Figure 4.02. Charge extracted from open-circuit over a wide range of voltages, set by the incident light intensity, for DSSCs containing 100 mM Li <sup>+</sup> (Black), Na <sup>+</sup> (Red), Mg <sup>2+</sup> (Blue), or Ca <sup>2+</sup> (Green) perchlorate, 250 mM TBAI, and 50 mM I <sub>2</sub> . ....	92
Figure 4.03. (A) Transient photovoltage decay measurements for a DSSC containing 100 mM NaClO <sub>4</sub> , 250 mM TBAI, 50 mM I <sub>2</sub> . (B) Electron lifetimes measured from the single-exponential decay in transient photovoltage	

measurements DSSCs containing 100 mM Li <sup>+</sup> (Black), Na <sup>+</sup> (Red), Mg <sup>2+</sup> (Blue), or Ca <sup>2+</sup> (Green) perchlorate with 250 mM TBAI, and 50 mM I <sub>2</sub> . .....	93
Figure 4.04. (A) Transient photocurrent decay measurements for a DSSC containing 100 mM NaClO <sub>4</sub> , 250 mM TBAI, 50 mM I <sub>2</sub> . (B) Diffusion coefficient calculated from the single-exponential decay in transient photocurrent measurements DSSCs containing 100 mM Li <sup>+</sup> (Black), Na <sup>+</sup> (Red), Mg <sup>2+</sup> (Blue), or Ca <sup>2+</sup> (Green) perchlorate with 250 mM TBAI, and 50 mM I <sub>2</sub> . .....	94
Figure 4.05. Electron lifetimes (A) and diffusion coefficients (B) for DSSCs containing 100 mM Li <sup>+</sup> (Black), Na <sup>+</sup> (Red), or Ca <sup>2+</sup> (Green) perchlorate with 135 mM Co <sup>II</sup> (dtb) <sub>3</sub> (PF <sub>6</sub> ) <sub>2</sub> , and 15 Co <sup>III</sup> (dtb) <sub>3</sub> (PF <sub>6</sub> ) <sub>3</sub> in CH <sub>3</sub> CN. ....	95
Figure 4.06. Difference between the shift of the TiO <sub>2</sub> acceptor state distribution and the change in V <sub>oc</sub> relative to Na <sup>+</sup> containing DSSCs as a function of the lifetime relative to Na <sup>+</sup> . .....	99
Figure 4.07. (A) Electron diffusion coefficient and lifetime as a function of TiO <sub>2</sub> (e <sup>-</sup> )s and (B) diffusion length calculated at matched electron concentrations for DSSCs containing 100 mM Li <sup>+</sup> (Black), Na <sup>+</sup> (Red), Mg <sup>2+</sup> (Blue), or Ca <sup>2+</sup> (Green) perchlorate, 250 mM TBAI, and 50 mM I <sub>2</sub> . .....	101
Figure 4.08. Dependence of electron lifetime on the relative DoS position for DSSCs containing 100 mM Li <sup>+</sup> (Black), Na <sup>+</sup> (Red), Mg <sup>2+</sup> (Blue), or Ca <sup>2+</sup> (Green) perchlorate, 250 mM TBAI, and 50 mM I <sub>2</sub> . Circles represent lifetimes measured in I <sup>-</sup> /I <sub>3</sub> <sup>-</sup> containing DSSCs while diamonds represent DSSCs using Co <sup>III/II</sup> redox mediators. ....	104
Figure 5.01. The spectroelectrochemical reduction of the indicated pyridiniums/TiO <sub>2</sub> in 0.1 M TBAClO <sub>4</sub> (left hand side) or LiClO <sub>4</sub> (right hand side) CH <sub>3</sub> CN electrolytes. ....	120
Figure 5.02. The UV/Visible absorption spectra of the indicated pyridiniums in 0.1 M LiClO <sub>4</sub> or TBAClO <sub>4</sub> CH <sub>3</sub> CN electrolyte. ....	122
Figure 5.03. The absorption change for an unfunctionalized TiO <sub>2</sub> thin film measured at 900 nm after a potential step from 0.2 V to the indicated potentials (mV) at time zero in 0.1 M TBAClO <sub>4</sub> (left hand side) and LiClO <sub>4</sub> (right hand side) CH <sub>3</sub> CN electrolyte. The potential was stepped back to +0.2 V after 45 s. ....	124
Figure 5.04. The normalized absorption change measured at the reduced pyridinium maximum wavelength after a step from +0.2 V to the indicated potentials (mV) at time zero in 0.1 M TBAClO <sub>4</sub> (left hand side) and LiClO <sub>4</sub> (right hand side) CH <sub>3</sub> CN electrolyte. The potential was stepped back to +0.2 V after 45 s. ....	126

Figure 5.05. UV/Vis absorbance changes for DPEV functionalized TiO <sub>2</sub> in 0.1 M TBAClO <sub>4</sub> /CH <sub>3</sub> CN during potential steps from +200 mV to -600 mV at time zero and back to +200 mV vs NHE at t = 30 seconds. Single wavelength traces (600 nm) are shown in (A), with close-ups in (C) and (E). Full spectra are shown just before and after each potential step in (D) and (F) to highlight the observation of DPEV <sup>+</sup> as an intermediate. Extinction coefficient spectra for DPEV <sup>2+</sup> , DPEV <sup>+</sup> , and DPEV <sup>0</sup> are shown in (B) for reference. Long wavelength absorption changes in (D) and (F) are caused by the broad absorption of TiO <sub>2</sub> electrons during reduction.....	129
Figure 5.06. The chemical capacitance of DPEV <sup>2+/+</sup> (blue) and MEV <sup>+/0</sup> (purple) and the TiO <sub>2</sub> (gray) measured in 0.1 M TBAClO <sub>4</sub> (left) and LiClO <sub>4</sub> (right) CH <sub>3</sub> CN electrolyte. ....	130
Figure 6.01. A) Raw and B) normalized absorption difference spectra of mesoporous, nanocrystalline TiO <sub>2</sub> thin film in 100 mM LiClO <sub>4</sub> acetonitrile electrolyte at increasingly negative applied potentials ranging from 0 V to -1.5 V vs Fc <sup>+</sup> /Fc. Overlaid on the normalized spectra in B is the calculated PAS (black). ....	143
Figure 6.02. A) Raw and B) normalized absorption difference spectra of mesoporous, nanocrystalline SnO <sub>2</sub> thin film in 100 mM Ca(ClO <sub>4</sub> ) <sub>2</sub> acetonitrile electrolyte at increasingly negative applied potentials ranging from 0 to -1.5 V vs Fc <sup>+</sup> /Fc. The inset in A) shows the raw difference spectra from 0 to -700 mV. C) PAS deconvolution of A). D) UV/Vis difference spectra of A) after returning to the initial potential overlaid with PAS 3. ....	145
Figure 6.03. Absorbance changes monitored at 950 nm for SnO <sub>2</sub> (A) and TiO <sub>2</sub> (B) thin films in 100 mM Li <sup>+</sup> (black), Na <sup>+</sup> (red), Mg <sup>2+</sup> (blue), Ca <sup>2+</sup> (green), and TBA <sup>+</sup> (brown) perchlorate acetonitrile electrolyte solutions at the indicated potentials. ....	147
Figure 6.04. Absorbance change at 900 nm during spectroelectrochemical charge extraction of TiO <sub>2</sub> (A) and SnO <sub>2</sub> (B) thin films immersed in 100 mM LiClO <sub>4</sub> acetonitrile electrolyte solutions. Charge extracted was normalized by the geometric area of the thin film. Overlaid in red are linear fits to equation 3.....	149
Figure 6.05. Cyclic voltammograms of SnO <sub>2</sub> (dashed) and TiO <sub>2</sub> (solid) thin films in 100 mM LiClO <sub>4</sub> (red) and TBAClO <sub>4</sub> (black) acetonitrile electrolyte solutions at a scan rate of 20 mV/s. Currents were normalized by the geometric area of the thin film.....	150
Figure 6.06. A) Chemical capacitance for TiO <sub>2</sub> (left) and SnO <sub>2</sub> (right) thin films in 100 mM metal perchlorate acetonitrile solutions of Li <sup>+</sup> (black), Na <sup>+</sup> (red), Mg <sup>2+</sup> (blue), Ca <sup>2+</sup> (green), and TBA <sup>+</sup> (brown). For SnO <sub>2</sub> thin films, the smaller distributions represent phantom electrons and the larger optically-active electrons.....	158

Figure 7.01. STRiVE white and blue LED arrays illuminating a typical DSSC .....	169
Figure 7.02. Relative spectral power distribution of the white LEDs .....	170
Figure 7.03. Relative spectral distribution of colored LEDs. Blue, Green, and Red are installed on the STRiVE.....	171
Figure 7.04. (Top) Schematic diagram of the integrated circuit used in the STRiVE. (Bottom) Picture of the actual board. On the left are MOSFETs used to hold the cell at open/short circuit or allow the potentiostat to be connected to the circuit. On the right are the amplifiers to accurately measure the current.....	173
Figure 7.05: Jsc and Voc Set Parameters dialog with typical values shown.....	178
Figure 7.06: Set iV Curve Parameters dialog showing typical experimental conditions for a cell with a $V_{OC}$ near 440 mV.....	180
Figure 7.07. Set Transient Photovoltage Parameters dialog showing typical values when employed as the first grouped experiment .....	184
Figure 7.08. Set Transient Photocurrent Parameters dialog displaying typical values when TCD is run as part of a series of grouped experiments (not the first).....	188
Figure 7.09. Charge Extraction Experimental Parameters dialog showing typical values when performed as ‘grouped’ and not the first experiment.....	190
Figure 7.10. Current Interrupt Voltage Parameters dialog with values for typical operation when performed as a ‘grouped’ (not the first) experiment .....	192
Figure 7.11. Comparison of charge extracted from open-circuit and $V_{oc}$ to the charge extracted at short-circuit and $V_{int}$ , the internal voltage calculated from current interrupt voltage.....	193
Figure 7.12. Open Circuit Photovoltage Decay Parameters dialog for typical values when performed in a series of ‘grouped’ experiments (not the first). .....	195
Figure A.01. STRiVE user interface ‘Front Panel’ where the experiments selected reflect normal operating procedure .....	197
Figure A.02. STRiVE user interface ‘Block Diagram.’ The left and right rectangles are event structures, which execute only for a user-defined event, such as selecting an experiment or zooming on a graph. In the center is a loop that executes all selected (ungrouped) experiments and then performs grouped experiments.....	198
Figure A.03. STRiVE user interface ‘Block Diagram’ selecting the first experiment, Jsc and Voc.....	199

Figure A.04. Measure $J_{sc}$ and $V_{oc}$ ‘Block Diagram’ depicting how $V_{oc}$ is measured. ....	200
Figure A.05. Measure $J_{sc}$ and $V_{oc}$ ‘Block Diagram’ depicting how $J_{sc}$ is measured. ....	200
Figure A.06. STRiVE user interface ‘Block Diagram’ selecting the second experiment, iV Curve.....	201
Figure A.07. iV Curve ‘Block Diagram’ Step 1: determine the time to wait between data points on the curve and connect the potentiostat. ....	202
Figure A.08 iV Curve ‘Block Diagram’ Step 2: run the dark iV curve. This code is essentially the same as the light-on iV curve.....	202
Figure A.09 iV Curve ‘Block Diagram’ Step 3: calculate $J_{sc}$ and then $V_{oc}$ and display the results.....	203
Figure A.10 iV Curve ‘Block Diagram’ Step 4: plot the dark, light, and power curves. ....	204
Figure A.11 iV Curve ‘Block Diagram’ Step 5: export the iV data as a .TDMS file and ensure the potentiostat is set to zero V. ....	205
Figure A.12. STRiVE 5.0 user interface ‘Block Diagram’ selecting the third experiment, transient photovoltage decay.....	206
Figure A.13. Transient photovoltage decay ‘Block Diagram’ where multiple experiments are performed and then the results are collected and plotted. ....	207
Figure A.14. Transient photovoltage decay experimental ‘Block Diagram’ step 1: calculate the sampling parameters.....	208
Figure A.15. Transient photovoltage decay experimental ‘Block Diagram’ step 2: start with the lights and potentiostat off. ....	209
Figure A.16. Transient photovoltage decay experimental ‘Block Diagram’ step 3: set the light intensity. As shown, a subVI is selected where the STRiVE finds the light intensity to give a desired $V_{oc}$ . This code is displayed in Figures A.24-A.27 .....	209
Figure A.17. Transient photovoltage decay experimental ‘Block Diagram’ step 4: set the pulse LED duration. As shown, the STRiVE will find the duration to give a desired ‘Voltage Spike.’ This code is displayed in Figure A.30.....	210

Figure A.18. Transient photovoltage decay experimental ‘Block Diagram’ step 5: finalize sampling parameters using the LED pulse time defined in step 4.....	211
Figure A.19. Transient photovoltage decay experimental ‘Block Diagram’ step 6: collect the data. This code is found in Figures A.28-29.....	212
Figure A.20. Transient photovoltage decay experimental ‘Block Diagram’ step 7: turn everything off.....	212
Figure A.21. Transient photovoltage decay experimental ‘Block Diagram’ step 8: baseline the data and calculate the electron lifetime .....	213
Figure A.22. Transient photovoltage decay experimental ‘Block Diagram’ step 9: display the results and export the data as a .TDMS file.....	214
Figure A.23. Set light intensity step 0: begin with the user defined current.....	215
Figure A.24. Set light intensity step 1: monitor the voltage as the light intensity is adjusted. The most 3 recent data points are used in a fit to better approximate the next light intensity output. ....	216
Figure A.25. Set light intensity step 2: set light intensity as the one that was produced the nearest $V_{OC}$ to the target.....	217
Figure A.26. Set light intensity step 3: Monitor the voltage for 5 seconds and check if the equilibrium value is within 5 mV of the target $V_{OC}$ .....	217
Figure A.27. Set light intensity step 4: Output the light intensity. ....	218
Figure A.28. Transient photovoltage decay Collect Data step 1: equilibrate with the light on. ....	219
Figure A.29. Transient photovoltage decay Collect Data step 2: use an internal time ‘counter’ to control the pulse LED and trigger data collection (Reference Digital Edge) that monitors the cell voltage. This process is repeated and averaged. ....	220
Figure A.30. Transient photovoltage decay ‘Set Voltage Spike’ key code. The pulse time is adjusted and the transient photovoltage peak is calculated. The most 3 recent pulses are used to fit and better estimate the required pulse time. ....	221
Figure A.31. STRiVE 5.0 user interface ‘Block Diagram’ selecting the fourth experiment, transient photocurrent decay.....	222
Figure A.32. Transient photocurrent decay ‘Block Diagram’ where multiple experiments are performed and then the results are collected and plotted. ....	223

Figure A.33. Transient photocurrent decay experimental ‘Block Diagram’ step 1: calculate the sampling parameters. ....	224
Figure A.34. Transient photocurrent decay experimental ‘Block Diagram’ step 2: start at short-circuit but with the light and potentiostat off.....	225
Figure A.35. Transient photocurrent decay experimental ‘Block Diagram’ step 3: set the light intensity. As shown the STRiVE will adjust the light intensity to get a defined $J_{SC}$ . This code is very similar to adjusting the light intensity to set the $V_{OC}$ , Figures A.24-27. ....	226
Figure A.36. Transient photocurrent decay experimental ‘Block Diagram’ step 4: set the pulse LED duration. As shown, the STRiVE will adjust the pulse time to reach the defined current spike. This code is shown in Figure A.43.....	227
Figure A.37. Transient photocurrent decay experimental ‘Block Diagram’ step 5: Apply the set parameters.....	228
Figure A.38. Transient photocurrent decay experimental ‘Block Diagram’ step 6: collect the data. This code can be found in Figure A.42. ....	229
Figure A.39. Transient photocurrent decay experimental ‘Block Diagram’ step 7: turn everything off and disconnect the potentiostat.....	230
Figure A.40. Transient photocurrent decay experimental ‘Block Diagram’ step 8: baseline the data and calculated the photocurrent lifetime. ....	231
Figure A.41. Transient photocurrent decay experimental ‘Block Diagram’ step 9: plot the data and export the results as a .TDMS file.....	232
Figure A.42. Transient photocurrent decay Collect Data ‘Block Diagram.’ An internal time counter is used to define the pulse time and trigger the start of data acquisition. This process is repeated a defined number of times and averaged. ....	233
Figure A.43. Transient photocurrent decay Set Current Spike ‘Block Diagram.’ The STRiVE adjusts the pulse time and monitors the current spike. The 3 most recent spikes are fit to more accurately determine the next pulse time. ....	234
Figure A.44. STRiVE 5.0 user interface ‘Block Diagram’ selecting the fifth experiment, charge extraction. ....	235
Figure A.45. Charge extraction ‘Block Diagram’ displaying how multiple experiments are performed and displayed .....	236
Figure A.46. Charge extraction experimental ‘Block Diagram’ step 1: define the experimental parameters. ....	237

Figure A.47. Charge extraction experimental ‘Block Diagram’ step 2: set the light intensity. As shown the STRiVE will find the light intensity for a given $V_{OC}$ . This code can be found in Figure A24-27.....	238
Figure A.48. Charge extraction experimental ‘Block Diagram’ step 3: perform the experiment and average the data. ....	239
Figure A.49. Charge extraction experimental ‘Block Diagram’ step 4: integrate the current to calculate the charge extracted. This code can be found in Figure A.52. ....	240
Figure A.50. Charge extraction experimental ‘Block Diagram’ step 5: display the results and export the data as a .TDMS file. ....	241
Figure A.51. Charge extraction collect data ‘Block Diagram.’ Use the digital output to switch between open and short-circuit and trigger acquisition. ....	242
Figure A.52. Charge extraction integrate current and calculate charge extracted ‘Block Diagram.’.....	243
Figure A.53. STRiVE 5.0 user interface ‘Block Diagram’ selecting the sixth experiment, current interrupt voltage.....	244
Figure A.54. Current interrupt voltage ‘Block Diagram’ where multiple experiments are performed and then the results are collected and displayed. ....	245
Figure A.55. Current interrupt voltage experimental ‘Block Diagram’ step 0: start at open-circuit with the light only the light on.....	246
Figure A.56. Current interrupt voltage experimental ‘Block Diagram’ step 1: set the light intensity. ....	247
Figure A.57. Current interrupt voltage experimental ‘Block Diagram’ step 2: perform the experiment a defined number of times and average the results. The code to collect the data can be found in Figure A.61. ....	248
Figure A.58. Current interrupt voltage experimental ‘Block Diagram’ step 3: display the data. ....	249
Figure A.59. Current interrupt voltage experimental ‘Block Diagram’ step 4: turn off the potentiostat, lights, and leave cell at open-circuit.....	250
Figure A.60. Current interrupt voltage experimental ‘Block Diagram’ step 5: export the data as a .TDMS file. ....	251
Figure A.61. Current interrupt voltage Collect Data ‘Block Diagram.’ An internal time counter is used to switch between short and open-circuit and trigger the start of data acquisition.....	252

Figure A.62. STRiVE 5.0 user interface ‘Block Diagram’ selecting the seventh experiment, open-circuit photovoltage decay.....	253
Figure A.63. Open-circuit photovoltage decay ‘Block Diagram’ where multiple experiments are performed and then the results are collected and displayed. ....	254
Figure A.64. Open-circuit photovoltage decay experimental ‘Block Diagram’ step 0: start with everything off. ....	255
Figure A.65. Open-circuit photovoltage decay experimental ‘Block Diagram’ step 1: set the light intensity. As shown the STRiVE adjusts the light intensity to produce the defined $V_{OC}$ . This code can be found in Figures A.24-27. ....	255
Figure A.66. Open-circuit photovoltage decay experimental ‘Block Diagram’ step 2a: collect data when the spacing between data points is greater than 35 ms. In this case, the end condition can be monitored and the experiment will stop when met. ....	256
Figure A.67. Open-circuit photovoltage decay experimental ‘Block Diagram’ step 2b: collect data when the spacing between data points is less than 35 ms. In this case, the end condition cannot be monitored and the experiment will stop when the time is reached. ....	257
Figure A.68. Open-circuit photovoltage decay experimental ‘Block Diagram’ step 3: export the data as a .TDMS file.....	258
Figure A.69. STRiVE 5.0 user interface ‘Block Diagram’ selecting the grouped experiment. ....	259
Figure A.70. Grouped experiments ‘Block Diagram’ showing how shared parameters are set. The rest of the code runs through the experiments similar to as shown above for the STRiVE 5.0.....	260

## LIST OF TABLES

Table 2.1. Photophysical and Electrochemical Properties of Ru(dtb) <sub>2</sub> (dcb)/TiO <sub>2</sub> in 100 mM Metal Perchlorate Acetonitrile Solutions.....	46
Table 2.2. Ionic Radii, Spectral Shifts, and Electric Field Strength for Ru(dtb) <sub>2</sub> (dcb)/TiO <sub>2</sub> .....	53
Table 3.1. TiO <sub>2</sub> (e <sup>-</sup> )+I <sub>3</sub> <sup>-</sup> → Charge Recombination with the Indicated Cations .....	78
Table 4.1. DSSC Figures of Merit from Current-Density Curve in the Indicated Cations .....	91
Table 4.2. TiO <sub>2</sub> DoS, V <sub>oc</sub> , and electron lifetime values relative to DSSCs in Na <sup>+</sup> electrolyte. ....	98
Table 5.1. Reduction Potentials and Ideality Factors for Pyridiniums in Solution and Anchored to TiO <sub>2</sub> .....	119
Table 5.2. UV/Visible Absorption Properties of the Pyridiniums .....	123
Table 6.1. Absorbance onset potentials for SnO <sub>2</sub> and TiO <sub>2</sub> thin films in the indicated 100 mM M <sup>n+</sup> (ClO <sub>4</sub> <sup>-</sup> ) <sub>n</sub> acetonitrile electrolytes .....	148
Table 6.2. Current onset potentials measured by cyclic voltammetry in the indicated 100 mM M <sup>+</sup> (ClO <sub>4</sub> <sup>-</sup> ) acetonitrile electrolytes .....	151

## LIST OF SCHEMES

Scheme 2.1: Structure of $\text{Ru}(\text{dtb})_2(\text{dcb})^{2+}$ .....	40
Scheme 2.2. Schematic Depiction of the Light- and Potentiostatically-Induced Generation of Injected Electrons .....	62
Scheme 4.1. $\text{Ru}(\text{dcb})(\text{dtb})_2(\text{PF}_6)_2$ Structure .....	87
Scheme 5.1 Pyridinium structures .....	113
Scheme 5.2. Energetics of the $\text{TiO}_2$ Acceptor States Compared to Reductive, $V_{\text{red}}$ , and Oxidative, $V_{\text{ox}}$ , Step Potentials for Interfacial Electron Transfer Between the $\text{TiO}_2$ Thin Film and the Conductive Contact, FTO.....	125

## LIST OF EQUATIONS

Equation 1.01 .....	7
Equation 1.02 .....	8
Equation 1.03 .....	8
Equation 1.04 .....	9
Equation 1.05 .....	13
Equation 1.06 .....	17
Equation 1.07 .....	17
Equation 1.08 .....	20
Equation 1.09 .....	20
Equation 1.10 .....	24
Equation 1.11 .....	27
Equation 1.12 .....	27
Equation 1.13 .....	28
Equation 1.14 .....	28
Equation 1.15 .....	29
Equation 1.16 .....	29
Equation 1.17 .....	30
Equation 1.18 .....	30
Equation 1.19 .....	30
Equation 2.01 .....	48
Equation 2.02 .....	48
Equation 2.03 .....	50
Equation 2.04 .....	50
Equation 2.05 .....	51

Equation 2.06 .....	54
Equation 3.01 .....	76
Equation 3.02 .....	77
Equation 3.03 .....	79
Equation 4.01 .....	93
Equation 4.02 .....	99
Equation 4.03 .....	100
Equation 5.01 .....	116
Equation 5.02 .....	120
Equation 5.03 .....	121
Equation 6.01 .....	142
Equation 6.02 .....	144
Equation 6.03 .....	148
Equation 7.01 .....	176
Equation 7.02 .....	181
Equation 7.03 .....	185
Equation 7.04 .....	185
Equation 7.05 .....	189
Equation 7.06 .....	189
Equation 7.07 .....	193

## CHAPTER 1: INTRODUCTION

### 1.1 The case for solar energy

The industrial revolution brought forth unprecedented power through the burning of energy rich fossil fuels that provided ample energy to forever change transportation, manufacturing, and nearly every aspect of daily life. Such power came with a price: the release of carbon dioxide into the atmosphere at rates never before recorded. Carbon dioxide is a known greenhouse gas, meaning it absorbs infrared light and converts it into thermal energy in the atmosphere. Global temperatures for the past 400,000 years have correlated with CO<sub>2</sub> concentration.<sup>1</sup> By 1950, CO<sub>2</sub> levels had surpassed 300 ppm, a concentration not recorded for the past 400,000 years and in 2016,<sup>1,2</sup> the concentration remained above the landmark 400 parts per million (ppm) threshold for the entire year.<sup>3</sup> There is ample evidence to show that the Earth is warming: an increase in global temperatures, rise in sea level, shrinking ice sheets, and more frequent extreme weather and all consistent with global warming.<sup>4</sup> The financial impact of global warming has already begun, where millions of dollars have been spent relocating people in low-lying regions due to rising sea levels.<sup>5,6</sup> Furthermore, CO<sub>2</sub> uptake by the ocean acidifies the water that harms marine organisms and corals that are sensitive to small changes in pH.

In 2017, humans are predicted to consume energy at an average rate of ~ 20 TW (20 x 10<sup>12</sup> W).<sup>7</sup> The United States alone consumes ~3.3 TW or ~ 16.5 % of the world energy consumption despite representing only 4.4 % of the world population.<sup>8</sup> By 2040, global energy uses are projected to increase to by 37 %, with a large fraction from by developing

countries. For example, the United States is expected to consume only ~6.7 % more energy while India is expected to consume ~110 % more energy.<sup>7</sup> From an environmental point of view the global increase in energy demand is frightening. The current rate of CO<sub>2</sub> release may already lead to irreversible global warming,<sup>9-11</sup> making efforts to decrease CO<sub>2</sub> production urgently needed.

In order to minimize CO<sub>2</sub> release and provide a sustainable future, alternative (non-fossil fuel) sources of power must be developed. Alternative energy sources are unlikely to completely replace fossil fuels as the main source of power in the foreseeable future, however, they can still have a significant impact by providing the 37 % energy increase that will help keep CO<sub>2</sub> production near current levels. One promising source of alternative energy is the sun. Solar illumination provides ~175,000 TW of power constantly to the earth. About 30 % is scattered and 20% absorbed by the surface,<sup>12</sup> resulting in ~90,000 TW reaching the surface that has the potential to be harnessed for human use.<sup>13</sup> Capturing just 0.015 % of the solar flux could power all current human needs. Using 10 % efficient solar cells, this would require about 0.17% of the earth's surface. For the United States (~3.3 TW), an area about the size of North Dakota would be required, which is comparable to the land covered by public roads.<sup>13</sup>

Most commercial solar cells use semiconductors to absorb the solar energy and separate charges to produce electrical power. The amount of light absorbed is directly related to the current, where one photon typically gives one electron. The probability a particular photon will be absorbed depends on the photon energy and the semiconductors bandgap, where essentially all photons with energy greater than the bandgap will be absorbed. Since

the maximum cell voltage is determined by the bandgap, this single property is critical when designing a solar cell.

All solar cell devices are defined by the amount of power (voltage x current) produced when illuminated with sunlight. Current is maximized by using a lower bandgap material that absorbs more photons, while voltage is optimized with a larger bandgap. Therefore, the bandgap must be chosen based on the solar spectrum to maximize power. The ideal bandgap can be calculated using the terrestrial solar spectrum, shown in Figure 1.01A<sup>14</sup> compared to an ideal blackbody emitter. The ideal blackbody spectrum differs from the theoretical AM 1.5 spectrum measured on the surface of the Earth due to absorption and scatter. Assuming 100 % of the incident photons with energy greater than or equal to the bandgap are absorbed and are collected and with the energy of the bandgap, an ideal bandgap of the semiconductor can be estimated, Figure 1.01B. For the terrestrial solar spectrum, the ideal absorption onset corresponds to a wavelength of 1108 nm, or a bandgap of 1.12 eV. However, any onset between 910 and 1380 nm (1.36 to 0.89 eV) is expected to differ by  $\leq 5$  %. The bandgap of silicon (1.1 eV = 1130 nm) lies in the middle of this range and is one reason for the dominance of Si solar cells in the industry.

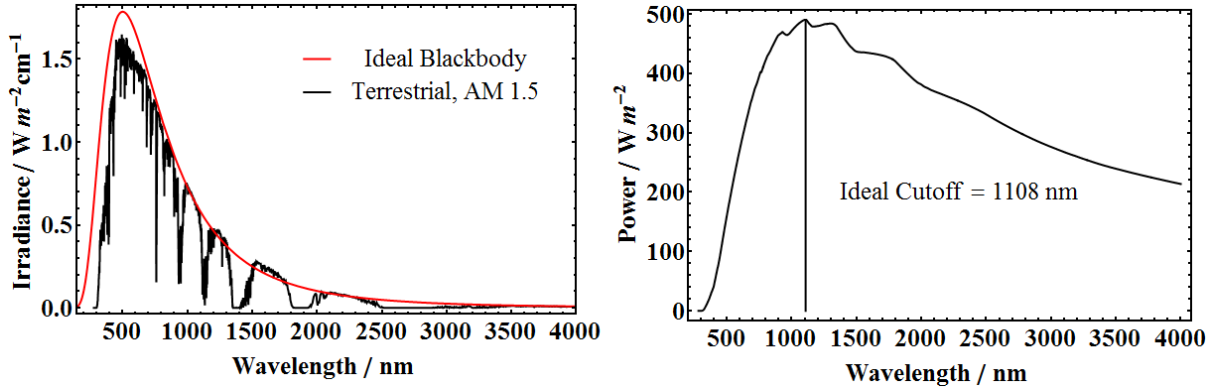


Figure 1.01. (A) Solar irradiance measured on the Earth's surface (terrestrial, black) compared to an ideal blackbody emitter at 5778 K (red). (B) Theoretical power output of a 100 % efficient solar cell absorbing all photons of higher energy than the cutoff value. The maximum power is termed the 'ideal cutoff.'

Although silicon solar cells are the most common and are decreasing in price rapidly,<sup>15</sup> they do not collect diffuse light efficiently, are still relatively expensive, and require high purity materials. An alternative solar cell that excels in all of these areas is the dye-sensitized solar cell. Due to the unique morphology, it collects diffuse light quite well and requires low purity  $TiO_2$  as a foundation, which allows for low fabrication costs.

## 1.2 The dye-sensitized solar cell

The possibility that solar energy could power present and future energy demands and a global awareness of climate change has led to increased public interest in solar power. One device that has received considerable interest over the past 25 years is the dye-sensitized solar cell (DSSC), popularized by Brian O'Regan and Michael Grätzel in 1991.<sup>16</sup> The DSSC uses molecular dyes to absorb light and transfer an electron into a wide bandgap semiconductor, typically  $TiO_2$ . The term 'sensitization' refers to the ability of a surface

bound dye to absorb (visible) photons and induce a photoelectric effect that was absent without the dye.

Sensitization was first observed over 100 years ago.<sup>17,18</sup> Dye-sensitization was studied on TiO<sub>2</sub> in the 1970s, but was hindered by the maximum amount of sunlight that could be harvested (< 1%) with a monolayer of dyes on a flat surface.<sup>19</sup> Better light absorption was achieved by having thick (~1 μm) dye layers, however this resulted in poor electron collection efficiencies due to the low exciton diffusion length.<sup>20</sup> The breakthrough design was to use a mesoporous thin film composed of small (~20 nm diameter) TiO<sub>2</sub> nanocrystallites that gave an active surface layer ~1000 times larger than the top down, geometric surface area. This method proved to have both high charge collection efficiencies and high light absorption producing record efficiencies of 7-8 %.<sup>16</sup> Two advantages of DSSCs over conventional silicon-based solar cells are the tunability, which is directly controlled by the dye, and the cost of fabrication, which has the potential to be very low due to the low purity requirement and high availability of TiO<sub>2</sub>.

A schematic diagram showing the basic electron transfer processes in a typical DSSC is shown in Figure 1.02. Solar energy is absorbed by the sensitizer to form an excited state on the surface. Excited-state electron injection into the TiO<sub>2</sub> acceptor states is often thermodynamically favorable and occurs on the fs-ps timescale with near unit efficiency. The oxidized sensitizer is then regenerated by a redox mediator, R<sup>+0</sup>, on the ns-μs timescale while the injected electron diffuses to the fluorine-doped tin oxide (FTO) back contact on the μs-ms timescale. After reaching the back contact, the electron travels through an external circuit where it can perform work before reducing the oxidized form of the redox mediator at a platinized counter electrode, completing the circuit.

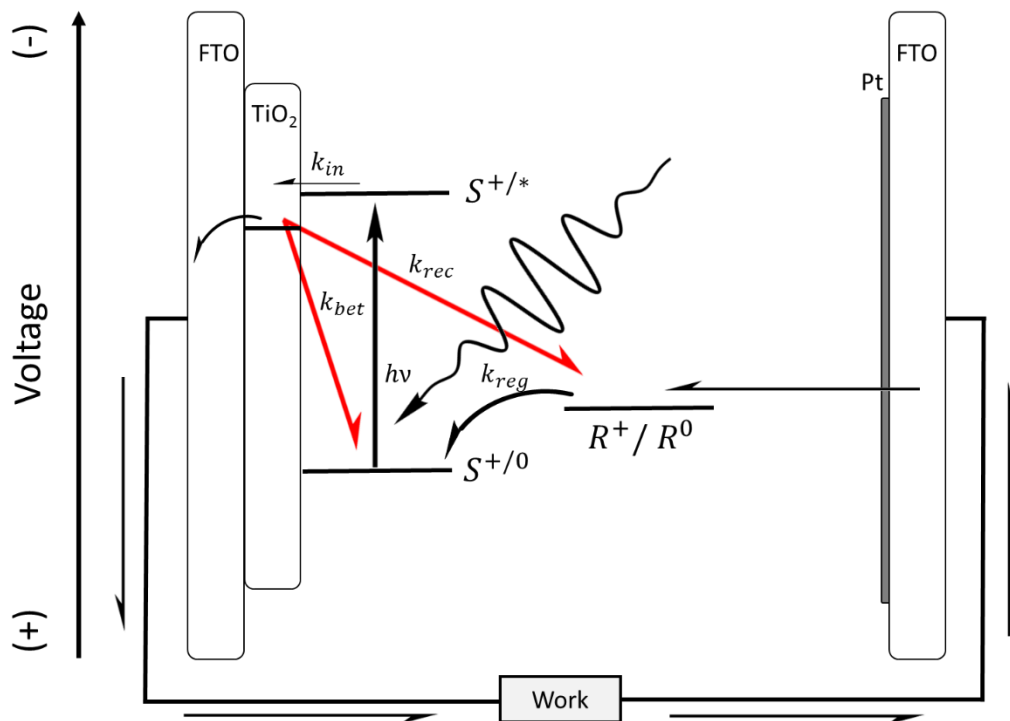


Figure 1.02. Schematic diagram of the desired (straight/curved black arrows) and unwanted (red arrows) electron transfer processes in a DSSC following light ( $h\nu$ , squiggly arrow) absorption by the sensitizer, S. Also included is a general redox mediator,  $R^{+0}$ , that mediates electron transfer between the oxidized sensitizer and the Pt counter electrode.

Two prominent electron loss pathways exist that prevent all the injected electrons from being collected: back electron transfer to the oxidized sensitizer and charge recombination to the oxidized redox mediator. Charge recombination is usually negligible at short circuit where electrons spend relatively short periods of time in the TiO<sub>2</sub> thin film. However, at the maximum power output of the cell or at open circuit, electron loss due to back electron transfer and charge recombination decrease device performance.<sup>21,22</sup> The average time an electron spends in the film before recombination by any mechanism is

known as the electron lifetime, which largely influences the maximum voltage a cell can build under illumination at open circuit.

As with all solar cells, the current is dictated by number of photons absorbed and collected at the back contact. For DSSCs, the number of photons absorbed is determined by the absorptance spectrum of the dye. The open circuit voltage in DSSCs is not dependent on the metal oxide bandgap, but rather the difference between the quasi-Fermi level of the current collectors, often approximated as the TiO<sub>2</sub> quasi-Fermi level and the potential of solution the redox mediator. Therefore, what controls current and voltage in a DSSC are decoupled and can be independently optimized. Of note, DSSCs are still a single junction solar cell and have the same thermodynamic limits as silicon single junction solar cells. As such, the ‘ideal cutoff’ of ~1100 nm still holds for DSSCs, where absorbing all light of wavelength shorter than 1100 nm leads to the optimum power. The following sections discuss in more detail some individual components of DSSCs related to this dissertation and how they relate to device performance.

### 1.3 Description of the electronic states in TiO<sub>2</sub>

The distribution of electronic states in bulk, single crystal semiconductors is well understood. For metal oxides, the valance band is typically formed by overlap of the oxygen p-orbitals and the conduction band by metal d-orbitals. In an ideal case, the density of states as a function of energy,  $N(E)$ , shows a parabolic dependence on energy as given by Equation 1.01:<sup>23</sup>

$$N(E) = \frac{1}{2\pi^2\hbar^3} (2m^*)^{3/2} E^{1/2} \quad 1.01$$

where  $m^*$  is the effective mass,  $\hbar$  is Plank’s constant divided by  $2\pi$ , and  $E$  is the potential.

The density of states is position independent within the bulk semiconductor, but is perturbed at the surface when placed in contact with a redox electrolyte. Equilibrium occurs by spontaneous electron transfer across the semiconductor-electrolyte interface until the Fermi levels align. For the case of n-type metal oxides such as TiO<sub>2</sub>, electrons are usually transferred from the semiconductor to the electrolyte. Excess charge within the semiconductor is not completely screened due to the low charge carrier density. This results in a space-charge or depletion layer where the majority carrier (electrons) are depleted at the interface relative to the bulk. In the region where the charge is not fully screened, an ‘internal’ electric field within the semiconductor exists such that an electron placed within the semiconductor at the interface would migrate away from the interface towards the bulk.

The electric potential and width of the space-charge layer can be calculated by solving Poisson’s equation with the appropriate boundary conditions. For a flat surface extending infinite distance in the x and y directions, the 1-D Poisson equation has been solved where the voltage and width of the space charge layer as a function of distance from the interface, z, is given in Equations 1.02 and 1.03:

$$V(z) = -\frac{eN_d}{2\epsilon\epsilon_0} (z - w)^2 \quad 1.02$$

$$w = \sqrt{\frac{2\epsilon\epsilon_0}{eN_d}} \quad 1.03$$

where, e is the (positive) elementary charge,  $N_d$  is the number of donors, w is the width of the space charge layer,  $\epsilon$  is the relative permittivity, and  $\epsilon_0$  is the permittivity of free space. With typical values for TiO<sub>2</sub>,  $N_d = 10^{17} \text{ cm}^{-3}$  and  $\epsilon_{\text{TiO}_2} = 100$ , the depletion layer would extend over 300 nm into the semiconductor.

The band bending in thin films of ~20 nm diameter TiO<sub>2</sub> nanocrystallites used in DSSCs is much different due to the shape and small size of the nanocrystallites. For particles of this size, the width of the depletion layer calculated for a flat interface would be much larger than the particle diameter. Furthermore, the interface of the spherical nanocrystallites are not accurately approximated as an infinitely flat surface. Albery and Bartlett solved Poisson equation for the case for a spherical nanoparticle, which results in the maximum potential difference between the center of the particle of radius r and the surface according to Equation 1.04:<sup>24,25</sup>

$$V_{max} = \frac{e r^2 N_d}{6 \epsilon \epsilon_0} \quad 1.04$$

For typical doping densities of a 10<sup>17</sup> cm<sup>-3</sup>,  $\epsilon_{\text{TiO}_2}=100$ , the potential difference between the interface and the center would be less 1 mV, much less than thermal energy,  $k_B T/e \approx 26$  mV. The result is that no conventional, i.e. internal, electric field and no significant band-bending occurs in 20 nm diameter TiO<sub>2</sub> nanocrystallites.

The morphological complexity of the nanocrystalline, mesoporous TiO<sub>2</sub> thin films with a large number of grain boundaries and surface sites suggests that localized states may be more relevant than carriers in delocalized bonds. Indeed, there appears to be an exponential distribution of localized acceptor states that may or may not be composed of ‘conduction band’ states. The ideal DOS is compared to the experimentally observed acceptor state distribution in Figure 1.03.

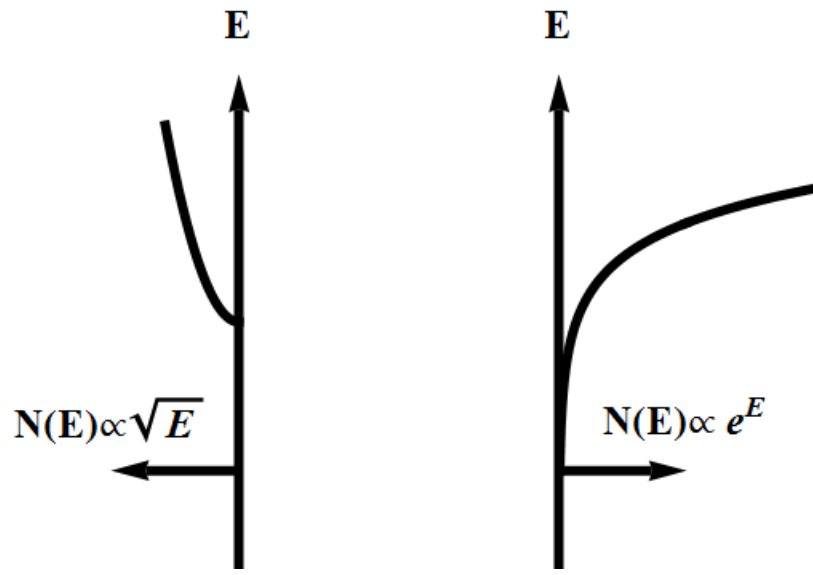


Figure 1.03. Theoretical energetic dependence of the density of states,  $N(E)$ , for a bulk semiconductor (left) and the experimentally observed density of states for mesoporous thin films of ~20 nm diameter  $\text{TiO}_2$  nanocrystallites (right).

Electrochemical reduction of  $\text{TiO}_2$  thin films results in population of the acceptor states and charge compensation by the electrolyte cation. However, it is experimentally difficult to ascertain whether the charge compensation mechanism involves cation adsorption to the surface or intercalation into the lattice. The intercalation of  $\text{Li}^+$  cations is known to occur in bulk<sup>26,27</sup> and nanostructured<sup>28</sup>  $\text{TiO}_2$  where the maximum Li/Ti ratio is  $\frac{1}{2}$ , corresponding to  $\text{Li}_{0.5}\text{TiO}_2$ . The intercalation behavior has been studied by in-situ X-ray diffraction by van de Krol et. al. when the  $\text{TiO}_2$  thin film was immersed in 1M  $\text{LiClO}_4$  propylene carbonate electrolyte.<sup>28</sup> A change in crystal structure was observed above at Li/Ti ratios above 5 %  $\text{Li}^+$ , indicating that intercalation was clearly occurring. However, this study could not identify the charge compensation mechanism below 5 %. Intercalation could be

present where the TiO<sub>2</sub> was able to support the addition of small amount of cations without lattice distortions, however cation adsorption may also have been present.

New insights were gained by carefully monitoring the UV/Vis spectrum of the TiO<sub>2</sub> thin film during the application of a negative bias in CH<sub>3</sub>CN electrolytes.<sup>29</sup> When a small amount of charge was transferred to the thin film, broad, superimposable UV/Vis absorption spectra were observed. The spectra bear some similarity to a classical Drude absorption for free electrons in a conduction band, where adjustments due to phonon scattering and ion impurities have been used for TiO<sub>2</sub> thin films to account for the discrepancies.<sup>30</sup> Furthermore, the spectrum was independent of the identity of the electrolyte cation and was observed with the non-intercalating tetrabutylamminium cation as the charge compensating ion. Therefore, the spectra taken under mildly reducing conditions are attributed to the population of the TiO<sub>2</sub> acceptor states without significant cation intercalation. Further reduction of the TiO<sub>2</sub> thin films results in a quantitatively different spectrum. The spectrum has a clear peak near 700 nm that is attributed to a more localized transition related to Li<sup>+</sup> intercalation into the lattice.<sup>29,30</sup>

The type of electronic state that is reduced upon application of mild biases is debated in the literature.<sup>31,32</sup> The primary differences between the models is the number of electronic states present. One theory is that there are multiple types of states and that the electron is typically localized or trapped, perhaps at a Ti<sup>III</sup> center, and only transiently occupies a higher lying 'conduction band' state. High vacuum (solventless) techniques have provided some evidence for localized Ti<sup>III</sup> trapped states below a conduction band.<sup>33,34</sup> In aqueous electrolytes, a pre-peak is often observed before bulk reduction in cyclic voltammetry experiments that may be associated with a small absorbance signature.<sup>35</sup> However, in CH<sub>3</sub>CN

electrolytes, superimposable UV/Vis absorption spectra and a lack of a pre-peak in cyclic voltammograms suggest there is only one type of electron acceptor.

The uncertainty about where the electron resides has become more prevalent when assigning the extinction coefficient of electrons within the thin film. The extinction coefficient has been measured by comparing the total charge within the film to the optical absorbance and is typically near  $1000 \text{ M}^{-1}\text{cm}^{-1}$  at  $700 \text{ nm}$ .<sup>30,36,37</sup> However, Hamman and co-workers have recently argued that the absorption feature is due to a small fraction of the total electron concentration that resides in a conduction band, which is distinct from trapped states where the majority of the electrons reside.<sup>38,39</sup> Using variable temperature spectroelectrochemistry, an extinction coefficient of  $\sim 10,000 \text{ M}^{-1}\text{cm}^{-1}$  for the conduction band electrons was reported. Throughout this dissertation the term ‘acceptor states’ is used to acknowledge the uncertainty in the assignment of the electronic states in nanocrystalline  $\text{TiO}_2$  thin films.

#### **1.4 Influence of electrolyte cations**

Electrolyte pH is known to influence the flatband potential of many bulk metal-oxide semiconductors, including  $\text{TiO}_2$ ,  $\text{SnO}_2$ ,  $\text{SrTiO}_3$ ,  $\text{ZnO}$ ,  $\text{Zn}_2\text{TiO}_4$ , and  $\text{KTaO}_3$ .<sup>40,41</sup> This behavior has been attributed to surface acid/base chemistry related to the protonation state surface oxygen atoms,  $-\text{O}^-/-\text{OH}$ . Determining the flatband potential for mesoporous thin films of anatase  $\text{TiO}_2$  nanocrystallites by the conventional Mott-Schottky approach is precluded by the lack of band bending in the nanocrystallites. Fitzmaurice et. al. applied spectroelectrochemistry to correlate optical changes to the presence of electrons within the thin film,<sup>32</sup> and reported a  $59 \text{ mV/pH}$  dependence on the absorption features in aqueous

electrolyte, indicating the Nernstian behavior of bulk semiconductors extended to nanocrystalline thin films.

When spectroelectrochemical studies were performed in non-aqueous solvents, the identity of the electrolyte cation was found to determine the potential onset where absorption changes were observed.<sup>42</sup> Such cations became known as ‘potential determining ions,’ because they determined the energetic position (akin to the flat band potential) of the TiO<sub>2</sub> acceptor states. For example, the position of the TiO<sub>2</sub> acceptor states was ~1 V more positive in Li<sup>+</sup> than TBA<sup>+</sup> containing electrolyte, where TBA<sup>+</sup> is tetrabutylammonium. The electrolyte cation was thought to be attracted to the negatively charged surface and interact through an adsorption or intercalation mechanism.

Directly related to the energetic position of the TiO<sub>2</sub> acceptor states are the electron injection efficiency,<sup>43</sup> sensitizer photoluminescence,<sup>44</sup> incident-photon-to-current efficiency,<sup>45</sup> and open circuit voltage.<sup>45</sup> The rate of electron injection is understood in the framework of Marcus-Gerischer theory according to Equation 1.05:<sup>46,47</sup>

$$k_{et} = \frac{4\pi^2}{h} \int g(E)f(E, E_F)|H_{AB}|^2W(E)dE \quad 1.05$$

Where  $g(E)$  is the distribution of acceptor (TiO<sub>2</sub>) states,  $f(E, E_F)$  is the Fermi-Dirac function that describes the occupancy of the acceptor states,  $H_{AB}$  is the electronic coupling element, and  $W(E)$  is the distribution of donor states related to solvent fluctuations and the reorganization energy. The rate of electron injection is optimized by increasing the energetic overlap between the donor and acceptor states. For a given sensitizer, the rate of electron injection can be tuned by the electrolyte cation to maximize injection. For example, in Li<sup>+</sup>

containing electrolyte, the energetic overlap between the donor states and the TiO<sub>2</sub> acceptor states is much greater than in TBA<sup>+</sup>, as shown in Figure 1.04.

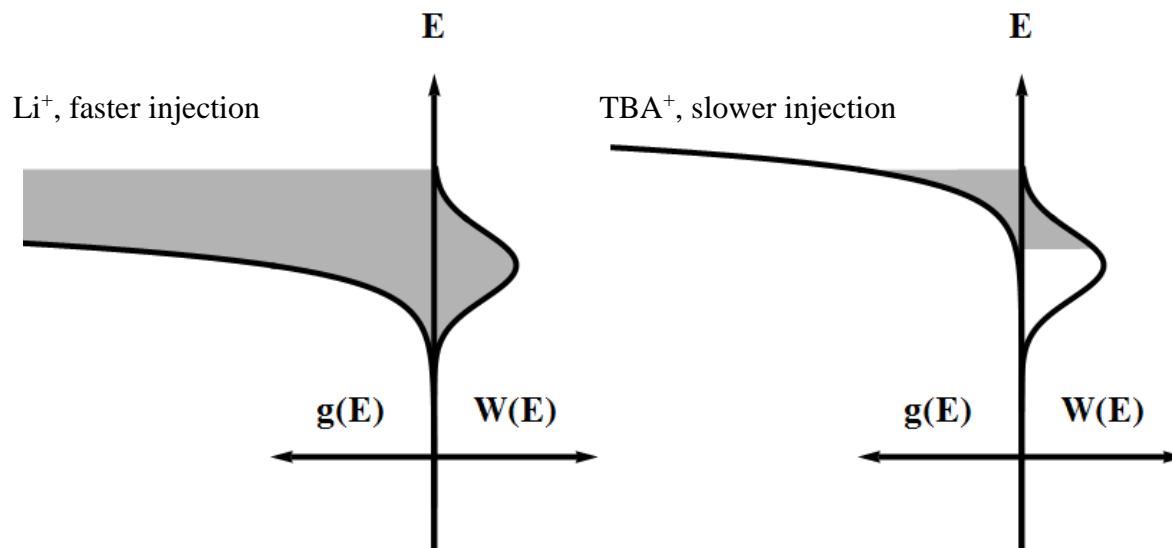


Figure 1.04. Comparison of strong (left, Li<sup>+</sup> containing electrolyte) and weak (right, TBA<sup>+</sup> containing electrolyte) energetic overlap between the electron donors, W(E), and acceptors, g(E), during charge injection into nanocrystalline TiO<sub>2</sub>. The area in gray represents regions of favorable energetic overlap.

Marcus-Gerischer theory describes the rate constant for electron transfer, not the overall quantum yield. Once the excited state is formed, a kinetic competition occurs between injection, radiative, and other non-radiative relaxation pathways. A faster charge injection rate constant leads to a greater fraction of excited chromophores relaxing through injection. In the case of ruthenium polypyridyl compounds used in DSSCs, the rate constant is large enough that unit efficiency can often be realized.

An indirect way to monitor electron injection is sensitizer photoluminescence (PL). Electron injection serves as a quenching mechanism for the excited state and decreases the

PL quantum yield. Kelly et. al. monitored sensitizer PL when the cation identity and concentration was systematically varied.<sup>43</sup> It was found that the degree of quenching correlated with the charge-to-size ratio of the cation and was consistent with the electrolyte cation tuning the energetic position of the TiO<sub>2</sub> acceptor states.

A second indirect measurement of electron injection is the incident-photon-to-current-efficiency (IPCE), sometimes called the external quantum efficiency (EQE). This technique reports the ratio of incident photons illuminating the cell and the number of electrons collected at the back contact. With some assumptions, this serves as a direct comparison of electron injection efficiency. Comparing IPCE values measured in electrolytes containing Lewis-acidic cations such as Li<sup>+</sup> to TBA<sup>+</sup> containing electrolytes indicates significantly less electron injection in TBA<sup>+</sup> containing electrolytes as seen by lower IPCE values.<sup>45</sup>

The open circuit voltage, V<sub>OC</sub>, represents the difference between the quasi-Fermi level of the electrodes, that is often assumed to be the quasi-Fermi level of the TiO<sub>2</sub> electrons versus the potential of the redox mediator. The influence of electrolyte cations on V<sub>OC</sub> is more complicated because the cation influences multiple cell parameters. For example, cations influence the energetic position of the TiO<sub>2</sub> acceptor states and the injection yield, both of which contribute to V<sub>OC</sub>. In general, a higher V<sub>OC</sub> either indicates a higher electron concentration within the thin film or a more negative TiO<sub>2</sub> acceptor state distribution, as depicted in Figure 1.05.

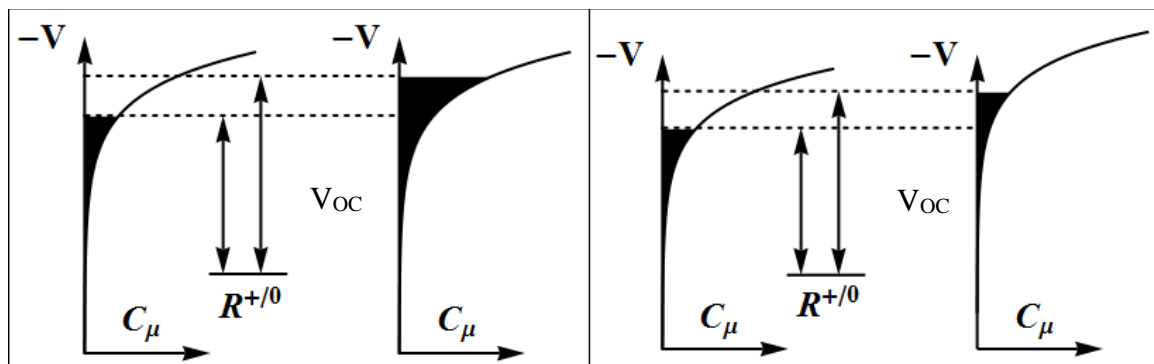


Figure 1.05. Influence of charge density (left) and energetic position (right) of the TiO<sub>2</sub> density of states on open circuit voltage ( $V_{OC}$ , double sided arrows). The  $V_{OC}$  value can be increased by adding more charge carriers to the film or by increasing the energetic position of the TiO<sub>2</sub> acceptor states.

### 1.5 Interfacial electric fields

In this section the detection and influence of local electric fields at dye-sensitized TiO<sub>2</sub> interfaces is discussed. However, it is important to keep in mind that what is typically measured are changes in the electric field following some perturbation. Strong electric fields may exist in the ground state, especially at semiconductor-electrolyte interfaces. These ground-state electric fields are often poorly understood and can cause unavoidably different equilibrium (dark) conditions.

Changes in electric fields, simply referred to hereafter as electric fields, are detected by the UV/Vis absorbance spectra of the dye in what is called an electroabsorption or Stark (sometimes LoSurdo-Stark) effect that was independently discovered by both Johannes Stark and Antonino Lo Surdo in 1913.<sup>48-51</sup> Strong electric fields induce shifts in the UV/Vis

absorbance spectrum that reflect the change in transition energy upon stabilization or destabilization of the ground and excited states in the presence of an electric field.<sup>52</sup>

The extent of (de)stabilization for a single state is usually dominated by the dipole moment,  $\vec{\mu}$ , and/or polarizability,  $\alpha$ , of each state according to Equation 1.06.<sup>53</sup> The electric field influences both the ground and excited states energies such that the observed change in transition energy corresponds to the difference in dipole moment,  $\Delta\vec{\mu}$ , and polarizability,  $\Delta\alpha$ , between the two states according to Equation 1.07:<sup>53</sup>

$$\Delta E_{single\ state}(\vec{E}) = -\vec{\mu} \cdot \vec{E} - \frac{1}{2} \vec{E} \cdot \alpha \cdot \vec{E} \quad 1.06$$

$$\Delta E_{trans}(\vec{E}) = -\Delta\vec{\mu} \cdot \vec{E} - \frac{1}{2} \vec{E} \cdot \Delta\alpha \cdot \vec{E} \quad 1.07$$

Note that these are vector (or tensor,  $\alpha$ ) quantities, which means the relative angle between the two is critically important. In classic Stark experiments, isotropically oriented molecules were immobilized in a rigid matrix between two parallel plate electrodes that were used to apply a unidirectional electric field. In this arrangement, equal numbers of molecules were aligned parallel and anti-parallel to the field, resulting in a broader peak and decreased amplitude, Figure 1.06. We shall now briefly consider how the relative orientation influences spectral shifts caused by dipole moment and polarizability differences separately.

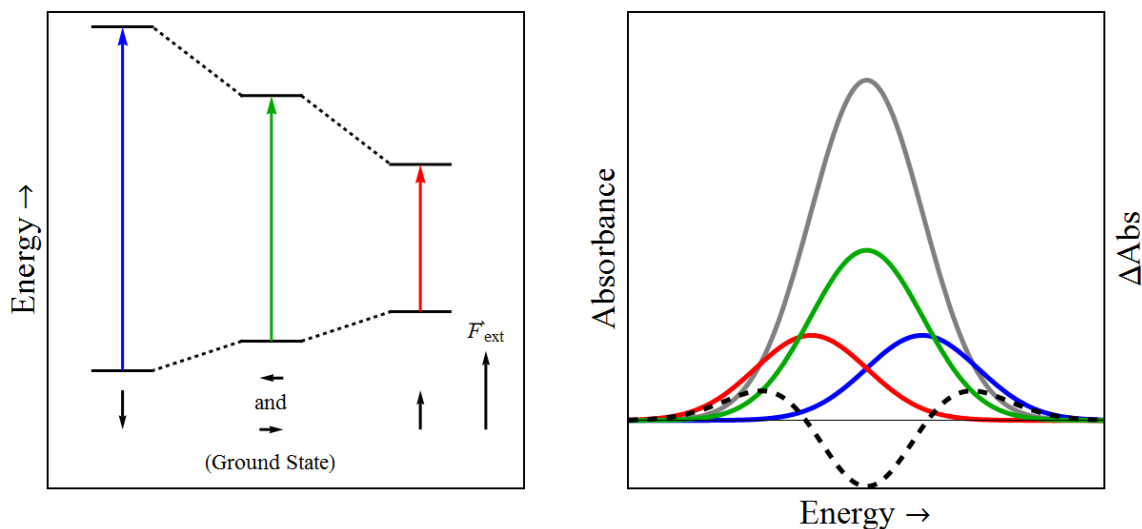


Figure 1.06. (A) Jablonski-type diagram depicting the ground and excited state energies for molecules aligned antiparallel (blue) orthogonal (green) and parallel (red) to the electric field,  $F_{\text{ext}}$ . Note the transition energy for the orthogonal transition is identical to the ground state transition energy. (B) UV/Vis spectra of an arbitrary transition in the presence of an electric field (gray). Also shown are the individual contributions for molecules oriented parallel (red), orthogonal (green) and antiparallel (blue) to the electric field.

The dipole moment represents the unequal distribution of charge in the molecule that is taken as a constant even in the presence of an electric field. Therefore, a given molecular state will either be stabilized or destabilized by the electric field due to the orientation between the two. When the ‘field-on’ spectrum of immobilized, isotropically oriented molecules is compared to the ‘field-off’ spectrum, the peak broadens and decreases in height due to the stabilization of some molecules and destabilization of others. The difference between these spectra can be well modelled by the second derivative of the ground state absorption spectrum as described by Liptay.<sup>54</sup>

The polarizability represents the ability of a molecule to redistribute its charges in response to an electric field. The polarizability acts as an induced dipole moment or a correction to the constant dipole moment in the presence of an electric field. The redistribution of charge occurs such that the net field across the molecule is minimized, which means that the induced dipole moment is typically aligned with the electric field regardless of the molecular orientation. The result is typically a stabilization of both the ground and excited states, however the magnitude of the stabilization may be different for the two states leading to either a red or blue shift for all molecules, regardless of orientation. Therefore, ‘field-on’ minus ‘field-off’ spectral changes due only to  $\Delta\alpha$  can be well-described by the first derivative of the ground state absorption spectrum because the transition energy increases (or decreases) for all molecules.

The electric fields detected in DSSCs represent a unique situation. In these materials, the anchoring of the chromophore to the surface dictates a limited range of binding angles and orientations between the molecule and the surface. Since these electric fields emanate from the surface, the molecules are oriented relative to the field. Every molecule exists in a similar orientation relative to the field which results in similar (de)stabilizations due to  $\Delta\vec{\mu}$  and  $\Delta\alpha$  for all molecules. The resulting spectral shift is unidirectional and well-fit by the first-derivative of the ground state absorption spectrum even for molecules whose change in dipole moment dictate the Stark spectrum. To distinguish between shifts caused by  $\Delta\vec{\mu}$  and  $\Delta\alpha$ , the field-dependence of the Stark spectrum must be investigated because  $\Delta\vec{\mu}$  scales with  $\vec{E}$  while  $\Delta\alpha$  scales with  $\vec{E}^2$ .

Experiments performed in our lab typically employ ruthenium poly-pyridyl compounds as dyes or sensitizers whose UV/Vis absorbance spectrum display metal-to-

ligand charge transfer (MLCT) transitions. In the presence of an electric field, changes in the MLCT excitation energy are dominated by  $\Delta\vec{\mu}$  associated with transferring an electron from the metal center to a ligand. The peak shift (in wavenumbers,  $\Delta\tilde{\nu}$ ) is related to the electric field according to Equation 1.08:

$$\Delta\tilde{\nu} = -\frac{|\Delta\vec{\mu}| \cdot |\vec{E}| \cos\theta}{100 hc} \quad 1.08$$

Where  $h$  is plank's constant,  $c$  is the speed of light,  $\Delta\vec{\mu}$  is the change in dipole moment between the ground and excited state,  $\vec{E}$  is the electric field magnitude,  $\theta$  is the angle between  $\Delta\vec{\mu}$  and  $\vec{E}$ , and 100 is a conversion factor between m and cm. Due to the broad nature of the MLCT bands, precisely determining the peak maximum (do find  $\Delta\tilde{\nu}$ ) is not always trivial. An alternative means to calculate the electric field is by fitting the difference spectrum to the derivative of the ground state spectrum according to Equation 1.09:

$$\Delta A = -\frac{dA}{d\nu} \frac{|\Delta\vec{\mu}| \cdot |\vec{E}| \cos\theta}{h} \quad 1.09$$

Where  $\Delta A$  is the difference absorption spectrum and  $dA/d\nu$  is the first derivative of the absorption spectrum in wavenumbers. This method generally provides more accurate results as there are more data points in the fit than a single point estimation of spectral shifts. For our calculations, it has been assumed that  $\theta = 180^\circ$ , which corresponds to the electron transfer from the Ru center to the anchoring ligand as normal to the surface.

The UV/Vis absorbance spectra of sensitized TiO<sub>2</sub> that is consistent with the presence of an electric field has been quantified in three independent experiments: following the

addition of  $\text{Li}^+$  to the acetonitrile electrolyte, upon electrochemical reduction of the  $\text{TiO}_2$  thin film, and following excited-state electron injection into  $\text{TiO}_2$  nanocrystallites. We will briefly discuss the evidence for electric fields and then several studies reporting the influence electric fields may have on device performance.

**Stark shifts with cation addition:** Addition of Lewis-acidic  $\text{Li}^+$  cations to the electrolyte surrounding a sensitized  $\text{TiO}_2$  thin film resulted in a large bathochromic (red) shift of both the MLCT absorbance and PL spectrum relative to that in neat  $\text{CH}_3\text{CN}$ , consistent with a decrease in the surface electric field.<sup>55</sup> The as-synthesized  $\text{TiO}_2$  nanoparticles are thought to have a negative charge on the surface caused by the deprotonation of surface Ti-OH groups.<sup>56,57</sup> The cationic  $\text{Li}^+$  ions would be attracted to the negatively charged surface and partially screen the surface electric field.

However, the location of the  $\text{Li}^+$  cations that screen the field is still unknown. Due to the direction of the shift, it is clear that net electric field reported by the sensitizer is attenuated indicating the cations reside within the Helmholtz layer, however it is unknown if they interact more directly with the  $\text{TiO}_2$  surface or the chromophore. It is known that related ruthenium complexes that differ from the compounds discussed here by the protonation state of the carboxylic acid (having deprotonated carboxylates instead of the carboxylic acids here) display similar red shifts upon  $\text{Li}^+$  addition in fluid solution.<sup>58</sup> In fluid solution, the red-shift was attributed to the Lewis-acidic cations interacting with carboxylate groups on the bipyridine ligands, but it was stated that inductive effects could not be distinguished from electric field effects. If direct interactions were occurring on the  $\text{TiO}_2$  surface, the chromophore would be expected to desorb. Since these shifts have been reported for chromophores with only one binding group without desorption,<sup>59</sup> it is likely that the

cations reside near the chromophore, but do not outcompete the TiO<sub>2</sub> surface for binding to the carboxylate anchoring group.

**Stark shift from excited-state electron injection:** Nanosecond pulsed laser excitation of sensitized TiO<sub>2</sub> thin films immersed in 100 mM LiClO<sub>4</sub> and 250 mM tetrabutylammonium iodide (TBAI) results in MLCT excitation and excited-state electron injection into the TiO<sub>2</sub> thin film on the fs to ps timescale and then regeneration of the oxidized sensitizer by iodide within 1 μs. The regeneration and recombination reactions were monitored by nanosecond transient absorption spectroscopy. Following sensitizer regeneration, the expected spectral signatures of TiO<sub>2</sub>(e<sup>-</sup>)s and triiodide were observed. However, in addition to these expected features, a large first-derivative shape consistent with a Stark shift of the ground-state MLCT transition was observed.<sup>55,60,61</sup> This feature was most easily seen when the oxidized chromophore was regenerated, but has also been identified in previous data from our group and others that did not regenerate the oxidized chromophore.<sup>60</sup>

**Stark shift from potentiostatically injected electrons:** Further support for the assignment of the spectral shifts as an electric field effect was found when sensitized TiO<sub>2</sub> thin films were employed as the working electrode in a standard 3-electrode setup. Application of forward (negative) bias to thin films immersed in 100 mM LiClO<sub>4</sub> acetonitrile electrolytes resulted in population of the TiO<sub>2</sub> acceptor states which could be quantified by the broad absorption of TiO<sub>2</sub> electrons (TiO<sub>2</sub>(e<sup>-</sup>)s) across the UV/Vis spectrum. At the same time, a blue-shift of the MLCT transition of surface-bound chromophore was observed consistent with a Stark effect.<sup>60</sup>

**Spatial extent of electric field:** The discovery of electric fields in dye-sensitized solar cells was surprising to some since macroscopic parameters, i.e. electron diffusion instead of migration within the mesoporous thin films, did not suggest their presence. Perhaps the injected electron resided as a localized electron on a  $\text{Ti}^{\text{III}}$  ion as a ‘trapped electron’ and only effected a single chromophore that did not affect bulk properties. In this light, two studies were conducted to investigate the spatial extent the electric field extended at the interface.

In the first,  $\text{TiO}_2$  thin films were co-sensitized with two sensitizers whose absorption spectra were distinct enough to permit selective excitation and monitoring of each sensitizer. Selective excitation of one chromophore resulted in excited-state electron injection and sensitizer regeneration. Transient difference spectra recorded at 1  $\mu\text{s}$  after the laser pulse displayed first-derivative features for *both* sensitizers. This clearly indicated that the electric field extended to laterally across the surface. The magnitude of the spectral shifts indicated that at least two neighboring sensitizers were maximally affected by the electric field, although this result was indistinguishable from a higher number of nearby sensitizers being effected to a lesser extent.

In the second study, a series of ruthenium compounds were synthesized where the distance between a surface anchoring group and the ruthenium center was systematically varied with phenylene ethynylene bridge units between the anchoring group and the ruthenium. The surface to Ru distances were estimated to range from 7 to 18.6  $\text{\AA}$ .<sup>62</sup> As the distance from the surface increased, the magnitude of the measured field decreased from 0.85 with zero bridge units to 0.22 MV/cm with two phenylene ethynylene units.<sup>62</sup> Together, these studies indicate electric fields extend nanometers across the surface and into solution.

**Non-Nernstian redox behavior:** The redox behavior of the dyes in dye-sensitized TiO<sub>2</sub> thin films has been reported to deviate from the Nernst equation, where a 59 mV change in applied potentials is expected to cause a factor of 10 change in the mole fraction of oxidized and reduced species for a one-electron process.<sup>63,64</sup> Instead, it often takes a much larger potential step to achieve a factor of 10 change in the mole fraction. Such data is modelled by the inclusion of an ideality factor,  $\alpha$ , into the Nernst equation, as shown in Equation 1.10. When  $\alpha$  is unity, Equation 1.10 reduces to the Nernst equation. It has been suggested that a distribution of reduction potentials,<sup>65</sup> intermolecular (Frumppkin) interactions,<sup>66,67</sup> or electric fields,<sup>68</sup> may be responsible for this non-Nernstian behavior.

$$E = E^0 - \alpha 59.2 \text{ mV} \log \left( \frac{[R]}{[O]} \right) \quad 1.10$$

Multiple studies have reported the non-ideal behavior to be surface coverage independent, ruling out Frumpkin-type interactions as the cause for non-ideal behavior. There is no a priori reason to believe there should be a distribution of reduction potentials on the surface, however there is evidence that strong electric fields are present at the surface. If surface electric fields were inducing non-Nernstian redox chemistry, the non-ideality is expected to be sensitive to the magnitude of the electric field. This hypothesis could be tested by studying compounds that underwent multiple one-electron reductions, either at the same or different locations, where the electric field was different for each reduction.

A study where both reductions occurred at the same location utilized a cobalt porphryn that underwent Co<sup>III/II</sup> and Co<sup>II/I</sup> reductions on the TiO<sub>2</sub> surface.<sup>63</sup> As the potential was stepped negative, electrons populated the acceptor states causing a surface electric field

proportional to the number of electrons. In TBA<sup>+</sup> containing electrolytes, the TiO<sub>2</sub> acceptor states were negative enough that the first and second reduction occurred with minimal change in the TiO<sub>2</sub>(e<sup>-</sup>) concentration and the ideality factors were within error the same (although still larger than 1). In Li<sup>+</sup> containing electrolytes, the distribution of TiO<sub>2</sub> acceptor states were more positive than in TBA<sup>+</sup> electrolytes. There were significantly more TiO<sub>2</sub>(e<sup>-</sup>)s during the second reduction than the first, corresponding to a larger electric field for the second reduction. A significantly larger ideality factor was observed for the second reduction, consistent with electric-field induced non-Nernstian behavior.

A second study that addressed the electric field influence on non-Nernstian redox behavior utilized a Ru-bridge-TPA, where TPA is triphenylamine, donor- $\pi$ -acceptor complex where both the Ru center and TPA moiety were redox active. The ruthenium center was bound to the surface and was approximately 15 Å closer than the TPA. Electrochemical oxidation was non-Nernstian at both redox centers, but the Ru center showed on average larger non-ideality than the TPA group. These two examples strongly support that electric fields induce the non-Nernstian redox chemistry on the surface of TiO<sub>2</sub>.

## **1.6 Charge transport and recombination in DSSCs:**

Understanding charge transport and recombination in DSSCs is critical for both practical and fundamental purposes. Practically, these two parameters determine the charge collection-and therefore total device- efficiency. The electrons must diffuse through the film and be collected at the back contact faster than they recombine with an oxidizing equivalent at the surface or in solution. A fundamental understanding of what controls transport and recombination therefore allows devices to be designed that optimize charge collection.

Charge transport in mesoporous thin films of TiO<sub>2</sub> nanoparticles has been measured by a number of techniques, including intensity-modulated photocurrent spectroscopy (IMPS),<sup>69</sup> electrochemical impedance spectroscopy (EIS),<sup>70–72</sup> pulsed laser transients,<sup>73</sup> stepped light-induced transient measurements (SLIM),<sup>74,75</sup> and transient photocurrent decay.<sup>11,76–79</sup> Likewise, the electron lifetime (inverse of charge recombination rate) has been investigated with intensity-modulated photovoltage spectroscopy (IMVS),<sup>80</sup> EIS,<sup>70–72</sup> open-circuit voltage decay,<sup>10</sup> and transient photovoltage decay.<sup>81</sup> Neither charge transport nor recombination are constant under all operating conditions (incident light intensity). The term ‘effective’ (effective diffusion coefficient or effective electron lifetime) is often used to highlight that the reported values are reported under specific conditions.

Due to the sensitivity of diffusion/recombination on the operating conditions, it has not always been clear how to compare devices, i.e. what independent variable serves as a reference. Early studies found the electron lifetime to exponentially decrease with voltage<sup>79</sup> and the diffusion coefficient increase with current.<sup>75</sup> Comparisons were therefore made at matched voltage or current values, however this analysis became invalid if the energetic position or density of the TiO<sub>2</sub> acceptor states changed between different DSSCs. With the development of several methods to measure the charge within the thin film,<sup>82,83</sup> it has become increasingly common to use total charge in the illuminated DSSC as the independent variable when investigating both electron lifetime and diffusion.

Electron diffusion and recombination appear to be intimately linked. As the light intensity increases, the effective diffusion coefficients increases while the effective lifetime decreases. Researchers have speculated that transport and recombination are mediated by a trapping/detrapping mechanism that influences both electron transport and recombination in

DSSCs.<sup>11</sup> Dispersive electron transport has been extensively studied for bulk, single crystal semiconductors and is often modelled by a multiple trapping<sup>84-87</sup> or continuous-time random walk<sup>88-90</sup> mechanism, both of which imply a distribution of bandgap states. More recently, a random flight model has been developed for nanostructured thin films, where a trapped electron can thermally access the conduction band and travel much farther than the nearest neighbor.<sup>91</sup> However, most, if not all, recent studies investigating charge transport and recombination in DSSCs are interpreted in the framework of the multiple trapping model as described by Bisquert and Vikhrenko.<sup>92</sup> This theory is the basis for comparing kinetic parameters at matched electron concentrations as summarized below.

The foundation of the multiple trapping model is based on multiple types of electronic states present in the TiO<sub>2</sub> thin film. They are often called conduction band states (that contain mobile electrons) and localized states (where the electron are effectively ‘trapped’,  $n_L$ ). Under steady state conditions, an equilibrium is established between the conduction band and localized electrons. The number of electrons in the conduction band,  $n_c$ , can be calculated for a given quasi-Fermi level,  $nE_F$ , using the total number of conduction band states,  $N_c$ , and the conduction band energy,  $E_c$ , by Boltzmann statistics, Equation 1.11. The occupancy of trapped states,  $f$ , is described by Fermi-Dirac statistics, Equation 1.12:

$$n_c = N_c e^{(nE_F - E_c)/k_b T} \quad 1.11$$

$$f = \frac{1}{1 + e^{(E_L - nE_f)/k_b T}} \quad 1.12$$

It is assumed that an equilibrium between the conduction band and localized states is maintained even when a small perturbation is applied to the total electron concentration

either by a light pulse or a change in the applied bias. This is called the quasi-static approximation and is mathematically represented by Equation 1.13:

$$\frac{dn_l}{dt} = \frac{dn_l}{dn_c} \frac{dn_c}{dt} \quad 1.13$$

The effective electron lifetime,  $\tau_n$ , of the electron is related to the free electron lifetime,  $\tau_0$ , according to Equation 1.14, where the final equality holds when  $\frac{dn_L}{dn_c} \gg 1$ :

$$\begin{aligned} \tau_n &= \left(1 + \frac{dn_L}{dn_c}\right) \tau_0 = \left(1 + \frac{dn_L}{dn_c} \frac{d_n E_F}{dn_c}\right) \tau_0 \\ &= \left(\frac{k_B T}{N_c} \exp\left(\frac{E_c - n E_F}{k_B T_0}\right) g(n E_F)\right) \tau_0 \end{aligned} \quad 1.14$$

Here,  $g(n E_F)$  is the distribution of trapped states that is often experimentally observed to increase exponentially with voltage. Equation 1.14 highlights that it is not the absolute voltage (quasi-Fermi level) applied to the cell that determines the electron lifetime, but the difference between the applied voltage and the conduction band energy,  $(E_c - n E_F)$ . The absolute value of the conduction band energy is influenced by the electrolyte and surface bound species. Therefore, comparisons made between different cells are often inaccurate when done at the same voltage because  $(E_c - n E_F)$  is not the same. Assuming the localized and conduction bands shift together (the relative density and energetic position of the localized and conduction band states is constant),  $(E_c - n E_F)$  will be matched in different cells when the cells have the same total electron concentration. Since it is difficult to determine the conduction band energy in mesoporous thin films of  $\text{TiO}_2$  nanocrystallites, the total charge is often used instead because it can be readily measured. It is worth noting the similarity of this method to measuring kinetic parameters in conventional systems (solution reaction rates, for

example), where the concentration of the reacting species must be explicitly taken into account.

As with the electron lifetime, the electron diffusion coefficient,  $D_n$ , can be expressed relative to the free electron diffusion coefficient,  $D_0$ , according to Equation 1.15:

$$D_n = \left(1 + \frac{dn_L}{dn_c}\right)^{-1} D_0 = \left(\frac{k_B T}{N_c} \exp\left(\frac{E_c - n E_F}{k_B T_0}\right) g(n E_F)\right)^{-1} D_0 \quad 1.15$$

Again it is clear that in this model, comparisons should be performed at matched ( $E_c - n E_F$ ) or total charge. In practice, the same charge often does not coincide with matched operating voltage or incident light intensity. Therefore, measurements are often performed under a wide range of operating conditions and compared over similar values in electron concentration.

Knowing the diffusion coefficient and electron lifetime, the diffusion length,  $L_n$ , defined to be the average distance an electron travels in the thin film before recombination, can be calculated. This model predicts a constant diffusion length according to Equation 1.16.

$$L_n = \sqrt{\tau_n D_n} = \sqrt{\tau_0 D_0} \quad 1.16$$

Reports of the diffusion length as a function of voltage are often observed to generally follow this model, i.e. are constant, however slight differences are often observed that have been attributed to nonlinear recombination or recombination from trapped states.<sup>93-95</sup>

Charge collection efficiency is related to the diffusion length by knowing the thickness of the TiO<sub>2</sub> thin film,  $d$ . If  $L_n \gg d$ , the collection efficiency is essentially unity. However, when  $L_n$  and  $d$  become comparable, electron losses are unavoidable. There have

been several reports of how to relate  $L_n$  to collection efficiency,  $\eta$ , shown in Equations 1.17-1.19:<sup>96</sup>

$$\eta = \frac{L}{d} \tanh\left(\frac{d}{L}\right) \quad 1.17$$

$$\eta = 1 - \frac{\tau_{c,n}}{\tau_{v,n}} \quad 1.18$$

$$\eta = 1 - \frac{\varphi_{oc}(V)}{\varphi_{sc}(V)} \quad 1.19$$

where  $\tau_{c,n}$  and  $\tau_{v,n}$  are the transient photocurrent and photovoltage lifetimes at electron concentration  $n$ , respectively, and  $\varphi_{oc}(n)$  and  $\varphi_{sc}(n)$  are the incident light intensities to generate a given electron concentration within the TiO<sub>2</sub> thin film at open circuit and short circuit, respectively. These methods generally agree for  $L_n/d > 2$ , which corresponds to ~90 % charge collection efficiency, but differ when significant losses occur. It is unclear how a constant diffusion length calculated this way is reconciled with several reports that the collection efficiency decreases at the power point or under open circuit conditions of DSSC.<sup>21,22</sup> It is possible that these authors observed a relatively small fraction of injected electron recombine prior to their impact on transient electronic techniques that measure the response at the collecting substrate.

Investigating the electron lifetime and diffusion coefficient as a function of total charge within the thin films provides a ‘snapshot’ of the fundamental processes governing cell efficiency. During the course of my Ph.D. studies I built an instrument, termed STRiVE for “Sequential Time-Resolved current (i) Voltage Experiments,” that is capable of automatically measuring these parameters under a wide range of operating conditions. For details about the hardware and software, see Chapter 7 and the Appendix.

## REFERENCES

- (1) Petit, J. R.; Jouzel, J.; Raynaud, D.; Barkov, N. I.; Barnola, J.-M.; Basile, I.; Bender, M.; Chappellaz, J.; Davis, M.; Delaygue, G.; et al. Climate and Atmospheric History of the Past 420,000 Years from the Vostok Ice Core, Antarctica. *Nature* **1999**, *399*, 429–436.
- (2) Etheridge, D. M.; Steele, L. P.; Langenfelds, R. L.; Francey, R. J.; Barnola, J.-M.; Morgan, V. I. Natural and Anthropogenic Changes in Atmospheric CO<sub>2</sub> over the Last 1000 Years from Air in Antarctic Ice and Firn. *J. Geophys. Res. Atmos.* **1996**, *101*, 4115–4128.
- (3) Laboratory, E. S. R. Atmospheric CO<sub>2</sub> at Mauna Loa Observatory <https://www.esrl.noaa.gov/gmd/obop/mlo/> (accessed Mar 16, 2017).
- (4) NASA. Climate change: How do we know? <https://climate.nasa.gov/evidence/> (accessed Mar 16, 2017).
- (5) Gillis, J. Flooding of Coast, Caused by Global Warming, Has Already Begun.
- (6) Milman, O.; Ryan, M. Sea Level Rise Is Already Driving People From the Marshall Islands <https://www.wired.com/2016/09/sea-level-rise-already-driving-people-marshall-islands/> (accessed Mar 10, 2016).
- (7) EIA. International Energy Outlook 2016 <https://www.eia.gov/outlooks/aeo/data/browser/#/?id=1-IEO2016&sourcekey=0> (accessed Mar 16, 2017).
- (8) U.S. and World Population Clock, United States Census Bureau <https://www.census.gov/popclock/> (accessed Mar 22, 2017).
- (9) Warrick, J.; Mooney, C. Effects of climate change “irreversible,” U.N. panel warns in report [https://www.washingtonpost.com/national/health-science/effects-of-climate-change-irreversible-un-panel-warns-in-report/2014/11/01/2d49aeec-6142-11e4-8b9e-2ccdac31a031\\_story.html](https://www.washingtonpost.com/national/health-science/effects-of-climate-change-irreversible-un-panel-warns-in-report/2014/11/01/2d49aeec-6142-11e4-8b9e-2ccdac31a031_story.html) (accessed Mar 21, 2017).
- (10) Zaban, A.; Greenshtein, M.; Bisquert, J. Determination of the Electron Lifetime in Nanocrystalline Dye Solar Cells by Open-Circuit Voltage Decay Measurements. *ChemPhysChem* **2003**, *4*, 859–864.
- (11) Schwarzburg, K.; Willig, F. Influence of Trap Filling on Photocurrent Transients in Polycrystalline TiO<sub>2</sub>. *Appl. Phys. Lett.* **1991**, *58*, 2520–2522.
- (12) Wallace, J. M.; Hobbs, P. V. *Atmospheric Science: An Introductory Survey*; Academic Press: San Diego, 1977.
- (13) Tsao, J.; Lewis, N.; Crabtree, G. Solar FAQs. *US Dep. Energy* **2006**, 1–24.
- (14) G173-03, A. Reference Solar Spectral Irradiance: Air Mass 1.5 <http://rredc.nrel.gov/solar/spectra/am1.5/> (accessed Mar 14, 2017).
- (15) International Energy Agency IEA. TECHNOLOGY ROADMAP. In *SpringerReference*; Springer-Verlag: Berlin/Heidelberg, 2014; p 60.
- (16) O’Regan, B.; Grätzel, M. A Low-Cost, High-Efficiency Solar Cell Based on Dye-

Sensitized Colloidal TiO<sub>2</sub> Films. *Nature* **1991**, 353, 737–740.

(17) Moser, J. Notiz Über Verstärkung Photoelektrischer Ströme Durch Optische Sensibilisierung. *Monatsh. Chem* **1887**, 8, 373.

(18) Rigollot, H. Effet Des Matières Colorantes Sur Les Phénomènes Actinoélectrique. *Compt. Rend. Acad. Sci.* **1893**, 116, 873.

(19) Spitler, M. T.; Calvin, M. Electron Transfer at Sensitized TiO<sub>2</sub> Electrodes. *J. Chem. Phys.* **1977**, 66, 4294–4305.

(20) Jaeger, C. D.; Fan, F. F.; Bard, A. J. Semiconductor Electrodes. 26. Spectral Sensitization of Semiconductors with Phthalocyanine. *J. Am. Chem. Soc.* **1980**, 102, 2592–2598.

(21) Li, F.; Jennings, J. R.; Wang, Q. Determination of Sensitizer Regeneration Efficiency in Dye-Sensitized Solar Cells. *ACS Nano* **2013**, 7, 8233–8242.

(22) Robson, K. C. D.; Hu, K.; Meyer, G. J.; Berlinguette, C. P. Atomic Level Resolution of Dye Regeneration in the Dye-Sensitized Solar Cell. *J. Am. Chem. Soc.* **2013**, 135, 1961–1971.

(23) Pankove, J. I. *Optical Processes in Semiconductors*, 1st ed.; Holonyak, N. J., Ed.; Prentice-Hall, Inc.: Englewood Cliffs, NJ, 1971.

(24) Zhang, Z.; Yates, J. T. Band Bending in Semiconductors: Chemical and Physical Consequences at Surfaces and Interfaces. *Chem. Rev.* **2012**, 112, 5520–5551.

(25) Albery, W. J.; Bartlett, P. N. The Transport and Kinetics of Photogenerated Carriers in Colloidal Semiconductor Electrode Particles. *J. Electrochem. Soc.* **1984**, 131, 315–325.

(26) Cava, R. J.; Murphy, D. W.; Zahurak, S.; Santoro, A.; Roth, R. S. The Crystal Structures of the Lithium-Inserted Metal Oxides Li<sub>0.5</sub>TiO<sub>2</sub> Anatase, LiTi<sub>2</sub>O<sub>4</sub> Spinel, and Li<sub>2</sub>Ti<sub>2</sub>O<sub>4</sub>. *J. Solid State Chem.* **1984**, 53, 64–75.

(27) Zachau-Christiansen, B.; West, K.; Jacobsen, T.; Atlung, S. Lithium Insertion in Different TiO<sub>2</sub> Modifications. *Solid State Ionics* **1988**, 28–30, 1176–1182.

(28) van de Krol, R.; Goossens, A.; Meulenkamp, E. A. In Situ X-Ray Diffraction of Lithium Intercalation in Nanostructured and Thin Film Anatase TiO<sub>2</sub>. *J. Electrochem. Soc.* **1999**, 146, 3150–3154.

(29) van de Krol, R.; Goossens, A.; Meulenkamp, E. A. Electrical and Optical Properties of TiO<sub>2</sub> in Accumulation and of Lithium Titanate Li<sub>0.5</sub>TiO<sub>2</sub>. *J. Appl. Phys.* **2001**, 90, 2235–2242.

(30) Boschloo, G.; Fitzmaurice, D. Electron Accumulation in Nanostructured TiO<sub>2</sub> (Anatase) Electrodes. *J. Electrochem. Soc.* **2000**, 147, 7860–7868.

(31) Cao, F.; Oskam, G.; Searson, P. C.; Stipkala, J. M.; Heimer, T. a; Farzad, F.; Meyer, G. J. Electrical and Optical Properties of Porous Nanocrystalline TiO<sub>2</sub> Films. *J. Phys. Chem.* **1995**, 99, 11974–11980.

- (32) Rothenberger, G.; Fitzmaurice, D.; Graetzel, M. Spectroscopy of Conduction Band Electrons in Transparent Metal Oxide Semiconductor Films: Optical Determination of the Flatband Potential of Colloidal Titanium Dioxide Films. *J. Phys. Chem.* **1992**, *96*, 5983–5986.
- (33) Schwanitz, K.; Mankel, E.; Hunger, R.; Mayer, T.; Jaegermann, W. Photoelectron Spectroscopy at the Solid–Liquid Interface of Dye–Sensitized Solar Cells: Unique Experiments with the Solid–Liquid Interface Analysis System SoLiAS at BESSY. *Chim. Int. J. Chem.* **2007**, *61*, 796–800.
- (34) Schwanitz, K.; Weiler, U.; Hunger, R.; Mayer, T.; Jaegermann, W. Synchrotron-Induced Photoelectron Spectroscopy of the Dye-Sensitized Nanocrystalline TiO<sub>2</sub>/Electrolyte Interface: Band Gap States and Their Interaction with Dye and Solvent Molecules. *J. Phys. Chem. C* **2007**, *111*, 849–854.
- (35) Boschloo, G.; Fitzmaurice, D. Spectroelectrochemical Investigation of Surface States in Nanostructured TiO<sub>2</sub> Electrodes. *J. Phys. Chem. B* **1999**, *103*, 2228–2231.
- (36) Berger, T.; Anta, J. A.; Morales-Flórez, V. Electrons in the Band Gap: Spectroscopic Characterization of Anatase TiO<sub>2</sub> Nanocrystal Electrodes under Fermi Level Control. *J. Phys. Chem. C* **2012**, *116*, 11444–11455.
- (37) Kay, A.; Humphry-Baker, R.; Graetzel, M. Artificial Photosynthesis. 2. Investigations on the Mechanism of Photosensitization of Nanocrystalline TiO<sub>2</sub> Solar Cells by Chlorophyll Derivatives. *J. Phys. Chem.* **1994**, *98*, 952–959.
- (38) Ondersma, J. W.; Hamann, T. W. Conduction Band Energy Determination by Variable Temperature Spectroelectrochemistry. *Energy Environ. Sci.* **2012**, *5*, 9476.
- (39) Mandal, D.; Hamann, T. W. Band Energies of Nanoparticle Semiconductor Electrodes Determined by Spectroelectrochemical Measurements of Free Electrons. *Phys. Chem. Chem. Phys.* **2015**, *17*, 11156–11160.
- (40) Matsumoto, Y.; Yoshikawa, T.; Sato, E. Dependence of the Band Bending of the Oxide Semiconductors on pH. *J. Electrochem. Soc.* **1989**, *136*, 1389–1391.
- (41) Bolts, J. M.; Wrighton, M. S. Correlation of Photocurrent-Voltage Curves with Flat-Band Potential for Stable Photoelectrodes for the Photoelectrolysis of Water. *J. Phys. Chem.* **1976**, *80*, 2641–2645.
- (42) Redmond, G.; Fitzmaurice, D. Spectroscopic Determination of Flatband Potentials for Polycrystalline Titania Electrodes in Nonaqueous Solvents. *J. Phys. Chem.* **1993**, *97*, 1426–1430.
- (43) Kelly, C. A.; Farzad, F.; Thompson, D. W.; Stipkala, J. M.; Meyer, G. J. Cation-Controlled Interfacial Charge Injection in Sensitized Nanocrystalline TiO<sub>2</sub>. **1999**, No. 7, 7047–7054.
- (44) O'Donnell, R. M.; Sampaio, R. N.; Barr, T. J.; Meyer, G. J. Electric Fields and Charge Screening in Dye Sensitized Mesoporous Nanocrystalline TiO<sub>2</sub> Thin Films. *J. Phys. Chem. C* **2014**, *118*, 16976–16986.

- (45) Wang, H.; Peter, L. M. Influence of Electrolyte Cations on Electron Transport and Electron Transfer in Dye-Sensitized Solar Cells. *J. Phys. Chem. C* **2012**, *116*, 10468–10475.
- (46) Gerischer, H. Electrochemical Techniques for the Study of Photosensitization. *Photochem. Photobiol.* **1972**, *16*, 243–260.
- (47) Gerischer, H. Electron-Transfer Kinetics of Redox Reactions at the Semiconductor/electrolyte Contact. A New Approach. *J. Phys. Chem.* **1991**, *95*, 1356–1359.
- (48) Stark, J. Observation of the Separation of Spectral Lines by an Electric Field. *Nature*. 1913, pp 401–401.
- (49) LoSurdo, A. Sul Fenomeno Analoge a Quello Di Zeeman Nel Campo Elettrico. *Atti R. Accad. Lincei* **1913**, *22*, 664–666.
- (50) Stark, J. Beobachtungen Über Den Effekt Des Elektrischen Feldes Auf Spektrallinien. II. Längseffekt. *Ann. Phys.* **1914**, *348*, 965–982.
- (51) Stark, J.; Wendt, G. Beobachtungen Über Den Effekt Des Elektrischen Feldes Auf Spektrallinien. II. Längseffekt. *Ann. Phys.* **1914**, *348*, 983–990.
- (52) Liptay, W. Electrochromism and Solvatochromism. *Angew. Chemie Int. Ed. English* **1969**, *8*, 177–188.
- (53) Boxer, S. G. Stark Realities †. *J. Phys. Chem. B* **2009**, *113*, 2972–2983.
- (54) Liptay, W. *Excited States*, 1st ed.; Academic: New York, 1974.
- (55) Staniszewski, A.; Ardo, S.; Sun, Y.; Castellano, F. N.; Meyer, G. J. Slow Cation Transfer Follows Sensitizer Regeneration at Anatase TiO<sub>2</sub> Interfaces. *J. Am. Chem. Soc.* **2008**, *130*, 11586–11587.
- (56) Pelet, S.; Moser, J.; Grätzel, M. Cooperative Effect of Adsorbed Cations and Iodide on the Interception of Back Electron Transfer in the Dye Sensitization of Nanocrystalline TiO<sub>2</sub>. *J. Phys. Chem. B* **2000**, *104*, 1791–1795.
- (57) Ridley, M. K.; Hackley, V. A.; Machesky, M. L. Characterization and Surface-Reactivity of Nanocrystalline Anatase in Aqueous Solutions. *Langmuir* **2006**, *22*, 10972–10982.
- (58) Beauvilliers, E. E.; Meyer, G. J. Evidence for Cation-Controlled Excited-State Localization in a Ruthenium Polypyridyl Compound. *Inorg. Chem.* **2016**, *55*, 7517–7526.
- (59) Sampaio, R. N.; Li, G.; Meyer, G. J. Continuous Surface Electric Field Contraction Accompanying Electron Transfer from TiO<sub>2</sub> to Oxidized Sensitizers. *ACS Energy Lett.* **2016**, *1*, 846–851.
- (60) Ardo, S.; Sun, Y.; Staniszewski, A.; Castellano, F. N.; Meyer, G. J. Stark Effects after Excited-State Interfacial Electron Transfer at Sensitized TiO<sub>2</sub> Nanocrystallites. *J. Am. Chem. Soc.* **2010**, *132*, 6696–6709.
- (61) Ardo, S.; Sun, Y.; Castellano, F. N.; Meyer, G. J. Excited-State Electron Transfer from Ruthenium-Polypyridyl Compounds to Anatase TiO<sub>2</sub> Nanocrystallites: Evidence for a Stark

Effect †. *J. Phys. Chem. B* **2010**, *114*, 14596–14604.

(62) Johansson, P. G.; Kopecky, A.; Galoppini, E.; Meyer, G. J. Distance Dependent Electron Transfer at TiO<sub>2</sub> Interfaces Sensitized with Phenylene Ethynylene Bridged Ru II – Isothiocyanate Compounds. *J. Am. Chem. Soc.* **2013**, *135*, 8331–8341.

(63) Ardo, S.; Achey, D.; Morris, A. J.; Abrahamsson, M.; Meyer, G. J. Non-Nernstian Two-Electron Transfer Photocatalysis at Metalloporphyrin- TiO<sub>2</sub> Interfaces. *J. Am. Chem. Soc.* **2011**, *133*, 16572–16580.

(64) Barr, T. J.; Morris, A. J.; Taheri, A.; Meyer, G. J. Charge Rectification at Molecular Nanocrystalline TiO<sub>2</sub> Interfaces: Overlap Optimization To Promote Vectorial Electron Transfer. *J. Phys. Chem. C* **2016**, *120*, 27173–27181.

(65) Albery, W. J.; Boutelle, M. G.; Colby, P. J.; Hillman, A. R. The Kinetics of Electron Transfer in the Thionine-Coated Electrode. *J. Electroanal. Chem. Interfacial Electrochem.* **1982**, *133*, 135–145.

(66) Chidsey, C. E. D.; Murray, R. W. Redox Capacity and Direct Current Electron Conductivity in Electroactive Materials. *J. Phys. Chem.* **1986**, *90*, 1479–1484.

(67) Brown, A. P.; Anson, F. C. Cyclic and Differential Pulse Voltammetric Behavior of Reactants Confined to the Electrode Surface. *Anal. Chem.* **1977**, *49*, 1589–1595.

(68) Zaban, A.; Ferrere, S.; Gregg, B. a. Relative Energetics at the Semiconductor/Sensitizing Dye/Electrolyte Interface. *J. Phys. Chem. B* **1998**, *102*, 452–460.

(69) Dloczik, L.; Ileperuma, O.; Lauerma, I.; Peter, L. M.; Ponomarev, E. A.; Redmond, G.; Shaw, N. J.; Uhlendorf, I. Dynamic Response of Dye-Sensitized Nanocrystalline Solar Cells: Characterization by Intensity-Modulated Photocurrent Spectroscopy. *J. Phys. Chem. B* **1997**, *101*, 10281–10289.

(70) Bisquert, J. Theory of the Impedance of Electron Diffusion and Recombination in a Thin Layer. *J. Phys. Chem. B* **2002**, *106*, 325–333.

(71) Bisquert, J.; Garcia-Belmonte, G.; Fabregat-Santiago, F.; Ferriols, N. S.; Bogdanoff, P.; Pereira, E. C. Doubling Exponent Models for the Analysis of Porous Film Electrodes by Impedance. Relaxation of TiO<sub>2</sub> Nanoporous in Aqueous Solution. *J. Phys. Chem. B* **2000**, *104*, 2287–2298.

(72) Kern, R.; Sastrawan, R.; Ferber, J.; Stangl, R.; Luther, J. Modeling and Interpretation of Electrical Impedance Spectra of Dye Solar Cells Operated under Open-Circuit Conditions. *Electrochim. Acta* **2002**, *47*, 4213–4225.

(73) Nakade, S.; Kambe, S.; Kitamura, T.; Wada, Y.; Yanagida, S. Effects of Lithium Ion Density on Electron Transport in Nanoporous TiO<sub>2</sub> Electrodes. *J. Phys. Chem. B* **2001**, *105*, 9150–9152.

(74) Look, D. C.; Reynolds, D. C.; Sizelove, J. R.; Jones, R. L.; Litton, C. W.; Cantwell, G.; Harsch, W. C. Electrical Properties of Bulk ZnO. *Solid State Commun.* **1998**, *105*, 399–401.

(75) Nakade, S.; Kanzaki, T.; Wada, Y.; Yanagida, S. Stepped Light-Induced Transient

Measurements of Photocurrent and Voltage in Dye-Sensitized Solar Cells: Application for Highly Viscous Electrolyte Systems. *Langmuir* **2005**, *21*, 10803–10807.

(76) Kopidakis, N.; Schiff, E. A.; Park, N.-G.; van de Lagemaat, J.; Frank, A. J. Ambipolar Diffusion of Photocarriers in Electrolyte-Filled, Nanoporous TiO<sub>2</sub> †. *J. Phys. Chem. B* **2000**, *104*, 3930–3936.

(77) Solbrand, A.; Lindström, H.; Rensmo, H.; Hagfeldt, A.; Lindquist, S.-E.; Södergren, S. Electron Transport in the Nanostructured TiO<sub>2</sub> –Electrolyte System Studied with Time-Resolved Photocurrents. *J. Phys. Chem. B* **1997**, *101*, 2514–2518.

(78) van de Lagemaat, J.; Frank, A. J. Nonthermalized Electron Transport in Dye-Sensitized Nanocrystalline TiO<sub>2</sub> Films: Transient Photocurrent and Random-Walk Modeling Studies. *J. Phys. Chem. B* **2001**, *105*, 11194–11205.

(79) O'Regan, B. C.; Lenzenmann, F. Charge Transport and Recombination in a Nanoscale Interpenetrating Network of N-Type and P-Type Semiconductors : Transient Photocurrent and Photovoltage Studies of TiO<sub>2</sub>/Dye/CuSCN Photovoltaic Cells. *J. Phys. Chem. B* **2004**, *108*, 4342–4350.

(80) Schlichthörl, G.; Huang, S. Y.; Sprague, J.; Frank, A. J. Band Edge Movement and Recombination Kinetics in Dye-Sensitized Nanocrystalline TiO<sub>2</sub> Solar Cells: A Study by Intensity Modulated Photovoltage Spectroscopy. *J. Phys. Chem. B* **1997**, *101*, 8141–8155.

(81) O'Regan, B. C.; Scully, S.; Mayer, A. C.; Palomares, E.; Durrant, J. The Effect of Al<sub>2</sub>O<sub>3</sub> Barrier Layers in TiO<sub>2</sub>/dye/CuSCN Photovoltaic Cells Explored by Recombination and DOS Characterization Using Transient Photovoltage Measurements. *J. Phys. Chem. B* **2005**, *109*, 4616–4623.

(82) Nguyen, T. T. O.; Peter, L. M.; Wang, H. Characterization of Electron Trapping in Dye-Sensitized Solar Cells by Near-IR Transmittance Measurements. *J. Phys. Chem. C* **2009**, *113*, 8532–8536.

(83) Duffy, N. ; Peter, L. ; Rajapakse, R. M. ; Wijayantha, K. G. . A Novel Charge Extraction Method for the Study of Electron Transport and Interfacial Transfer in Dye Sensitized Nanocrystalline Solar Cells. *Electrochem. commun.* **2000**, *2*, 658–662.

(84) Schmidlin, F. W. Theory of Trap-Controlled Transient Photoconduction. *Phys. Rev. B* **1977**, *16*, 2362–2385.

(85) Noolandi, J. Equivalence of Multiple-Trapping Model and Time-Dependent Random Walk. *Phys. Rev. B* **1977**, *16*, 4474–4479.

(86) Rudenko, A. I.; Arkhipov, V. I. Drift and Diffusion in Materials with Traps. *Philos. Mag. Part B* **1982**, *45*, 177–187.

(87) Adriaenssens, G. J.; Baranovskii, S. D.; Fuhs, W.; Jansen, J.; Öktü, Ö. Photoconductivity Response Time in Amorphous Semiconductors. *Phys. Rev. B* **1995**, *51*, 9661–9667.

(88) Scher, H.; Montroll, E. W. Anomalous Transit-Time Dispersion in Amorphous Solids. *Phys. Rev. B* **1975**, *12*, 2455–2477.

- (89) Blumen, A.; Klafter, J.; Zumofen, G. Recombination in Amorphous Materials as a Continuous-Time Random-Walk Problem. *Phys. Rev. B* **1983**, *27*, 3429–3435.
- (90) Blumen, A.; Zumofen, G.; Klafter, J. Target Annihilation by Random Walkers. *Phys. Rev. B* **1984**, *30*, 5379–5382.
- (91) Barzykin, A. V.; Tachiya, M. Mechanism of Charge Recombination in Dye-Sensitized Nanocrystalline Semiconductors: Random Flight Model. *J. Phys. Chem. B* **2002**, *106*, 4356–4363.
- (92) Bisquert, J.; Vikhrenko, V. S. Interpretation of the Time Constants Measured by Kinetic Techniques in Nanostructured Semiconductor Electrodes and Dye-Sensitized Solar Cells. *J. Phys. Chem. B* **2004**, *108*, 2313–2322.
- (93) Bisquert, J.; Mora-Seró, I. Simulation of Steady-State Characteristics of Dye-Sensitized Solar Cells and the Interpretation of the Diffusion Length. *J. Phys. Chem. Lett.* **2010**, *1*, 450–456.
- (94) Villanueva-Cab, J.; Wang, H.; Oskam, G.; Peter, L. M. Electron Diffusion and Back Reaction in Dye-Sensitized Solar Cells: The Effect of Nonlinear Recombination Kinetics. *J. Phys. Chem. Lett.* **2010**, *1*, 748–751.
- (95) Barnes, P. R. F.; O'Regan, B. C. Electron Recombination Kinetics and the Analysis of Collection Efficiency and Diffusion Length Measurements in Dye Sensitized Solar Cells. *J. Phys. Chem. C* **2010**, *114*, 19134–19140.
- (96) Barnes, P. R. F.; Miettunen, K.; Li, X.; Anderson, A. Y.; Bessho, T.; Gratzel, M.; O'Regan, B. C. Interpretation of Optoelectronic Transient and Charge Extraction Measurements in Dye-Sensitized Solar Cells. *Adv. Mater.* **2013**, *25*, 1881–1922.

## CHAPTER 2: ELECTRIC FIELDS AND CHARGE SCREENING IN DYE SENSITIZED MESOPOROUS NANOCRYSTALLINE TiO<sub>2</sub> THIN FILMS\*

### 2.1 Introduction

The 1991 Nature paper by Grätzel and O'Regan introduced the clever idea of utilizing mesoporous thin films of nanocrystalline TiO<sub>2</sub> in photoelectrochemical cells.<sup>1</sup> The idea turned out to be revolutionary and created whole new fields of science based on energy conversion with nanometer-sized semiconductor materials.<sup>2,3</sup> The nanometer length scale often results in very different photoelectrochemical behavior than that observed with bulk semiconductor materials. For example, in single crystal and thin films materials, electron–hole pairs are efficiently separated by a surface electric field (the “depletion” or “space charge” region) that is absent in weakly doped semiconductor nanocrystallites.<sup>4</sup> In fact, the three bias conditions identified for single crystal semiconductor materials, that is, depletion, inversion, and accumulation, are not particularly useful for quantifying or modeling the photo-electrochemistry of semiconductor nanocrystallites. In the case of dye-sensitized solar cells (DSSCs), it has generally been assumed that any electric fields that might be present under illumination would be completely screened from the surface anchored dye molecules by the large dielectric constant of TiO<sub>2</sub>,  $\epsilon_r = 7-50$ ;<sup>5</sup> the high permittivity of acetonitrile,  $\epsilon_r = 37$ ;<sup>6</sup> and the half molar ionic strength of the electrolyte.

---

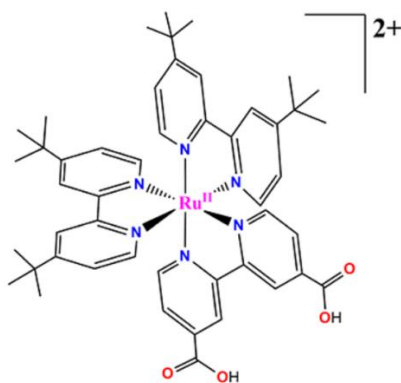
\*This chapter previously appeared as an article in the Journal of Physical Chemistry C. Reprinted (adapted) with permission from (O'Donnell, R. M.; Sampaio, R. N.; Barr, T. J.; Meyer, G. J. Electric Fields and Charge Screening in Dye Sensitized Mesoporous Nanocrystalline TiO<sub>2</sub> Thin Films. *J. Phys. Chem. C* **2014**, *118*, 16976–16986.). Copyright (2014) American Chemical Society.

The assumption of quantitative charge screening at sensitized TiO<sub>2</sub> interfaces was proven to be incorrect in 2010, when two groups reported that electrons injected into TiO<sub>2</sub> had a profound influence on the absorption spectrum of dye molecules anchored to the surface.<sup>7,8</sup> The absorption changes measured after the injection of charge were similar to those previously reported in traditional Stark spectroscopic measurements<sup>9-12</sup> but were unidirectional due to the fixed orientation of the molecular dipole moment relative to the TiO<sub>2</sub> surface. With some assumptions, the spectral shifts reported directly on the magnitude of the electric field that was found to be substantial, on the order of 2.7 MV/cm.<sup>7</sup> It remains unclear whether this electric field or charge screening is relevant to power conversion in DSSCs. The spectral shift of the dye molecules is generally small and does not appreciably change the light harvesting efficiency of the sensitized thin film. Likewise, the potential drop experienced by the dye molecules represents a fairly small value of ~40 mV that corresponds to only about 5% of the open circuit photovoltages reported for gold standard DSSCs.<sup>7</sup> In fact, charge screening may have a deleterious influence on energy conversion efficiencies with anionic redox mediators like  $\Gamma/I_3^-$ . Synonymous to increasing the width of the space-charge layer in bulk semiconductor solar cells, increasing the Debye length for charge screening at the semiconductor electrolyte interface should aid in the generation of even further spatially separated and longer-lived anionic charges, that is, TiO<sub>2</sub>(e<sup>-</sup>)s and I<sub>3</sub><sup>-</sup>, and, hence, improve solar conversion efficiencies. While speculative, fundamental studies of surface electric fields and charge screening may provide new insights into the fabrication of superior DSSCs. Such studies are also of intellectual interest in their own right.

An intriguing observation from previous research was that following pulsed laser excitation of sensitized TiO<sub>2</sub> thin films immersed in an acetonitrile electrolyte, the magnitude

of the Stark effect decreased over time periods in which the  $\text{TiO}_2(e^-)$  concentration was constant.<sup>7</sup> This behavior was attributed to the reorganization of interfacial ions and solvent molecules responding to the electrons that were photoinjected into  $\text{TiO}_2$ , a process often referred to as “screening.” While screening of this type is well-known in the electrochemical and photoelectrochemical literature,<sup>13–18</sup> to our knowledge this represents the first opportunity to probe the dynamics of this process on short time scales. The kinetics for charge screening were reported to be sensitive to whether  $\text{Mg}^{2+}$  or  $\text{Li}^+$  cations were present in the electrolyte.<sup>19</sup> The study of  $[\text{Ru}(\text{dtb})_2(\text{dcb})](\text{PF}_6)_2$ , where dtb is 4,4'-(tert-butyl)<sub>2</sub>-2,2'-bipyridine and dcb is 4,4'-(CO<sub>2</sub>H)<sub>2</sub>-2,2'-bipyridine, was utilized as the compound is a particularly sensitive probe of the surface electric field, Scheme 2.1. Here these studies were expanded to include  $\text{Li}^+$ ,  $\text{Na}^+$ ,  $\text{Mg}^{2+}$ , and  $\text{Ca}^{2+}$ . These ions influenced the magnitude of the electric field experienced by the compound as well as the screening dynamics quantified after excited state injection. These cations were also found to alter the interfacial density of states and the excited state injection yields.

Scheme 2.1: Structure of  $\text{Ru}(\text{dtb})_2(\text{dcb})^{2+}$



## 2.2 Experimental

**Materials:** The following reagents and substrates were used as received from the indicated commercial suppliers: acetonitrile (CH<sub>3</sub>CN; Burdick & Jackson, spectrophotometric grade); deionized water; lithium perchlorate (LiClO<sub>4</sub>; Sigma-Aldrich 99.99%); sodium perchlorate (NaClO<sub>4</sub>; Sigma-Aldrich, 99%); magnesium perchlorate (Mg(ClO<sub>4</sub>)<sub>2</sub>; Sigma-Aldrich, ACS reagent); calcium perchlorate tetrahydrate (Ca(ClO<sub>4</sub>)<sub>2</sub> · 4H<sub>2</sub>O; Sigma-Aldrich, 99%); tetra-*n*-butylammonium perchlorate (TBAClO<sub>4</sub>; Aldrich, ≥99.0%); tetra-*n*-butylammonium iodide (TBAI; Fluka, ≥99.0%); argon gas (Airgas, >99.998%); oxygen gas (Airgas, industrial grade); titanium(IV) isopropoxide (Sigma-Aldrich, 97%); fluorine-doped SnO<sub>2</sub>-coated glass (FTO; Hartford Glass Co., Inc., 2.3 mm thick, 15 Ω/□); and glass microscope slides (Fisher Scientific, 1 mm thick). [Ru(dtb)<sub>2</sub>(dcb)](PF<sub>6</sub>)<sub>2</sub> was available from previous studies.<sup>7</sup>

**Preparations:** Transparent TiO<sub>2</sub> nanocrystallites (anatase, ~15 nm in diameter) were prepared by acid hydrolysis of Ti(*i*-OPr)<sub>4</sub> using a sol-gel method previously described in the literature.<sup>20</sup> The sols were cast as transparent mesoporous thin films by doctor blading onto glass microscope slides for spectroscopic measurements and transparent FTO conductive substrates for electrochemical measurements with the aid of transparent cellophane tape as a mask and spacer (~10 μm thick). The films were sintered at 450 °C for 30 min under an atmosphere of O<sub>2</sub> flow and either used immediately or stored in an oven for future use. Sensitization was achieved by immersing the thin films in acetonitrile sensitizer solutions (mM concentrations) for hours to days depending on the desired surface coverage. Unless otherwise noted, the thin films were sensitized to roughly maximum surface coverage,  $\Gamma \sim 7 \times 10^{-8}$  mol/cm<sup>2</sup>, which was determined using a modified Beer-Lambert law,<sup>21</sup>

$$Abs = 1000 \times \varepsilon \times \Gamma$$

2.01

where  $\varepsilon$  is the molar decadic extinction (absorption) coefficient ( $16400 \text{ M}^{-1}\text{cm}^{-1}$  at 465 nm) that was assumed to have the same value when anchored to the surface. Sensitized films were soaked in neat acetonitrile for at least 1 h prior to experimentation.

**Spectroscopy:** *UV-Visible Absorption:* Steady-state UV-visible absorption spectra were obtained on a Varian Cary 50 or an Agilent Cary 60 spectrophotometer at room temperature in 1.0 cm path length quartz cuvettes. Sensitized  $\text{TiO}_2$  thin films were positioned at a  $45^\circ$  angle in cuvettes filled with the indicated acetonitrile solutions. The solutions were purged with argon gas for a minimum of 30 min prior to transient absorption and spectroelectrochemical studies.

*Photoluminescence:* Steady-state photoluminescence (PL) spectra were obtained with a Spex Fluorolog spectrophotometer equipped with a 450 W Xe lamp for the excitation source. PL spectra of sensitized thin films were obtained under ambient conditions at room temperature with excitation  $45^\circ$  to the surface and detection from the front face of the sample. Quenching experiments were performed by obtaining the PL spectrum of the sensitized thin film in neat solvent and after replacement of the neat solvent with the electrolyte solution of interest.

*Transient Absorption:* Nanosecond transient absorption measurements were obtained with an apparatus similar to that which has been previously described in the literature.<sup>22</sup> Briefly, samples were excited by a Q-switched, pulsed Nd:YAG laser (Quantel U.S.A. (BigSky) Brilliant B; 5–6 ns full width at half- maximum (fwhm), 1 Hz,  $\sim 10$  mm in diameter) tuned to 532 nm with the appropriate nonlinear optics. The excitation fluence was measured by a

thermopile power meter (Molelectron) and was typically 1–5 mJ/pulse so that the absorbed fluence was typically <1 mJ/pulse. A 150 W xenon arc lamp served as the probe beam and was aligned orthogonal to the laser excitation light. The lamp was pulsed with 100 V for detection at sub-100  $\mu$ s time scales. Detection was achieved with a monochromator (Spex 1702/04) optically coupled to an R928 photomultiplier tube (Hamamatsu). Appropriate glass filters were positioned between the probe lamp/sample and the sample/detection monochromator. Transient data was acquired with a computer-interfaced digital oscilloscope (LeCroy 9450, Dual 350 MHz) with an overall instrument response time of  $\sim$ 10 ns. Typically, 30 laser pulses were averaged at each observation wavelength over the range 400–750 nm, at 3 or 5 nm intervals. Full spectra were generated by averaging 2–10 points on either side of the desired time value to reduce noise in the raw data. For single wavelength measurements, 90–180 laser pulses were typically averaged to achieve satisfactory signal-to-noise ratios. Relative excited-state electron injection yields were measured by comparative actinometry on the nanosecond time scale for samples in different metal cation solutions using lithium as the reference.<sup>23,24</sup>

**Electrochemistry:** A potentiostat (Bioanalytical Scientific Instruments, Inc. (BAS) model CV-50W or EC Epsilon electrochemical analyzer) was employed for electrochemical measurements in a standard three-electrode arrangement with a TiO<sub>2</sub> thin film working electrode, a Pt gauze counter electrode (BAS), and a nonaqueous silver reference electrode (BAS). The ferrocenium/ferrocene (Fc<sup>+0</sup>) half-wave potential was measured both before and after experiments in a 100 mM TBAClO<sub>4</sub>/acetonitrile electrolyte that was used as an external standard to calibrate the reference electrode. All potentials are reported versus the normal hydrogen electrode (NHE) through the use of a conversion constant of –630 mV from NHE

to  $\text{Fc}^{+/0}$  in acetonitrile at 25 °C.<sup>25</sup> Spectroelectrochemistry was conducted via simultaneous application of an applied potential while monitoring the UV–vis absorption spectra of  $\text{TiO}_2$  thin-film electrodes in the indicated electrolytes. Each applied potential was held for 2–3 min, until the absorbance in the 700–900 nm region became invariant in time. Single-wavelength absorption features plotted as a function of the applied potential were proportional to the cumulative formation/loss of states; for the  $\text{TiO}_2(\text{e}^-)$  absorption features, this was directly related to the cumulative  $\text{TiO}_2$  density of acceptor states.<sup>26</sup>

Spectroelectrochemical charge extraction measurements were performed on unsensitized  $\text{TiO}_2$  thin films to obtain the extinction coefficient of the  $\text{TiO}_2(\text{e}^-)$ s. In these experiments, the absorbance at 700 nm was recorded as the potential was stepped from +200 mV to increasingly negative values. The charge present in the film was measured coulometrically after stepping the potential back to the original +200 mV value.<sup>27–29</sup> The absorption values were corrected for the 45° angle of the thin film in relation to the optical path. Each charge extraction cycle was repeated 3 times at each applied bias.

**Data Fitting:** Kinetic data fitting and spectral modeling were performed in Origin 9.0 with least-squares error minimization accomplished using the Levenberg–Marquardt iteration method.

### 2.3 Results

Thin films of  $\text{TiO}_2$  on glass substrates were reacted with  $\text{Ru}(\text{dtb})_2(\text{dcb})^{2+}$ , abbreviated  $\text{Ru}(\text{dtb})_2(\text{dcb})/\text{TiO}_2$ , in acetonitrile solutions to a maximum surface coverage,  $\Gamma \sim 7 \times 10^{-8} \text{ M}^{-1} \text{ cm}^2$ .<sup>7</sup> Representative absorption spectra of  $\text{Ru}(\text{dtb})_2(\text{dcb})/\text{TiO}_2$  immersed in neat acetonitrile and 100 mM perchlorate acetonitrile solutions are shown in Figure 2.01.

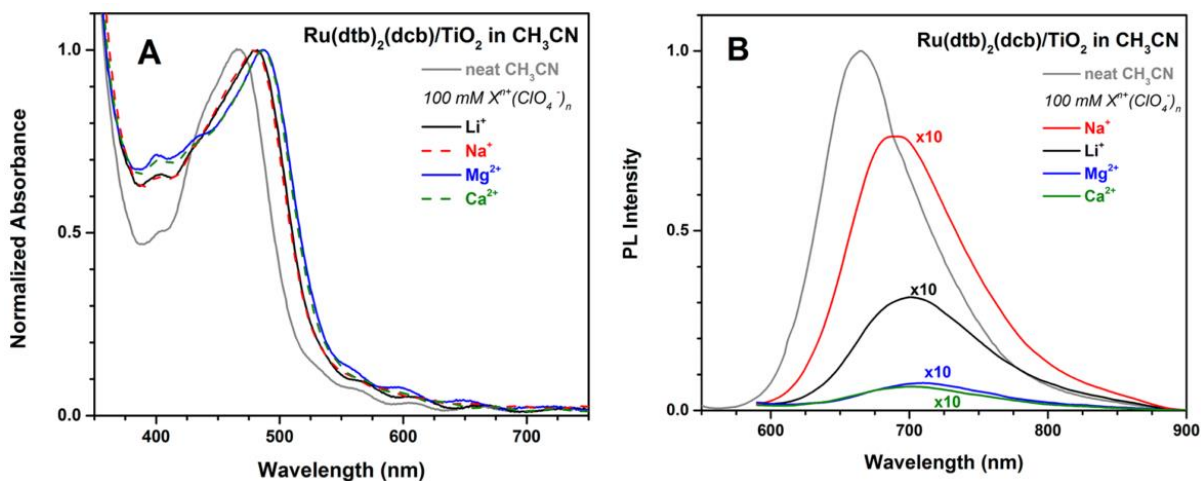


Figure 2.01. Steady-state UV-vis absorbance (A) and photoluminescence (B) spectra of  $\text{Ru}(\text{dtb})_2(\text{dcb})/\text{TiO}_2$  in neat acetonitrile and in the presence of 100 mM metal perchlorate electrolyte.

The  $\text{Ru}(\text{dtb})_2(\text{dcb})/\text{TiO}_2$  samples exhibit a metal-to-ligand charge transfer (MLCT) absorption band centered at 465 nm in neat acetonitrile and the fundamental  $\text{TiO}_2$  absorption below 380 nm. The spectrum measured in neat acetonitrile and in 100 mM TBAClO<sub>4</sub> (where TBA is tetra-*n*-butylammonium) were within experimental error the same. Replacement of the neat acetonitrile solvent bath with 100 mM metal perchlorate salt acetonitrile electrolytes resulted in a bathochromic shift, the magnitude of which was dependent on the cation. The MLCT absorption shifts to ~480 nm for monovalent cations,  $\text{Li}^+$  and  $\text{Na}^+$ , and to ~486 nm for divalent cations,  $\text{Mg}^{2+}$  and  $\text{Ca}^{2+}$ , shown in Figure 2.01A.

Visible light excitation of the MLCT absorption band resulted in room temperature photoluminescence (PL), shown in Figure 2.01B. In neat acetonitrile,  $\text{Ru}(\text{dtb})_2(\text{dcb})/\text{TiO}_2$  exhibited a PL maximum at 665 nm. Upon replacement of the neat solvent with 100 mM

metal perchlorate electrolytes: the PL maximum red-shifted and the PL intensity was quenched to varying extents dependent on the nature of the cation. The corresponding quantities are compiled in Table 2.1.

Table 2.1. Photophysical and Electrochemical Properties of Ru(dtb)<sub>2</sub>(dcb)/TiO<sub>2</sub> in 100 mM Metal Perchlorate Acetonitrile Solutions

<i>cation</i>	<i>Abs<sub>max</sub><sup>a</sup></i> (nm)	<i>PL<sub>max</sub></i> (nm)	<i>ΔG<sub>es</sub><sup>b</sup></i> (eV)	<i>E<sup>0</sup>(Ru<sup>III/II</sup>)<sup>c</sup></i> (V vs NHE) and ( <i>α</i> )	<i>E<sup>0</sup>(Ru<sup>III/II*</sup>)<sup>d</sup></i> (V vs NHE)
<i>Neat</i> <i>CH<sub>3</sub>CN</i>	465	665	2.05		
<i>Li<sup>+</sup></i>	480	700	1.86	1.46 (1.39)	-0.40
<i>Na<sup>+</sup></i>	480	690	1.88	1.43 (1.35)	-0.45
<i>Mg<sup>2+</sup></i>	486	710	1.88	1.49 (1.58)	-0.39
<i>Ca<sup>2+</sup></i>	486	700	1.90	1.50 (1.74)	-0.40

<sup>a</sup>Wavelengths are ±1 nm. <sup>b</sup>The free energy stored in the excited state. <sup>c</sup>The Ru<sup>III/II</sup> reduction potential and the ideality factor, *α*. <sup>d</sup>The excited state reduction potential calculated using Equation 2.03.

Electrochemical reduction of unsensitized TiO<sub>2</sub> thin films resulted in a blue shift of the fundamental absorption and the appearance of a broad absorption in the visible region. When measured as difference spectra, the blue shift of the fundamental absorption appears as a bleach, the magnitude of which was sensitive to the identity of the cation. Charge extraction experiments were performed on unsensitized TiO<sub>2</sub> thin films to determine the molar extinction coefficients of the TiO<sub>2</sub>(e<sup>-</sup>) absorption band in each of the four metal

perchlorate electrolytes. The absorption at 700 nm was monitored while the applied potential was stepped from 200 mV to  $-400$  mV vs NHE for 65 s and then returned to the initial 200 mV potential. The absorption was corrected for the  $45^\circ$  angle of the thin film relative to the optical path. Plotting the corrected absorbance versus the extracted charge from the film at multiple potentials allowed for determination of the molar extinction coefficient from the slope of a linear fit to the data, shown in Figure 2.02. The extinction coefficient was independent of the electrolyte composition within experimental error and was determined to be  $\epsilon(\text{TiO}_2(e^-)) = 930 \pm 50 \text{ M}^{-1}\text{cm}^{-1}$  at 700 nm. The application of more negative potentials, that is,  $<-1.2$  V, resulted in new absorption features that were not studied in detail due to the irreversible nature of the absorption changes.

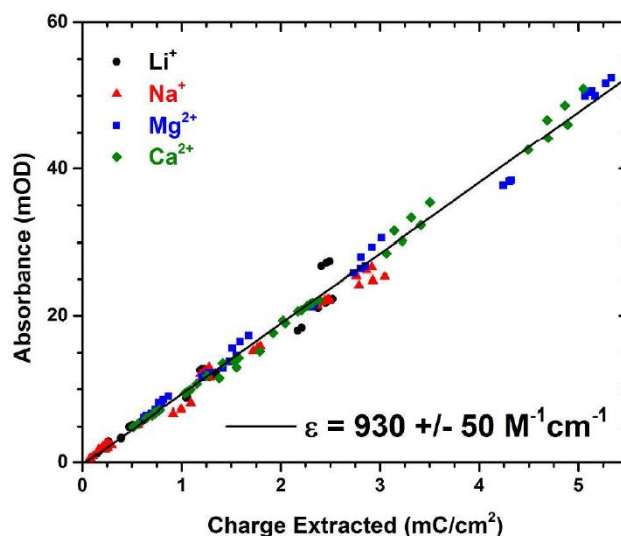


Figure 2.02. Absorbance as a function of the charge extracted from un-sensitized  $\text{TiO}_2$  thin films immersed in 100 mM metal perchlorate acetonitrile solutions. The black line indicates the best fit to the data which yields a molar extinction coefficient of  $930 \pm 50 \text{ M}^{-1}\text{cm}^{-1}$ .

In order to understand the ground-state behavior, spectroelectrochemistry was performed on sensitized  $\text{TiO}_2$  thin films in 100 mM metal perchlorate acetonitrile

electrolytes. Application of a positive applied potential resulted in spectral changes consistent with the oxidation of Ru<sup>II</sup> to Ru<sup>III</sup>. The equilibrium potential where the concentration of Ru<sup>II</sup> and Ru<sup>III</sup> were equal was taken as the E°(Ru<sup>III/II</sup>) reduction potential for Ru(dtb)<sub>2</sub>(dcb)/TiO<sub>2</sub>. The spectroelectrochemical data were fit to Equation 2.01

$$x = \frac{1}{1 + 10 \exp\left(\frac{E_{app} - E^0}{\alpha \times 59 \text{ mV}}\right)} \quad 2.01$$

where x is the fraction of molecules in each oxidation state, E<sub>app</sub> is the applied potential, and α is the ideality factor. Knowledge of E°(Ru<sup>III/II</sup>) allowed for the estimation of the reducing power of the excited state, which was calculated through a free energy cycle using Equation 2.02:

$$E^0(Ru^{III/II*}) = E^0(Ru^{III/II}) - \Delta G_{ES} \quad 2.02$$

where ΔG<sub>ES</sub> is the Gibbs free energy stored in the MLCT excited state determined by a tangent line extrapolation back to zero intensity on the high energy side of the PL spectrum. The formal reduction potentials and ideality factors are summarized in Table 2.1.

Application of a forward (negative) bias resulted in reduction of TiO<sub>2</sub> that was monitored by the characteristic broad absorption features from 400 to 1100 nm attributed to TiO<sub>2</sub>(e<sup>-</sup>)s. Concomitant with the appearance of TiO<sub>2</sub>(e<sup>-</sup>)s, the MLCT absorption band blue-shifted. Both of these spectral features are evident in Figure 2.03 for a Ru(dtb)<sub>2</sub>(dcb)/TiO<sub>2</sub> thin film in 100 mM LiClO<sub>4</sub> acetonitrile solution with an applied bias ranging from 150 to -750 mV vs NHE. The normalized spectroelectrochemical absorption spectra are shown in

Figure 2.03A and after subtraction of the contributions from  $\text{TiO}_2(e^-)$ s in Figure 2.03B.

Difference spectra of these same data are shown in Figure 2.03C,D.

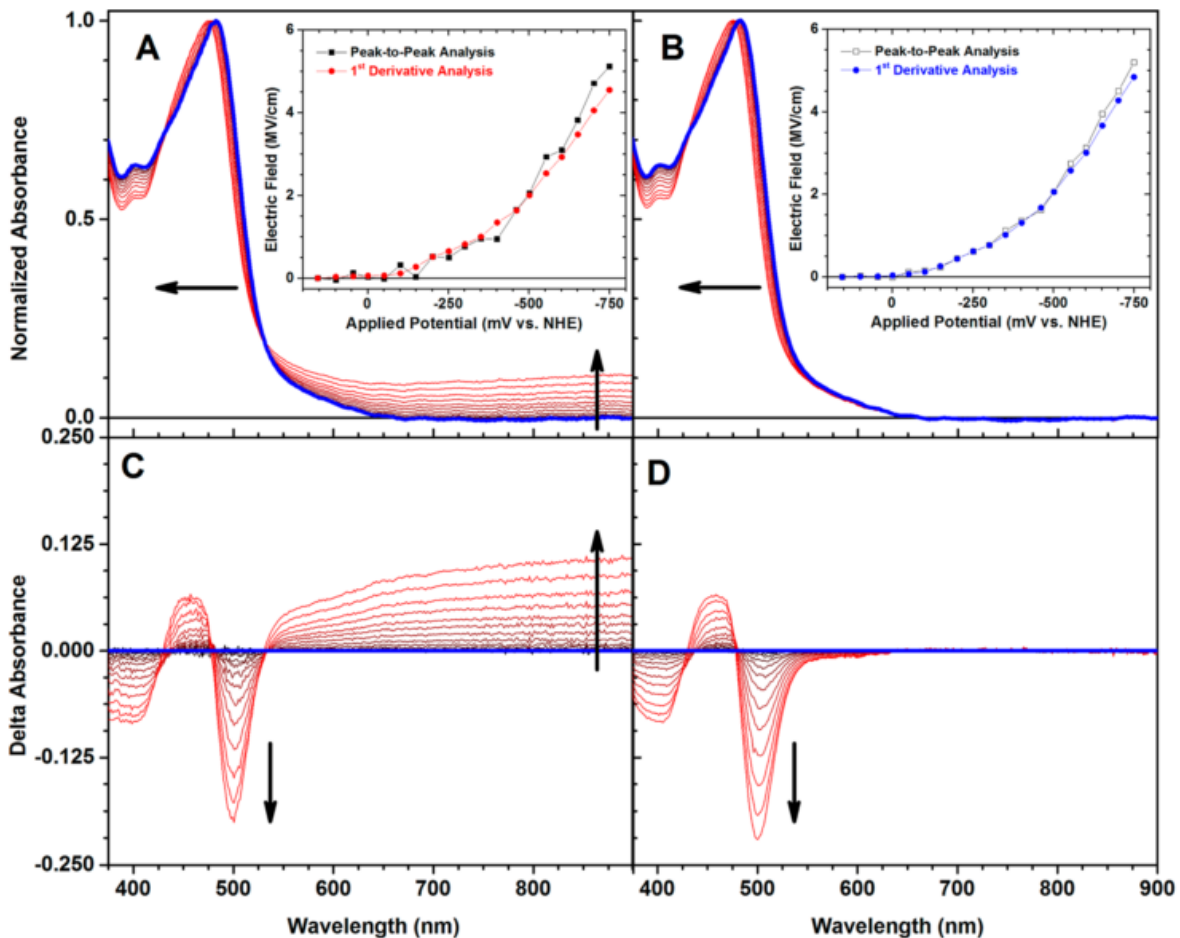


Figure 2.03. Spectra of a potentiostatically controlled  $\text{Ru}(\text{dtb})_2(\text{dcb})/\text{TiO}_2$  film in 100 mM  $\text{LiClO}_4$  acetonitrile solution (A) and after subtraction of the long-wavelength  $\text{TiO}_2(e^-)$  absorption (B). The difference spectra for the data shown in A and B are given in C and D, respectively. The insets in A and B indicate the electric field strength calculated by two different analyses. The spectra in dark blue were recorded at +150 mV and spectra recorded at more negative potentials (up to  $-750$  mV) are indicated in red. The arrows indicate the direction of change with increased negative applied potential.

The electric field experienced by the surface-bound sensitizers as a function of the applied potential bias was calculated using both peak-to-peak and first-derivative analysis methods and are compared in the insets of Figure 2.03A,B. For the peak-to-peak analysis, the electric field was calculated using Equation 2.03:

$$\Delta\nu = -\frac{|\Delta\vec{\mu}| |\vec{E}| \cos \theta}{100 hc} \quad 2.03$$

where  $h$  is Planck's constant,  $c$  is the speed of light in a vacuum,  $\Delta\nu$  is the change in spectroscopic peak maximum (in wavenumbers),  $\Delta\vec{\mu}$  is the change in dipole moment vector between the ground and the excited state,  $\vec{E}$  is the electric field vector, and  $\theta$  is the angle between the latter two quantities. With the assumption of  $\theta = 180^\circ$  and  $\Delta\vec{\mu} = 4.75 \text{ D}$ ,<sup>9,30</sup> the electric field was calculated at each applied bias. Similarly, the first-derivative analysis was performed using Equation 2.04:

$$\Delta\nu = -\frac{dA}{d\nu} \frac{\Delta\vec{\mu}\vec{E}}{h} \quad 2.04$$

where  $\Delta A$  is the difference spectrum, or delta absorbance, and  $dA/d\nu$  is the first derivative of the absorbance spectrum (in wavenumbers).<sup>8</sup> The electric field calculated using both the peak-to-peak analysis and the first-derivative analysis were in good agreement, as seen in the insets of Figure 2.03A,B.

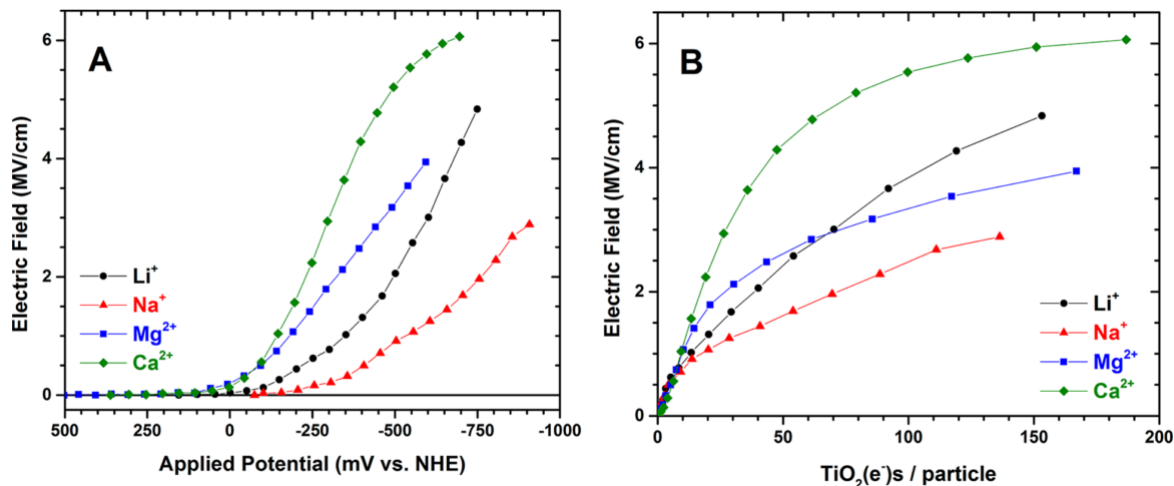


Figure 2.04. Electric field experienced by Ru(dtb)<sub>2</sub>(dcb)/TiO<sub>2</sub> in acetonitrile solutions containing 100 mM Li<sup>+</sup>, Na<sup>+</sup>, Mg<sup>2+</sup>, or Ca<sup>2+</sup> as a function of (A) the applied potential and (B) the number of TiO<sub>2</sub>(e<sup>-</sup>)s on a per particle basis.

The electric field experienced by the surface-bound sensitizers was calculated using the electron corrected spectra and the first-derivative method for all four cations and is shown in Figure 2.04 as a function of the applied potential (A) and the estimated electron concentration per TiO<sub>2</sub> nanoparticle (B). The latter was calculated by converting the applied potential to the number of TiO<sub>2</sub>(e<sup>-</sup>)s per 15 nm diameter particle through the measured absorbance and Beer's law using the measured extinction coefficient and the effective optical path length for a 10 μm thick film of 50% porosity.<sup>31</sup> For example, in 100 mM metal perchlorate solution where  $\epsilon = 930 \text{ M}^{-1}\text{cm}^{-1}$ , an absorbance of 0.0124 would correspond to 20 TiO<sub>2</sub>(e<sup>-</sup>)s/particle with Equation 2.05:

$$\begin{aligned}
 Abs &= \epsilon \times l \times c(\text{TiO}_2(e^-)) \\
 &= 930 \text{ (M}^{-1}\text{cm}^{-1}) \times 14.14 \times 10^{-4} \text{ (cm)} \times 50\%
 \end{aligned}
 \tag{2.05}$$

$$\times \frac{TiO_2(e^-)}{(4/3)\pi(7.5 \times 10^{-9}(m))^3 \times N_A \times 10^3(L/m^3)}$$

The relative injection yields were measured by comparative actinometry 100 ns after pulsed 532 nm light excitation of Ru(dtb)<sub>2</sub>(dcb)/TiO<sub>2</sub> in 100 mM metal perchlorate acetonitrile solutions.<sup>12</sup> The yields were within experimental error unity for Li<sup>+</sup>, Mg<sup>2+</sup>, and Ca<sup>2+</sup> and were found to be 0.95 for Na<sup>+</sup>.

Pulsed light excitation into the MLCT absorption band of Ru(dtb)<sub>2</sub>(dcb)/TiO<sub>2</sub> thin films immersed in 100 mM metal perchlorate solutions with 250 mM of tetrabutylammonium iodide, present to regenerate the sensitizer, generated long-lived charge separated states, composed of TiO<sub>2</sub>(e<sup>-</sup>)s and triiodide. Representative transient absorption spectra shown in Figure 2.05.

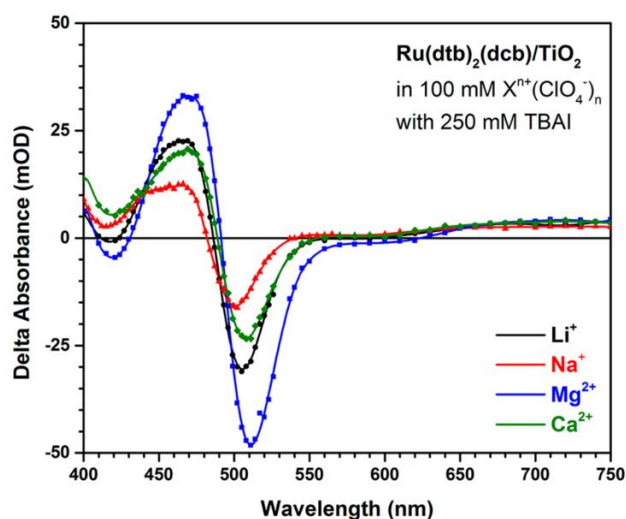


Figure 2.05. Transient absorption spectra obtained 2.5  $\mu$ s after pulsed 532 nm excitation of Ru(dtb)<sub>2</sub>(dcb)/TiO<sub>2</sub> in acetonitrile electrolyte solutions containing 100 mM of the indicated perchlorate salts and 250 mM tetra-*n*-butylammonium iodide.

were obtained 2.5  $\mu$ s after laser excitation, a delay time chosen to ensure that all sensitizers had been regenerated and all iodide oxidation chemistry was complete. The transient absorption spectra exhibit (1) small absorption features from 400–425 nm, attributed to formation of triiodide; (2) a first-derivative shaped feature centered around 485 nm, attributed to the  $\text{TiO}_2(e^-)$ -induced Stark effect; and (3) absorption from 600–750 nm, attributed to  $\text{TiO}_2(e^-)$ s. The transient absorption spectra were modeled with first-derivatives of the ground-state absorption spectra and the electric fields calculated using Equation 2.04 are collected in Table 2.2.

Table 2.2. Ionic Radii, Spectral Shifts, and Electric Field Strength for  $\text{Ru}(\text{dtb})_2(\text{dcb})/\text{TiO}_2$

<i>cation</i>	<i>ionic radii<sup>a</sup></i>	<i>electrochemically accumulated <math>\text{TiO}_2(e^-)</math>s<sup>b</sup></i>		<i>photoinjected <math>\text{TiO}_2(e^-)</math>s<sup>c</sup></i>	
		electric field (MV/cm)	$\Delta\nu$ ( $\text{cm}^{-1}$ )	electric field (MV/cm)	
<i>Li<sup>+</sup></i>	0.76	1.3	53	0.66	
<i>Na<sup>+</sup></i>	1.02	1.1	22	0.28	
<i>Mg<sup>2+</sup></i>	0.72	1.8	78	0.98	
<i>Ca<sup>2+</sup></i>	1.00	2.2	30	0.38	

<sup>a</sup>Ionic radii obtained from Shannon, ref 33. <sup>b</sup>Electric field change measured after the potentiostatic injection of approximately 20  $\text{TiO}_2(e^-)$  per nanoparticle. <sup>c</sup>Change in electric field measured 2.5  $\mu$ s after pulsed laser excitation.

Single-wavelength absorption changes monitored at wavelengths characteristic for  $\text{TiO}_2(e^-)$ s and the Stark effect were quantified over 7 orders of magnitude, from 100 ns to 1 s, shown in Figure 2.06. Care was taken to adjust the incident irradiance such that the long wavelength absorption measured 2.5  $\mu$ s after the laser excitation was the same for all the sensitized materials, such that the number of  $\text{TiO}_2(e^-)$ s was constant. The observed kinetics

were nonexponential, but were well-modeled by the Kohlrausch–Williams–Watts (KWW) stretched exponential function, Equation 2.06

$$I(t) = I_0 \exp[(-kt)^\beta] \quad 2.06$$

where  $I_0$  is the initial amplitude,  $k$  is a characteristic rate constant, and  $\beta$  is inversely proportional to the width of an underlying Lévy distribution of rate constants,  $0 < \beta < 1$ .<sup>7,32</sup>

The data were fit with  $\beta$  fixed to a value of 0.2 and the abstracted rate constants were  $k_{\text{Li}^+, \text{Na}^+} = 5 \times 10^4 \text{ s}^{-1}$  and  $k_{\text{Mg}^{2+}, \text{Ca}^{2+}} = 5 \times 10^2 \text{ s}^{-1}$ .

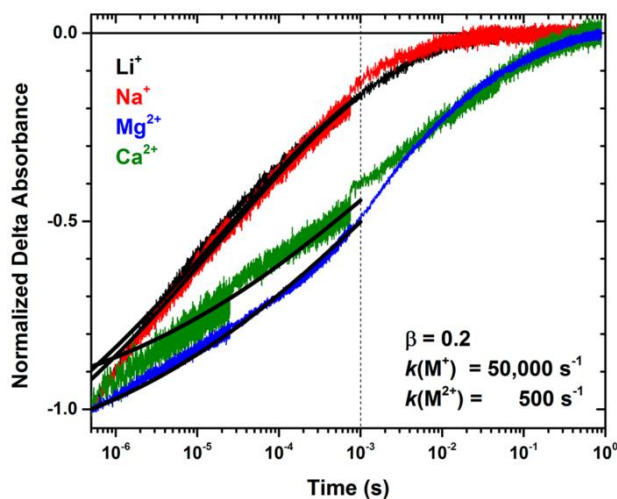


Figure 2.06. Single-wavelength transient absorption kinetic data of  $\text{Ru}(\text{dtb})_2(\text{dcb})/\text{TiO}_2$  in acetonitrile electrolyte solutions containing 100 mM of the indicated perchlorate salts with 250 mM tetra-*n*-butylammonium iodide observed at the maximum of the Stark effect bleach,  $\sim 500\text{--}510$  nm. Overlaid in black are fits to the KWW function. The dotted vertical line represents the time when the  $\text{TiO}_2(\text{e}^-)$  concentration began to decrease due to recombination with the redox mediator.

## 2.4 Discussion

The nature of the cations present in 100 mM acetonitrile electrolytes surrounding a Ru(dtb)<sub>2</sub>(dcb)/TiO<sub>2</sub> sensitized thin film were varied to test whether they had an influence on the surface electric field and the dynamics of interfacial charge screening. This was indeed realized and both the kinetics and the electric field were found to be acutely sensitive to the nature of the cation. As is often found to be the case in studies of sensitized materials, the alteration of this one cation variable influenced many properties of the sensitized material, including the interfacial energetics and, hence, the excited state injection yields. The plausible origin(s) of the cation-dependent interfacial energetics are described first followed by a description of the electric fields and charge screening dynamics.

**Cation Dependent Interfacial Redox Properties:** The adsorption of ions on semiconductor surfaces is known to have a strong influence on the valence and conduction band edge positions. A well-documented example for metal oxide semiconductors in aqueous solution is the 59 mV shift of the band edges that accompanies a factor of 10 change in the proton concentration.<sup>26,34,35</sup> The surface adsorption of alkali and alkaline earth metal cations can have a similar influence and are hence sometimes referred to as “potential determining ions”.<sup>36–39</sup> In general, cation adsorption shifts the band edge positions positive on an electrochemical scale away from the vacuum level. High efficiency dye-sensitized solar cells (DSSCs) utilize anatase TiO<sub>2</sub> in nonaqueous solvents, very often CH<sub>3</sub>CN, where dramatic energetic shifts have been reported. For example, the conduction band edge position has been reported to be -2.1 V vs SCE in 1.0 M TBAClO<sub>4</sub>, where the tetrabutylammonium (TBA) cation was reasonably asserted to interact only weakly with the TiO<sub>2</sub> surface, and shifted 1.1 V positive when Lewis acidic Li<sup>+</sup> cations were present.<sup>36</sup> Similar behavior has been reported

in other nonaqueous electrolytes.<sup>37,40</sup> The band edge position often varies nonlinearly with cation concentration and one generally needs to determine the values experimentally under the conditions of interest.

Spectro-electrochemistry has been widely utilized to characterize the acceptor states of the mesoporous anatase TiO<sub>2</sub> thin films used in DSSCs.<sup>29,41,42</sup> Reduction of TiO<sub>2</sub> results in a black coloration as well as a blue shift of the fundamental absorption. For a given cation, the measured spectra were normalizable over the potential range that was investigated, 0.0 to -1.0 V vs NHE. The extinction coefficients were calculated from the measured absorption spectra and the amount of charge present in the film as was determined by the charge extraction technique of unsensitized TiO<sub>2</sub>.<sup>27-29</sup> The value measured at 700 nm of  $\epsilon = 930 \pm 50 \text{ M}^{-1} \text{ cm}^{-1}$  were within experimental error the same and in good agreement with previously published values.<sup>29,40,43</sup>

While the coloration associated with TiO<sub>2</sub> reduction is well-known, an assignment of the underlying electronic transition(s) is not. The blue shift of the fundamental absorption has been attributed to both an electric field<sup>15,44,45</sup> and a band-filling, that is, a Burstein–Moss shift effect.<sup>40,42,46</sup> There is no consensus on which assignment is correct. Under the conditions described herein, the absorption increases through the visible region and displays no clear peak out to 1100 nm. The lack of a maximum and the high extinction coefficient are inconsistent with assignment as a ligand field ( $t_{2g} \rightarrow e_g^*$ ) transition, like that seen in Ti(III) compounds such as  $\text{Ti}(\text{H}_2\text{O})_6^{3+}$ ,  $\lambda_{\text{max}} = 475 \text{ nm}$ , and  $\epsilon = 5 \text{ M}^{-1} \text{ cm}^{-1}$ .<sup>47</sup> This implies that the long wavelength TiO<sub>2</sub> absorption has some intervalence  $\text{Ti}^{\text{IV/III}}$  character and results from electronic transitions that are not easily reconciled on a molecular level. All the unsolvated cations under study are small enough to intercalate into the (101) anatase TiO<sub>2</sub> lattice where

they could inductively interact with Ti centers throughout the nanocrystallite.<sup>33,36,40,48–51</sup>

Under more strongly reducing conditions, new absorption features appear that were clearly dependent on the nature of the cation present. The spectra measured in a Li<sup>+</sup> electrolyte were consistent with the known spectrum of the fully intercalated Li<sub>0.5</sub>TiO<sub>2</sub> phase.<sup>40,52</sup> Strong reduction in the presence of the other cations may also lead to intercalated phases; however, this was not studied in as much detail, as such conditions were found to irreversibly change the TiO<sub>2</sub> material, as evidenced by significant hysteresis in absorption versus applied potential scans.

Application of a sufficiently positive potential to a Ru(dtb)<sub>2</sub>(dcb)/TiO<sub>2</sub> thin film resulted in absorption changes due to the oxidation of Ru(II) to Ru(III). The electrochemistry itself was non-Nernstian. The equilibrium potential where the concentrations of the two redox states were equal was taken as an estimate of the formal reduction potential. The E<sup>0</sup>(Ru<sup>III/II</sup>) values were about 50 mV more positive with the dicationic Mg<sup>2+</sup> and Ca<sup>2+</sup> relative to Na<sup>+</sup> and Li<sup>+</sup>, that is, E<sup>0</sup>(Ru<sup>III/II</sup>) = 1.50 V versus E<sup>0</sup>(Ru<sup>III/II</sup>) = 1.45. More significant were the deviations from Nernstian behavior, where a factor of 10 change in concentration required 80 mV for Li<sup>+</sup> and 103 mV for Ca<sup>2+</sup>, Table 2.1. Previous studies of non-Nernstian redox chemistry of molecules anchored to TiO<sub>2</sub> concluded that the nonidealities resulted from surface electric fields.<sup>53,54</sup> Since cation adsorption does significantly influence the electric field experienced by the sensitizer (see below), the results here are in agreement with this conclusion.

The spectro-electrochemical data was utilized to construct a density of states diagram using a previously described method<sup>53,55,56</sup> for Ru(dtb)<sub>2</sub>(dcb)/TiO<sub>2</sub> in the different electrolytes, Figure 2.07. The density of TiO<sub>2</sub> acceptor states was found to increase

exponentially as the Fermi-level was raised toward the vacuum level, behavior that is consistent with many other reports.<sup>4,55</sup> The cation dependency is clearly seen at any potential of interest. For example at  $-0.5$  V, a potential that corresponds with the excited state reduction potential, the density increases in the order  $\text{Na}^+ < \text{Li}^+ < \text{Ca}^{2+} < \text{Mg}^{2+}$ , a trend that was clear at all potentials where a measurable concentration of  $\text{TiO}_2(\text{e}^-)$ s were present. The chemical capacitance distributions for the  $\text{Ru}^{\text{III/II}}$  redox chemistry are not Gaussian and reflect the non-Nernstian redox chemistry described above. The magnitudes of the chemical capacitances were proportional to the surface coverage, and the different values given in Figure 2.07 were not significant and likely result from the unknown extinction coefficients of the surface anchored compounds. The reduction potential of the thermally equilibrated excited states,  $E^0(\text{Ru}^{\text{III/II}*})$ , were calculated through a thermochemical cycle, and the distribution was assumed to be the same as the ground state.

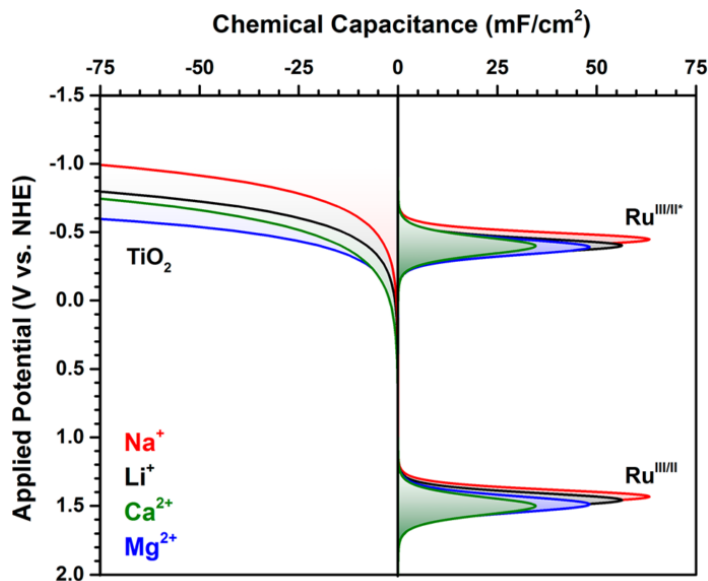


Figure 2.07. Density of states obtained from spectroelectrochemical measurements of  $\text{Ru}(\text{dtb})_2(\text{dcb})/\text{TiO}_2$  sensitized thin films in 100 mM acetonitrile electrolytes of the indicated perchlorate salts.

The free energy stored in the thermally equilibrated excited state  $\Delta G_{\text{es}}$  was abstracted from the steady state photoluminescence (PL) spectra. It was found that the presence of 100 mM of these cations in the electrolyte that surrounded a  $\text{Ru}(\text{dtb})_2(\text{dcb})/\text{TiO}_2$  thin film resulted in a bathochromic (red) shift of both the absorption and the PL spectra of magnitude  $\text{Na}^+ < \text{Li}^+ < \text{Ca}^{2+} < \text{Mg}^{2+}$ , Figure 2.01. The absorption data is discussed in more detail in the following section. The PL spectral shifts were accompanied by a dramatic quenching of PL intensity. The decrease in intensity is reasonably attributed to quenching by the  $\text{TiO}_2$  acceptor states. Indeed, the interfacial density of states shown in Figure 2.07 indicates that excited state injection should be favorable for  $\text{Ru}(\text{dtb})_2(\text{dcb})/\text{TiO}_2$  under all conditions. However, PL is an indirect probe of electron transfer and the radiative and nonradiative rate constants for excited state relaxation may also be influenced by cation adsorption. Indeed, it was recently

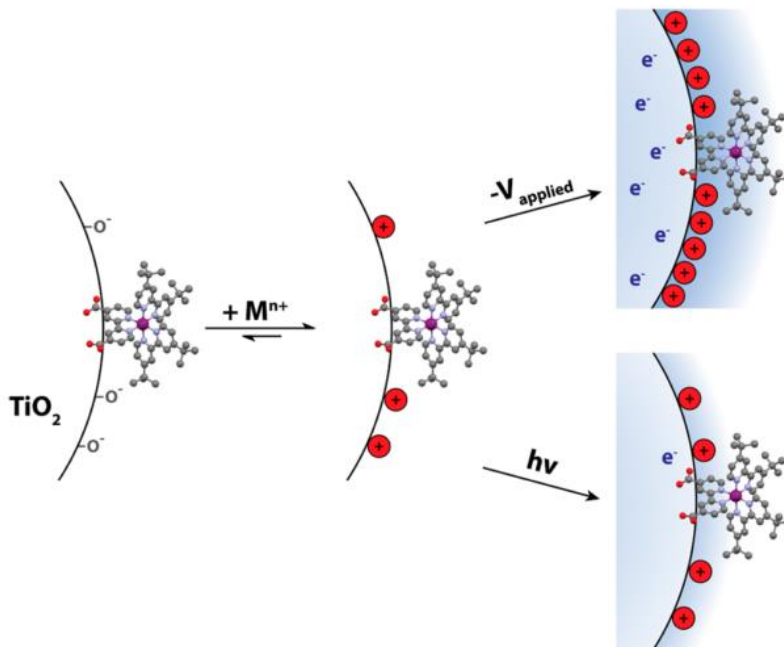
shown that the PL spectra of Ru(dtb)<sub>2</sub>(dcb)/TiO<sub>2</sub> was sensitive to the excitation irradiance and blue-shifted as the number of incident photons was increased, behavior attributed to a local electric field.<sup>30</sup> If the PL quenching were solely due to excited state injection and injection did not occur in neat acetonitrile, then the PL data would indicate injection yields of 0.95 for Na<sup>+</sup> and essentially unity for the other cations. The values measured by comparative actinometry 100 ns after laser excitation were found to be unity for all the cations except Na<sup>+</sup>, indicating that excited state electron transfer to TiO<sub>2</sub> was indeed the main excited state relaxation pathway. The injection yields were consistent with previous studies that showed a correlation between injection yields and the charge-to-size ratio.<sup>39</sup> This prior work was done at only 2 mM concentrations where the present studies were performed under concentrations where the influence of the cation had reached its maximum value.

**Electric Fields and Screening:** Abstraction of the electric field strength from the absorption data was accomplished by an analysis described in the Results and in previous publications.<sup>7,8,19,30</sup> In brief, the magnitude of the absorption shift that accompanied a change in the electric field experienced by the surface anchored Ru compounds was quantified by both first- derivative and peak-to-peak analyses and found to give the same values within experimental error. The first-derivative spectral features indicated that the field was collinear with the dipole moment change that was assumed to be  $\Delta\vec{\mu} = 4.75$  D under all conditions studied.<sup>9,30</sup> Previous studies have shown that orientation of the dipole moment vector change that accompanies light excitation parallel or antiparallel to the surface electric field results in absorption shifts that occur in opposite directions.<sup>8</sup> Very recent studies have shown that electroabsorption can be used to quantify the distance between the molecular chromophore and the TiO<sub>2</sub> surface.<sup>57</sup> The data reported herein have enabled characterization of electric

field changes that accompany injection in the presence of electrolytes where only the identity of the cation was altered.

The adsorption of ions to semiconductor surfaces is known and expected to generate local electric fields.<sup>38,58–63</sup> Previous studies have focused mainly on  $\text{Li}^+$  cations that are most widely utilized in DSSCs. Adsorption isotherms provided an estimate of the room temperature equilibrium constant,  $K = 15\text{--}80 \text{ M}^{-1}$ .<sup>7</sup> Here it was discovered that closely related spectral shifts were observed with  $\text{Na}^+$  and alkaline earth metal cations. The data support the widely held notion that prior to any surface treatments the sol–gel processed  $\text{TiO}_2$  nanocrystallites present in the mesoporous  $\text{TiO}_2$  thin films are negatively charged.<sup>38</sup> This negative charge is not attributed to injected electrons as there is no spectroscopic evidence for their presence and the spectral shifts were observed in air saturated solutions, conditions where the injected electrons are known to rapidly react. Instead the charge is attributed to specific functional groups, most likely deprotonated titanol groups, Scheme 2.2.

Scheme 2.2. Schematic Depiction of the Light- and Potentiostatically-Induced Generation of Injected Electrons



Whatever their chemical nature might be, the significant bathochromic (red) shift of the MLCT absorption that accompanied cation exposure reflects both the screening of this charge from the sensitizer and the field that is generated by the cation adsorption itself. The magnitude was sensitive to the identity of the cation and followed the trend  $\text{Na}^+ < \text{Li}^+ < \text{Ca}^{2+} < \text{Mg}^{2+}$ . A key point though is that there is no a priori reason to expect that the surface charge due to cation adsorption is the same for each cation. This is important as the electric fields quantified after excited state injection or electrochemical reduction represent the change in the electric field from the initial condition of 100 mM cation concentration, as is shown in Scheme 2.2.

Injection of electrons into a Ru(dtb)<sub>2</sub>(dcb)/TiO<sub>2</sub> thin film resulted in a bathochromic shift of the MLCT absorption that was opposite in sign to that measured with cation

adsorption. Measurements as a function of applied potential revealed a strong cation dependence, Figure 2.03. The potential dependent data was recast as the number of  $\text{TiO}_2(e^-)$ s per anatase nanocrystallite. While some experimental uncertainty was introduced by this conversion, the trends reported remain the same. The conversion was important for internal comparisons as the number of electrons present at any applied potential were found to be cation dependent. For all four cations studied, the magnitude of the electric field first increased linearly with the number of  $\text{TiO}_2(e^-)$ s and then more slowly with the number of  $\text{TiO}_2(e^-)$ s, Figure 2.04. The data suggests that the first electrons injected into  $\text{TiO}_2$  reside near the interface and subsequent electrons reside further away from the surface where they have a smaller influence on the surface anchored compounds.

About 20  $\text{TiO}_2(e^-)$ s are thought to reside in each nanocrystallite at the power point condition of optimized DSSCs,<sup>5,64</sup> so it is of interest to compare the electric fields reported by the sensitizer at this condition. The field strengths varied by about a factor of 2 and increased in the order  $\text{Na}^+ < \text{Li}^+ < \text{Mg}^{2+} < \text{Ca}^{2+}$ , Table 2.2. Since the number of  $\text{TiO}_2(e^-)$ s was the same, the variations in field reflect the ability of the cations to screen the  $\text{TiO}_2(e^-)$ s charge from the surface anchored Ru compound. The largest diameter cation,  $\text{Ca}^{2+}$ , was the poorest at screening charge yet  $\text{Na}^+$  was more effective than the smaller  $\text{Li}^+$ . Interestingly,  $\text{Mg}^{2+}$  was found to screen the field more effectively than did  $\text{Li}^+$ , but only when the number of  $\text{TiO}_2(e^-)$ s per nanoparticle exceeded about 70. Hence, the dication  $\text{Mg}^{2+}$  was more effective at charge screening when the number of  $\text{TiO}_2(e^-)$ s was large. As was described in the Introduction, it is not clear whether electric fields and charge screening influence the efficiency of DSSCs; however, for recombination to negatively charged acceptors like  $\text{I}_3^-$ , screening could be detrimental.<sup>38,60</sup>

Pulsed laser excitation enabled charge screening dynamics to be probed after excited state injection. Experimentally, it was found that this was most easily accomplished when iodide was present in the cell. Charge recombination to the oxidized iodide species was much slower than to the oxidized dye and the first derivative absorption signature associated with the Stark effect was much more easily observed spectroscopically after regeneration by iodide, Figure 2.05. The magnitudes of the field measured 2.5  $\mu\text{s}$  after the laser excitation followed the trend  $\text{Na}^+ < \text{Ca}^{2+} < \text{Li}^+ < \text{Mg}^{2+}$ , Table 2.2. However, the amplitudes of the Stark effect were time dependent for each cation making comparisons difficult. After pulsed laser excitation and regeneration by iodide, there existed a large time window between 500 ns and 1 ms where the number of  $\text{TiO}_2(e^-)$ s was constant, yet the spectral feature associated with the electric field decreased rapidly. Burdziński and co-workers have suggested that these dynamics reflect electron trapping at grain boundaries.<sup>65</sup> The strong cation dependence reported here indicates that this is not the sole source of the observed dynamics, as there is no a priori reason to believe that trapping at grain boundaries would also be cation dependent. It was found that the monovalent cations screened charge much more rapidly than did the dications,  $k_{\text{Li}^+, \text{Na}^+} = 5.0 \times 10^4 \text{ s}^{-1}$  and  $k_{\text{Mg}^{2+}, \text{Ca}^{2+}} = 5.0 \times 10^2 \text{ s}^{-1}$  (see Figure 2.06), presumably because the small number of electrons injected into  $\text{TiO}_2$  resulted in spatially isolated Ti(III) sites that were more easily screened by the monovalent cations. These rate constants indicate that charge screening of the field generated by excited state injection was not fully established before recombination to oxidized iodide occurred. Hence, the use of an alternative redox mediator that underwent slower charge recombination with  $\text{TiO}_2(e^-)$ s would be expected to enable more complete screening by these cations.

## 2.5 Conclusion

Local electric fields are generated when electrons are injected into TiO<sub>2</sub> nanocrystallites interconnected in the mesoporous thin films commonly used in dye-sensitized solar cells. The MLCT absorption of Ru(dtb)<sub>2</sub>(dcb)<sup>2+</sup> compounds anchored to the TiO<sub>2</sub> surface were found to be sensitive probes of these electric fields. Exposure of a Ru(dtb)<sub>2</sub>(dcb)/TiO<sub>2</sub> thin film immersed in acetonitrile to cations resulted in bathochromic (red) shifts of the MLCT absorption that followed the trend Na<sup>+</sup> < Li<sup>+</sup> < Ca<sup>2+</sup> < Mg<sup>2+</sup>. Injection of electrons into TiO<sub>2</sub>, from a potentiostat or an excited state, resulted in hypsochromic (blue) shifts. Pulsed laser excitation enabled the kinetics for charge screening at the interface to be quantified. On average, screening was about 100× faster for the alkali cations relative to the alkaline earths. This behavior was attributed to excited state injection yielding localized Ti(III) states that were more easily screened by ions with a single positive charge.

### Associated Content:

#### Supporting Information

Spectroelectrochemical difference spectra of unsensitized TiO<sub>2</sub> thin films, charge extraction data, molar extinction coefficient determination, spectroelectrochemical absorbance spectra of Ru(dtb)<sub>2</sub>(dcb)/TiO<sub>2</sub> oxidation, and transient absorption spectra modeled with overlaid first-derivative spectra. This material is available free of charge via the Internet at <http://pubs.acs.org>.

### Author Information

Corresponding Author \*E-mail: [gjmeyer@email.unc.edu](mailto:gjmeyer@email.unc.edu).

Present Address ‡Department of Chemistry, University of North Carolina at Chapel Hill,  
Chapel Hill, North Carolina, 27599, United States (R.M.O., T.J.B., and G.J.M.).

### **Notes**

The authors declare no competing financial interest

### **Acknowledgements**

The Division of Chemical Sciences, Geosciences, and Biosciences, Office of Basic Energy Sciences of the U.S. Department of Energy through Grant DE-FG02-96ER14662 is gratefully acknowledged for support (G.J.M.). R.M.O. would also like to thank the National Science Foundation for a Graduate Research Fellowship under Grant No. DGE-1232825. R.N.S. would like to thank the National Council for Scientific and Technological Development (CNPq) for support under Grant No. 244501/2012-2.

## REFERENCES

- (1) O'Regan, B.; Grätzel, M. A Low-Cost, High-Efficiency Solar Cell Based on Dye-Sensitized Colloidal TiO<sub>2</sub> Films. *Nature* **1991**, 353, 737–740.
- (2) Kamat, P. V. Meeting the Clean Energy Demand: Nanostructure Architectures for Solar Energy Conversion. *J. Phys. Chem. C* **2007**, 111, 2834–2860.
- (3) Kamat, P. V. Quantum Dot Solar Cells. The Next Big Thing in Photovoltaics. *J. Phys. Chem. Lett.* **2013**, 4, 908–918.
- (4) Albery, W. J.; Bartlett, P. N. The Transport and Kinetics of Photogenerated Carriers in Colloidal Semiconductor Electrode Particles. *J. Electrochem. Soc.* **1984**, 131, 315–325.
- (5) O'Regan, B. C.; Durrant, J. R. Kinetic and Energetic Paradigms for Dye-Sensitized Solar Cells: Moving from the Ideal to the Real. *Acc. Chem. Res.* **2009**, 42, 1799–1808.
- (6) *CRC Handbook of Chemistry and Physics*, 91st ed.; CRC Press: Boca Raton, FL, **2010**.
- (7) Ardo, S.; Sun, Y.; Staniszewski, A.; Castellano, F. N.; Meyer, G. J. Stark Effects after Excited-State Interfacial Electron Transfer at Sensitized TiO<sub>2</sub> Nanocrystallites. *J. Am. Chem. Soc.* **2010**, 132, 6696–6709.
- (8) Cappel, U. B.; Feldt, S. M.; Schöneboom, J.; Hagfeldt, A.; Boschloo, G. The Influence of Local Electric Fields on Photoinduced Absorption in Dye-Sensitized Solar Cells. *J. Am. Chem. Soc.* **2010**, 132, 9096–9101.
- (9) Oh, D. H.; Boxer, S. G. Stark Effect Spectra of Ru(diimine)<sub>3</sub><sup>2+</sup> Complexes. *J. Am. Chem. Soc.* **1989**, 111, 1130–1131.
- (10) Vance, F. W.; Hupp, J. T. Probing the Symmetry of the Nonlinear Optic Chromophore Ru(trans-4,4'-diethylaminostyryl-2,2'-bipyridine)<sub>3</sub><sup>2+</sup>: Insight from Polarized Hyper-Rayleigh Scattering and Electroabsorption (Stark) Spectroscopy. *J. Am. Chem. Soc.* **1999**, 121, 4047–4053. (11) Karki, L.; Hupp, J. T. Electroabsorption Studies of Metal-to-Ligand Charge Transfer in Ru(phenanthroline)<sub>3</sub><sup>2+</sup>: Evidence for Intrinsic Charge Localization in the Initially Formed Excited State. *Inorg. Chem.* **1997**, 36, 3318–3321.
- (12) Hug, S. J.; Boxer, S. G. Dipolar Character of Ligand-Centered Transitions in Transition Metal Tris-bipyridyl Complexes. *Inorg. Chim. Acta* **1996**, 242, 323–327.
- (13) Gregg, B. A. Interfacial Processes in the Dye-Sensitized Solar Cell. *Coord. Chem. Rev.* **2004**, 248, 1215–1224.
- (14) Schwarzburg, K.; Willig, F. Origin of Photovoltage and Photocurrent in the Nanoporous Dye-Sensitized Electrochemical Solar Cell. *J. Phys. Chem. B* **1999**, 103, 5743–5746.
- (15) Zaban, A.; Meier, A.; Gregg, B. A. Electric Potential Distribution and Short-Range Screening in Nanoporous TiO<sub>2</sub> Electrodes. *J. Phys. Chem. B* **1997**, 101, 7985–7990.
- (16) Kytin, V.; Dittrich, T.; Bisquert, J.; Lebedev, E. A.; Koch, F. Limitation of the Mobility of Charge Carriers in a Nanoscaled Heterogeneous System by Dynamical Coulomb Screening. *Phys. Rev. B* **2003**, 68, 195308.

- (17) Brus, L. Model for Carrier Dynamics and Photoluminescence Quenching in Wet and Dry Porous Silicon Thin Films. *Phys. Rev. B* **1996**, 53, 4649–4656.
- (18) Cahen, D.; Hodes, G.; Grätzel, M.; Guillemoles, J. F.; Riess, I. Nature of Photovoltaic Action in Dye-Sensitized Solar Cells. *J. Phys. Chem. B* **2000**, 104, 2053–2059.
- (19) O'Donnell, R. M.; Ardo, S.; Meyer, G. J. Charge-Screening Kinetics at Sensitized TiO<sub>2</sub> Interfaces. *J. Phys. Chem. Lett.* **2013**, 4, 2817–2821.
- (20) Heimer, T. A.; D'Arcangelis, S. T.; Farzad, F.; Stipkala, J. M.; Meyer, G. J. An Acetylacetonate-Based Semiconductor–Sensitizer Linkage. *Inorg. Chem.* **1996**, 35, 5319–5324. (21) Trammell, S. A.; Meyer, T. J. Diffusional Mediation of Surface Electron Transfer on TiO<sub>2</sub>. *J. Phys. Chem. B* **1998**, 103, 104–107.
- (22) Argazzi, R.; Bignozzi, C. A.; Heimer, T. A.; Castellano, F. N.; Meyer, G. J. Enhanced Spectral Sensitivity from Ruthenium(II) Polypyridyl Based Photovoltaic Devices. *Inorg. Chem.* **1994**, 33, 5741–5749.
- (23) Johansson, P. G.; Rowley, J. G.; Taheri, A.; Meyer, G. J.; Singh, S. P.; Islam, A.; Han, L. Long-Wavelength Sensitization of TiO<sub>2</sub> by Ruthenium Diimine Compounds with Low-Lying  $\pi^*$  Orbitals. *Langmuir* **2011**, 27, 14522–14531.
- (24) Bergeron, B. V.; Kelly, C. A.; Meyer, G. J. Thin Film Actinometers for Transient Absorption Spectroscopy: Applications to Dye-Sensitized Solar Cells. *Langmuir* **2003**, 19, 8389–8394.
- (25) Pavlishchuk, V. V.; Addison, A. W. Conversion Constants for Redox Potentials Measured versus Different Reference Electrodes in Acetonitrile Solutions at 25 °C. *Inorg. Chim. Acta* **2000**, 298, 97–102.
- (26) Rothenberger, G.; Fitzmaurice, D.; Grätzel, M. Spectroscopy of Conduction Band Electrons in Transparent Metal Oxide Semiconductor Films: Optical Determination of the Flatband Potential of Colloidal Titanium Dioxide Films. *J. Phys. Chem.* **1992**, 96, 5983–5986.
- (27) Duffy, N. W.; Peter, L. M.; Rajapakse, R. M. G.; Wijayantha, K. G. U. A Novel Charge Extraction Method for the Study of Electron Transport and Interfacial Transfer in Dye Sensitized Nanocrystalline Solar Cells. *Electrochem. Commun.* **2000**, 2, 658–662.
- (28) O'Regan, B. C.; Walley, K.; Juozapavicius, M.; Anderson, A.; Matar, F.; Ghaddar, T.; Zakeeruddin, S. M.; Klein, C. D.; Durrant, J. R. Structure/Function Relationships in Dyes for Solar Energy Conversion: A Two-Atom Change in Dye Structure and the Mechanism for Its Effect on Cell Voltage. *J. Am. Chem. Soc.* **2009**, 131, 3541–3548.
- (29) Berger, T.; Anta, J. A.; Morales-Flórez, V. Electrons in the Band Gap: Spectroscopic Characterization of Anatase TiO<sub>2</sub> Nanocrystal Electrodes Under Fermi Level Control. *J. Phys. Chem. C* **2012**, 116, 11444–11455.
- (30) Ardo, S.; Sun, Y.; Castellano, F. N.; Meyer, G. J. Excited-State Electron Transfer from Ruthenium-Polypyridyl Compounds to Anatase TiO<sub>2</sub> Nanocrystallites: Evidence for a Stark Effect. *J. Phys. Chem. B* **2010**, 114, 14596–14604.

- (31) Robson, K. C. D.; Hu, K.; Meyer, G. J.; Berlinguette, C. P. Atomic Level Resolution of Dye Regeneration in the Dye-Sensitized Solar Cell. *J. Am. Chem. Soc.* **2013**, 135, 1961–1971.
- (32) Jonscher, A. K. The “Universal” Dielectric Response. *Nature* **1977**, 267, 673–679.
- (33) Shannon, R. Revised Effective Ionic Radii and Systematic Studies of Interatomic Distances in Halides and Chalcogenides. *Acta Crystallogr., Sect. A* **1976**, 32, 751–767.
- (34) Bolts, J. M.; Wrighton, M. S. Correlation of Photocurrent- Voltage Curves with Flat-Band Potential for Stable Photoelectrodes for the Photoelectrolysis of Water. *J. Phys. Chem.* **1976**, 80, 2641–2645.
- (35) Lyon, L. A.; Hupp, J. T. Energetics of the Nanocrystalline Titanium Dioxide/Aqueous Solution Interface: Approximate Conduction Band Edge Variations Between  $H_0 = -10$  and  $H_- = +26$ . *J. Phys. Chem. B* **1999**, 103, 4623–4628.
- (36) Redmond, G.; Fitzmaurice, D. Spectroscopic Determination of Flatband Potentials for Polycrystalline Titania Electrodes in Non- aqueous Solvents. *J. Phys. Chem.* **1993**, 97, 1426–1430.
- (37) Enright, B.; Redmond, G.; Fitzmaurice, D. Spectroscopic Determination of Flatband Potentials for Polycrystalline  $TiO_2$  Electrodes in Mixed Solvent Systems. *J. Phys. Chem.* **1994**, 98, 6195–6200.
- (38) Pelet, S.; Moser, J.-E.; Grätzel, M. Cooperative Effect of Adsorbed Cations and Iodide on the Interception of Back Electron Transfer in the Dye Sensitization of Nanocrystalline  $TiO_2$ . *J. Phys. Chem. B* **2000**, 104, 1791–1795.
- (39) Kelly, C. A.; Farzad, F.; Thompson, D. W.; Stipkala, J. M.; Meyer, G. J. Cation-Controlled Interfacial Charge Injection in Sensitized Nanocrystalline  $TiO_2$ . *Langmuir* **1999**, 15, 7047–7054.
- (40) Boschloo, G.; Fitzmaurice, D. Electron Accumulation in Nanostructured  $TiO_2$  (Anatase) Electrodes. *J. Phys. Chem. B* **1999**, 103, 7860–7868.
- (41) Ardo, S.; Meyer, G. J. Photodriven Heterogeneous Charge Transfer with Transition-Metal Compounds Anchored to  $TiO_2$  Semiconductor Surfaces. *Chem. Soc. Rev.* **2009**, 38, 115–164.
- (42) O’Regan, B.; Grätzel, M.; Fitzmaurice, D. Optical Electro- chemistry I: Steady-State Spectroscopy of Conduction-Band Electrons in a Metal Oxide Semiconductor Electrode. *Chem. Phys. Lett.* **1991**, 183, 89–93.
- (43) Kay, A.; Humphry-Baker, R.; Grätzel, M. Artificial Photosynthesis. 2. Investigations on the Mechanism of Photosensitization of Nanocrystalline  $TiO_2$  Solar Cells by Chlorophyll Derivatives. *J. Phys. Chem.* **1994**, 98, 952–959.
- (44) Norris, D. J.; Sacra, A.; Murray, C. B.; Bawendi, M. G. Measurement of the Size Dependent Hole Spectrum in CdSe Quantum Dots. *Phys. Rev. Lett.* **1994**, 72, 2612–2615.

- (45) Szczepankiewicz, S. H.; Moss, J. A.; Hoffmann, M. R. Electron Traps and the Stark Effect on Hydroxylated Titania Photocatalysts. *J. Phys. Chem. B* **2002**, 106, 7654–7658.
- (46) Burstein, E. Anomalous Optical Absorption Limit in InSb. *Phys. Rev.* **1954**, 93, 632–633.
- (47) Drago, R. S. *Physical Methods for Chemists*, 2nd ed.; Saunders College Publishing: Philadelphia, **1992**.
- (48) Södergren, S.; Siegbahn, H.; Rensmo, H.; Lindström, H.; Hagfeldt, A.; Lindquist, S.-E. Lithium Intercalation in Nanoporous Anatase TiO<sub>2</sub> Studied with XPS. *J. Phys. Chem. B* **1997**, 101, 3087–3090.
- (49) Wagemaker, M.; Lützenkirchen-Hecht, D.; van Well, A. A.; Frahm, R. Atomic and Electronic Bulk versus Surface Structure: Lithium Intercalation in Anatase TiO<sub>2</sub>. *J. Phys. Chem. B* **2004**, 108, 12456–12464.
- (50) Olson, C. L.; Nelson, J.; Islam, M. S. Defect Chemistry, Surface Structures, and Lithium Insertion in Anatase TiO<sub>2</sub>. *J. Phys. Chem. B* **2006**, 110, 9995–10001.
- (51) Hengerer, R.; Kavan, L.; Krtil, P.; Grätzel, M. Orientation Dependence of Charge-Transfer Processes on TiO<sub>2</sub> (Anatase) Single Crystals. *J. Electrochem. Soc.* **2000**, 147, 1467–1472.
- (52) Krol, R. V. d.; Meulenkamp, E. A.; Goossens, A.; Schoonman, J. In-Situ X-ray Diffraction Study of Lithium Intercalation in Nano-structured Anatase Titanium Dioxide. *MRS Online Proceedings Library* **1998**, 536, 337–340.
- (53) Ardo, S.; Achey, D.; Morris, A. J.; Abrahamsson, M.; Meyer, G. J. Non-Nernstian Two-Electron Transfer Photocatalysis at Metalloporphyrin–TiO<sub>2</sub> Interfaces. *J. Am. Chem. Soc.* **2011**, 133, 16572–16580.
- (54) Hu, K.; Robson, K. C. D.; Johansson, P. G.; Berlinguette, C. P.; Meyer, G. J. Intramolecular Hole Transfer at Sensitized TiO<sub>2</sub> Interfaces. *J. Am. Chem. Soc.* **2012**, 134, 8352–8355.
- (55) Bisquert, J.; Fabregat-Santiago, F.; Mora-Seró, I.; Garcia-Belmonte, G.; Barea, E. M.; Palomares, E. A Review of Recent Results on Electrochemical Determination of the Density of Electronic States of Nanostructured Metal-Oxide Semiconductors and Organic Hole Conductors. *Inorg. Chim. Acta* **2008**, 361, 684–698.
- (56) Chidsey, C. E. D.; Murray, R. W. Redox Capacity and Direct Current Electron Conductivity in Electroactive Materials. *J. Phys. Chem.* **1986**, 90, 1479–1484.
- (57) Johansson, P. G.; Kopecky, A.; Galoppini, E.; Meyer, G. J. Distance Dependent Electron Transfer at TiO<sub>2</sub> Interfaces Sensitized with Phenylene Ethynylene Bridged Ru<sup>II</sup>–Isothiocyanate Compounds. *J. Am. Chem. Soc.* **2013**, 135, 8331–8341.
- (58) Kislenco, S. A.; Amirov, R. H.; Samoylov, I. S. Effect of Cations on the TiO<sub>2</sub>/Acetonitrile Interface Structure: A Molecular Dynamics Study. *J. Phys. Chem. C* **2013**, 117, 10589–10596.

- (59) Wang, H.; He, J.; Boschloo, G.; Lindström, H.; Hagfeldt, A.; Lindquist, S.-E. Electrochemical Investigation of Traps in a Nanostructured TiO<sub>2</sub> Film. *J. Phys. Chem. B* **2001**, 105, 2529–2533. (60) Wang, H.; Bell, J.; Desilvestro, J.; Bertoz, M.; Evans, G. Effect of Inorganic Iodides on Performance of Dye-Sensitized Solar Cells. *J. Phys. Chem. C* **2007**, 111, 15125–15131.
- (61) Wang, H.; Peter, L. M. Influence of Electrolyte Cations on Electron Transport and Electron Transfer in Dye-Sensitized Solar Cells. *J. Phys. Chem. C* **2012**, 116, 10468–10475.
- (62) Fredin, K.; Nissfolk, J.; Boschloo, G.; Hagfeldt, A. The Influence of Cations on Charge Accumulation in Dye-Sensitized Solar Cells. *J. Electroanal. Chem.* **2007**, 609, 55–60.
- (63) Zhang, C.; et al. Photoelectrochemical Analysis of the Dyed TiO<sub>2</sub>/Electrolyte Interface in Long-Term Stability of Dye-Sensitized Solar Cells. *J. Phys. Chem. C* **2012**, 116, 19807–19813.
- (64) Hagfeldt, A.; Boschloo, G.; Sun, L.; Kloo, L.; Pettersson, H. Dye-Sensitized Solar Cells. *Chem. Rev.* **2010**, 110, 6595–6663.
- (65) Burdzinski, G.; Karolczak, J.; Ziolk, M. Dynamics of Local Stark Effect Observed for a Complete D149 Dye-Sensitized Solar Cell. *Phys. Chem. Chem. Phys.* **2013**, 15, 3889–3896

## CHAPTER 3: ELECTRIC FIELDS CONTROL $\text{TiO}_2(e^-)+\text{I}_3^- \rightarrow \text{CHARGE RECOMBINATION IN DYE-SENSITIZED SOLAR CELLS}^*$

### 3.1 Introduction

Electrons injected into the mesoporous  $\text{TiO}_2$  nanocrystalline (anatase) thin films commonly used in dye-sensitized solar cells (DSSCs) generate an electric field that significantly perturbs the absorption spectra of the dye molecules anchored to its surface. The electroabsorption signature, similar to that observed in Stark spectroscopy, and the  $>1$  MV/cm electric field magnitude were only recently discovered, and a full appreciation of how the presence of this field might be exploited for practical applications remains uncertain.<sup>1,2</sup> The electroabsorption signature appears as a first derivative of the ground-state absorption that has proven to be a valuable experimental tool for the characterization of dye-sensitized  $\text{TiO}_2$  interfaces.<sup>3-7</sup> Indeed, insight into the relative orientation of the molecular dipole as well as the dye–semiconductor distance has been revealed through systematic studies with different dye molecules.<sup>2,8</sup> In addition, pulsed laser excitation has permitted the dynamics for charge screening by the electrolyte to be quantified on microsecond and longer time scales.<sup>9-11</sup> Yet despite these advances in fundamental science, there is no clear indication that these electric fields have any practical relevance to the light-driven electron-transfer reactions that promote or inhibit electrical power generation in DSSCs. One would reasonably anticipate that the surface electric field would repel anions like tri-iodide and

---

\*This chapter previously appeared as an article in the Journal of Physical Chemistry Letters. Reprinted (adapted) with permission from (Sampaio, R. N.; O'Donnell, R. M.; Barr, T. J.; Meyer, G. J. Electric Fields Control  $\text{TiO}_2(e^-) + \text{I}_3^- \rightarrow \text{Charge Recombination in Dye-Sensitized Solar Cells}$ . *J. Phys. Chem. Lett.* **2014**, 5, 3265–3268.). Copyright (2014) American Chemical Society.

hence inhibit the unwanted charge recombination reaction with electrons injected into TiO<sub>2</sub>. However, until now, there has been no compelling evidence that the anionic nature of these redox mediators is at all relevant to operational DSSCs.

### 3.2 Results and Discussion

The mesoporous TiO<sub>2</sub> thin films utilized in this study were sensitized to visible light by [Ru(dtb)<sub>2</sub>(dcb)](PF<sub>6</sub>)<sub>2</sub>, where dtb is 4,4'-(tert-butyl)<sub>2</sub>-2,2'-bipyridine and dcb is 4,4'-(CO<sub>2</sub>H)<sub>2</sub>-2,2'-bipyridine, abbreviated Ru(dtb)<sub>2</sub>(dcb)/TiO<sub>2</sub>. This sensitizer was selected as it gives rise to a very large amplitude electroabsorption signature, although conventional sensitizers such as isothiocyanate Ru polypyridyl compounds as well as D-π-A type organic compounds behave similarly.<sup>1,2</sup> Figure 3.01 shows the visible absorption spectra of a Ru(dtb)<sub>2</sub>(dcb)/TiO<sub>2</sub> thin film immersed in neat acetonitrile and in acetonitrile solutions that contain 100 mM iodide with Li<sup>+</sup>, Na<sup>+</sup>, Mg<sup>2+</sup>, or Ca<sup>2+</sup> cations. The extinction coefficients were calculated relative to Ru(dtb)<sub>2</sub>(dcb)/TiO<sub>2</sub> in CH<sub>3</sub>CN, which was assumed to have the same value as the [Ru(dtb)<sub>2</sub>(dcb)](PF<sub>6</sub>)<sub>2</sub> dissolved in CH<sub>3</sub>CN. A significant red shift in the metal-to-ligand charge-transfer (MLCT) absorption was observed in the electrolyte solutions relative to neat CH<sub>3</sub>CN as well as a small decrease in the maximum absorption intensity. The magnitude of the red shift increased in the order Na<sup>+</sup> < Li<sup>+</sup> < Mg<sup>2+</sup> ≈ Ca<sup>2+</sup>. These data with the iodide salts are in excellent agreement with that previously reported for the perchlorate salts, which is consistent with the proposal that adsorption of these Lewis acidic cations to TiO<sub>2</sub> induces the spectral shifts with negligible contributions from the anions.<sup>10</sup>

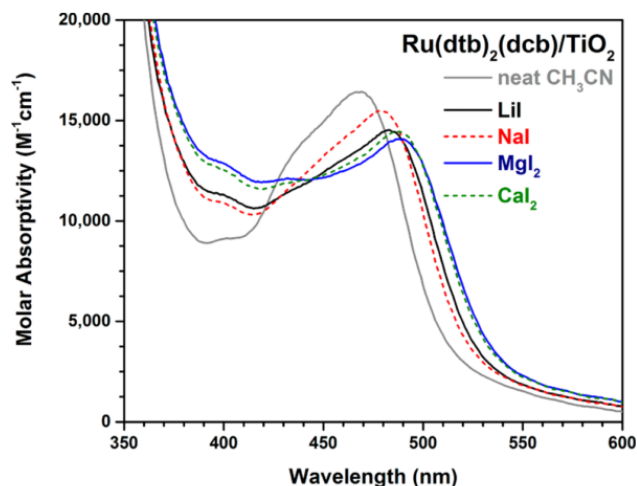


Figure 3.01. Visible absorbance spectra of a  $\text{Ru}(\text{dtb})_2(\text{dcb})/\text{TiO}_2$  thin film immersed in acetonitrile in the absence (gray) or presence of 100 mM LiI (black), 100 mM NaI (red), 50 mM  $\text{MgI}_2$  (blue), and 50 mM  $\text{CaI}_2$  (green).

Partial electrochemical reduction of the sensitized  $\text{TiO}_2$  thin films in a standard three-electrode cell results in a blue shift of the MLCT absorption, as has been previously described.<sup>1,10</sup> Figure 3.02A shows such data as difference spectra where the absorption spectra of the reduced film are subtracted from the initial spectrum under conditions where about 20 electrons were present in each  $\text{TiO}_2$  nanocrystallite.

Pulsed laser excitation of the  $\text{Ru}(\text{dtb})_2(\text{dcb})/\text{TiO}_2$  thin films immersed in the iodide acetonitrile electrolytes gave rise to significant absorption changes that were monitored on nanosecond and longer time scales. Light absorption by the Ru sensitizer resulted in rapid excited-state injection and sensitizer regeneration through iodide oxidation that were complete within a microsecond. The oxidation of iodide to tri-iodide in DSSCs is known to occur through disproportionation of an  $\text{I}_2^{\cdot -}$  intermediate. Disproportionation within the mesopores of  $\text{TiO}_2$  occurs with the same rate constant as that in fluid solution,  $k = 3 \times$

$10^9 M^{-1} s^{-1}$ .<sup>12</sup> Hence, only the injected electrons and tri-iodide were expected to appreciably absorb light in the visible region on time scales greater than 1  $\mu s$ . Shown in Figure 3.02B are representative spectra recorded 2.5  $\mu s$  after laser excitation of the Ru(dtb)<sub>2</sub>(dcb)/TiO<sub>2</sub> in acetonitrile electrolytes that represented the extremes that were observed, 100 mM NaI or 50 mM CaI<sub>2</sub>. The characteristic absorption of I<sub>3</sub><sup>-</sup> at  $\sim 360$  nm and the weak absorption of the injected electrons at 600 nm were evident.<sup>13</sup>

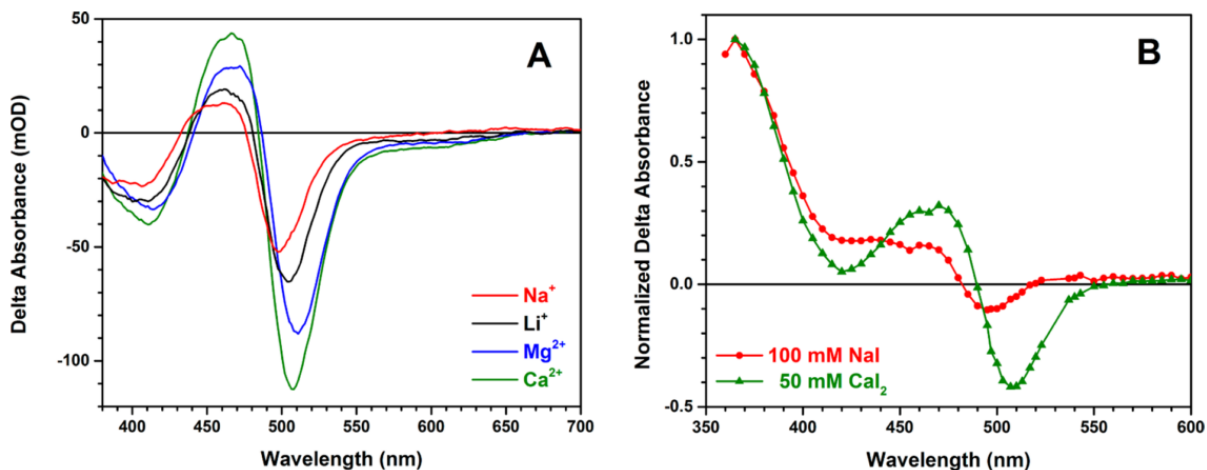


Figure 3.02. Absorbance change of Ru(dtb)<sub>2</sub>(dcb)/TiO<sub>2</sub> thin films measured (A) under conditions of approximately 20 TiO<sub>2</sub>(e<sup>-</sup>)s per TiO<sub>2</sub> nanoparticle electrochemically generated in 100 mM solutions of NaClO<sub>4</sub> (red), LiClO<sub>4</sub> (black), Mg(ClO<sub>4</sub>)<sub>2</sub> (blue), and Ca(ClO<sub>4</sub>)<sub>2</sub> (green) and (B) 2.5  $\mu s$  after pulsed 532 nm light excitation in 100 mM NaI (red, circles) and 50 mM CaI<sub>2</sub> (green, triangles) acetonitrile solutions.

The large first-derivative feature between  $\sim 450$  and 550 nm arises from a unidirectional shift of the ground-state absorption spectra induced by the injected electrons. In other words, the electrons injected into TiO<sub>2</sub> generate an electric field that significantly blue shifts the MLCT absorption of the ruthenium compounds anchored to the surface.<sup>1</sup> The

magnitude of the intensity change and the spectral shift were significantly more pronounced when  $\text{Ca}^{2+}$ -containing electrolytes were employed, behavior attributed to less effective screening of the electric field from the sensitizer. The field strengths were found to follow the order  $\text{Na}^+ < \text{Li}^+ < \text{Mg}^{2+} < \text{Ca}^{2+}$ .<sup>10</sup> The electric field strength reported by the Ru sensitizers was 1.1 MV/cm for  $\text{Na}^+$  and 2.2 MV/cm for  $\text{Ca}^{2+}$ , with the magnitude of the electric fields calculated using previously reported methods and assumptions.<sup>1,10,14,15</sup> Because the number of  $\text{TiO}_2$  electrons was held constant, the different field strengths were attributed to the ability of the cations to screen the field from the surface anchored sensitizers.

Shown in Figure 3.03 are absorption changes monitored at 375 nm. This observation wavelength was chosen as the  $\text{I}_3^-$  anion absorbs strongly there and it represents an isosbestic point between  $\text{I}_2^{\bullet-}$  and  $\text{I}_3^-$ .<sup>12</sup> As a result, the concentration of  $\text{I}_3^-$  can be uniquely probed at this wavelength. The nonexponential kinetics were well described by the Kohlrausch–Williams–Watts (KWW) model, Equation 3.01.

$$I(t) = I_0 \exp[(-kt)^\beta] \quad 3.01$$

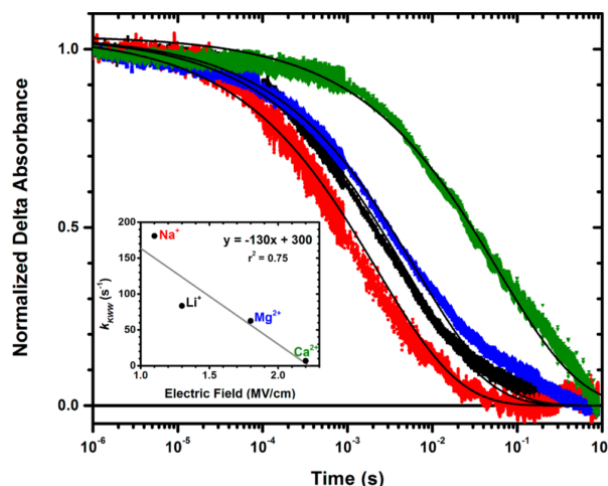


Figure 3.03. Absorption changes that correspond to  $\text{TiO}_2(\text{e}^-) + \text{I}_3^- \rightarrow$  charge recombination measured in 100 mM  $\text{LiClO}_4$  (black),  $\text{NaClO}_4$  (red),  $\text{Mg}(\text{ClO}_4)_2$  (blue), and mM  $\text{Ca}(\text{ClO}_4)_2$  (green) acetonitrile solutions with 250 mM TBAI. Overlaid on the data are fits to the KWW function with  $\beta = 0.45$ . The inset shows a plot of the recombination rate constant versus the electric field.

Here,  $\beta$  is inversely related to the width of an underlying Lévy distribution of rate constants,  $0 < \beta < 1$ , and  $k$  is a characteristic rate constant. In kinetic analysis, the value of  $\beta$  was fixed to be 0.45, and  $k$  was allowed to float. An “average” rate constant was calculated as the first moment of this distribution using Equation 3.02, and data are given in Table 3.1.

$$k_{KWW} = \frac{k\beta}{\Gamma\left(\frac{1}{\beta}\right)} \quad 3.02$$

Table 3.1.  $\text{TiO}_2(\text{e}^-)+\text{I}_3^- \rightarrow$  Charge Recombination with the Indicated Cations

	<i>Electric field</i> (MV/cm) <sup>a</sup>	<i>k</i> (s <sup>-1</sup> ) <sup>b</sup>	<i>k<sub>KWW</sub></i> (s <sup>-1</sup> )	<i>t</i>
<i>Na</i> <sup>+</sup>	1.1	450	180	0.40
<i>Li</i> <sup>+</sup>	1.3	210	80	0.73
<i>Mg</i> <sup>2+</sup>	1.8	160	60	0.80
<i>Ca</i> <sup>2+</sup>	2.2	20	10	0.97

<sup>a</sup>Electric field change measured after the potentiostatic injection of approximately 20  $\text{TiO}_2(\text{e}^-)$ s per nanoparticle. <sup>b</sup> $\beta$  fixed to 0.45.

The inset of Figure 3.03 is a plot of the recombination rate constant versus the electric field. This and the raw experimental data clearly show a marked electric field dependence for the unwanted  $\text{TiO}_2(\text{e}^-)+\text{I}_3^- \rightarrow$  charge recombination rate constant. This correlation provides compelling evidence that the larger the electric field, the slower the unwanted charge recombination reaction with  $\text{I}_3^-$ . Recall that  $\text{I}_3^-$  is generated within the mesopores after the disproportionation of two  $\text{I}_2^*$  ions. Mass transfer of  $\text{I}_3^-$  by both diffusion and migration to the  $\text{TiO}_2$  surface must then occur before recombination is possible. Extrapolation of the best-fit line to zero electric field provides an estimate of the diffusional contributions to the recombination reaction that occurs in the absence of an electric field,  $k = 300 \text{ s}^{-1}$ . Because rate constants are proportional to current, the total current at zero field is the diffusional current,  $i_0 = i_d$ . The rate constants decrease when electrons are injected into  $\text{TiO}_2$  because the anionic charge of the  $\text{I}_3^-$  is repelled by the field generated by the  $\text{TiO}_2(\text{e}^-)$ s. Hence, the total current decreases in the presence of the field due to migration of  $\text{I}_3^-$  away from the  $\text{TiO}_2$  interface,  $i = i_d - i_m$ . The ratio of the average rate constant measured in the presence of the field to that in the absence has some analogy to transference coefficients,  $t = i/i_0$ , that have

been quantified in electrochemical cells.<sup>16</sup> Here,  $t$  represents the fractional ability of the electric field to block the unwanted  $\text{TiO}_2(\text{e}^-) + \text{I}_3^- \rightarrow$  charge recombination reaction. The  $t$  values are given in Table 3.1.

It should be pointed out that other iodine species may also accept electrons in DSSCs. Indeed, there exists compelling evidence that molecular iodine  $\text{I}_2$  is reduced by  $\text{TiO}_2(\text{e}^-)$ s. As tri-iodide and molecular iodine are in equilibrium, Equation 3.03, both are always present in solution.<sup>17</sup> However, under the current experimental conditions, iodide was the only species present before laser excitation, and the concentrations of  $\text{I}_3^-$  generated with light were on the order of 10  $\mu\text{M}$ , rendering the equilibrium concentration of  $\text{I}_2$  negligibly small. Hence, the present study has effectively stacked the deck to ensure that recombination occurs predominantly to tri-iodide. This differs from an operational DSSC where a mixture of 0.5 M LiI and 0.05 M  $\text{I}_2$  in an acetonitrile solution is typically utilized. The equilibrium constant for reaction 4 has been estimated to be  $K_{\text{eq}} = 10^6$ , indicating that equilibrium concentrations are 0.45M  $\text{I}^-$ , 0.05 M  $\text{I}_3^-$ , and 2  $\mu\text{M}$   $\text{I}_2$ .<sup>13</sup>



It should also be emphasized that changing the cations in the electrolytes of DSSCs influences many parameters, including the transport of the injected electrons,<sup>18–20</sup> dye regeneration,<sup>21</sup> and the energy levels of the  $\text{TiO}_2$  acceptor states.<sup>10,22,23</sup> Nevertheless, the implications of the results presented herein to DSSCs are clear and significant. Akin to enlarging the space-charge layer thickness in single semiconductor solar cells, increasing the Debye length for charge screening supports more spatially separated and longer-lived  $\text{TiO}_2(\text{e}^-)$ ,  $\text{I}_3^-$  donor-acceptor pairs. Hence, screening of the electric field by these alkali and alkaline earth cations in the electrolyte is detrimental to the solar conversion efficiency. This

is particularly important at the power point and open-circuit conditions where the number of electrons is large and the  $\text{TiO}_2(\text{e}^-)$ s may be capable of accessing the two-electron reduction of  $\text{I}_3^-$ ,  $E^0(\text{I}_3^-/3\text{I}^-) = 0.35 \text{ V}$ , which is much more favorable than the one-electron reduction potential,  $E^0(\text{I}_3^-/\text{I}_2^{\bullet-}, \Gamma) = -0.35 \text{ V}$  versus NHE.<sup>13</sup> Interestingly, complete screening of the electric field should instead be beneficial for the cationic Co(III/II) redox mediators, such as  $[\text{Co}(\text{bpy})_3]^{3+/2+}$ , employed in champion DSSCs<sup>24</sup> because migration will enhance the mass transfer of Co(III) to the interface where recombination with injected electrons occurs.

### **Author Information**

Corresponding Author \*E-mail: gjmeyer@email.unc.edu.

Present Address §R.M.O., T.J.B., and G.J.M.: Department of Chemistry, University of North Carolina at Chapel Hill, Chapel Hill, North Carolina 27599, United States.

Notes

The authors declare no competing financial interest.

### **Acknowledgments**

The Division of Chemical Sciences, Geosciences, and Biosciences, Office of Basic Energy Sciences of the U.S. Department of Energy through Grant DE-FG02-96ER14662 is gratefully acknowledged for support (G.J.M.). R.M.O. would also like to thank the National Science Foundation for a Graduate Research Fellowship under Grant No. DGE-1232825. R.N.S. would like to thank the National Council for Scientific and Technological Development (CNPq) for support under Grant No. 244501/2012-2.

## REFERENCES

- (1) Ardo, S.; Sun, Y.; Staniszewski, A.; Castellano, F. N.; Meyer, G. J. Stark Effects after Excited-State Interfacial Electron Transfer at Sensitized TiO<sub>2</sub> Nanocrystallites. *J. Am. Chem. Soc.* **2010**, 132, 6696–6709.
- (2) Cappel, U. B.; Feldt, S. M.; Schöneboom, J.; Hagfeldt, A.; Boschloo, G. The Influence of Local Electric Fields on Photoinduced Absorption in Dye-Sensitized Solar Cells. *J. Am. Chem. Soc.* **2010**, 132, 9096–9101.
- (3) Burdzinski, G.; Karolczak, J.; Ziolk, M. Dynamics of Local Stark Effect Observed for a Complete D149 Dye-Sensitized Solar Cell. *Phys. Chem. Chem. Phys.* **2013**, 15, 3889–3896.
- (4) Farnum, B. H.; Morseth, Z. A.; Lapidés, A. M.; Rieth, A. J.; Hoertz, P. G.; Brennaman, M. K.; Papanikolas, J. M.; Meyer, T. J. Photoinduced Interfacial Electron Transfer within a Mesoporous Transparent Conducting Oxide Film. *J. Am. Chem. Soc.* **2014**, 136, 2208–2211.
- (5) Bairu, S. G.; et al. Ultrafast Interfacial Charge-Transfer Dynamics in a Donor- $\pi$ -Acceptor Chromophore Sensitized TiO<sub>2</sub> Nanocomposite. *J. Phys. Chem. C* **2013**, 117, 4824–4835.
- (6) Meister, M.; Baumeier, B.; Pschirer, N.; Sens, R.; Bruder, I.; Laquai, F.; Andrienko, D.; Howard, I. A. Observing Charge Dynamics in Surface Reactions by Time-Resolved Stark Effects. *J. Phys. Chem. C* **2013**, 117, 9171–9177.
- (7) Oum, K.; Flender, O.; Lohse, P. W.; Scholz, M.; Hagfeldt, A.; Boschloo, G.; Lenzer, T. Electron and Hole Transfer Dynamics of a Triarylamine-Based Dye with Peripheral Hole Acceptors on TiO<sub>2</sub> in the Absence and Presence of Solvent. *Phys. Chem. Chem. Phys.* **2014**, 16, 8019–8029.
- (8) Johansson, P. G.; Kopecky, A.; Galoppini, E.; Meyer, G. J. Distance Dependent Electron Transfer at TiO<sub>2</sub> Interfaces Sensitized with Phenylene Ethynylene Bridged Ru<sup>II</sup>-Isothiocyanate Compounds. *J. Am. Chem. Soc.* **2013**, 135, 8331–8341.
- (9) O'Donnell, R. M.; Ardo, S.; Meyer, G. J. Charge-Screening Kinetics at Sensitized TiO<sub>2</sub> Interfaces. *J. Phys. Chem. Lett.* **2013**, 4, 2817–2821.
- (10) O'Donnell, R. M.; Sampaio, R. N.; Barr, T. J.; Meyer, G. J. Electric Fields and Charge Screening in Dye Sensitized Mesoporous Nanocrystalline TiO<sub>2</sub> Thin Films. *J. Phys. Chem. C* **2014**, 118, 16976–16986.
- (11) Song, W.; Luo, H.; Hanson, K.; Concepcion, J. J.; Brennaman, M. K.; Meyer, T. J. Visualization of Cation Diffusion at the TiO<sub>2</sub> Interface in Dye Sensitized Photoelectrosynthesis Cells (DSPEC). *Energy Environ. Sci.* **2013**, 6, 1240–1248.
- (12) Rowley, J. G.; Meyer, G. J. Di- and Tri-iodide Reactivity at Illuminated Titanium Dioxide Interfaces. *J. Phys. Chem. C* **2011**, 115, 6156–6161.
- (13) Rowley, J. G.; Farnum, B. H.; Ardo, S.; Meyer, G. J. Iodide Chemistry in Dye-Sensitized Solar Cells: Making and Breaking I–I Bonds for Solar Energy Conversion. *J. Phys. Chem. Lett.* **2010**, 1, 3132–3140.

- (14) Oh, D. H.; Boxer, S. G. Stark Effect Spectra of Ru(diimine)<sub>3</sub><sup>2+</sup> Complexes. *J. Am. Chem. Soc.* **1989**, 111, 1130–1131.
- (15) Ardo, S.; Sun, Y.; Castellano, F. N.; Meyer, G. J. Excited-State Electron Transfer from Ruthenium-Polypyridyl Compounds to Anatase TiO<sub>2</sub> Nanocrystallites: Evidence for a Stark Effect. *J. Phys. Chem. B* **2010**, 114, 14596–14604.
- (16) Bard, A. J.; Faulkner, L. R. *Electrochemical Methods: Fundamentals and Applications*; John Wiley & Sons: Hoboken, NJ, **2001**; pp 66–68 and 137–143.
- (17) Richards, C. E.; Anderson, A. Y.; Martiniani, S.; Law, C.; O'Regan, B. C. The Mechanism of Iodine Reduction by TiO<sub>2</sub> Electrons and the Kinetics of Recombination in Dye-Sensitized Solar Cells. *J. Phys. Chem. Lett.* **2012**, 3, 1980–1984.
- (18) Kambe, S.; Nakade, S.; Kitamura, T.; Wada, Y.; Yanagida, S. Influence of the Electrolytes on Electron Transport in Mesoporous TiO<sub>2</sub>-Electrolyte Systems. *J. Phys. Chem. B* **2002**, 106, 2967–2972.
- (19) Wang, H.; Bell, J.; Desilvestro, J.; Bertoz, M.; Evans, G. Effect of Inorganic Iodides on Performance of Dye-Sensitized Solar Cells. *J. Phys. Chem. C* **2007**, 111, 15125–15131.
- (20) Wang, H.; Peter, L. M. Influence of Electrolyte Cations on Electron Transport and Electron Transfer in Dye-Sensitized Solar Cells. *J. Phys. Chem. C* **2012**, 116, 10468–10475.
- (21) Pelet, S.; Moser, J.-E.; Grätzel, M. Cooperative Effect of Adsorbed Cations and Iodide on the Interception of Back Electron Transfer in the Dye Sensitization of Nanocrystalline TiO<sub>2</sub>. *J. Phys. Chem. B* **2000**, 104, 1791–1795.
- (22) Kelly, C. A.; Farzad, F.; Thompson, D. W.; Stipkala, J. M.; Meyer, G. J. Cation-Controlled Interfacial Charge Injection in Sensitized Nanocrystalline TiO<sub>2</sub>. *Langmuir* **1999**, 15, 7047–7054.
- (23) Redmond, G.; Fitzmaurice, D. Spectroscopic Determination of Flatband Potentials for Polycrystalline Titania Electrodes in Non-aqueous Solvents. *J. Phys. Chem.* **1993**, 97, 1426–1430.
- (24) Mathew, S.; et al. Dye-Sensitized Solar Cells with 13% Efficiency Achieved Through the Molecular Engineering of Porphyrin Sensitizers. *Nat. Chem.* **2014**, 6, 242–247.

## CHAPTER 4: ELECTROLYTE CATION CONTROLS DRIVING FORCE FOR CHARGE RECOMBINATION IN DYE-SENSITIZED SOLAR CELLS

### 4.1 Introduction

Interfacial electron transfer reactions are critically important to dye-sensitized solar cells (DSSCs), where the desired electron injection and unwanted charge recombination reactions occur at the interface. The maximum current a solar cell can produce,  $J_{sc}$ , is directly related to the spectral harvesting of the sensitizer and how many of the absorbed photons lead to injected electrons. Once injected, there are two primary loss pathways, where the electrons recombine with either the oxidized sensitizer or the oxidized redox mediator. The average time an electron remains in the  $TiO_2$  thin film before recombining is known as the electron lifetime, which influences the ability of cell to build a voltage at open circuit,  $V_{oc}$ . It is now clear that the electron lifetime also influences the maximum power output of a cell, where electrons are lost due to back electron transfer to the oxidized sensitizer.<sup>1,2</sup> Therefore, understanding the charge recombination reaction and what controls the electron lifetime in operational DSSCs is critically important to optimize device performance.

Previous studies in our group have investigated charge recombination to  $I_3^-$ ,  $TPA^+$ , and  $PTZ^+$ , where TPA is triphenylamine and PTZ is phenothiazine, that were sensitive to the identity of the Lewis-acidic cation in the surrounding electrolyte.<sup>3,4</sup> Three mechanisms have been proposed to account for these observations: electric fields, electron diffusion, and driving force. Unravelling which of these influences is the dominant feature controlling the

electron lifetime is complicated by the fact that electrolyte cation may influence each of these parameters separately.

Electron transfer reactions are known to be dependent on the thermodynamic driving force in the framework of Marcus,<sup>5,6</sup> or, at the interface, Marcus-Gerischer theory.<sup>7,8</sup> Attempts to alter the driving force by modifying the identity of the electron acceptor in solution or bound to the surface have been reported for charge recombination. Charge recombination to the oxidized sensitizer typically has a driving force well over 1 eV and has been reported to be in the Marcus-inverted region, i.e. larger driving force leads to slower charge recombination,<sup>9,10</sup> although this behavior is not always observed.<sup>11,12</sup> In contrast, charge recombination to the redox mediator is typically reported in the Marcus-normal region, i.e. larger driving force leads to faster charge recombination.<sup>13-17</sup>

An alternative means to vary the driving force would be to adjust the reducing power of electrons within the TiO<sub>2</sub> thin film (TiO<sub>2</sub>(e<sup>-</sup>)s). This has been attempted by doping,<sup>18,19</sup> the addition of Lewis acidic or Lewis basic additives to the surrounding electrolyte,<sup>20-22</sup> or, in aqueous systems, by adjusting the electrolyte pH.<sup>16</sup> Lewis-acidic cations are known to shift the energetic position of the TiO<sub>2</sub> acceptor states positive on an electrochemical scale to a degree that roughly correlates with the charge-to-size ratio of the cation,<sup>23,24</sup> similar to how electrolyte pH influences the flat-band position of many semiconductors in aqueous electrolyte.<sup>25,26</sup> Directly related to the position of the TiO<sub>2</sub> acceptor states are the electron injection efficiency,<sup>27</sup> sensitizer photoluminescence,<sup>24</sup> incident-photon-to-current efficiency,<sup>28</sup> and open circuit voltage.<sup>28</sup>

In order for the driving force to have a significant influence on charge recombination, the reaction must not be diffusion limited by the ability of the injected electron and oxidizing

equivalent to encounter each another. This is known as the reaction limited regime. In DSSCs, the conditions for reaction limited and diffusion limited charge recombination have been theoretically studied by Ansari-Rad *et.al.*<sup>29</sup> The authors concluded that in typical  $I/I_3^-$  based DSSCs, charge recombination is most likely in the reaction limited regime. The examples for driving force dependent charge recombination listed above suggest this is correct, however the fact that driving force is not universally observed to influence charge recombination hints that recombination may be on the border of between the reaction limited and diffusion limited regimes depending on the experimental conditions. Factors such as surface electric fields and slow electron diffusion coefficients may be enough to tip the scale towards the diffusion limited regime.

Surface electric fields have been observed following excited-state electron injection into  $TiO_2$  nanocrystallites. These fields have been reported by surface-bound sensitizers to be on the order of 2 MV/cm.<sup>30,31</sup> They are known to extend nanometers into the electrolyte<sup>32</sup> and across the surface.<sup>31</sup> Cations in the surrounding acetonitrile electrolyte rearrange to screen the electric field,<sup>33-35</sup> where the dynamics of charge screening are sensitive to the identity of the Lewis-acidic electrolyte cation.<sup>24</sup>

Although these fields are well characterized, their impact on device performance remains unknown. Evidence for electric-field controlled, and charge screening dependent, charge recombination to  $I_3^-$  has been reported.<sup>4</sup> If the electric field repelled the negatively charged  $I_3^-$ , the concentration of acceptors at the interface would decrease and the observed recombination rate would decrease even if the rate constant was unaffected. Screening of the field by cations in the electrolyte would therefore be deleterious and increase charge recombination. That conclusion has recently been challenged by using neutral/cationic redox

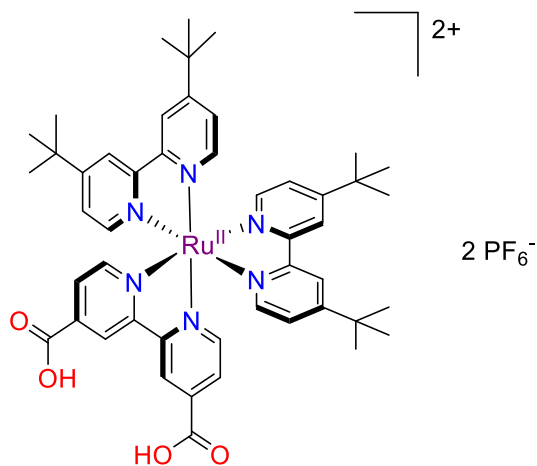
mediators as the electron acceptor.<sup>3</sup> Their results displayed a similar charge screening dependence, inconsistent with the idea that electric fields significantly influenced charge recombination. However, the timescale for charge recombination was much faster and competed with the charge screening process.

Similar to how electric fields may influence the arrival of electron acceptors to the surface, electron diffusion may dictate the arrival of  $\text{TiO}_2(e^-)$ s to recombination centers. Early studies examining charge transport in DSSCs at matched  $J_{sc}$  values suggested that the diffusion coefficient of  $\text{TiO}_2(e^-)$ s was sensitive to the electrolyte cation through an ambipolar mechanism.<sup>36</sup> However, it has become increasingly clear that for DSSCs, kinetic parameters should be compared at matched electron concentrations. More recent studies have reexamined electron diffusion at matched  $\text{TiO}_2(e^-)$ s concentrations and found no cation dependence on the diffusion coefficient,<sup>28</sup> however the generality of this finding has yet to be established.

Here, complete DSSCs were constructed and analyzed on an in-lab purpose built instrument, termed STRiVE (Sequential Time Resolved current(i) Voltage Experiments), which is similar to other reported devices.<sup>37-39</sup> The STRiVE allows for direct measurement of the electron concentration, lifetime, and diffusion coefficient under a wide range on incident light intensities. This makes it possible to directly investigate the possible influence of driving force and electron diffusion on the electron lifetime. Furthermore, by comparing DSSCs constructed with the anionic iodide/triiodide redox mediator to those with a cationic cobalt redox mediator, the influence of electric fields on charge recombination can be directly tested. The sensitizer,  $\text{Ru}(\text{dcb})(\text{dtb})_2(\text{PF}_6)_2$  (Scheme 4.1), was chosen because it was used in previous studies where the electric field has been thoroughly characterized.<sup>3,4,24,31,33</sup>

The results indicate that driving force largely controls the cation-dependence of charge recombination in DSSCs with minimal contribution from electron diffusion or electric fields.

Scheme 4.1. Ru(dcb)(dtb)<sub>2</sub>(PF<sub>6</sub>)<sub>2</sub> Structure



## 4.2 Experimental

**Materials:** The following reagents were used as received: lithium perchlorate (LiClO<sub>4</sub>; Sigma-Aldrich, 99.99%); sodium perchlorate (NaClO<sub>4</sub>; Sigma-Aldrich, ≥ 98.0%); magnesium perchlorate (Mg(ClO<sub>4</sub>)<sub>2</sub>; Sigma-Aldrich, ACS reagent); calcium perchlorate tetrahydrate (Ca(ClO<sub>4</sub>)<sub>2</sub>•4H<sub>2</sub>O; Sigma-Aldrich, ≥ 99%); hydrogen hexachloroplatinate(IV) hydrate (H<sub>2</sub>PtCl<sub>6</sub>•xH<sub>2</sub>O; Aldrich); oxygen gas (Airgas, industrial grade); titanium(IV) isopropoxide (Sigma-Aldrich, 97%); nitric acid (HNO<sub>3</sub>, Fisher, Certified ACS); fluorine-doped tin oxide-coated glass (FTO; Hartford Glass Co., Inc., 2.3 mm thick, 15 Ω/□); acetonitrile (CH<sub>3</sub>CN, Fluka, 99.9%); 2-propanol ((CH<sub>3</sub>)<sub>2</sub>CHOH, Fisher Scientific, 99.9%); methanol (CH<sub>3</sub>OH, Fisher, 99.9%); Surlyn (Meltonix 1170-25, Solaronix, 25 μm); glass cover slip (Microscope Cover Glass 12-541-A, Fisher Scientific); cobalt(II) chloride

hexahydrate ( $\text{CoCl}_2 \cdot 6\text{H}_2\text{O}$ , Sigma-Aldrich, 98%); 4,4'-di-*tert*-butyl-2,2'-bipyridine ( $\text{C}_{18}\text{H}_{24}\text{N}_2$ , Sigma-Aldrich, 98%); silver hexafluorophosphate ( $\text{AgPF}_6$ , Strem Chemicals, 98%); potassium hexafluorophosphate ( $\text{KPF}_6$ , Sigma-Aldrich, 98%); bromine ( $\text{Br}_2$ , Sigma-Aldrich, reagent grade);

**Synthesis of the  $\text{Co}^{\text{III}}(\text{dtb})_3$  redox couple:** Synthesis of  $[\text{Co}(\text{dtb})_3](\text{PF}_6)_2$  was carried out according to previous reports.<sup>40,41</sup> Briefly, 3.5 g (3.1 eq.) of 4,4'-di-*tert*-butyl-2,2'-bipyridine (dtb) was added to 1 g  $\text{CoCl}_2 \cdot 6\text{H}_2\text{O}$  in 100 mL  $\text{CH}_3\text{OH}$ . The solution immediately changed color but was refluxed for 1 h to ensure complete reaction. After cooling to room temperature, 2 g (2.5 eq.)  $\text{KPF}_6$  in minimal  $\text{H}_2\text{O}$  was added to the solution, which was filtered, washed with  $\text{H}_2\text{O}$  and  $\text{CH}_3\text{OH}$ , and dried in a vacuum oven at  $100^\circ\text{C}$  to give the desired product (98 % yield). Oxidation of  $[\text{Co}(\text{dtb})_3](\text{PF}_6)_2$  was accomplished by adding 45  $\mu\text{L}$   $\text{Br}_2$  (*l*) to 0.33 g  $[\text{Co}(\text{dtb})_3](\text{PF}_6)_2$  dissolved in minimal  $\text{CH}_3\text{CN}$  (~10 mL). The solution was stirred for 30 mins at room temperature and then 0.075 g  $\text{AgPF}_6$  was added to for the anion metathesis. After filtering the  $\text{AgBr}$ , the solvent was removed under reduced pressure at  $50^\circ\text{C}$ . The solid was washed with deionized water to remove any excess  $\text{AgPF}_6$  and dried in a vacuum oven at  $100^\circ\text{C}$  to give the desired product (88% yield).

**Cell Fabrication:** Synthesis of approximately 15 nm diameter  $\text{TiO}_2$  nanoparticles of was carried out by the acid hydrolysis of titanium(IV) isopropoxide as previously reported.<sup>42</sup> Thin films were cast on fluorine-doped tin oxide glass (FTO) by doctor blading using Scotch tape as the spacer. After resting for 30 minutes, films were sintered in an oven at  $450^\circ\text{C}$  for 30 minutes under oxygen flow. Excess  $\text{TiO}_2$  was manually removed from the FTO surface using glass microscope slides to prevent iron contamination. The resulting electrode measured  $\sim 2.5 \times 1.5 \text{ cm}^2$  with a  $\text{TiO}_2$  active area of  $\sim 0.3 \text{ cm}^2$ . Platinized counter electrodes were prepared by

evaporating two drops of 6.5 mg/mL  $\text{H}_2\text{PtCl}_6$  in 2-propanol onto a cleaned FTO surface followed by heating at 450 °C for approximately 20 minutes. Cells were heat sealed with a thermal gasket (Surlyn, ~25  $\mu\text{m}$ ). Electrolyte was introduced into the cell through a hole pre-drilled in the Pt counter electrode by the vacuum backfilling method. This hole was sealed with a piece of Surlyn and a glass cover slip.

**Device Analysis:** The performance of DSSCs was tested on an in-lab built system, termed ‘STRiVE,’ which is similar to other reported systems.<sup>37–39</sup> Cell current was measured by the voltage drop across a 1 Ohm resistor in series with the external circuit. This voltage was amplified by an instrument amplifier (INA 128, Texas Instruments) using gains between 100 and 5000 depending on the operating conditions. The amplified voltage as well as the operating voltage between the working and counter electrode could be simultaneously measured by a 16-bit data acquisition board (NI-6251) with a maximum sampling rate of 1.25 MHz. The cell was held at open or short circuit by fast solid state switches (MOSFETs). Illumination was provided by an array of white LEDs (not a solar spectrum) and/or an array of colored LEDs controlled by fast solid-state switches with switching times of ~250 ns. Potentials were applied to the cell using a PAR 362 scanning potentiostat.

**Transient Photovoltage Decay:** Cell voltage was set at open circuit by the intensity of the white background LEDs. After a 45 second equilibration time, a pulse of blue LED light was superimposed on the background light. The voltage perturbation was recorded and the decay could be easily fit to a single exponential decay. The magnitude of the perturbation was kept at ~4 mV, controlled by the duration of the colored LED pulse, which was typically 10-500  $\mu\text{s}$ .

**Transient Photocurrent Decay:** Transient photocurrent decay was done similarly to transient photovoltage decay. The current was set at short circuit by the intensity of the white background LEDs. Cells were equilibrated for 30 seconds before being illuminated by a pulse of blue LED light. The current perturbation was set to  $\sim 25 \mu\text{A}$  by adjusting the pulse time.

**Charge Extraction:** The cell was held at either open or short circuit depending on the experiment for 45 seconds under a given light intensity. The light was then turned off and, if the cell was originally at open circuit, was short circuited. The resulting current transient was recorded for 4 seconds and integrated to give the charge.

### 4.3 Results

The performance of DSSCs sensitized with  $[\text{Ru}(\text{dtb})_2(\text{dcb})](\text{PF}_6)_2$ , where dcb is 4,4'-( $\text{CO}_2\text{H}$ )<sub>2</sub>-2,2'-bipyridine and dtb is 4,4'-( $\text{C}(\text{CH}_3)_3$ )<sub>2</sub>-2,2'-bipyridine, and a  $\text{CH}_3\text{CN}$  electrolyte containing 100 mM  $\text{Li}^+$ ,  $\text{Na}^+$ ,  $\text{Mg}^{2+}$ , or  $\text{Ca}^{2+}$  perchlorate, 250 mM tetrabutylammonium iodide, and 50 mM iodine is shown in Figure 4.01 and summarized in Table 4.1. The short-circuit current density,  $J_{\text{sc}}$ , was nominally independent of the electrolyte cation. The low currents reflected the limited spectral harvesting of the sensitizer (Figure 4.01B) and not the poor electron collection efficiency of these DSSCs. The open-circuit voltage,  $V_{\text{oc}}$ , was strongly dependent on the electrolyte cation and followed the trend  $\text{Mg}^{2+} < \text{Ca}^{2+} < \text{Li}^+ < \text{Na}^+$ .

Table 4.1.DSSC Figures of Merit from Current-Density Curve in the Indicated Cations

	$V_{oc} / mV$	$J_{sc} / mA\ cm^{-2}$	Fill Factor	Efficiency*
$Li^+$	$445 \pm 5$	$5.4 \pm 0.3$	$0.52 \pm 0.01$	$1.26 \pm 0.04$
$Na^+$	$470 \pm 5$	$5.5 \pm 0.3$	$0.57 \pm 0.02$	$1.49 \pm 0.03$
$Mg^{2+}$	$375 \pm 15$	$5.7 \pm 0.4$	$0.45 \pm 0.03$	$0.95 \pm 0.1$
$Ca^{2+}$	$420 \pm 10$	$6.1 \pm 0.1$	$0.48 \pm 0.01$	$1.24 \pm 0.05$

\*Due to the lack of a true solar spectrum, reported efficiencies are estimates and should only be used for comparative purposes.

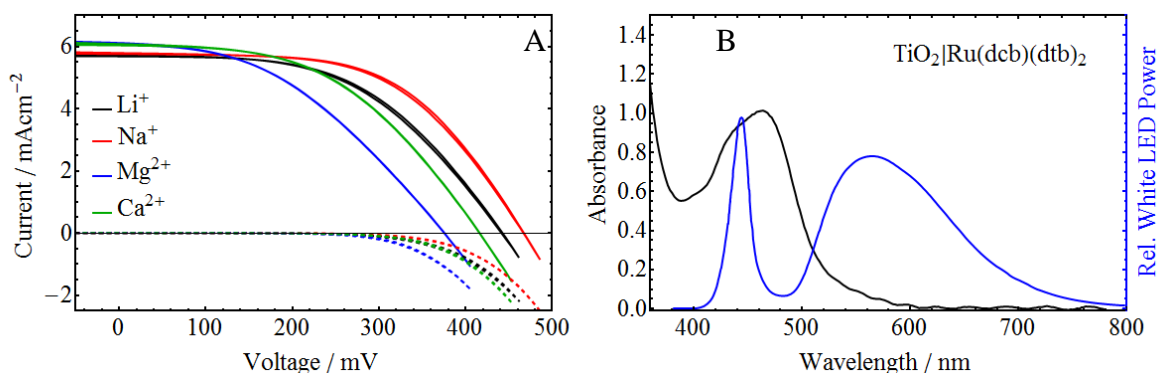


Figure 4.01. (A) Current density voltage curves for DSSCs composed of [Ru(dtb)<sub>2</sub>(dcb)](PF<sub>6</sub>)<sub>2</sub> sensitized TiO<sub>2</sub> thin film and a CH<sub>3</sub>CN electrolyte containing 100 mM Li<sup>+</sup>, Na<sup>+</sup>, Mg<sup>2+</sup>, or Ca<sup>2+</sup> perchlorate, 250 mM tetrabutylammonium iodide, and 50 mM iodine under approximately 1 sun illumination. (B) Typical UV/Vis spectrum of Ru(dtb)<sub>2</sub>(dcb) bound to TiO<sub>2</sub> overlaid with the relative power distribution output from the white LEDs.

The concentration of electrons within the TiO<sub>2</sub> thin film was estimated by charge extraction (Figure 4.02). The shape of the TiO<sub>2</sub> acceptor states was independent of the electrolyte cation, as be seen by the parallel slopes in Figure 4.02. However, the energetic position of the acceptor states was dependent on the electrolyte cation and followed the trend  $Mg^{2+} \approx Ca^{2+} < Li^+ < Na^+$ . The acceptor state distribution in Ca<sup>2+</sup> and Mg<sup>2+</sup> was about 70

mV more positive than  $\text{Li}^+$  and 120 mV more positive than  $\text{Na}^+$ . This trend has been reported previously<sup>24</sup> and is similar to the pH control of the flat-band potential of bulk semiconductors in aqueous solution.<sup>25,26</sup>

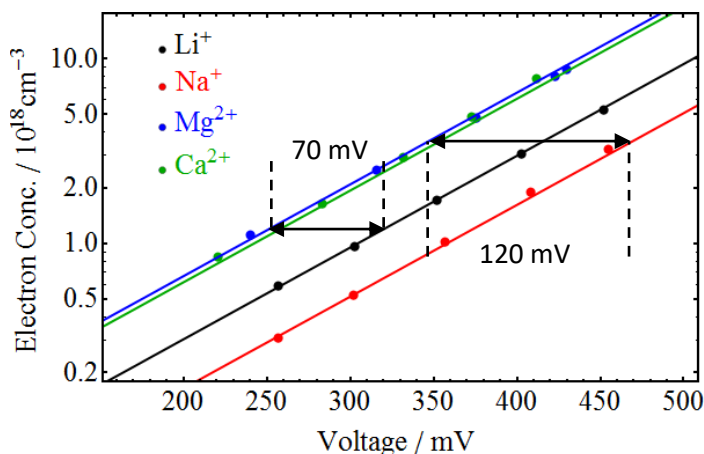


Figure 4.02. Charge extracted from open-circuit over a wide range of voltages, set by the incident light intensity, for DSSCs containing 100 mM  $\text{Li}^+$  (Black),  $\text{Na}^+$  (Red),  $\text{Mg}^{2+}$  (Blue), or  $\text{Ca}^{2+}$  (Green) perchlorate, 250 mM TBAI, and 50 mM  $\text{I}_2$ .

Charge recombination was measured at open circuit using transient photovoltage decay. Since the electron lifetime is known to be a function of the incident light intensity, this measurement was repeated under a wide range of light intensities and plotted against the charge extracted from the device under matched conditions. The results are given in Figure 4.03. The electron lifetime at any electron concentration (Figure 4.03) showed a clear cation-dependence that followed the trend  $\text{Na}^+ < \text{Li}^+ < \text{Mg}^{2+} < \text{Ca}^{2+}$ .

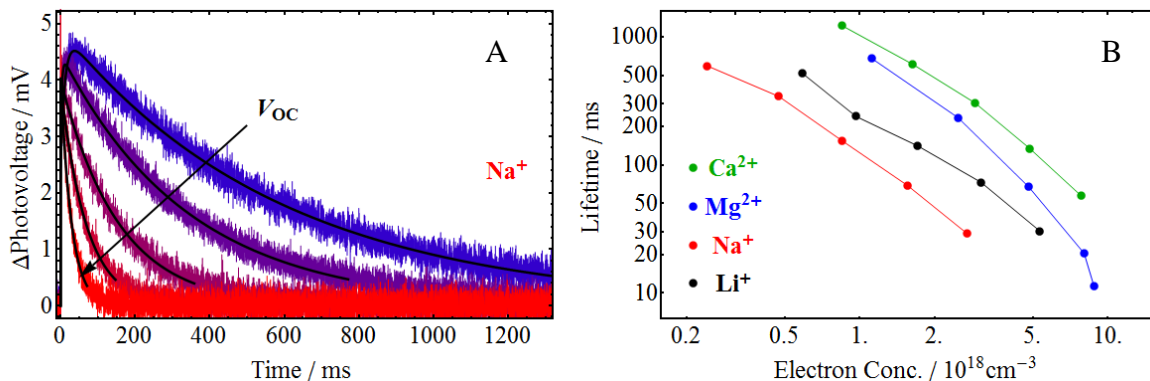


Figure 4.03. (A) Transient photovoltage decay measurements for a DSSC containing 100 mM NaClO<sub>4</sub>, 250 mM TBAI, 50 mM I<sub>2</sub>. (B) Electron lifetimes measured from the single-exponential decay in transient photovoltage measurements DSSCs containing 100 mM Li<sup>+</sup> (Black), Na<sup>+</sup> (Red), Mg<sup>2+</sup> (Blue), or Ca<sup>2+</sup> (Green) perchlorate with 250 mM TBAI, and 50 mM I<sub>2</sub>.

Diffusion coefficients were measured by transient photocurrent decay at short circuit where the photocurrent lifetime was related to the diffusion coefficient by Equation 4.01:

$$D_n = \frac{d^2}{2.77 t_n} \quad 4.01$$

where  $d$  is the film thickness,  $D_n$  and  $t_n$  are the diffusion coefficient and photocurrent decay lifetime at electron concentration  $n$ . This expression has been used by several other groups<sup>43-46</sup> where the factor of 2.77 comes from the time it takes half the electrons to diffuse half the film thickness.<sup>43</sup> At any given electron concentration, the diffusion coefficient was independent of the electrolyte cation (Figure 4.04).

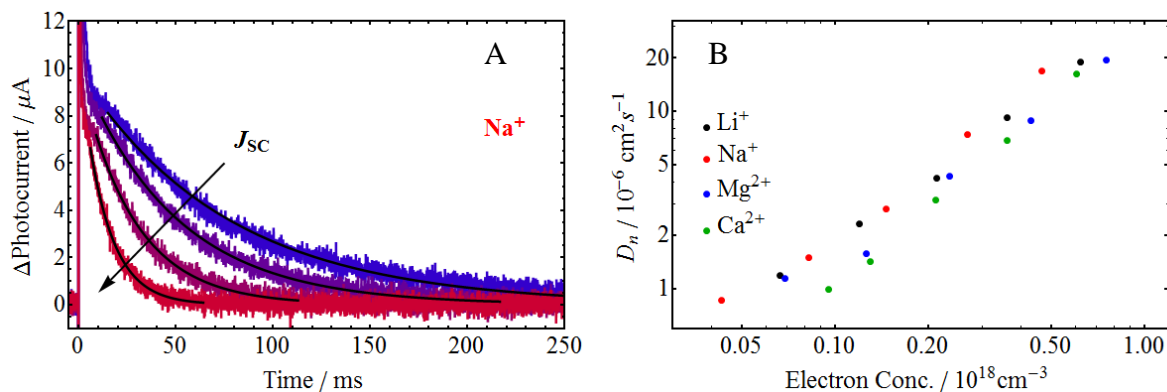


Figure 4.04. (A) Transient photocurrent decay measurements for a DSSC containing 100 mM NaClO<sub>4</sub>, 250 mM TBAI, 50 mM I<sub>2</sub>. (B) Diffusion coefficient calculated from the single-exponential decay in transient photocurrent measurements DSSCs containing 100 mM Li<sup>+</sup> (Black), Na<sup>+</sup> (Red), Mg<sup>2+</sup> (Blue), or Ca<sup>2+</sup> (Green) perchlorate with 250 mM TBAI, and 50 mM I<sub>2</sub>.

Charge extraction, transient photovoltage, and transient photocurrent studies were also conducted on DSSCs containing [Co<sup>III/II</sup>(dtb)<sub>3</sub>]<sup>3+/2+</sup> redox mediator to investigate the possibility of electric fields influencing charge recombination reaction. The results are shown in Figure 4.05. Note data for Mg<sup>2+</sup> are not shown as the electrolyte was unstable and formed a precipitate over the course of several hours. Diffusion coefficients at matched electron concentrations were independent of the electrolyte cation (Figure 4.05B). The electron lifetime displayed a strong cation dependence, following the trend  $Na^+ < Li^+ < Ca^{2+}$  at any matched electron concentration.

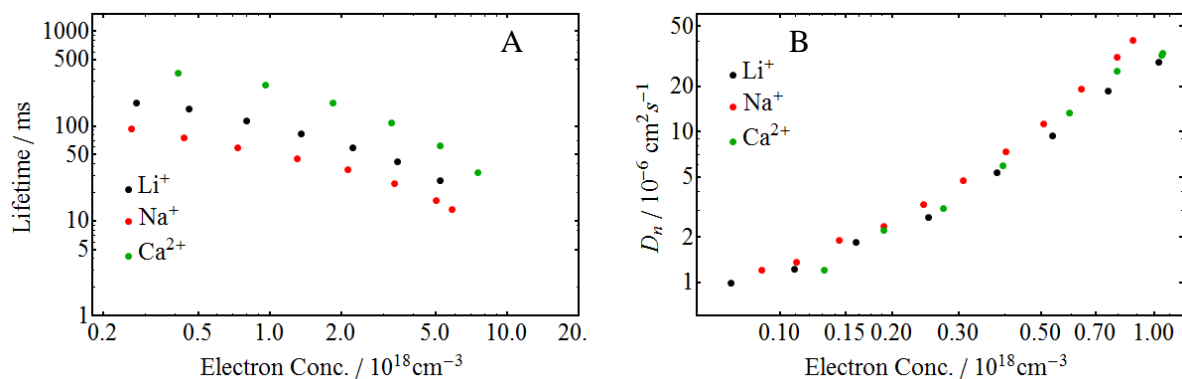


Figure 4.05. Electron lifetimes (A) and diffusion coefficients (B) for DSSCs containing 100 mM  $\text{Li}^+$  (Black),  $\text{Na}^+$  (Red), or  $\text{Ca}^{2+}$  (Green) perchlorate with 135 mM  $\text{Co}^{\text{II}}(\text{dtb})_3(\text{PF}_6)_2$ , and 15  $\text{Co}^{\text{III}}(\text{dtb})_3(\text{PF}_6)_3$  in  $\text{CH}_3\text{CN}$ .

#### 4.4 Discussion

Charge recombination in DSSCs can influence the voltage and current a cell produces. Therefore, understanding what controls charge recombination is critically important to optimize performance. Our group has previously investigated the charge recombination reaction between  $\text{TiO}_2(e^-)$ s and solution phase electron acceptors by transient absorption spectroscopy (with only the  $\text{TiO}_2$  photoanode in  $\text{CH}_3\text{CN}$  electrolyte) when the identity of the electron acceptor was  $\text{I}_3^-$ ,  $\text{TPA}^+$ , and  $\text{PTZ}^+$ , where TPA is triphenylamine and PTZ is phenothiazine. In all of these cases, the recombination rate was dependent on the identity of the electrolyte cation and followed trend  $\text{Ca}^{2+} < \text{Mg}^{2+} < \text{Li}^+ < \text{Na}^+$ . Two questions immediately come to mind: does this reaction matter in complete DSSCs and what is the fundamental reason charge recombination cares about the electrolyte cation. It is expected that charge recombination will influence  $V_{\text{oc}}$  and the maximum power output of a cell but is not expected to significantly influence  $J_{\text{sc}}$ , as was observed herein. Three possibilities have been discussed to account for the cation-dependence on the charge recombination rate

constant: driving force, electron diffusion, and electric fields. By expanding our studies to complete devices, the electron lifetime, diffusion coefficient, and energetic position of the TiO<sub>2</sub> acceptor states could be independently monitored to disentangle the effects of electron diffusion and driving force on charge recombination. Then, by comparing anionic and cationic redox mediators, the impact surface electric fields have on charge recombination could be assessed.

Analyzing complete devices by our home-built STRiVE instrument introduced several experimental differences from our previous transient absorption (TA) studies. In full devices, both the oxidized and reduced form of the redox mediator were present in mM concentrations, where in the TA experiments only the reduced form was needed to regenerate the oxidized sensitizer. Furthermore, the equilibrium or reference electron concentration was different between the two instruments. TA monitored absorbance changes relative to the dark, where background illumination was often used in STRiVE experiments. Finally, TA monitors optical changes on the nanosecond and longer timescale while the STRiVE monitors the current/voltage response of the substrate on the  $\mu$ s and longer timescale. Therefore, processes that occur on the sub-microsecond timescale cannot be observed by the STRiVE.

There have been several reports of electrolyte effects on DSSC performance, including a paper by Wang *et al.* investigating a similar series of Lewis acidic cations in acetonitrile electrolytes.<sup>28</sup> Their results displayed the *opposite* trend in electron lifetime as we report here and in our previous model studies<sup>3,4</sup> and was one reason why we undertook the present study. Several key differences between their DSSCs and ours exist. We limited our electrolytes to only iodine, iodide, the cations of interest, and spectator counter-ions. The performance

enhancer 4-*tert*-butylpyridine was not present nor was a  $\text{TiCl}_4$  treatment of the  $\text{TiO}_2$  thin film performed. Furthermore, they sensitized their  $\text{TiO}_2$  with N719 while this study used  $\text{Ru}(\text{dcb})(\text{dtb})_2(\text{PF}_6)_2$ . This was done to keep the results comparable to our previous reports on the model systems. We found the same cation-dependence on electron lifetime as our previous studies,<sup>3,4,24</sup> highlighting the importance of systematic studies on related systems. The mechanism that underlies the different cation effects is under investigation and will be reported shortly.

**DSSC Performance:** The open circuit voltage ( $V_{\text{oc}}$ ) showed a clear cation dependence following the trend  $\text{Mg}^{2+} < \text{Ca}^{2+} < \text{Li}^+ < \text{Na}^+$ . When electron injection is the same, these differences are dominated by the position of the  $\text{TiO}_2$  acceptor states and/or the electron lifetime. These two properties were independently investigated to identify the underlying cause for the different  $V_{\text{oc}}$ 's. Comparing the position of the  $\text{TiO}_2$  acceptor states to the open circuit voltages revealed that the  $V_{\text{oc}}$  differences were smaller than would be expected from a simple shift in the  $\text{TiO}_2$  acceptor states. For example, the position of the  $\text{TiO}_2$  acceptor states in  $\text{Ca}^{2+}$  containing electrolyte measured by charge extraction was 115 mV more positive than in  $\text{Na}^+$  electrolyte, yet the  $V_{\text{oc}}$ 's were only separated by 50 mV. This is illustrated in Table 4.2, where the position of the  $\text{TiO}_2$  acceptor state distribution and  $V_{\text{oc}}$  are listed relative to their values in  $\text{Na}^+$  containing electrolyte. As can be seen, the  $V_{\text{oc}}$  did not shift as much as the  $\text{TiO}_2$  acceptor state distribution, confirming that the electron lifetime (charge recombination rate) at open circuit is influenced by the electrolyte cation. This is highlighted when comparing  $\text{Mg}^{2+}$  to  $\text{Ca}^{2+}$  containing electrolytes. The energetic position of the  $\text{TiO}_2$  acceptor states for  $\text{Mg}^{2+}$  or  $\text{Ca}^{2+}$  containing electrolytes were essentially identical, yet large differences in  $V_{\text{oc}}$  were reported between these two cations.

Table 4.2. TiO<sub>2</sub> DoS, V<sub>oc</sub>, and electron lifetime values relative to DSSCs in Na<sup>+</sup> electrolyte.

	$\Delta DoS$	$\Delta V_{oc}$	$\frac{\Delta DoS}{\Delta V_{oc}}$	$\frac{TVD}{\tau_{Na^+}}$	$\frac{TA^*}{\tau_{Na^+}}$
<i>Li</i> <sup>+</sup>	55	25	30	2.5	2.3
<i>Na</i> <sup>+</sup>	0	0	0	1	1
<i>Mg</i> <sup>2+</sup>	120	95	25	5.3	3
<i>Ca</i> <sup>2+</sup>	115	50	65	12.5	18

\*Values measured by transient absorption from ref. 29.

It has become increasingly clear that electronic characteristics of TiO<sub>2</sub> thin films, i.e. the electron lifetime, diffusion coefficient, and diffusion length, should be compared at matched electron concentrations.<sup>28,47,48</sup> Using electron concentration as a reference state is based on a trap-limited diffusion/recombination model where electrons reside in ‘traps’ and can be thermally excited to occupy a more mobile state from which they can diffuse or recombine.<sup>47</sup> The number of electrons in the mobile states is related to the total electron concentration in the film. Therefore, for comparisons between different DSSCs to be accurate they must be done at matched electron concentrations.

Our results indicate that the electron lifetime in Li<sup>+</sup>, Na<sup>+</sup>, Mg<sup>2+</sup>, and Ca<sup>2+</sup> electrolyte displayed essentially the same sensitivity to the TiO<sub>2</sub> electron concentration (same slope), yet had an inherent offset that was determined by the electrolyte cation. The relative rates compared at any electron concentration are comparable to those measured by transient absorption in a previous study,<sup>4</sup> Table 4.2, highlighting the translation of our previous model studies to complete devices. The measurements here suggest the electron concentration in the film during the transient absorption studies, which was not directly measured, was 1-2 x 10<sup>18</sup> cm<sup>-3</sup>.

The electron lifetime is known in influence  $V_{oc}$ . One model that quantitatively describes this relationship is the diode,<sup>49</sup> Equation 4.02:

$$V_{oc} = \frac{k_B T}{q} \ln \left( \frac{\Phi \Gamma_0}{n k [A]} \right) \quad 4.02$$

where  $k_B$  is Boltzman's constant,  $T$  is the absolute temperature,  $q$  is the elementary charge,  $\Phi$  is the quantum yield for electron injection,  $\Gamma_0$  is the photon flux,  $n$  is the equilibrium surface electron concentration,  $k$  is the rate constant for electron transfer, and  $[A]$  is the concentration of acceptor species. This model predicts a 59 mV decrease in  $V_{oc}$  for every order of magnitude increase in charge recombination rate. Comparing the relative lifetimes to the difference between the acceptor state and  $V_{oc}$  shift reveals a logarithmic dependence that has a slope near 59 mV/decade (Figure 4.06). This indicates that the inability of  $V_{oc}$  to simply track shifts in the  $TiO_2$  acceptor states is a result of the increase in charge recombination rate.

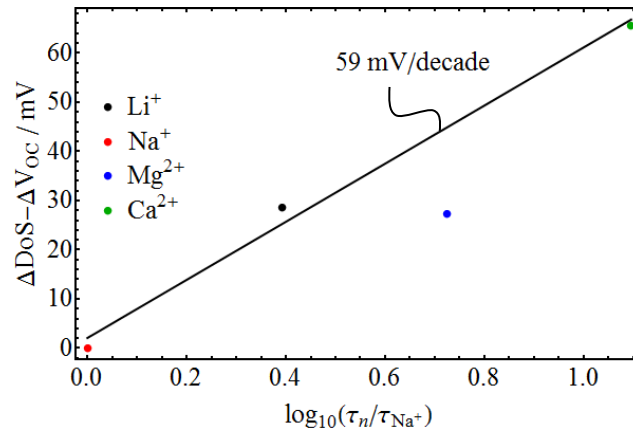


Figure 4.06. Difference between the shift of the  $TiO_2$  acceptor state distribution and the change in  $V_{oc}$  relative to  $Na^+$  containing DSSCs as a function of the lifetime relative to  $Na^+$ .

Most every study on the electron transport in DSSCs has concluded that the diffusion coefficient under typical operating conditions (high salt concentration) was dominated by electron diffusion within the TiO<sub>2</sub> thin film without significant influence from the electrolyte cation.<sup>50-52</sup> The results presented herein agree with this finding, where the diffusion coefficient was independent of the electrolyte cation when compared at matched electron concentrations in both iodide/triiodide and cobalt based redox mediators.

The electron diffusion length,  $L_n$ , is often of interest when studying DSSCs and is calculated according to Equation 4.03:<sup>47,53-55</sup>

$$L_n = \sqrt{D_n t_n} \quad 4.03$$

In order to accurately calculate the diffusion length, the diffusion coefficient and lifetime values were compared at matched concentrations of TiO<sub>2</sub>(e<sup>-</sup>)s. However, in our experiments the lifetime was measured at open-circuit while the diffusion coefficient was measured at short circuit, leading to large differences between the electron concentration in the two experiments (Figure 4.07A). Therefore, a fit to the diffusion coefficient vs. electron concentration was extrapolated to the electron concentrations used in the transient photovoltage decay measurements. The resulting diffusion lengths are shown in Figure 4.07B. Included in Figure 4.07B is a line representing the thickness of the TiO<sub>2</sub> film. All the diffusion lengths calculated here are at least a factor of 3 longer than the film thickness, indicating quantitative electron collection in these devices. Comparing diffusion lengths measured in different electrolyte cations reveals same the cation-dependence seen throughout this study,  $Na^+ < Li^+ < Mg^{2+} < Ca^{2+}$ .

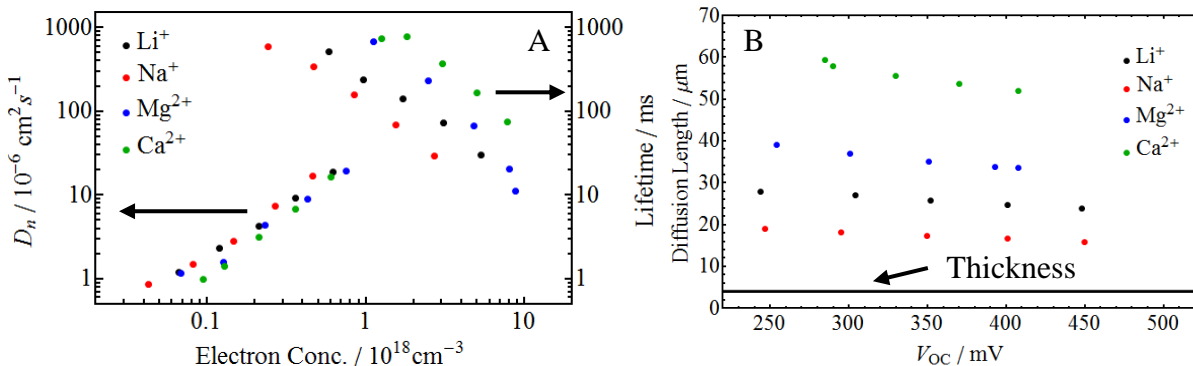


Figure 4.07. (A) Electron diffusion coefficient and lifetime as a function of  $\text{TiO}_2(e^-)$ s and (B) diffusion length calculated at matched electron concentrations for DSSCs containing 100 mM  $\text{Li}^+$  (Black),  $\text{Na}^+$  (Red),  $\text{Mg}^{2+}$  (Blue), or  $\text{Ca}^{2+}$  (Green) perchlorate, 250 mM TBAI, and 50 mM  $\text{I}_2$ .

**Cation Influence on Charge Recombination:** One purpose of this investigation was to investigate why the identity of the electrolyte cation influenced charge recombination. Three possible factors that could influence charge recombination were discussed previously:<sup>3</sup> electron diffusion, driving force, or surface electric fields. Using complete DSSCs, each of these possibilities could be uniquely tested as described below.

*Electron Diffusion:* Electron diffusion would be expected to control charge recombination in the diffusion limited regime. Since electron lifetimes are measured on the millisecond and longer timescale, they would not be diffusion limited if the two reactants were free to diffuse in fluid solution. However, electron motion within the nanocrystalline  $\text{TiO}_2$  network is restricted and often modelled in a multiple trapping model. In this model, electrons typically reside in ‘localized’ states and are thermally excited to ‘mobile’ states from which they can

diffuse (and then re-trap) or recombine. Diffusion limited recombination would be related to the time spent in the localized vs mobile states or the rate of trapping/detrapping.

Pushing the diffusion limited recombination case to the extreme, charge recombination would simply be controlled by the detrapping event, where recombination would occur following every detrapping event. This extreme case is of course not realistic because electrons are collected at the back contact and must undergo many trapping/detrapping events to diffuse the length of the thin film. Trapping/detrapping must therefore occur many times prior to a charge recombination event, but experimentally measuring the trapping/detrapping rate is challenging. However, the diffusion coefficient is expected to be proportional to the rate of trapping/detrapping, hence comparing the diffusion coefficient in a series of electrolytes gives an estimate for the relative trapping/detrapping rate. If charge recombination were diffusion limited, faster charge recombination would be accompanied by faster electron diffusion. The electron diffusion coefficient measured here was independent of the electrolyte cation in both  $I^-/I_3^-$  and cobalt redox mediators. The fact that different charge recombination rates were observed yet the diffusion coefficient was identical indicates that charge recombination was not controlled by the electron diffusion under these experimental conditions.

*Electric Fields:* Our group has extensively studied surface electric fields following electron injection into  $TiO_2$  nanocrystallites. Field strengths on the order of 2 MV/cm have been reported by surface anchored chromophores.<sup>30,31</sup> Fields of this magnitude are expected to influence the motion of ions near the surface and evidence for cation motion to screen the field has been reported.<sup>33-35</sup> The extent of charge screening is sensitive to the identity of the electrolyte cation and follows the trend  $Ca^{2+} < Mg^{2+} \sim Li^+ < Na^+$ .<sup>24</sup> Since the field would

be expected to repel triiodide, screening the field more effectively ( $\text{Na}^+$ ) would lead to faster recombination than less screening ( $\text{Ca}^{2+}$ ). This trend was indeed found, which led to the initial assignment of the recombination rates being related to surface electric fields.<sup>4</sup>

Similar studies were performed using neutral/cationic redox mediators, but the timescale for charge recombination competed with charge screening.<sup>3</sup> Transient absorption experiments where both the reduced and oxidized form of the redox mediator were cationic and had slow enough charge recombination to allow for screening were hindered due to the minimal UV/Vis absorption of cobalt polypyridyl compounds. Here, charge recombination was monitored electrically and could easily be tested where both forms of the redox mediator were either anionic or cationic. The same cation-dependence on the electron lifetime was observed in using either redox mediator, indicating electric fields are not the primary influence on charge recombination under these conditions.

*Driving Force:* The thermodynamic driving force is expected to influence the rate of charge recombination in either the Marcus or Marcus-Gerischer theory of electron transfer.<sup>5-8</sup> For DSSCs, the driving force for charge recombination is typically tuned through the identity of the electron acceptor in solution.<sup>13-15</sup> Alternatively, the reducing power of the  $\text{TiO}_2(e^-)$  could be tuned by the composition of the surrounding electrolyte. This has been experimentally attempted in several cases by the addition of Lewis-acidic or Lewis-based additives.<sup>20-22</sup> However, the reducing power of  $\text{TiO}_2(e^-)$  using the Alkali and Alkaline Earth ions investigated here has not been discussed in the context of charge recombination.

Charge recombination to the redox mediator is typically observed in the Marcus normal region, where larger driving forces correspond to faster rates of charge recombination. In the context of interfacial electron transfer and Marcus-Gerischer theory,

electron transfer rate constants correspond to greater energetic overlap between the donor and acceptor states. If driving force did control the rate of electron transfer here, a more negative acceptor state distribution ( $\text{Na}^+$ ) would be expected to increase the rate of charge recombination. Figure 4.08 shows the relative electron lifetime as a function of DoS position reported here. This is strong evidence that identity of the electrolyte cation tunes the  $\text{TiO}_2(e^-)$  reducing power and controls the rate constant for charge recombination.

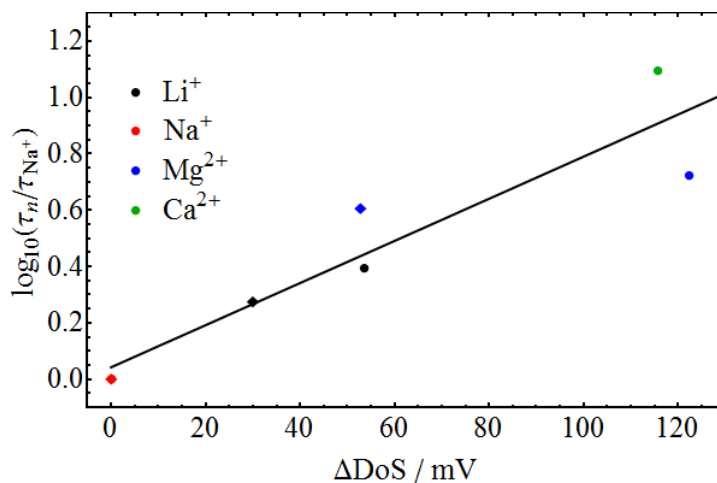


Figure 4.08. Dependence of electron lifetime on the relative DoS position for DSSCs containing 100 mM  $\text{Li}^+$  (Black),  $\text{Na}^+$  (Red),  $\text{Mg}^{2+}$  (Blue), or  $\text{Ca}^{2+}$  (Green) perchlorate, 250 mM TBAI, and 50 mM  $\text{I}_2$ . Circles represent lifetimes measured in  $\text{I}^-/\text{I}_3^-$  containing DSSCs while diamonds represent DSSCs using  $\text{Co}^{\text{III/II}}$  redox mediators.

The slope reports on the free energy dependence of the rate constant for charge recombination. According to Marcus-Gerischer theory,<sup>8</sup> this value is dependent on the reorganization energy and the energetic overlap between the donor and acceptor states. Note that recombination to both the iodide/triiodide (circles) and cobalt based redox mediators (diamonds) show a similar dependence on the energetic position of the  $\text{TiO}_2$  acceptor states. Even though there are large difference in the reorganization energy for the one-electron

reduction of  $\text{Co}^{\text{III}}(\text{dtb})_3$  and  $\text{I}_3^-$  or  $\text{I}_2$  ( $>1.25$  eV for cobalt redox mediators<sup>56</sup> which is must greater than for iodide/triiodide<sup>57</sup>) the relatively small range in driving forces probed here ( $<150$  mV) prevents differences from being readily detected.

#### **4.5 Conclusions**

Charge recombination was investigated in  $\text{Li}^+$ ,  $\text{Na}^+$ ,  $\text{Mg}^{2+}$ , and  $\text{Ca}^{2+}$  containing electrolytes with both the traditional iodide/triiodide and an alternative  $\text{Co}^{\text{III/II}}$  redox mediator. The results were analyzed in the context of the driving force, electron diffusion, and electric field influence on charge recombination. It was found that the energetic position of the  $\text{TiO}_2$  acceptor states had a strong impact on the charge recombination rate constant with negligible influences from either electric fields or electron diffusion.

#### **Author Information**

Corresponding Author

\*Gerald J. Meyer. Email: [gjmeyer@email.unc.edu](mailto:gjmeyer@email.unc.edu). Phone: 919-962-6320.

#### **Acknowledgements**

The authors acknowledge support by a grant from the Division of Chemical Sciences, Office of Basic Energy Sciences, Office of Energy Research, U.S. Department of Energy (Grant DE-SC0013461).

## REFERENCES

- (1) Robson, K. C. D.; Hu, K.; Meyer, G. J.; Berlinguette, C. P. Atomic Level Resolution of Dye Regeneration in the Dye-Sensitized Solar Cell. *J. Am. Chem. Soc.* **2013**, *135*, 1961–1971.
- (2) Li, F.; Jennings, J. R.; Wang, Q. Determination of Sensitizer Regeneration Efficiency in Dye-Sensitized Solar Cells. *ACS Nano* **2013**, *7*, 8233–8242.
- (3) DiMarco, B. N.; O'Donnell, R. M.; Meyer, G. J. Cation-Dependent Charge Recombination to Organic Mediators in Dye-Sensitized Solar Cells. *J. Phys. Chem. C* **2015**, *119*, 21599–21604.
- (4) Sampaio, R. N.; O'Donnell, R. M.; Barr, T. J.; Meyer, G. J. Electric Fields Control  $\text{TiO}_2$  ( $e^-$ ) +  $\text{I}_3^- \rightarrow$  Charge Recombination in Dye-Sensitized Solar Cells. *J. Phys. Chem. Lett.* **2014**, *5*, 3265–3268.
- (5) Marcus, R. a. On the Theory of Oxidation-Reduction Reactions Involving Electron Transfer. I. *J. Chem. Phys.* **1956**, *24*, 966.
- (6) Marcus, R. a. Chemical and Electrochemical Electron-Transfer Theory. *Annu. Rev. Phys. Chem.* **1964**, *15*, 155–196.
- (7) Gerischer, H. Electron-Transfer Kinetics of Redox Reactions at the Semiconductor/electrolyte Contact. A New Approach. *J. Phys. Chem.* **1991**, *95*, 1356–1359.
- (8) Gerischer, H. Electrochemical Techniques for the Study of Photosensitization. *Photochem. Photobiol.* **1972**, *16*, 243–260.
- (9) Kuciauskas, D.; Freund, M. S.; Gray, H. B.; Winkler, J. R.; Lewis, N. S. Electron Transfer Dynamics in Nanocrystalline Titanium Dioxide Solar Cells Sensitized with Ruthenium or Osmium Polypyridyl Complexes. *J. Phys. Chem. B* **2001**, *105*, 392–403.
- (10) Gaal, D. A.; McGarrah, J. E.; Liu, F.; Cook, J. E.; Hupp, J. T. Nonadiabatic Electron Transfer at the Nanoscale Tin-Oxide Semiconductor/aqueous Solution interface. *Photochem. Photobiol. Sci.* **2004**, *3*, 240.
- (11) Hasselmann, G. M.; Meyer, G. J. Diffusion-Limited Interfacial Electron Transfer with Large Apparent Driving Forces. *J. Phys. Chem. B* **1999**, *103*, 7671–7675.
- (12) Yan, S. G.; Prieskorn, J. S.; Kim, Y.; Hupp, J. T. In Search of the Inverted Region: Chromophore-Based Driving Force Dependence of Interfacial Electron Transfer Reactivity at the Nanocrystalline Titanium Dioxide Semiconductor/Solution Interface †. *J. Phys. Chem. B* **2000**, *104*, 10871–10877.
- (13) DeVries, M. J.; Pellin, M. J.; Hupp, J. T. Dye-Sensitized Solar Cells: Driving-Force Effects on Electron Recombination Dynamics with Cobalt-Based Shuttles. *Langmuir* **2010**, *26*, 9082–9087.
- (14) Feldt, S. M.; Wang, G.; Boschloo, G.; Hagfeldt, A. Effects of Driving Forces for Recombination and Regeneration on the Photovoltaic Performance of Dye-Sensitized Solar Cells Using Cobalt Polypyridine Redox Couples. *J. Phys. Chem. C* **2011**, *115*, 21500–21507.

- (15) Hamann, T. W.; Farha, O. K.; Hupp, J. T. Outer-Sphere Redox Couples as Shuttles in Dye-Sensitized Solar Cells. Performance Enhancement Based on Photoelectrode Modification via Atomic Layer Deposition. *J. Phys. Chem. C* **2008**, *112*, 19756–19764.
- (16) Gaal, D. A.; Hupp, J. T. Thermally Activated, Inverted Interfacial Electron Transfer Kinetics: High Driving Force Reactions between Tin Oxide Nanoparticles and Electrostatically-Bound Molecular Reactants. *J. Am. Chem. Soc.* **2000**, *122*, 10956–10963.
- (17) Yan, S. G.; Hupp, J. T. Semiconductor-Based Interfacial Electron-Transfer Reactivity: Decoupling Kinetics from pH-Dependent Band Energetics in a Dye-Sensitized Titanium Dioxide/Aqueous Solution System. *J. Phys. Chem.* **1996**, *100*, 6867–6870.
- (18) Yu, J.; Yang, Y.-L.; Fan, R.-Q.; Li, L.; Wei, L.-G. Mechanism of Performance Enhancement via Fluorine Doped Titanium Dioxide Nanoparticles in Dye Sensitized Solar Cells. *J. Fluor. Chem.* **2015**, *176*, 71–77.
- (19) Zhang, X.; Liu, F.; Huang, Q.-L.; Zhou, G.; Wang, Z.-S. Dye-Sensitized W-Doped TiO<sub>2</sub> Solar Cells with a Tunable Conduction Band and Suppressed Charge Recombination. *J. Phys. Chem. C* **2011**, *115*, 12665–12671.
- (20) Kopidakis, N.; Neale, N. R.; Frank, A. J. Effect of an Adsorbent on Recombination and Band-Edge Movement in Dye-Sensitized TiO<sub>2</sub> Solar Cells: Evidence for Surface Passivation. *J. Phys. Chem. B* **2006**, *110*, 12485–12489.
- (21) Yin, X.; Zhao, H.; Chen, L.; Tan, W.; Zhang, J.; Weng, Y.; Shuai, Z.; Xiao, X.; Zhou, X.; Li, X.; et al. The Effects of Pyridine Derivative Additives on Interface Processes at Nanocrystalline TiO<sub>2</sub> Thin Film in Dye-Sensitized Solar Cells. *Surf. Interface Anal.* **2007**, *39*, 809–816.
- (22) Katz, M. J.; DeVries Vermeer, M. J.; Farha, O. K.; Pellin, M. J.; Hupp, J. T. Dynamics of Back Electron Transfer in Dye-Sensitized Solar Cells Featuring 4-Tert-Butyl-Pyridine and Atomic-Layer-Deposited Alumina as Surface Modifiers. *J. Phys. Chem. B* **2015**, *119*, 7162–7169.
- (23) Redmond, G.; Fitzmaurice, D. Spectroscopic Determination of Flatband Potentials for Polycrystalline Titania Electrodes in Nonaqueous Solvents. *J. Phys. Chem.* **1993**, *97*, 1426–1430.
- (24) O'Donnell, R. M.; Sampaio, R. N.; Barr, T. J.; Meyer, G. J. Electric Fields and Charge Screening in Dye Sensitized Mesoporous Nanocrystalline TiO<sub>2</sub> Thin Films. *J. Phys. Chem. C* **2014**, *118*, 16976–16986.
- (25) Bolts, J. M.; Wrighton, M. S. Correlation of Photocurrent-Voltage Curves with Flat-Band Potential for Stable Photoelectrodes for the Photoelectrolysis of Water. *J. Phys. Chem.* **1976**, *80*, 2641–2645.
- (26) Matsumoto, Y.; Yoshikawa, T.; Sato, E. ichi. Dependence of the Band Bending of the Oxide Semiconductors on pH. *J. Electrochem. Soc.* **1989**, *136*, 1389–1391.
- (27) Kelly, C. A.; Farzad, F.; Thompson, D. W.; Stipkala, J. M.; Meyer, G. J. Cation-Controlled Interfacial Charge Injection in Sensitized Nanocrystalline TiO<sub>2</sub>. *Langmuir* **1999**, *15*, 7047–7054.

- (28) Wang, H.; Peter, L. M. Influence of Electrolyte Cations on Electron Transport and Electron Transfer in Dye-Sensitized Solar Cells. *J. Phys. Chem. C* **2012**, *116*, 10468–10475.
- (29) Ansari-Rad, M.; Anta, J. A.; Arzi, E. Conditions for Diffusion-Limited and Reaction-Limited Recombination in Nanostructured Solar Cells. *J. Chem. Phys.* **2014**, *140*, 134702.
- (30) Cappel, U. B.; Feldt, S. M.; Schöneboom, J.; Hagfeldt, A.; Boschloo, G. The Influence of Local Electric Fields on Photoinduced Absorption in Dye-Sensitized Solar Cells. *J. Am. Chem. Soc.* **2010**, *132*, 9096–9101.
- (31) Ardo, S.; Sun, Y.; Staniszewski, A.; Castellano, F. N.; Meyer, G. J. Stark Effects after Excited-State Interfacial Electron Transfer at Sensitized TiO<sub>2</sub> Nanocrystallites. *J. Am. Chem. Soc.* **2010**, *132*, 6696–6709.
- (32) Johansson, P. G.; Kopecky, A.; Galoppini, E.; Meyer, G. J. Distance Dependent Electron Transfer at TiO<sub>2</sub> Interfaces Sensitized with Phenylene Ethynylene Bridged Ru<sup>II</sup>-Isothiocyanate Compounds. *J. Am. Chem. Soc.* **2013**, *135*, 8331–8341.
- (33) Ardo, S.; Sun, Y.; Castellano, F. N.; Meyer, G. J. Excited-State Electron Transfer from Ruthenium-Polypyridyl Compounds to Anatase TiO<sub>2</sub> Nanocrystallites: Evidence for a Stark Effect. *J. Phys. Chem. B* **2010**, *114*, 14596–14604.
- (34) Kuwahara, S.; Taya, S.; Osada, N.; Shen, Q.; Toyoda, T.; Katayama, K. Effect of Electrolyte Constituents on the Motion of Ionic Species and Recombination Kinetics in Dye-Sensitized Solar Cells. *Phys. Chem. Chem. Phys.* **2014**, *16*, 5242–5249.
- (35) Song, W.; Luo, H.; Hanson, K.; Concepcion, J. J.; Brennaman, M. K.; Meyer, T. J. Visualization of Cation Diffusion at the TiO<sub>2</sub> Interface in Dye Sensitized Photoelectrosynthesis Cells (DSPEC). *Energy Environ. Sci.* **2013**, *6*, 1240.
- (36) Kambe, S.; Nakade, S.; Kitamura, T.; Wada, Y.; Yanagida, S. Influence of the Electrolytes on Electron Transport in Mesoporous TiO<sub>2</sub>-Electrolyte Systems. **2002**, 2967–2972.
- (37) O'Regan, B. C.; Lenzmann, F. Charge Transport and Recombination in a Nanoscale Interpenetrating Network of N-Type and P-Type Semiconductors : Transient Photocurrent and Photovoltage Studies of TiO<sub>2</sub>/Dye/CuSCN Photovoltaic Cells. *J. Phys. Chem. B* **2004**, *108*, 4342–4350.
- (38) O'Regan, B. C.; Scully, S.; Mayer, a C.; Palomares, E.; Durrant, J. The Effect of Al<sub>2</sub>O<sub>3</sub> Barrier Layers in TiO<sub>2</sub>/dye/CuSCN Photovoltaic Cells Explored by Recombination and DOS Characterization Using Transient Photovoltage Measurements. *J. Phys. Chem. B* **2005**, *109*, 4616–4623.
- (39) Wang, X.; Karanjit, S.; Zhang, L.; Fong, H.; Qiao, Q.; Zhu, Z. Transient Photocurrent and Photovoltage Studies on Charge Transport in Dye Sensitized Solar Cells Made from the Composites of TiO<sub>2</sub> Nanofibers and Nanoparticles. *Appl. Phys. Lett.* **2011**, *98*, 82114.
- (40) Klahr, B. M.; Hamann, T. W. Performance Enhancement and Limitations of Cobalt Bipyridyl Redox Shuttles in Dye-Sensitized Solar Cells. *J. Phys. Chem. C* **2009**, *113*, 14040–14045.

- (41) Sapp, S. A.; Elliott, C. M.; Contado, C.; Caramori, S.; Bignozzi, C. A. Substituted Polypyridine Complexes of cobalt(II/III) as Efficient Electron-Transfer Mediators in Dye-Sensitized Solar Cells. *J. Am. Chem. Soc.* **2002**, *124*, 11215–11222.
- (42) Heimer, T. A.; D’Arcangelis, S. T.; Farzad, F.; Stipkala, J. M.; Meyer, G. J. An Acetylacetonate-Based Semiconductor–Sensitizer Linkage. *Inorg. Chem.* **1996**, *35*, 5319–5324.
- (43) Nakade, S.; Kanzaki, T.; Wada, Y.; Yanagida, S. Stepped Light-Induced Transient Measurements of Photocurrent and Voltage in Dye-Sensitized Solar Cells: Application for Highly Viscous Electrolyte Systems. *Langmuir* **2005**, *21*, 10803–10807.
- (44) Kanzaki, T.; Nakade, S.; Wada, Y.; Yanagida, S. Retardation of Interfacial Charge Recombination by Addition of Quaternary Ammonium Cation and Its Application to Low Temperature Processed Dye-Sensitized Solar Cells. *Photochem. Photobiol. Sci.* **2006**, *5*, 389–394.
- (45) Fukai, Y.; Kondo, Y.; Mori, S.; Suzuki, E. Highly Efficient Dye-Sensitized SnO<sub>2</sub> Solar Cells Having Sufficient Electron Diffusion Length. *Electrochem. commun.* **2007**, *9*, 1439–1443.
- (46) Nakade, S.; Kanzaki, T.; Kambe, S.; Wada, Y.; Yanagida, S. Investigation of Cation-Induced Degradation of Dye-Sensitized Solar Cells for a New Strategy to Long-Term Stability. **2005**, No. 12, 11414–11417.
- (47) Bisquert, J.; Vikhrenko, V. S. Interpretation of the Time Constants Measured by Kinetic Techniques in Nanostructured Semiconductor Electrodes and Dye-Sensitized Solar Cells. *J. Phys. Chem. B* **2004**, *108*, 2313–2322.
- (48) Barnes, P. R. F.; Miettunen, K.; Li, X.; Anderson, A. Y.; Bessho, T.; Gratzel, M.; O’Regan, B. C. Interpretation of Optoelectronic Transient and Charge Extraction Measurements in Dye-Sensitized Solar Cells. *Adv. Mater.* **2013**, *25*, 1881–1922.
- (49) Kumar, A.; Santangelo, P. G.; Lewis, N. S. Electrolysis of Water at Strontium Titanate (SrTiO<sub>3</sub>) Photoelectrodes: Distinguishing between the Statistical and Stochastic Formalisms for Electron-Transfer Processes in Fuel-Forming Photoelectrochemical Systems. *J. Phys. Chem.* **1992**, *96*, 834–842.
- (50) Kambe, S.; Nakade, S.; Kitamura, T.; Wada, Y.; Yanagida, S. Influence of the Electrolytes on Electron Transport in Mesoporous TiO<sub>2</sub>–Electrolyte Systems. *J. Phys. Chem. B* **2002**, *106*, 2967–2972.
- (51) Nakade, S.; Kambe, S.; Kitamura, T.; Wada, Y.; Yanagida, S. Effects of Lithium Ion Density on Electron Transport in Nanoporous TiO<sub>2</sub> Electrodes. *J. Phys. Chem. B* **2001**, *105*, 9150–9152.
- (52) Nakade, S.; Kanzaki, T.; Kubo, W.; Kitamura, T.; Wada, Y.; Yanagida, S. Role of Electrolytes on Charge Recombination in Dye-Sensitized TiO<sub>2</sub> Solar Cell ( 1 ): The Case of Solar Cells Using the I<sup>-</sup>/I<sub>3</sub><sup>-</sup> Redox Couple. **2005**, No. 1, 3480–3487.
- (53) Barnes, P. R. F.; Liu, L.; Li, X.; Anderson, A. Y.; Kisserwan, H.; Ghaddar, T. H.; Durrant, J. R.; O’Regan, B. C. Re-Evaluation of Recombination Losses in Dye-Sensitized

Cells: The Failure of Dynamic Relaxation Methods to Correctly Predict Diffusion Length in Nanoporous Photoelectrodes. *Nano Lett.* **2009**, *9*, 3532–3538.

(54) Peter, L. M.; Wijayantha, K. G. U. Intensity Dependence of the Electron Diffusion Length in Dye-Sensitized Nanocrystalline TiO<sub>2</sub> Photovoltaic Cells. *Electrochemistry Communications*. 1999, pp 576–580.

(55) Schlichthörl, G.; Park, N. G.; Frank, A. J. Evaluation of the Charge-Collection Efficiency of Dye-Sensitized Nanocrystalline TiO<sub>2</sub> Solar Cells. *J. Phys. Chem. B* **1999**, *103*, 782–791.

(56) Ondersma, J. W.; Hamann, T. W. Measurements and Modeling of Recombination from Nanoparticle TiO<sub>2</sub> Electrodes. *J. Am. Chem. Soc.* **2011**, *133*, 8264–8271.

(57) Idígoras, J.; Pellejà, L.; Palomares, E.; Anta, J. a. The Redox Pair Chemical Environment Influence on the Recombination Loss in Dye-Sensitized Solar Cells. *J. Phys. Chem. C* **2014**, *118*, 3878–3889.

## CHAPTER 5: CHARGE RECTIFICATION AT MOLECULAR-NANOCRYSTALLINE TiO<sub>2</sub> INTERFACES: OVERLAP OPTIMIZATION TO PROMOTE VECTORIAL ELECTRON TRANSFER\*

### 5.1 Introduction

Separation of semiconductor electron-hole pairs generated upon supra band gap light absorption is critical to the performance of photovoltaics.<sup>1</sup> Electron-hole pairs created within the depletion region of silicon are rapidly and quantitatively separated by the electric field that defines it; behavior that underlies the dominance of these materials in the photovoltaic industry.<sup>1</sup> However, when the semiconductor's physical dimensions are reduced to the nanometer length scale, the depletion region no longer plays a significant role in charge separation particularly when the material has a low dopant density.<sup>2</sup> Hodes and Peter suggested a new concept in nanocrystalline photovoltaic cells wherein control of the rate constants for interfacial electron and hole transfer would result in efficient charge separation even in the absence of a depletion region.<sup>3</sup> Gerischer predicted that such rate constants would be determined by the overlap of the molecular and semiconductor electronic states.<sup>4</sup> Herein, we have characterized electrochemically driven redox chemistry at pyridinium-TiO<sub>2</sub> nanocrystallite interfaces where this overlap was systematically varied. The interfacial density of states was quantified by *in situ* spectroelectrochemistry and was optimized through

---

\*This chapter previously appeared as an article in the Journal of Physical Chemistry C. Reprinted (adapted) with permission from (Barr, T. J.; Morris, A. J.; Taheri, A.; Meyer, G. J. Charge Rectification at Molecular Nanocrystalline TiO<sub>2</sub> Interfaces: Overlap Optimization To Promote Vectorial Electron Transfer. *J. Phys. Chem. C* **2016**, *120*, 27173–27181.). Copyright (2016) American Chemical Society.

the identity of the pyridinium acceptor and by the presence of potential determining cations in the external electrolyte.

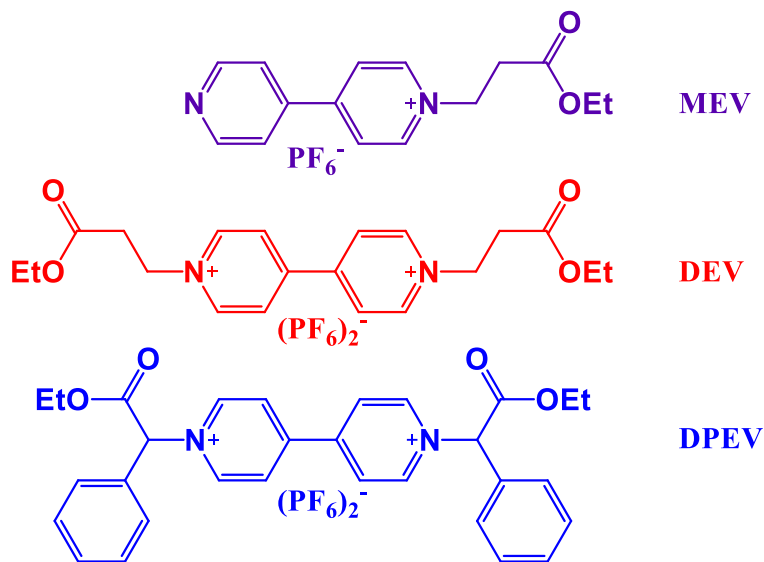
The materials under study are the mesoporous nanocrystalline TiO<sub>2</sub> thin films commonly used in dye-sensitized solar cells. It is well known that redox active molecules anchored to the surfaces of these materials can be reversibly oxidized and reduced when employed as working electrodes in a standard three-electrode electrochemical cell.<sup>5,6,7</sup> Two discrete mechanisms for this redox chemistry have been identified.<sup>8</sup> In the first, electron transfer is initiated at the transparent conductive oxide (TCO) that supports the mesoporous thin film, and proceeds away from the surface by lateral intermolecular self-exchange electron transfer, a process sometimes called ‘hole hopping’.<sup>9</sup> Complete oxidation of all the molecules within the film requires a surface coverage greater than about 1/2 the saturation value such that a percolation pathway to each molecule is present.<sup>10</sup> Such lateral hole hopping has also been observed after excited state injection by a dye molecule and hence can be initiated with light.<sup>11,12</sup>

The second mechanism involves the direct participation of the redox active states in TiO<sub>2</sub> that are sometimes idealized to be conduction band states, but appear to be better considered as localized Ti<sup>IV/III</sup> species or trap states.<sup>8</sup> An advantage of this mechanism is that the redox active molecules may be present in very low surface coverages as a percolation pathway is not required. In this regard, the electrochemistry is similar to that observed on highly-doped degenerate semiconductors like those commonly used as TCOs.<sup>13,14</sup> A disadvantage however, is that the formal reduction potentials of the molecules must be proximate to the Ti<sup>IV/III</sup> potentials that mediate the molecular redox chemistry, a requirement that excludes large classes of molecules such as the dye molecules commonly used in dye-

sensitized solar cells. This study focuses on such TiO<sub>2</sub> mediated molecular redox chemistry that provides insights into the kinetics for interfacial electron transfer.

The three pyridiniums [1-(2-ethoxycarbonyl-ethyl)-4,4'-bipyridine]<sup>+</sup> (MEV), [1,1'-(2-ethoxycarbonyl-ethyl)<sub>2</sub>-4,4'-bipyridine]<sup>2+</sup> (DEV), and [1,1'-(ethoxycarbonyl-phenyl-methyl)<sub>2</sub>-4,4'-bipyridine]<sup>2+</sup> (DPEV) were characterized in fluid acetonitrile electrolytes and when anchored to the mesoporous TiO<sub>2</sub> thin films. These pyridiniums given in Scheme 5.1 are listed in order of increasing reduction potentials and span a 660 mV range. They were selected as the first reductions occur commensurate with or after the reduction of the TiO<sub>2</sub> nanocrystallites that comprise the mesoporous thin film. In addition, pyridinium reduction results in significant color changes that enabled the redox chemistry to be quantified spectroscopically.

Scheme 5.1 Pyridinium structures



## 5.2 Experimental

**Materials:** The following reagents were used as received: lithium perchlorate ( $\text{LiClO}_4$ ; Sigma-Aldrich, 99.99%); tetrabutylammonium perchlorate ( $\text{TBAClO}_4$ ; Sigma-Aldrich,  $\geq 99.0\%$ ); ammonium hexafluorophosphate ( $\text{NH}_4\text{PF}_6$ ; Fluka,  $\geq 98.0\%$ ); ethyl-3-bromopropanoate (Sigma-Aldrich, 98%); ethyl  $\alpha$ -bromophenylacetate (Alfa Aesar, 97%); 4-phenylpyridine (Sigma-Aldrich, 97%); 4,4'-bipyridine (Sigma-Aldrich, 98%); argon gas (Airgas,  $>99.998\%$ ); oxygen gas (Airgas, industrial grade); titanium(IV) isopropoxide (Sigma-Aldrich, 97%); fluorine-doped tin oxide-coated glass (FTO; Hartford Glass Co., Inc., 2.3 mm thick,  $15 \Omega/\square$ ); acetonitrile ( $\text{CH}_3\text{CN}$ , Fluka, 99.9%); deuterated acetonitrile ( $\text{CD}_3\text{CN}$ ; Cambridge Isotope Laboratories, Inc., D 99.8%); chloroform ( $\text{CHCl}_3$ ; Fisher, 99.9%); ethyl acetate (Fischer, 99.9%); ethanol (EtOH; Decon Laboratories, Inc., 200 proof); hexanes (Fischer, mixture of isomers).

**NMR:** NMR spectra were obtained on a Bruker Avance III 400 MHz spectrometer in  $\text{CD}_3\text{CN}$  at approximately 298 K. All peaks are referenced to the solvent peak at 1.96 and are in units of  $\delta$  (ppm).<sup>15</sup>

**ESI-MS:** High resolution electrospray ionization mass spectrometry data were collected with a Thermo LTQ FT hybrid mass spectrometer using a micro-electrospray source at a flow rate of 3  $\mu\text{L}/\text{min}$ .

**Synthesis:** Synthesis of 1,1'-(ethoxycarbonyl-phenyl-methyl)<sub>2</sub>-4,4'-bipyridinium hexafluorophosphate (DPEV) was accomplished by reacting a 6:1 molar ratio of ethyl  $\alpha$ -bromophenylacetate and 4,4'-bipyridine in 25 mL  $\text{CH}_3\text{CN}$  for 24 hours. The resulting yellow solid was filtered and washed with  $\text{CH}_3\text{CN}$ , ethyl acetate, and  $\text{CHCl}_3$  then dissolved in water. The  $\text{PF}_6$  salt was crashed out of the aqueous solution after the addition of a minimal amount

of aqueous  $\text{NH}_4\text{PF}_6$ . The resulting solid was filtered and washed with water to give the desired product.  $^1\text{H}$  NMR in  $\text{CD}_3\text{CN}$  resulted in resonances at  $\delta$  8.97 (4H, d), 8.38 (4H, d), 7.61 (10H, m), 6.90 (2H, s), 4.42 (4H, m), and 1.31 (6H, t). ESI-MS resulted in peaks corresponding to ( $m/z$ ):  $[\text{M} - (\text{PF}_6)]^+$  calcd for  $\text{C}_{30}\text{H}_{30}\text{N}_2\text{O}_4\text{P}_1\text{F}_6$ , 627.18419; found 627.18419, and  $[\text{M}_2 - (\text{PF}_6)]^+$  calcd for  $\text{C}_{60}\text{H}_{60}\text{N}_4\text{O}_8\text{P}_3\text{F}_{18}$ , 1399.33311; found 1399.33195.

Synthesis of 1,1'-(2-ethoxycarbonyl-ethyl)<sub>2</sub>-4,4'-bipyridinium hexafluorophosphate (DEV) was achieved by reacting a 6:1 molar ratio of ethyl 3-bromopropanoate and 4,4'-bipyridine in 25 mL  $\text{CH}_3\text{CN}$  for 24 hours. The resulting yellow solid was filtered, washed with  $\text{CH}_3\text{CN}$ , and dissolved in water. The  $\text{PF}_6$  salt was crashed out of water after addition of a minimal amount of aqueous  $\text{NH}_4\text{PF}_6$ , which was filtered and washed with water.  $^1\text{H}$  NMR in  $\text{CD}_3\text{CN}$  resulted in resonances at  $\delta$  8.99 (4H, d), 8.39 (4H, d), 4.89 (4H, t), 4.13 (4H, q), 3.13 (4H, t), 1.22 (6H, t). ESI-MS resulted in peaks corresponding to ( $m/z$ ):  $[\text{M} - (\text{PF}_6)]^+$  calc for  $\text{C}_{20}\text{H}_{26}\text{N}_2\text{O}_4\text{PF}_6$ , 503.15288; found 503.15306 and  $[\text{M}_2 - (\text{PF}_6)]^+$  calc for  $\text{C}_{40}\text{H}_{52}\text{N}_4\text{O}_8\text{P}_3\text{F}_{18}$ , 1151.27051; found 1151.27072.

Synthesis of 1-(2-ethoxycarbonyl-ethyl)-4,4'-bipyridinium hexafluorophosphate (MEV) was accomplished by an overnight reaction of a 1.2:1 molar ratio of ethyl 3-bromopropanoate and 4,4'-bipyridine and in 100 mL  $\text{CH}_3\text{CN}$ . The  $\text{CH}_3\text{CN}$  was removed under vacuum and the remaining oil, a mixture of unreacted starting materials and both mono- and di-substituted products, was dissolved in water. This solution was washed with  $\text{CHCl}_3$  and then hexanes to remove any unreacted starting materials. The  $\text{PF}_6$  salts of mono- and di-substituted products were obtained by adding a minimal amount of aqueous  $\text{NH}_4\text{PF}_6$ , filtering, and washing with water. MEV was purified from DEV on an alumina column using 3:1  $\text{EtOH}/\text{H}_2\text{O}$  as the eluent. The solution was removed under vacuum and washed with

EtOH to give the pure product.  $^1\text{H}$  NMR in  $\text{CD}_3\text{CN}$  resulted in resonances at  $\delta$  8.86 (4H, m), 8.32 (2H, d), 7.80 (2H, m), 4.81 (2H, t), 4.12 (2H, q), 3.09 (2H, t), 1.22 (3H, t). ESI-MS resulted in peaks corresponding to ( $m/z$ ):  $[\text{M} - (\text{PF}_6) - \text{C}_2\text{H}_4]^+$  calcd for  $\text{C}_{13}\text{H}_{13}\text{N}_2\text{O}_2$ , 229.09715; found 229.09706,  $[\text{M} - (\text{PF}_6)]^+$  calcd for  $\text{C}_{15}\text{H}_{17}\text{N}_2\text{O}_2$ , 257.1274; found 257.12829, and  $[\text{M}_2 - (\text{PF}_6)]^+$  calcd for  $\text{C}_{30}\text{H}_{34}\text{N}_4\text{O}_4\text{PF}_6$ , 659.22164; found 659.22033.

**TiO<sub>2</sub> Thin Film Preparation:** Synthesis of TiO<sub>2</sub> nanoparticles of approximately 20 nm diameter was carried out by the acid hydrolysis of titanium(IV) isopropoxide as previously described.<sup>5</sup> Thin films of approximately 5  $\mu\text{m}$  were prepared by doctor blading the colloidal solution onto transparent FTO using cellophane tape as the spacer, followed by sintering at 450 °C for 30 minutes under oxygen flow. Thin films were either used immediately or stored in an oven at  $\sim 80$  °C until use. Attachment of pyridiniums to the surface was carried out by overnight immersion in micro- to milli-molar acetonitrile (depending on target surface coverage) solutions of the desired viologen. Surface coverages could not be determined prior to starting an experiment as the ground state viologen absorption ( $\sim 260$  nm) is obscured by the absorbance of the TiO<sub>2</sub> thin film, which absorbs below  $\sim 370$  nm. However, surface coverages often could be estimated *in situ* using the absorbance of the reduced compounds and a modified Beer-Lambert law, Equation 5.01:

$$\Gamma = \text{Abs}/(1000\varepsilon) \quad 5.01$$

where  $\Gamma$  is the surface coverage ( $\text{mol}/\text{cm}^2$ ),  $\varepsilon$  is the extinction coefficient ( $\text{M}^{-1}\text{cm}^{-1}$ ) and 1000 is a conversion factor between  $\text{cm}^3$  and L.

**Electrochemistry:** *Cyclic voltammetry:* Cyclic voltammetry was performed in argon purged 100 mM TBAClO<sub>4</sub> acetonitrile or 100 mM LiClO<sub>4</sub> acetonitrile solutions in a standard 3 electrode configuration. Both the working and counter electrodes were platinum disks and the potential was applied versus a non-aqueous Ag/AgCl reference electrode. The average ferrocinium/ferrocene half-wave potential measured in 100 mM TBAClO<sub>4</sub> CH<sub>3</sub>CN solutions before and after each experiment was used to serve as an external standard for the calibration of the non-aqueous reference electrode. The value for the ferrocinium/ferrocene half-wave potential was taken to be +630 mV vs NHE in acetonitrile.<sup>16</sup>

*Solution Spectroelectrochemistry:* The spectra of the reduced pyridiniums was obtained by bulk reduction at Pt honeycomb working electrode (Pine Research Instrumentation) in argon purged 100 mM Li<sup>+</sup> or TBA<sup>+</sup> perchlorate acetonitrile solutions. This specially designed electrode was used in a standard 3 electrode configuration with a Pt counter electrode and a non-aqueous Ag/AgCl reference electrode described above. Spectra were monitored by an Avantes AvaLight DHc light source coupled to an Avantes StarLine AvaSpec-2048 UV/Visible spectrometer synchronized to a Pine Wavenow Potentiostat controlled by Aftermath software (Pine).

*Surface Spectroelectrochemistry:* Spectroelectrochemistry of bare and viologen-anchored TiO<sub>2</sub> thin films was performed by monitoring the UV/Vis absorption spectrum during the application of an applied potential. Potentials were applied by a BASi CV-50W potentiostat operating in a standard 3 electrode configuration where the TiO<sub>2</sub> thin film was the working electrode and Pt gauze electrode (BASi) was the counter electrode in argon purged 100 mM TBAClO<sub>4</sub> or LiClO<sub>4</sub> acetonitrile solutions. Potentials were applied versus a non-aqueous Ag/AgCl reference electrode (BASi) described above while the UV/Vis absorbance was

monitored on a Varian Cary 50 Spectrophotometer. Experiments were performed by stepping and holding at (typically) increasingly negative potentials while monitoring the absorption spectra. When no more spectral changes were observed (~2-3 minutes), the potential was moved to the next value.

Spectroelectrochemical charge extraction measurements were performed by monitoring the UV/Vis absorption spectrum of TiO<sub>2</sub> thin films with and without pyridiniums anchored to the surface during two potential steps. Starting from +200 mV vs NHE, the bias was stepped to a potential negative of the viologen reduction potential, held for typically 45 seconds, and then returned to the initial potential. The UV/Vis absorbance spectra during these steps were monitored by either an Avantes AvaLight DHc light source coupled to an Avantes StarLine AvaSpec-2048 UV/Visible spectrometer or an HP 8453 UV/Vis spectrophotometer while a Pine Wavenow Potentiostat controlled by Aftermath software (Pine) or an EC Epsilon (BASi) applied the desired voltage in the same 3-electrode configuration described above. A 400 nm long pass filter (GG400) was used to prevent direct excitation of the TiO<sub>2</sub>. The spectral changes observed were similar to those during the steady state spectroelectrochemistry, however the CCD detector allowed complete spectra to be obtained with 0.5 s resolution, providing accurate kinetic data throughout the experiment.

### **5.3 Results and Discussion**

Cyclic voltammetry was used to quantify the pyridinium formal reduction potentials in acetonitrile electrolytes. Two single reductions were observed for DPEV and DEV while only one was observed for MEV with potential excursions to -1.0 V vs NHE. The redox chemistry is best classified as quasi-reversible as the anodic and cathode peak potentials were

the same,  $i_{pa}/i_{pc} = 1$ , and the peak-to-peak separation was greater than 59 mV. The formal reduction potentials are tabulated in Table 5.1.

Table 5.1. Reduction Potentials and Ideality Factors for Pyridiniums in Solution and Anchored to the TiO<sub>2</sub> surface.

<i>Pyridinium</i>	<i>E</i> <sup>0</sup> in Solution <i>mV vs NHE</i>		<i>E</i> <sup>0</sup> on TiO <sub>2</sub> <i>mV vs NHE (α)</i>	
	1 <sup>st</sup> Red	2 <sup>nd</sup> Red	TBA <sup>+</sup>	Li <sup>+</sup>
<i>MEV</i>	-680 ± 10	-	-700 ± 50 (2.3)	-310 ± 50 (1.3)
<i>DEV</i>	-150 ± 10	-570 ± 10	-400 ± 40 (2.4)	-240 ± 50 (1.9)
<i>DPEV</i>	-20 ± 10	-440 ± 10	-270 ± 20 (2.2)	-130 ± 30 (1.3)

The pyridiniums were anchored to mesoporous nanocrystalline (20 nm anatase) TiO<sub>2</sub> thin films deposited on fluorine-doped tin oxide (FTO) glass by overnight reactions in CH<sub>3</sub>CN. Surface coverages were controlled by the solution concentration and for kinetic experiments were kept below 1/3 of the saturation surface coverage,  $\sim 1.5 \times 10^{-8}$  mol/cm<sup>2</sup>, which was lower than the percolation threshold required for lateral intermolecular electron/hole-hopping.<sup>10</sup>

Electrochemical reduction of the surface functionalized TiO<sub>2</sub> thin films in a standard three-electrode cell resulted in the expected absorption features from the reduced pyridiniums and the TiO<sub>2</sub>(e<sup>-</sup>s).<sup>7,8</sup> The potential dependent concentration of these two species were quantified spectroscopically using the Beer-Lambert Law. An exponential rise of the TiO<sub>2</sub>(e<sup>-</sup>) concentration, determined from the magnitude of the near IR absorption, was observed as the Fermi level of the FTO substrate was raised toward the vacuum level. The density at any potential was dependent on the nature and concentration of cations present in the CH<sub>3</sub>CN

solution. Surface adsorption of Lewis acid  $\text{Li}^+$ , often referred to as a ‘potential determining’ ion, resulted in a strong positive shift in the electrochemical reduction of  $\text{TiO}_2$  relative to that measured in tetrabutyl ammonium electrolytes, Figure 5.01.<sup>7,8</sup>

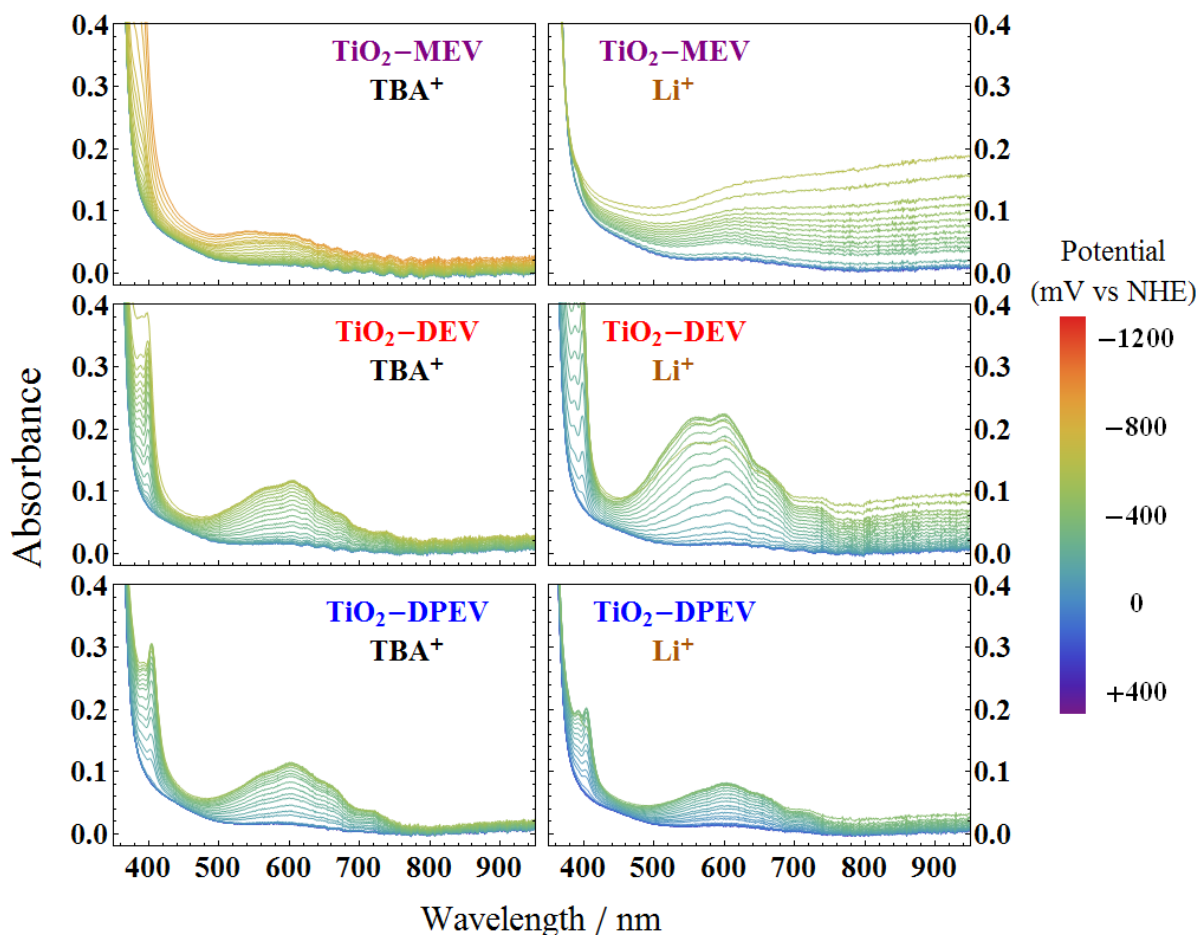


Figure 5.01. The spectroelectrochemical reduction of the indicated pyridiniums/ $\text{TiO}_2$  in 0.1 M  $\text{TBAClO}_4$  (left hand side) or  $\text{LiClO}_4$  (right hand side)  $\text{CH}_3\text{CN}$  electrolytes.

The pyridinium redox chemistry did not follow the Nernst equation, which for a one electron transfer equilibrium at room temperature is given in Equation 5.02,

$$E = E^o - 59\text{mV} \log_{10} \frac{[\text{red}]}{[\text{ox}]} \quad 5.01$$

where  $E$  is the applied potential and  $E^0$  is the formal reduction potential. An ideality factor,  $\alpha$ , was introduced into the Nernst Equation that with rearrangement led to Equation 5.03,<sup>9</sup>

$$x = \frac{1}{1 + 10^{\frac{E-E^0}{\alpha \times 59 \text{ mV}}}} \quad 5.03$$

where  $x$  is the fraction of pyridinium present in the reduced state.

Although the origin(s) of the non-ideality remain uncertain, those measured in TBA<sup>+</sup> containing electrolytes were on average larger  $\alpha = 2.2 \pm 0.2$  than those measured in Li<sup>+</sup> electrolytes,  $\alpha = 1.6 \pm 0.3$ , data consistent with the notion that surface electric fields induce the non-ideal behavior and that Li<sup>+</sup> is able to screen such fields more effectively than does TBA<sup>+</sup>.<sup>17,18</sup> The appearance of non-Nernstian behavior raises questions about the value of the formal reduction potentials that were approximated herein to be the equilibrium potential where the concentrations of the pyridinium and its reduced form were present in equal concentrations, Table 5.1.

Pyridiniums of this class are known to aggregate, behavior that could influence interfacial behavior on TiO<sub>2</sub>.<sup>19-21</sup> For this reason, comparative spectroelectrochemical generation of the reduced pyridiniums by bulk electrolysis from dilute CH<sub>3</sub>CN electrolytes was also performed, Figure 5.02. The absorption spectra of DPEV<sup>+</sup> and DEV<sup>+</sup> were very similar to that for singly reduced methyl viologen in dilute solution.<sup>22</sup> Extinction coefficients were estimated by comparing the absorbance of the reduced species to the ground state absorbance where the extinction coefficients were measured. The maximum visible extinction coefficient for MEV<sup>0</sup> was less than 1/2 that of the other two pyridiniums, Table 5.2.

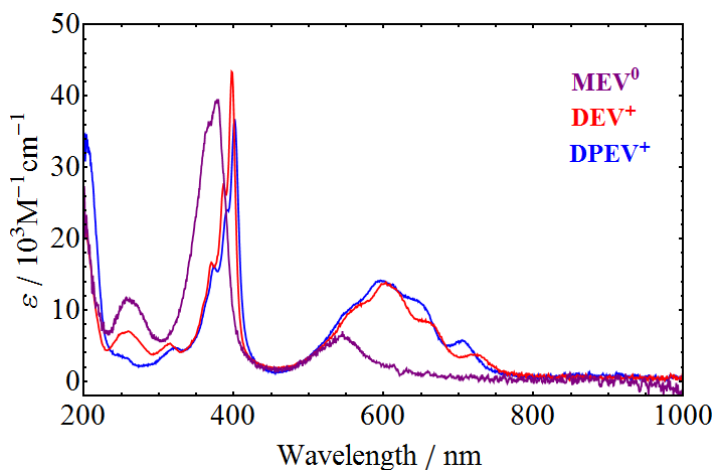


Figure 5.02. The UV/Visible absorption spectra of the indicated pyridiniums in 0.1 M LiClO<sub>4</sub> or TBAClO<sub>4</sub> CH<sub>3</sub>CN electrolyte.

The absorption spectra of the reduced pyridiniums on TiO<sub>2</sub> were in good agreement with that measured in fluid CH<sub>3</sub>CN solution, Table 5.2. Note that the maximum wavelengths given in Table 5.2 for the pyridiniums on TiO<sub>2</sub> were not corrected for the underlying absorption of the TiO<sub>2</sub>(e<sup>-</sup>)s and this is the likely origin of the small red shifts in the reported maxima. However, when higher surface coverages were employed significant deviations from solution spectra were evident. Application of a forward bias to DPEV anchored TiO<sub>2</sub> thin films with surface coverages greater than  $1 \times 10^{-8}$  mol/cm<sup>2</sup> resulted in a growth along the high energy side of the visible absorption and a broad absorbance trailing into the near-infrared region. The spectral data were consistent with aggregation of the singly reduced species, DPEV<sup>+</sup>, on the TiO<sub>2</sub> surface and served as an upper limit for surface coverages used in the study.<sup>19,20</sup> It is worth noting that the presence of such aggregation was monitored for DPEV in both Li<sup>+</sup> and TBA<sup>+</sup> electrolytes and did not affect the observed sluggish oxidation kinetics discussed below.

Table 5.2. UV/Visible Absorption Properties of the Pyridiniums

	<i>DPEV</i> <sup>2+</sup>	<i>DEV</i> <sup>2+</sup>	<i>MEV</i> <sup>+</sup>	<i>DPEV</i> <sup>+</sup>	<i>DEV</i> <sup>+</sup>	<i>MEV</i> <sup>0</sup>
$\lambda_{max}^a / nm$	263	261	263	597	603	545
(on <i>TiO</i> <sub>2</sub> )				(603)	(605)	(545)
$\epsilon / M^{-1}cm^{-1}$	24,600	23,200	31,600	14,100	13,800	6,700

a. Peak maxima are taken to be  $\pm 2$  nm. <sup>1</sup>

The reduction kinetics were quantified by chronoabsorptometry after a potential step that induced redox chemistry. Figure 5.03 shows representative data for a mesoporous *TiO*<sub>2</sub> thin film in *TBA*<sup>+</sup> or *Li*<sup>+</sup> containing electrolytes that did not contain surface anchored pyridiniums. As the potential was stepped to more negative values the magnitude of the absorption change associated with the presence of *TiO*<sub>2</sub>(e<sup>-</sup>)s increased exponentially. The time required to reach a steady state *TiO*<sub>2</sub>(e<sup>-</sup>) concentration also increased as the final potential was made more negative. The data shown in Figure 5.03 were normalized to emphasize this kinetic behavior. About 25 seconds were required to achieve a steady state *TiO*<sub>2</sub>(e<sup>-</sup>) concentration at the most negative potentials shown for data recorded in *TBA*<sup>+</sup> containing acetonitrile electrolyte. In sharp contrast, greater than the 40 s were acquired to reach the highest steady state *TiO*<sub>2</sub>(e<sup>-</sup>) concentration in the *Li*<sup>+</sup> containing electrolyte, presumably due to *Li*<sup>+</sup>-*TiO*<sub>2</sub> surface interactions that were absent in *TBA*<sup>+</sup> containing electrolytes.

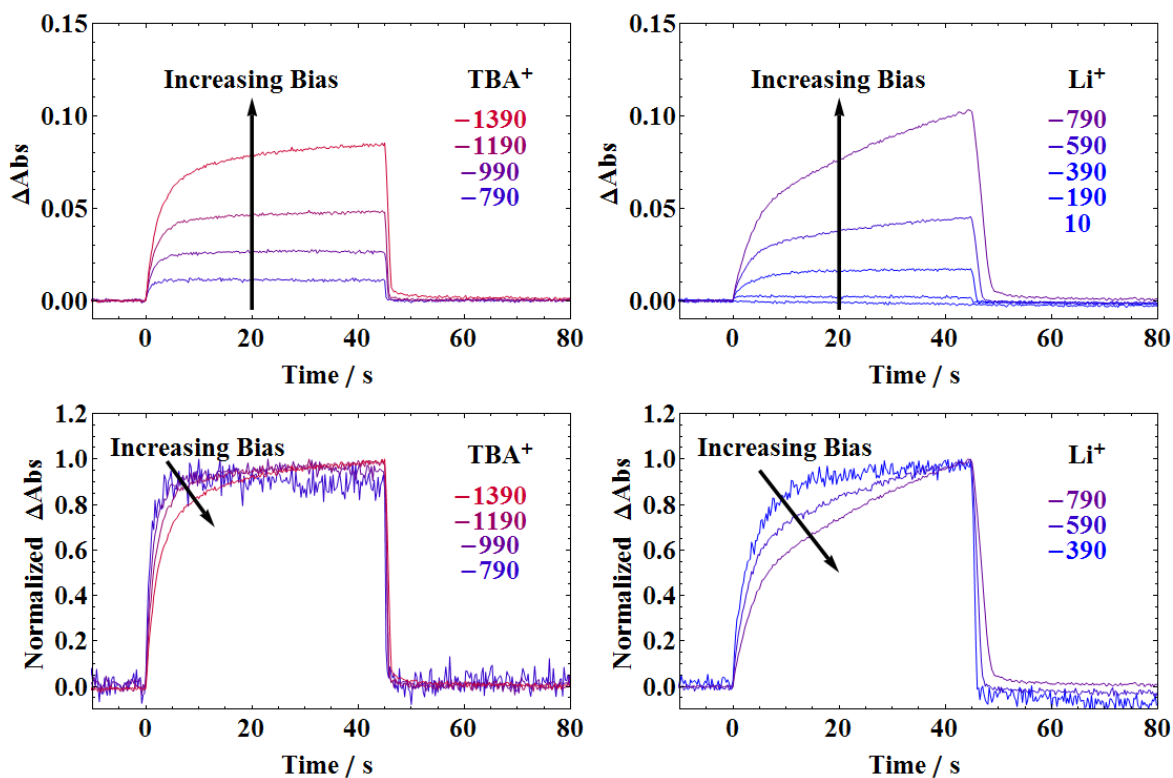
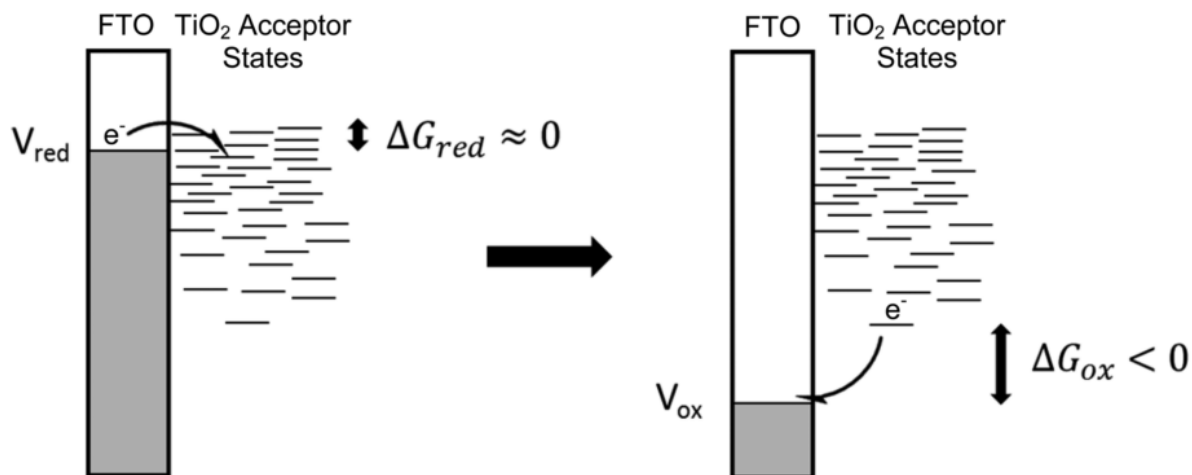


Figure 5.03. The absorption change for an unfunctionalized  $\text{TiO}_2$  thin film measured at 900 nm after a potential step from 0.2 V to the indicated potentials (mV) at time zero in 0.1 M  $\text{TBAClO}_4$  (left hand side) and  $\text{LiClO}_4$  (right hand side)  $\text{CH}_3\text{CN}$  electrolyte. The potential was stepped back to +0.2 V after 45 s.

Stepping the potential back to the initial value resulted in oxidation of the  $\text{TiO}_2(e^-)$  and the time scale for this was approximately independent of the number of  $\text{TiO}_2(e^-)$ s that were present in the mesoporous thin film. While the origin of the slow reduction and fast oxidation kinetics are not fully understood, this behavior has been reported elsewhere and is well documented in the literature.<sup>23,24</sup> One possible explanation is understood with the depiction in Scheme 5.2. Since the applied potential for reduction,  $V_{\text{red}}$ , lies within a high density of  $\text{TiO}_2$  acceptor states, there was no significant driving force for filling the highest lying states and complete reduction took tens of seconds to minutes. This was contrasted to

the oxidative step where the oxidizing potential,  $V_{ox}$ , was more positive with a very low density of  $TiO_2$  states. In that case, there was *always* a strong driving force for oxidation and it was correspondingly faster. Another possible consideration for the disparate redox dynamics is diffusion of electrons in the  $TiO_2$  thin film. It is known that  $TiO_2$  reduction is accompanied by uptake of  $Li^+$  cations from the electrolyte<sup>25</sup> while for  $TiO_2$  oxidation cations in/on the surface may slowly release after the electron leaves  $TiO_2$ .

Scheme 5.2. Energetics of the  $TiO_2$  Acceptor States Compared to Reductive,  $V_{red}$ , and Oxidative,  $V_{ox}$ , Step Potentials for Interfacial Electron Transfer Between the  $TiO_2$  Thin Film and the Conductive Contact, FTO.



The chronoabsorptometry measurements were repeated for the pyridinium functionalized  $TiO_2$ , representative data is given in Figure 5.04 where the step potential was sufficient to produce the singly reduced pyridinium. The absorption changes were monitored at the wavelengths of maximum pyridinium absorption change determined from the steady state spectro-electrochemical data, Figure 5.01 and Table 5.2. Although the  $TiO_2(e^-)$ s also

absorb at these wavelengths, least-squares spectral deconvolution using the solution spectra and the known spectra of  $\text{TiO}_2(\text{e}^-)$ s confirmed that the single wavelength kinetics reported here accurately represent the appearance of reduced viologen.

The time required to reduce the surface anchored pyridiniums was dependent upon the final applied potential. The kinetics were non-exponential and the general trends were emphasized herein. For any given pyridinium the time required to reach an equilibrium concentration of the reduced form was dependent on the magnitude of the potential step and followed the same trend as that observed for the  $\text{TiO}_2(\text{e}^-)$ : the more negative the potential the more time necessary for achievement of equilibrium. For example, MEV required the most negative potential step for significant reduction and it required about 20 seconds to reach a steady-state value while DPEV, which was the most easily reduced, required less than five seconds.

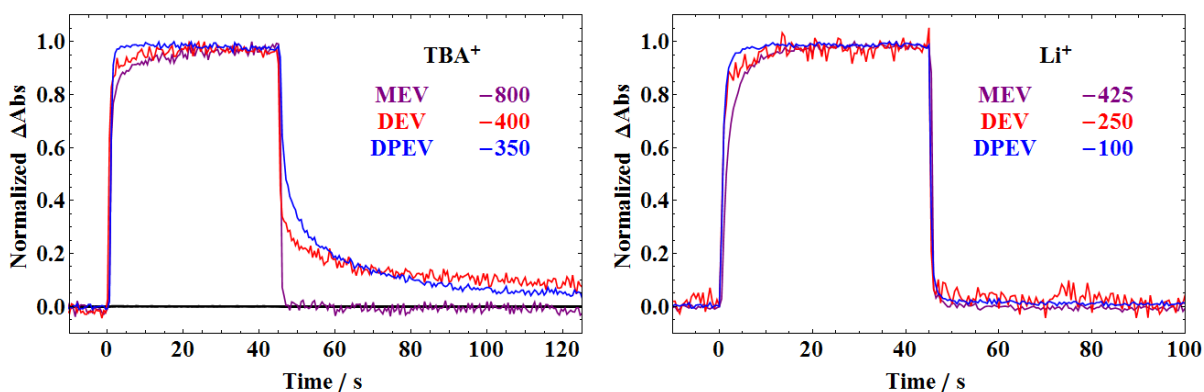


Figure 5.04. The normalized absorption change measured at the reduced pyridinium maximum wavelength after a step from +0.2 V to the indicated potentials (mV) at time zero in 0.1 M  $\text{TBAClO}_4$  (left hand side) and  $\text{LiClO}_4$  (right hand side)  $\text{CH}_3\text{CN}$  electrolyte. The potential was stepped back to +0.2 V after 45 s.

The oxidation of the reduced pyridiniums in  $\text{Li}^+$  containing electrolytes was independent of the identity of the pyridinium and was similar to that observed for oxidation of  $\text{TiO}_2(e^-)$ . The reduced pyridinium oxidation in  $\text{TBA}^+$  electrolyte was more interesting;  $\text{DEV}^+$  and  $\text{DPEV}^+$  oxidation showed a slow component that tailed out into the tens of seconds timescales that was absent for  $\text{MEV}^0$  oxidation.

Chronoabsorptometry measurements were also performed with potential steps into the second reduction of DPEV in  $\text{TBA}^+$  containing electrolyte, Figure 5.05. Time dependent absorption spectra were observed consistent with the sequential one electron reductions of  $\text{DPEV}^{2+}$  to  $\text{DPEV}^+$ , and then to  $\text{DPEV}^0$ . The large absorption changes present when the reactions were monitored at a single wavelength resulted from the fact that the singly reduced  $\text{DPEV}^+$  species absorbed more visible light than did the doubly reduced  $\text{DPEV}^0$ . A potential step back to the initial value resulted in the oxidation of  $\text{DPEV}^0$  to  $\text{DPEV}^+$  followed by production of the initial  $\text{DPEV}^{2+}$  state. The absorption spectra revealed about 30% of the surface anchored DPEV molecules were present in the intermediate  $\text{DPEV}^+$  state, however it is suspected that all of the pyridiniums underwent two sequential one-electron transfers and that the slow  $\sim 0.5$  s time resolution did not allow all of them to be quantified.<sup>26</sup>

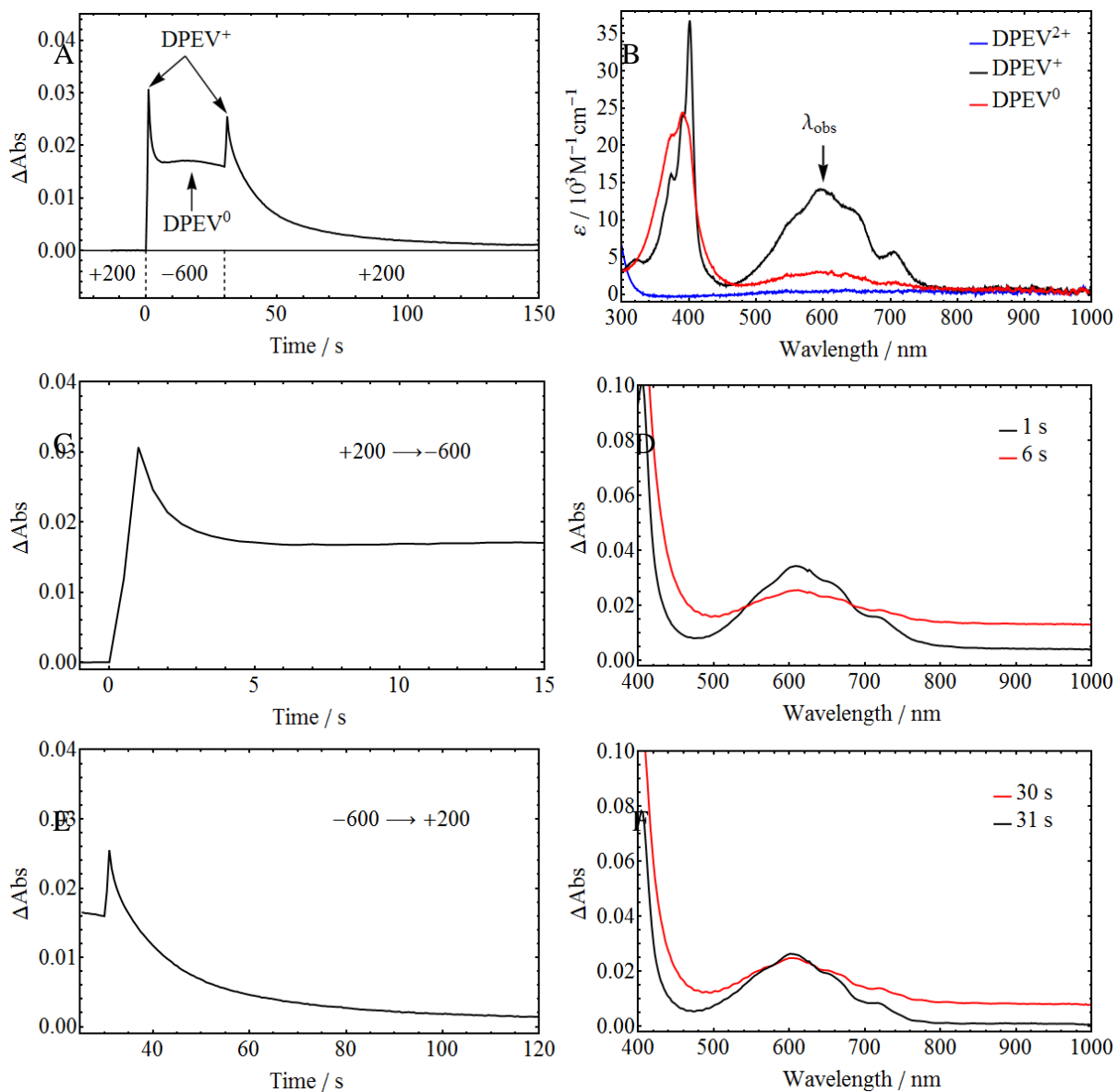


Figure 5.05. UV/Vis absorbance changes for DPEV functionalized  $\text{TiO}_2$  in 0.1 M  $\text{TBAClO}_4/\text{CH}_3\text{CN}$  during potential steps from +200 mV to -600 mV at time zero and back to +200 mV vs NHE at  $t = 30$  seconds. Single wavelength traces (600 nm) are shown in (A), with close-ups in (C) and (E). Full spectra are shown just before and after each potential step in (D) and (F) to highlight the observation of  $\text{DPEV}^+$  as an intermediate. Extinction coefficient spectra for  $\text{DPEV}^{2+}$ ,  $\text{DPEV}^+$ , and  $\text{DPEV}^0$  are shown in (B) for reference. Long

wavelength absorption changes in (D) and (F) are caused by the broad absorption of TiO<sub>2</sub> electrons during reduction.

The interfacial pyridinium redox kinetics can be understood with thermodynamic data recast in Figure 5.06 where the measured cumulative charge was differentiated and expressed as a chemical capacitance, a metric very similar to the density of states.<sup>27,28</sup> These distributions are not Gaussian and should not be confused with the those often depicted in Gerischer diagrams, which are not directly probed by electrochemical measurements.<sup>4</sup> The peaks of the distributions represent the equilibrium potentials where equal concentrations of the pyridinium and its one electron reduced form were present and were taken as the formal reduction potential. The two pyridiniums chosen for this Figure, DPEV<sup>2+/+</sup> and MEV<sup>+/0</sup>, represent the extremes in potential characterized in this study. Also shown is the TiO<sub>2</sub> chemical capacitance that displayed an exponential dependence on the applied potential.

The reduction data can be understood as a ‘band filling’ or ‘cup of wine’ analogy, we prefer the latter as it is most likely that the TiO<sub>2</sub> electronic states do not comprise the conduction band. Under this simplistic model electrons injected into the TiO<sub>2</sub> film from the FTO substrate quickly relax to the lowest available energy level and the acceptor states are effectively filled from the bottom up as a cup of wine is filled. A more negative applied potential is analogous to filling the cup to a higher level which requires more time. In other words, the fill (pour) rate is fixed and the time required is determined only by the number of states (volume) available. Hence the longer time required at a fixed potential in a Li<sup>+</sup> containing acetonitrile electrolytes relative to a TBA<sup>+</sup> containing electrolytes reflects the higher density of TiO<sub>2</sub> acceptor states in Li<sup>+</sup> electrolytes much like filling a larger cup requires more time. One would anticipate that thicker TiO<sub>2</sub> films would result in even slower

reduction kinetics. Surprisingly, the cup filled with approximately the same rate regardless of whether the acceptor state was the  $\text{TiO}_2$  itself or the surface anchored pyridinium. One might have suspected that the two would be different due to coulombic repulsion between electrons within  $\text{TiO}_2$  and the large electric field that were created with continued reduction. The more positive formal reduction potentials of the surface anchored pyridiniums in 0.1 M  $\text{Li}^+/\text{CH}_3\text{CN}$  relative to 0.1 M  $\text{TBA}^+/\text{CH}_3\text{CN}$  electrolytes likely reflect the interfacial electric field yet it does not appear to influence the kinetics.<sup>29,30</sup>

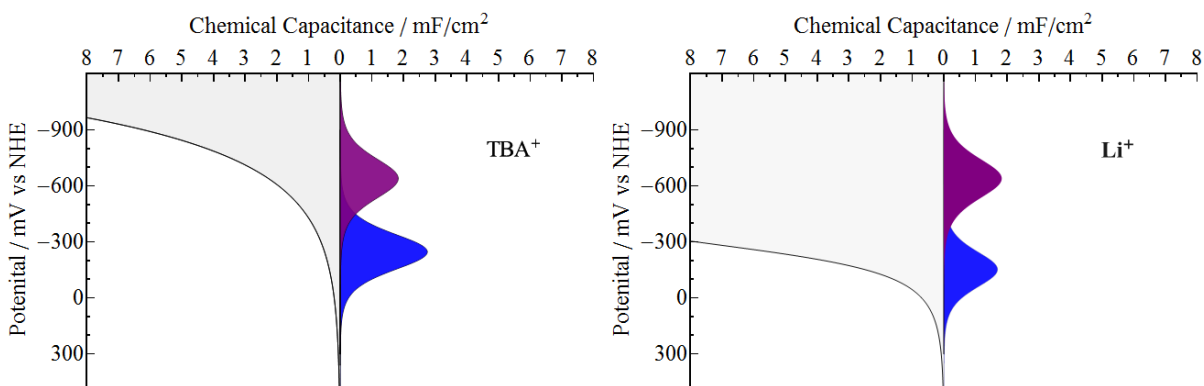


Figure 5.06. The chemical capacitance of  $\text{DPEV}^{2+/+}$  (blue) and  $\text{MEV}^{+/0}$  (purple) and the  $\text{TiO}_2$  (gray) measured in 0.1 M  $\text{TBAClO}_4$  (left) and  $\text{LiClO}_4$  (right)  $\text{CH}_3\text{CN}$  electrolyte.

An additional complication with these nanocrystalline films was that the potential step at the FTO interface was immediate yet the time required for this potential change to extend through the mesoporous thin film was unknown. Hence, pyridiniums and  $\text{TiO}_2$  nanocrystallites near the FTO surface were likely to undergo electron transfer first after the potential step while those farther from the FTO surface would require more time. While some spatial inhomogeneity of this type likely occurred within the films before steady-state was achieved, the observation of two sequential one-electron transfer events for DPEV in  $\text{TBA}^+/\text{CH}_3\text{CN}$  strongly suggests that the slow approach to steady-state was not due to

inhomogeneous reduction of the TiO<sub>2</sub> thin film but was in fact due to quasi-Fermi level changes as steady-state was neared described by the ‘cup of wine’ model.

When the overlap between the viologen donor states and the TiO<sub>2</sub> acceptor states was large, the oxidation of the films occurred as if the cup were being drained from the bottom. The oxidation required less time than the reduction presumably because of a larger thermodynamic driving force for the reaction. For measurements in Li<sup>+</sup> containing electrolyte and for MEV<sup>0</sup> and DPEV<sup>0</sup> oxidation in TBA<sup>+</sup> electrolyte, the oxidation of the pyridiniums was fast and indistinguishable from that of the un-functionalized TiO<sub>2</sub> thin films. For these interfaces, the overlap of the electronic states with the unfilled states in TiO<sub>2</sub> was sufficiently high such that interfacial electron transfer was fast relative to extraction of electrons from the thin film. This allowed a quasi-equilibrium to be maintained during oxidation and the ‘cup of wine’ model alone was sufficient to describe the oxidation behavior. In contrast, the oxidation of DPEV<sup>+</sup> and DEV<sup>+</sup> in 0.1 M TBA<sup>+</sup> was slow and distinctly different than oxidation of un-functionalized thin films. For these interfaces, the ‘cup of wine’ analogy alone was insufficient to completely describe the oxidation behavior because the energetic overlap between the viologen donor states and TiO<sub>2</sub> acceptor states was low such that interfacial electron transfer was slow and a quasi-equilibrium could not be maintained during oxidation.

The slow oxidation that did occur was attributed to activated electron transfer to the TiO<sub>2</sub> acceptor states. While it could not be proved directly, it is likely that those reduced pyridiniums with the longest lifetimes corresponded to those that were furthest from the fluorine doped tin oxide (FTO) substrate where the redox chemistry was initiated. One would expect that redox active molecules with more positive formal reduction potentials

would have even longer lifetimes and could possibly be permanently trapped in their reduced forms in these potential step experiments. Potential steps that initiated two sequential 1-electron transfer reactions with the pyridiniums provided additional evidence for the ‘cup of wine’ model. The DPEV<sup>2+/+</sup> donor states had a much lower overlap with the TiO<sub>2</sub> acceptor states than did the DPEV<sup>+/0</sup> donor states resulting in slow and fast electron transfer, respectively.

We note that the rapid reduction of pyridiniums after bandgap excitation of TiO<sub>2</sub> is well documented in the literature and has been exploited for ultrafast color displays<sup>15,16</sup> and photochromics.<sup>31</sup> These light-induced reactions are inherently different as interfacial electron transfer is not rate limited by charge transport from the FTO substrate.<sup>32</sup> The redox chemistry reported here bares some similarity to the forward bias condition of rutile TiO<sub>2</sub> single crystals in electrochemical cells where the high density of conduction band states can result in reversible redox chemistry with molecules that have sufficiently negative formal reduction potentials that they lie within the conduction band.<sup>33</sup> For the interfacial studies carried out here, the exponential tail of the semiconductor nanocrystallite density of states represents an interesting situation. These electronic states provide sufficient overlap for rapid reduction of the surface anchored pyridiniums yet do not as effectively accept an electron from the reduced pyridinium providing a means of charge rectification. As a tailing density of states may be a common feature of nanocrystalline semiconductor materials, we anticipate that the rapid charge separation and inhibited charge recombination reported represents general behavior that can be optimized at the molecular level for solar energy conversion and other applications with semiconductor nanocrystalline thin films.

## 5.4 Conclusions

Three pyridinium molecules anchored to mesoporous TiO<sub>2</sub> thin films displayed non-Nernstian behavior that was well modelled by the inclusion of ideality factors. The reduction of TiO<sub>2</sub> and the pyridiniums occurred with rates that were within experimental error the same, consistent with a ‘cup of wine’ model where the number of states reduced determined the time required. The oxidation of the reduced pyridiniums was rapid when the formal reduction of the pyridinium had a high overlap with the TiO<sub>2</sub> density of states; however, this redox chemistry was much more sluggish when the overlap was low. This slower redox chemistry was attributed to activated transport through the mesoporous thin film to the conductive substrate. The data hence provides a new means for controlling interfacial redox chemistry that cannot be realized with lateral ‘hole hopping’ when the surface coverage exceeds the percolation threshold.

## Author Information

### Corresponding Author

\* Gerald J. Meyer. E-mail: gjmeyer@email.unc.edu. Phone: 919-962-6320.

**Acknowledgement.** The research is supported by the National Science Foundation (NSF) under Award CHE-1213357.

## REFERENCES

- (1) Singh, J. *Semiconductor Devices: Basic Principles*; John Wiley & Sons, Inc.: New York, 2001.
- (2) Albery, W. J.; Bartlett, P. N. The Transport and Kinetics of Photogenerated Carriers in Colloidal Semiconductor Electrode Particles. *J. Electrochem. Soc.* **1984**, *131*, 315–325.
- (3) Hodes, G.; Howell, I. D. J.; Peter, L. M. Nanocrystalline Photoelectrochemical Cells. *J. Electrochem. Soc.* **1992**, *139*, 3136–3140.
- (4) Gerischer, H. Electrochemical Techniques for the Study of Photosensitization. *Photochem. Photobiol.* **1972**, *16*, 243–260.
- (5) Heimer, T. A.; D’Arcangelis, S. T.; Farzad, F.; Stipkala, J. M.; Meyer, G. J. An Acetylacetonate-Based Semiconductor–Sensitizer Linkage. *Inorg. Chem.* **1996**, *35*, 5319–5324.
- (6) Cummins, D.; Boschloo, G.; Ryan, M.; Corr, D.; Rao, S. N.; Fitzmaurice, D. Ultrafast Electrochromic Windows Based on Redox-Chromophore Modified Nanostructured Semiconducting and Conducting Films. *J. Phys. Chem. B* **2000**, *104*, 11449–11459.
- (7) Grätzel, M. Ultrafast Colour Displays. *Nature* **2001**, *409*, 575–576.
- (8) Staniszewski, A.; Morris, A. J.; Ito, T.; Meyer, G. J. Conduction Band Mediated Electron Transfer Across Nanocrystalline TiO<sub>2</sub> Surfaces. *J. Phys. Chem. B* **2007**, *111*, 6822–6828.
- (9) Hu, K.; Meyer, G. J. Lateral Intermolecular Self-Exchange Reactions for Hole and Energy Transport on Mesoporous Metal Oxide Thin Films. *Langmuir* **2015**, *31*, 11164–11178.
- (10) Bonhôte, P.; Gogniat, E.; Tingry, S.; Barbé, C.; Vlachopoulos, N.; Lenzenmann, F.; Comte, P.; Grätzel, M. Efficient Lateral Electron Transport inside a Monolayer of Aromatic Amines Anchored on Nanocrystalline Metal Oxide Films. *J. Phys. Chem. B* **1998**, *102*, 1498–1507.
- (11) Hu, K.; Robson, K. C. D.; Beauvilliers, E. E.; Schott, E.; Zarate, X.; Arratia-Perez, R.; Berlinguette, C. P.; Meyer, G. J. Intramolecular and Lateral Intermolecular Hole Transfer at the Sensitized TiO<sub>2</sub> Interface. *J. Am. Chem. Soc.* **2014**, *136*, 1034–1046.
- (12) Ardo, S.; Meyer, G. J. Direct Observation of Photodriven Intermolecular Hole Transfer across TiO<sub>2</sub> Nanocrystallites: Lateral Self-Exchange Reactions and Catalyst Oxidation. *J. Am. Chem. Soc.* **2010**, *132*, 9283–9285.
- (13) Meyer, T. J.; Meyer, G. J.; Pfennig, B. W.; Schoonover, J. R.; Timpson, C. J.; Wall, J. F.; Kobusch, C.; Chen, X.; Peek, B. M.; Wall, C. G.; et al. Molecular-Level Electron Transfer and Excited State Assemblies on Surfaces of Metal Oxides and Glass. *Inorg. Chem.* **1994**, *33*, 3952–3964.
- (14) Hamd, W.; Chavarot-Kerlidou, M.; Fize, J.; Muller, G.; Leyris, A.; Matheron, M.; Courtin, E.; Fontecave, M.; Sanchez, C.; Artero, V.; et al. Dye-Sensitized Nanostructured Crystalline Mesoporous Tin-Doped Indium Oxide Films with Tunable Thickness for

Photoelectrochemical Applications. *J. Mater. Chem. A* **2013**, *1*, 8217-8225.

(15) Fulmer, G. R.; Miller, A. J. M.; Sherden, N. H.; Gottlieb, H. E.; Nudelman, A.; Stoltz, B. M.; Bercaw, J. E.; Goldberg, K. I. NMR Chemical Shifts of Trace Impurities: Common Laboratory Solvents, Organics, and Gases in Deuterated Solvents Relevant to the Organometallic Chemist. *Organometallics* **2010**, *29*, 2176–2179.

(16) Pavlishchuk, V. V.; Addison, A. W. Conversion Constants for Redox Potentials Measured versus Different Reference Electrodes in Acetonitrile Solutions at 25°C. *Inorg. Chim. Acta* **2000**, *298*, 97–102.

(17) Zaban, A.; Meier, A.; Gregg, B. A. Electric Potential Distribution and Short-Range Screening in Nanoporous TiO<sub>2</sub> Electrodes. *J. Phys. Chem. B* **1997**, *101*, 7985–7990.

(18) Ardo, S.; Achey, D.; Morris, A. J.; Abrahamsson, M.; Meyer, G. J. Non-Nernstian Two-Electron Transfer Photocatalysis at Metalloporphyrin- TiO<sub>2</sub> Interfaces. *J. Am. Chem. Soc.* **2011**, *133*, 16572–16580.

(19) Lee, C.; Moon, M. S.; Park, J. W. Spectroelectrochemical Study on Monomer/Dimer Equilibria of Methylalkylviologen Cation Radicals with and without  $\alpha$ -Cyclodextrin. *J. Electroanal. Chem.* **1996**, *407*, 161–167.

(20) Lee, C.; Lee, Y. M.; Moon, M. S.; Park, S. H.; Park, J. W.; Kim, K. G.; Jeon, S.-J. UV-Vis-NIR and Raman Spectroelectrochemical Studies on Viologen Cation Radicals: Evidence for the Presence of Various Types of Aggregate Species. *J. Electroanal. Chem.* **1996**, *416*, 139–144.

(21) Tang, X.; Schneider, T. W.; Walker, J. W.; Buttry, D. A. Dimerized  $\pi$ -Complexes in Self-Assembled Monolayers Containing Viologens: An Origin of Unusual Wave Shapes in the Voltammetry of Monolayers. *Langmuir* **1996**, *12*, 5921–5933.

(22) Watanabe, T.; Honda, K. Measurement of the Extinction Coefficient of the Methyl Viologen Cation Radical and the Efficiency of Its Formation by Semiconductor Photocatalysis. *J. Phys. Chem.* **1982**, *86*, 2617–2619.

(23) Berger, T.; Anta, J. A.; Morales-Flórez, V. Electrons in the Band Gap: Spectroscopic Characterization of Anatase TiO<sub>2</sub> Nanocrystal Electrodes under Fermi Level Control. *J. Phys. Chem. C* **2012**, *116*, 11444–11455.

(24) Edwards, M. O. M.; Gruszecki, T.; Pettersson, H.; Thuraisingham, G.; Hagfeldt, A. A Semi-Empirical Model for the Charging and Discharging of Electric-Paint Displays. *Electrochem. Commun.* **2002**, *4*, 963–967.

(25) Lyon, L. A.; Hupp, J. T. Energetics of Semiconductor Electrode/Solution Interfaces: EQCM Evidence for Charge-Compensating Cation Adsorption and Intercalation during Accumulation Layer Formation in the Titanium Dioxide/Acetonitrile System. *J. Phys. Chem.* **1995**, *99*, 15718–15720.

(26) Moser, J.; Grätzel, M. Light-Induced Electron Transfer in Colloidal Semiconductor Dispersions: Single vs. Dielectronic Reduction of Acceptors by Conduction-Band Electrons. *J. Am. Chem. Soc.* **1983**, *105*, 6547–6555.

- (27) Bisquert, J.; Fabregat-Santiago, F.; Mora-Seró, I.; Garcia-Belmonte, G.; Barea, E. M.; Palomares, E. A Review of Recent Results on Electrochemical Determination of the Density of Electronic States of Nanostructured Metal-Oxide Semiconductors and Organic Hole Conductors. *Inorg. Chim. Acta* **2008**, *361*, 684–698.
- (28) Chidsey, C. E. D.; Murray, R. W. Redox Capacity and Direct Current Electron Conductivity in Electroactive Materials. *J. Phys. Chem.* **1986**, *90*, 1479–1484.
- (29) Ardo, S.; Sun, Y.; Staniszewski, A.; Castellano, F. N.; Meyer, G. J. Stark Effects after Excited-State Interfacial Electron Transfer at Sensitized TiO<sub>2</sub> Nanocrystallites. *J. Am. Chem. Soc.* **2010**, *132*, 6696–6709.
- (30) Cappel, U. B.; Feldt, S. M.; Schöneboom, J.; Hagfeldt, A.; Boschloo, G. The Influence of Local Electric Fields on Photoinduced Absorption in Dye-Sensitized Solar Cells. *J. Am. Chem. Soc.* **2010**, *132*, 9096–9101.
- (31) Ohko, Y.; Tatsuma, T.; Fujii, T.; Naoi, K.; Niwa, C.; Kubota, Y.; Fujishima, A. Multicolour Photochromism of TiO<sub>2</sub> Films Loaded with Silver Nanoparticles. *Nat. Mater.* **2003**, *2*, 29–31.
- (32) Duonghong, D.; Ramsden, J.; Grätzel, M. Dynamics of Interfacial Electron-Transfer Processes in Colloidal Semiconductor Systems. *J. Am. Chem. Soc.* **1982**, *104*, 2977–2985.
- (33) Frank, S. N.; Bard, A. J. Semiconductor Electrodes. II. Electrochemistry at n-Type Titanium Dioxide Electrodes in Acetonitrile Solutions. *J. Am. Chem. Soc.* **1975**, *97*, 7427–7433.

## CHAPTER 6: PHANTOM ELECTRONS IN MESOPOROUS NANOCRYSTALLINE SnO<sub>2</sub> THIN FILMS WITH CATION DEPENDENT REDUCTION ONSETS

### 6.1 Introduction

Mesoporous thin films composed of wide band-gap semiconducting metal oxide nanocrystallites have been the focus of intense study due to their applications in solar energy conversion,<sup>1</sup> photocatalysis,<sup>2</sup> photochromics,<sup>3</sup> and lithium-ion batteries.<sup>4,5</sup> Dye-sensitized solar cells (DSSCs) utilize metal oxide semiconductors as an electron acceptor and transport material that facilitates charge separation and collection remarkably well. Photons are absorbed by surface anchored chromophores that then undergo excited-state electron transfer, termed ‘injection,’ into the oxide material. Ideally, the injected electrons are transported through the thin film to a conductive back contact where they are collected in an external cell. The efficiency of electron injection has been predicted,<sup>6</sup> and experimentally observed,<sup>7–10</sup> to be related to the energetic overlap between the semiconductor acceptor states and the donor states of the excited chromophore. The ‘acceptor states’ of the metal oxide nanocrystallites are often idealized as conduction band states. Therefore, knowledge about the energetic position and density of states is crucial for the strategic design of DSSCs.

---

\*This chapter previously appeared as an article in Chemistry of Materials. \*Reprinted (adapted) with permission from (Barr, T. J.; Sampaio, R. N.; DiMarco, B. N.; James, E. M.; Meyer, G. J. Phantom Electrons in Mesoporous Nanocrystalline SnO<sub>2</sub> Thin Films with Cation-Dependent Reduction Onsets. *Chem. Mater.* **2017**, 29, 3919–3927.). Copyright (2016) American Chemical Society.

The most widely used metal oxide for DSSCs has been TiO<sub>2</sub>, largely due to the favorable band-edge position and ability to transport injected electrons micrometer distances without significant loss. However, SnO<sub>2</sub> has considerable promise as a replacement for TiO<sub>2</sub> due to a ~100 times larger electron diffusion coefficient<sup>11,12</sup> and a ~0.5 V more positive conduction band position.<sup>13,14</sup> These two properties would, in theory, allow for more efficient electron collection with near-IR absorbing chromophores that are weak photoreductants.

The ‘acceptor states’ in these nanocrystalline thin films is often experimentally modelled as an exponential distribution of localized acceptor states, sometimes referred to as ‘trap’ states. Due to the large surface area and number of grain boundaries in these polycrystalline thin films, the presence of multiple types of electronic states, i.e. trapped states vs conduction band states, is often discussed.<sup>15,16</sup> A significant reduction in charge recombination has been observed after just a single atomic layer deposition of TiO<sub>2</sub> onto SnO<sub>2</sub> nanoparticles that was attributed to surface state passivation.<sup>17,18</sup> Additional evidence for electron trapping in SnO<sub>2</sub> thin films has been obtained by terahertz spectroscopy.<sup>19</sup> While models often require, and common sense suggests, that both conduction band and localized ‘trap’ states should be present, little spectroscopic evidence for multiple electronic states exists, particularly for TiO<sub>2</sub> thin films in acetonitrile electrolytes at applied potentials relevant to DSSCs. In TiO<sub>2</sub> thin films, population of these acceptor states results in a broad optical absorption band across the visible into the near-IR region.<sup>20,21,22</sup> This absorption has been shown to be linearly related to the total charge within the thin film, in accordance with Beer’s Law, and has led to the wide use of this absorption signature as a direct measurement of their occupancy.<sup>23,24</sup> Although the UV/Vis absorbance of SnO<sub>2</sub> thin films under forward

bias conditions displays similar spectral signatures,<sup>25</sup> detailed studies reported herein show that the direct relationship between absorbance and charge is not present.

The band-edge position of semiconductor materials in photoelectrochemical cells is known to be intimately related to the composition of the electrolyte. For example, solution pH influences the flat-band potentials of metal-oxide semiconductors in a Nernstian manner through surface hydroxyl protonation/deprotonation acid-base chemistry.<sup>13,26</sup> Such behavior has also been reported for nanocrystalline TiO<sub>2</sub> and SnO<sub>2</sub> thin films.<sup>20,27</sup> More recently, it has become evident that the electrolyte cation influences the position of TiO<sub>2</sub> acceptor states to a degree that roughly correlates with the cation's Lewis acidity in the organic nitrile solvents commonly used in DSSCs.<sup>24,28</sup> The generality of this behavior in other metal oxides, such as the SnO<sub>2</sub> thin films reported here, is unknown.

Here, we report electrochemical and spectroelectrochemical studies of nanocrystalline SnO<sub>2</sub> thin films in acetonitrile electrolytes and compare the results to the well-known TiO<sub>2</sub> thin films commonly used in DSSCs. Reduction of the SnO<sub>2</sub> thin films resulted in absorption spectra that were potential-dependent over an applied potential window where only one state was observed for TiO<sub>2</sub>. At low applied potentials, the majority of electrons in SnO<sub>2</sub> appeared to reside in optically-inactive states, termed 'phantom electrons,' that may account for the reported examples of 'trap states' in SnO<sub>2</sub> thin films. More negative applied potentials results in spectra for SnO<sub>2</sub> and TiO<sub>2</sub> thin films that were very similar. These spectroscopic features were found to be reversible when the applied potential was stepped back to positive values. At applied potentials more negative than -1.3 V vs Fc<sup>+</sup>/Fc, a new absorption appeared in the ultraviolet region for SnO<sub>2</sub> thin films that was not completely reversible. The importance of this redox chemistry to applications in solar energy conversion are discussed.

## 6.2 Experimental

**Materials:** The following reagents were used as received: lithium perchlorate ( $\text{LiClO}_4$ ; Sigma-Aldrich, 99.99%); sodium perchlorate ( $\text{NaClO}_4$ ; Sigma-Aldrich,  $\geq 98.0\%$ ); magnesium perchlorate ( $\text{Mg}(\text{ClO}_2)_2$ ; Sigma-Aldrich, ACS reagent); calcium perchlorate tetrahydrate ( $\text{Ca}(\text{ClO}_4)_2 \cdot 4\text{H}_2\text{O}$ ; Sigma-Aldrich,  $\geq 99\%$ ) tetrabutylammonium perchlorate ( $\text{TBAClO}_4$ ; Sigma-Aldrich,  $\geq 99.0\%$ );  $\text{SnO}_2$  nanoparticles (15% w/v, 15 nm diameter, Alfa-Aesar), argon gas (Airgas,  $>99.998\%$ ); oxygen gas (Airgas, industrial grade); titanium(IV) isopropoxide (Sigma-Aldrich, 97%); fluorine-doped tin oxide-coated glass (FTO; Hartford Glass Co., Inc., 2.3 mm thick,  $15 \Omega/\square$ ); acetonitrile (ACN, Fluka, 99.9%); glacial acetic acid ( $\text{C}_2\text{H}_4\text{O}_2$ ; Fisher, 99.7%); polyethylene glycol ( $\text{H}(\text{OCH}_2\text{CH}_2)_n\text{OH}$ , Alfa Aesar, MW = 12,000) ; polyethylene oxide ( $-\text{CH}_2\text{CH}_2\text{O}$ ) $_n$ , Alfa Aesar, MW = 100,000).

**$\text{SnO}_2$  and  $\text{TiO}_2$  Thin Film Preparation:**  $\text{SnO}_2$  nanoparticles were synthesized according to a previously described method.<sup>27,29</sup> Briefly, 0.5 mL of glacial acetic acid was added dropwise to 15 mL of rapidly stirring colloidal suspension of  $\text{SnO}_2$  nanoparticles, which was allowed to stir for approximately 12 hours. The resulting solution was transferred to a hydrothermal digestion vessel and heated at  $450^\circ\text{C}$  for 60 hours. The resulting mixture was sonicated for 10 minutes and then polyethylene glycol and polyethylene oxide polymers (12,000 and 100,000 Da) were each added to 2.5 wt%. Synthesis of  $\text{TiO}_2$  nanoparticles of approximately 15 nm diameter was carried out by the acid hydrolysis of titanium(IV) isopropoxide as previously described.<sup>30</sup> Thin films of  $\text{SnO}_2$  and  $\text{TiO}_2$  nanoparticles of 3-5  $\mu\text{m}$  were prepared by doctor blading the colloidal solution onto transparent FTO using Scotch tape ( $\sim 35 \mu\text{m}$ ) as the spacer, followed by sintering at  $450^\circ\text{C}$  for 30 minutes under oxygen flow. Thin films were either used immediately or stored in an oven at  $\sim 80^\circ\text{C}$  until use. The geometric area and

height of samples was measured using a profilometer (Bruker DektakXT Profilometer). Film porosity was estimated comparing the mass of the thin film removed from the FTO surface to the predicted mass based on the estimated volume of the film.

**Electrochemistry:** Spectroelectrochemistry was performed on SnO<sub>2</sub> and TiO<sub>2</sub> thin films immersed in Ar-saturated CH<sub>3</sub>CN in a standard 3 electrode configuration using the metal-oxide thin film as the working electrode and a platinum gauze counter electrode. Potentials were applied by a BASi CV50W potentiostat referenced to a non-aqueous Ag/AgCl pseudo-reference electrode calibrated to the ferrocinium/ferrocene half wave potential taken to be +630 mV vs NHE.<sup>31</sup> While under applied bias, UV/Vis absorption spectra of the thin films were measured by a Cary 50 UV/Vis spectrophotometer. Equilibrium spectra were taken when the spectra no longer changed with time, which typically took 2 minutes.

Charge extraction measurements were performed in a standard 3 electrode setup with the metal-oxide thin film as the working electrode, a platinum gauze counter electrode, and a non-aqueous pseudo-reference electrode in Ar-saturated CH<sub>3</sub>CN as described above. Spectra were monitored by an Avantes AvaLight DHc light source coupled to an Avantes StarLine AvaSpec-2048 UV/Visible spectrometer while potentials were applied by a Pine Research Instrumentation (PRI) Wavenow Potentiostat controlled by Aftermath software (PRI). Current transients monitored during potential steps were integrated to give the total charge as a function of time.

Cyclic voltammograms were taken on a PRI Wavenow Potentiostat in a standard 3 electrode setup with the metal-oxide thin film as the working electrode, a platinum gauze counter electrode, and a non-aqueous reference electrode described above immersed in Ar-saturated CH<sub>3</sub>CN at a scan rate of 20 mV/s.

### 6.3 Results

The absorption spectra of TiO<sub>2</sub> thin films immersed in 100 mM Li<sup>+</sup>, Na<sup>+</sup>, Mg<sup>2+</sup>, Ca<sup>2+</sup>, and TBA<sup>+</sup> (where TBA<sup>+</sup> is tetrabutylammonium) perchlorate acetonitrile electrolyte were monitored at increasingly negative applied biases. Representative difference spectra in 100 mM LiClO<sub>4</sub> acetonitrile electrolyte are shown in Figure 6.01A. The data were in good agreement with previous studies<sup>22</sup> that reported normalizable spectral changes for TiO<sub>2</sub> reduction under moderate applied potentials. We note that at much more negative applied potentials the absorption spectra of the Li<sup>+</sup> intercalated TiO<sub>2</sub>, Li<sub>0.5</sub>TiO<sub>2</sub>, was observed but was not a focus of this study.<sup>32,33</sup> For TiO<sub>2</sub>, an exponential function was used in the potential associated spectra (PAS) analysis (see discussion for details) because it is well known that the TiO<sub>2</sub> acceptor states show an exponential dependence on applied potential, Equation 6.01:

$$\Delta Abs(E, \lambda) = a(\lambda)e^{-b E} \quad 6.01$$

where *b* was an adjustable parameter held constant for a given electrolyte and the wavelength-dependent amplitude, *a*(*λ*), was varied to fit the data as a function of potential, *E*. The calculated PAS here was in good agreement with the normalized spectral changes on TiO<sub>2</sub> as seen in Figure 6.01B.

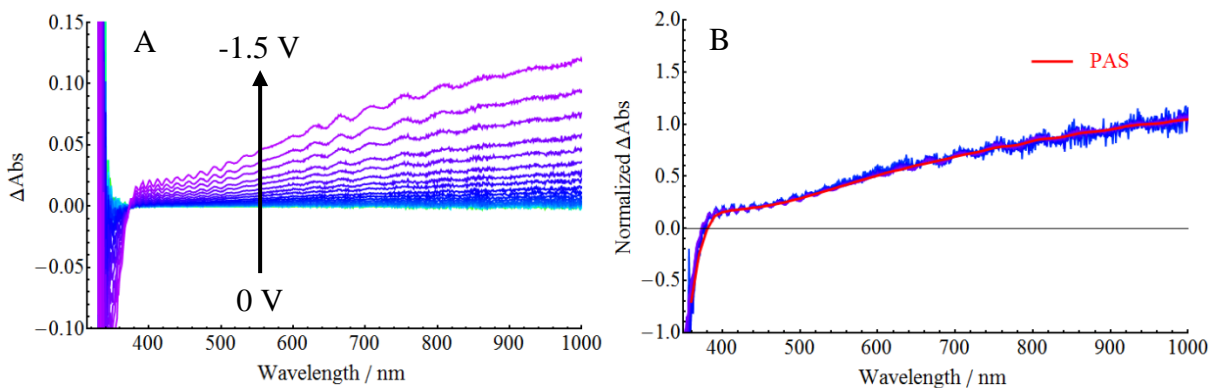


Figure 6.01. A) Raw and B) normalized absorption difference spectra of mesoporous, nanocrystalline  $\text{TiO}_2$  thin film in 100 mM  $\text{LiClO}_4$  acetonitrile electrolyte at increasingly negative applied potentials ranging from 0 V to -1.5 V vs  $\text{Fc}^+/\text{Fc}$ . Overlaid on the normalized spectra in B is the calculated PAS (black).

UV/Vis absorption difference spectra taken at increasingly negative applied potentials for a  $\text{SnO}_2$  thin film in 100 mM  $\text{Ca}(\text{ClO}_4)_2$  acetonitrile solution are shown in Figure 6.02A. The normalized difference spectra were non-superimposable, Figure 6.02B, and displayed three distinct features: (1) a broad absorbance across the visible region attributed to electrons in the  $\text{SnO}_2$  nanocrystallites ( $\text{SnO}_2(e^-)$ s), (2) a loss of absorbance at wavelengths less than 350 nm consistent with a hypsochromic (blue) shift of the fundamental (valance band to conduction band) absorption, and (3) an irreversible absorption peak at  $< 400$  nm that shifted towards shorter wavelengths at increasingly negative biases. Spectra measured in 100 mM  $\text{Li}^+$ ,  $\text{Na}^+$ ,  $\text{Mg}^{2+}$ , and  $\text{TBA}^+$  perchlorate acetonitrile electrolytes were insensitive to the identity of the cation, but the potential onset at which these spectra appeared was cation dependent.

The UV/Vis absorption spectra were deconvoluted using the PAS method into three distinct spectra, shown in Figure 6.02C. Because the absorption spectra were non-

normalizable, additional functions were required to fit the single-wavelength absorbance at each applied potential, Equation 6.02:

$$\Delta Abs(E, \lambda) = \frac{a_1(\lambda)}{1 + 10^{\left(\frac{E_1 - E}{\alpha_1 59.2 \text{ mV}}\right)}} + \frac{a_2(\lambda)}{1 + 10^{\left(\frac{E_2 - E}{\alpha_2 59.2 \text{ mV}}\right)}} + a_3(\lambda)e^{-bE} \quad 6.02$$

where  $E_1$ ,  $E_2$ ,  $\alpha_1$ ,  $\alpha_2$ , and  $b$  were adjustable parameters held constant in a given cation and  $a_1(\lambda)$ ,  $a_2(\lambda)$ , and  $a_3(\lambda)$  were varied to fit the data as a function of potential,  $E$ , and wavelength,  $\lambda$ . The additional sigmoidal functions chosen had previously been used to model localized redox transitions,<sup>34,35</sup> however their success in the modelling does not necessarily indicate that a localized redox state is present. The UV/Vis absorbance changes in all electrolytes could be accurately reconstructed from the three PAS shown.

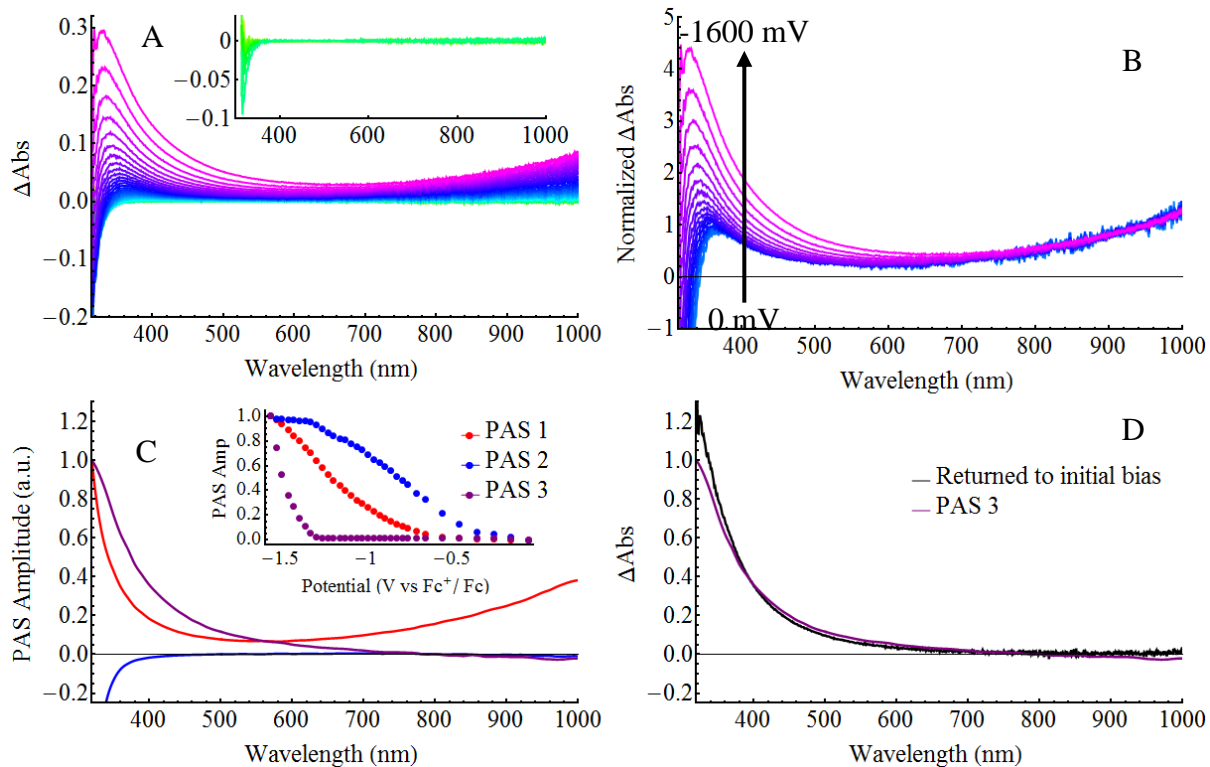


Figure 6.02. A) Raw and B) normalized absorption difference spectra of mesoporous, nanocrystalline  $\text{SnO}_2$  thin film in 100 mM  $\text{Ca}(\text{ClO}_4)_2$  acetonitrile electrolyte at increasingly negative applied potentials ranging from 0 to -1.5 V vs  $\text{Fc}^+/\text{Fc}$ . The inset in A) shows the raw difference spectra from 0 to -700 mV. C) PAS deconvolution of A). D) UV/Vis difference spectra of A) after returning to the initial potential overlaid with PAS 3.

Indeed, the three PAS correlate well with the spectroelectrochemical data: PAS 1 accounts for the long-wavelength absorption, PAS 2 for the blue-shift of the fundamental absorption, and PAS 3 is a growth along the fundamental absorption. Interestingly, the blue-shift of the fundamental absorption (PAS 2) occurred prior to significant growth at long wavelengths (PAS 1). Additionally, what appeared as a peak near 360 nm in the raw data was revealed to be the superposition of a bleach of the fundamental absorption (PAS 2) and a growth in a similar spectral region (PAS 3). Comparing PAS 3 (the growth) to the spectrum

of SnO<sub>2</sub> after returning to positive potentials, seen in Figure 6.02D, gives credence to its shape and the assertion that while a peak in the raw data was observed, there exists no distinct species that has a peak in this spectral region.

Single wavelength absorption changes monitored at 950 nm for TiO<sub>2</sub> and SnO<sub>2</sub> thin films immersed in 100 mM Li<sup>+</sup>, Na<sup>+</sup>, Mg<sup>2+</sup>, Ca<sup>2+</sup>, and TBA<sup>+</sup> perchlorate electrolytes as a function of applied potential are shown in Figure 6.03. This wavelength was chosen because only one PAS for each metal oxide contributed to this absorption with an extinction coefficient that was very similar for the two metal oxide materials, *vide infra*. The potential onset at which an absorbance change was first quantified are listed in Table 6.1. These values were estimated by a linear extrapolation of absorption vs. applied potential plots to zero absorbance change; this estimation gave potentials similar to that when the absorption intensity had a signal-to-noise ratio greater than 3. Absorbance features were observed at potentials  $300 \pm 100$  mV more positive for SnO<sub>2</sub> thin films compared to TiO<sub>2</sub> thin films when the electrolyte cation was the same. Additionally, both semiconductors were sensitive to the nature of the electrolyte cation, where the onset potential of absorbance changes followed  $TBA^+ < Na^+ < Li^+ < Mg^{2+} \approx Ca^{2+}$ .

At potentials where the reduced oxide thin films were colored, the absorptivity of the TiO<sub>2</sub> thin films was much more sensitive to the applied potential than were the SnO<sub>2</sub> thin films. For example, in Li<sup>+</sup> containing electrolytes a potential step of ~1 V was needed to increase the absorbance by ~0.05 for SnO<sub>2</sub> thin films, but a comparable absorption was observed for TiO<sub>2</sub> with only ~450 mV potential change. The thin films were measured to be between 3-4 μm thick by profilometry and in all cases, the SnO<sub>2</sub> thin film was as thick or thicker than the comparable TiO<sub>2</sub> film. Porosity estimates were calculated by comparing the

mass of the metal oxide thin films mechanically removed from the FTO substrate to the expected mass based on the measured volume and reported density. For anatase  $\text{TiO}_2$ , this value was taken as  $3.9 \text{ g/cm}^3$ , and  $\text{SnO}_2$  was taken as  $6.85 \text{ g/cm}^3$ .<sup>36</sup> The results indicate that the thin films have similar porosities,  $68 \pm 3 \%$ .

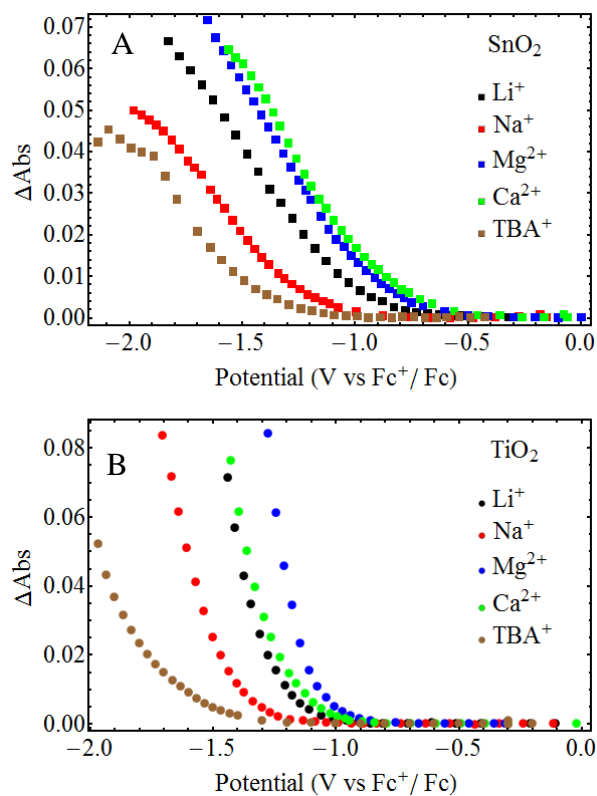


Figure 6.03. Absorbance changes monitored at 950 nm for  $\text{SnO}_2$  (A) and  $\text{TiO}_2$  (B) thin films in 100 mM  $\text{Li}^+$  (black),  $\text{Na}^+$  (red),  $\text{Mg}^{2+}$  (blue),  $\text{Ca}^{2+}$  (green), and  $\text{TBA}^+$  (brown) perchlorate acetonitrile electrolyte solutions at the indicated potentials.

Table 6.1. Absorbance onset potentials for SnO<sub>2</sub> and TiO<sub>2</sub> thin films in the indicated 100 mM M<sup>n+</sup>(ClO<sub>4</sub><sup>-</sup>)<sub>n</sub> acetonitrile electrolytes.

Substrate	Absorbance Onset Potential (mV vs Fc <sup>+</sup> /Fc)				
	Li <sup>+</sup>	Na <sup>+</sup>	Mg <sup>2+</sup>	Ca <sup>2+</sup>	TBA <sup>+</sup>
SnO <sub>2</sub>	-700	-950	-650	-500	-1100
TiO <sub>2</sub>	-900	-1100	-850	-900	-1300

Spectroelectrochemical charge extraction was performed to correlate the charge density within the film to the absorbance magnitude in 0.1 M LiClO<sub>4</sub>/CH<sub>3</sub>CN. This method has been successfully used to determine the extinction coefficient of TiO<sub>2</sub> electrons in the past,<sup>23,24</sup> and the results are comparable to other methods, such as redox titrations<sup>37</sup> or cyclic voltammetry.<sup>38</sup> Experiments performed on TiO<sub>2</sub> thin films resulted in a linear relationship between charge extracted and the absorbance with an intercept at the origin (x-intercept 0.01 ± 0.01 C cm<sup>-2</sup>), shown in Figure 6.04A. The data were well-fit by a modified Beer-Lambert Law given in Equation 6.03 (derived in the Appendix):

$$\Delta Abs = \frac{1000\varepsilon}{F \sin\theta} \left( \frac{C}{A} \right) \quad 6.03$$

where  $\varepsilon$  is the molar (decadic) extinction coefficient, F is Faraday's constant,  $\theta$  is the angle of the thin film relative to the beam path (45°), C is the charge extracted in Coulombs, A is the film area in cm<sup>2</sup>, and 1000 is a conversion factor between L and cm<sup>3</sup>. An extinction coefficient for TiO<sub>2</sub>(e<sup>-</sup>)s of 970 M<sup>-1</sup>cm<sup>-1</sup> at 700 nm and 1200 M<sup>-1</sup>cm<sup>-1</sup> at 900 nm is abstracted from the slope, in good agreement with previous studies.<sup>24</sup>

When the same procedure was performed with SnO<sub>2</sub> electrodes, significant deviation from linearity was observed in plots of absorbance versus charge density. This indicated that

the absorbance did not follow Beer's Law, Figure 6.04B. Instead, an offset from the origin was observed where significant charge was extracted with a much smaller color change than that measured at more negative applied potentials where Beer's Law did appear to hold. A linear fit of the charge abstracted at more negative potentials provided an  $\text{SnO}_2(e^-)$  extinction coefficient of  $910 \text{ M}^{-1}\text{cm}^{-1}$  at 900 nm and a large x-intercept of  $0.69 \pm 0.08 \text{ C cm}^{-2}$ .

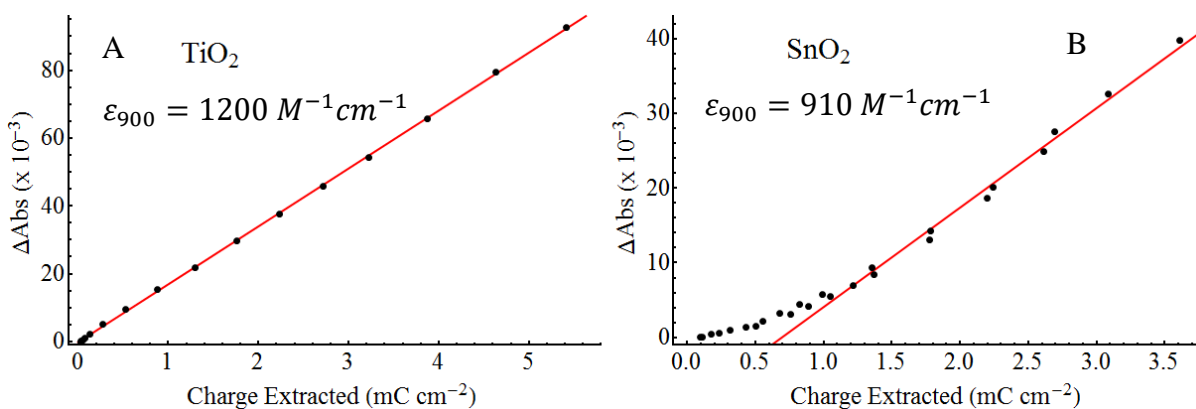


Figure 6.04. Absorbance change at 900 nm during spectroelectrochemical charge extraction of  $\text{TiO}_2$  (A) and  $\text{SnO}_2$  (B) thin films immersed in 100 mM  $\text{LiClO}_4$  acetonitrile electrolyte solutions. Charge extracted was normalized by the geometric area of the thin film. Overlaid in red are linear fits to Equation 6.03.

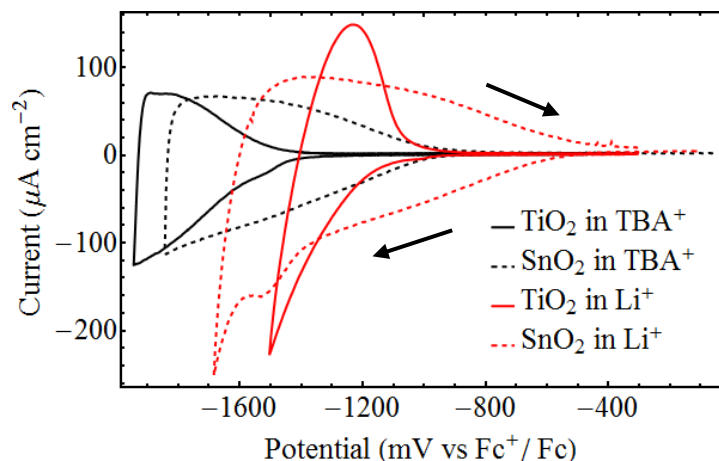


Figure 6.05. Cyclic voltammograms of SnO<sub>2</sub> (dashed) and TiO<sub>2</sub> (solid) thin films in 100 mM LiClO<sub>4</sub> (red) and TBAClO<sub>4</sub> (black) acetonitrile electrolyte solutions at a scan rate of 20 mV/s. Currents were normalized by the geometric area of the thin film.

Cyclic voltammograms of SnO<sub>2</sub> and TiO<sub>2</sub> thin films in Li<sup>+</sup> and TBA<sup>+</sup> containing electrolytes are shown in Figure 6.05. Current onset potentials (COPs) given in Table 6.2 show that both SnO<sub>2</sub> and TiO<sub>2</sub> thin films were sensitive to the the electrolyte cation. The COPs were calculated as the intersection between a linear fit to the baseline (non-Faradaic) current and a linear extrapolation of the Faradaic onset. The COPs in Li<sup>+</sup> electrolyte were approximately  $475 \pm 25$  mV more positive than those in TBA<sup>+</sup> containing electrolyte for both TiO<sub>2</sub> and SnO<sub>2</sub> thin films, in agreement with the spectroelectrochemical studies. Additionally, SnO<sub>2</sub> thin films were found to have a  $425 \pm 25$  mV more positive COP than TiO<sub>2</sub> in both electrolytes. Interestingly, an irreversible peak was observed for SnO<sub>2</sub> thin films in Li<sup>+</sup> electrolytes at  $\sim -1500$  mV vs Fc<sup>+</sup>/Fc. This potential coincided with the irreversible features observed in spectroelectrochemical experiments and further supports the belief that irreversible chemical changes occur at sufficiently negative applied biases.

Table 6.2. Current onset potentials measured by cyclic voltammetry in the indicated 100 mM  $M^+(\text{ClO}_4^-)$  acetonitrile electrolytes.

<i>Substrate</i>	<i>Current Onset Potential</i> ( <i>mV vs Fc<sup>+</sup>/Fc</i> )	
	<i>Li<sup>+</sup></i>	<i>TBA<sup>+</sup></i>
<i>SnO<sub>2</sub></i>	-500	-950
<i>TiO<sub>2</sub></i>	-900	-1400

#### 6.4 Discussion

In this study, the energetic position and distribution of the acceptor states in mesoporous, thin films comprised of  $\text{SnO}_2$  nanocrystallites was investigated by spectroscopic and electrochemical techniques and compared to the more well studied thin films comprised of anatase  $\text{TiO}_2$  nanocrystallites. Comparative studies between mesoporous metal oxide thin films are complicated by the fact that it is experimentally difficult to change only the identity of the metal oxide without also influencing other parameters. It is therefore useful to briefly state the physical characteristics of the  $\text{SnO}_2$  and  $\text{TiO}_2$  films used in this study. In both materials, nanocrystallites of  $\sim 15$  nm in diameter composed of metal ions coordinated to six oxygen ions in a pseudo-octahedral arrangement were used. The  $\text{SnO}_2$  was present as rutile nanocrystallites while the  $\text{TiO}_2$  were in the anatase polymorph. Mesoporous thin films were cast of each metal oxide measuring 3-4  $\mu\text{m}$  in thickness and porosities of  $\sim 65\%$ . Therefore, direct comparisons of absorption and currents are reasonable without consideration of the film thickness or morphology.

A key result was that over the potential window of -200 to -1800 mV vs  $\text{Fc}^+/\text{Fc}$ , three unique spectra were observed for  $\text{SnO}_2$  reduction, while only one was observed for  $\text{TiO}_2$ .

The most easily reduced states in SnO<sub>2</sub> induced a small blue-shift in the fundamental absorption, but did not absorb light appreciably in the visible region and were hence termed ‘phantom electrons.’ More negative applied potentials yielded SnO<sub>2</sub> electrons that had absorption features remarkably similar to that observed for TiO<sub>2</sub>. At potentials more negative than about -1.3 V vs Fc<sup>+</sup>/Fc, a new absorption spectrum was identified that led to irreversible chemistry and was not examined in detail.

A new method was developed to quantify the potential dependence of the spectral features when the underlying spectra were unknown. This method, termed ‘potential associated spectra’ (PAS), was closely related to the ‘decay associated spectra’ (DAS) deconvolution method previously used to deconvolute photoluminescence spectra.<sup>39,40</sup> Both methods utilize simultaneous analysis of multiple data sets with parameters held constant that can experimentally be overdetermined. The analysis provides spectra that can be compared to experimental values to test specific models. For TiO<sub>2</sub> reduction, only a single state was observed that displayed an exponential dependence on the applied potential. For SnO<sub>2</sub>, three different spectra were observed and the PAS analysis provided their amplitude at each applied potential. Although individual PAS may correspond to a single chemical species, this need not be the case. The PAS method cannot differentiate between correlated spectral changes and instead demonstrates that a global analysis of all the spectral data reveals that it is well described by three underlying absorption spectra.

We note that two distinct processes have been suggested to counterbalance charge during the electrochemical reduction of metal oxides: cation adsorption and cation intercalation. It is often difficult experimentally to differentiate between these two processes. However, for anatase TiO<sub>2</sub> thin films in Li<sup>+</sup> containing CH<sub>3</sub>CN electrolyte, two unique

UV/Vis spectra have been identified.<sup>33,41,32,42</sup> One spectrum corresponds to the Li<sup>+</sup> intercalated material which shows a maximum absorbance in the visible region that was not observed herein. The other spectrum shows no measurable sensitivity to the nature of the cations present in the electrolyte like that reported herein. This characteristic spectra shows no clear maximum and has been assigned to the absorption by electrons in the metal oxide similar to Drude absorption that displays a monotonic increase into the near IR region. Such spectra are also observed in electrolytes that contain the non-intercalating tetrabutylammonium cation<sup>43</sup> and have been reported for reduced WO<sub>3</sub> and ZnO thin films.<sup>25,44,45</sup> Therefore, we tentatively assign the monotonically increasing absorption in these SnO<sub>2</sub> thin films under forward bias to the SnO<sub>2</sub>(e<sup>-</sup>)s yet acknowledge that some cation intercalation that does not alter this spectrum may be occurring.

**Evidence for phantom electrons:** The spectroscopic and electrochemical behavior of the mesoporous TiO<sub>2</sub> and SnO<sub>2</sub> thin films were quantitatively different. Reduction of the TiO<sub>2</sub> thin films in a standard 3-electrode configuration resulted in a broad absorbance increase across the visible region and into the near-IR with a blue-shift of the fundamental absorption. These absorbance features were normalizable over a wide range of applied potentials as has been reported previously.<sup>22</sup> The long-wavelength absorption has been attributed to the presence of electrons within the TiO<sub>2</sub> thin film.<sup>20</sup> Likewise, the blue-shift of the fundamental absorption signals an increase in the apparent band-gap that has been rationalized by the filling of acceptor states, i.e. a Burstin-Moss shift,<sup>46,47</sup> or an electric field (Stark) effect.<sup>48,49</sup>

Spectroelectrochemical reduction of SnO<sub>2</sub> thin films resulted three distinct spectra: 1) a broad absorbance increase across the visible region, 2) a blue-shift of the fundamental UV absorption, and 3) a potential-dependent peak at wavelengths less than 400 nm. Unlike the

TiO<sub>2</sub> thin films, the absorbance features of SnO<sub>2</sub> thin films measured at different applied potentials were not normalizable. Conventional spectral deconvolution was not possible because the distinct absorbance features were not known. Therefore, the new deconvolution method to identify potential-induced absorbance spectra, termed potential associated spectra (PAS) was developed as described above.

Applying the PAS method to SnO<sub>2</sub> thin films under forward bias resulted in three spectra that were consistent with the above observations yet revealed that the potential-dependent peak was in fact a superposition of a blue-shift in the fundamental absorption and a separate, more broad, absorption increase at potentials negative of -1300 mV. For SnO<sub>2</sub> thin films, the fundamental absorption blue-shifted before significant absorption was observed in the visible region, behavior in contrast with TiO<sub>2</sub> thin films where both features appeared concurrently. This observation was most consistent with the presence of electrons in the SnO<sub>2</sub> thin film that did not absorb visible light, but still induced a bleach of the fundamental absorption through either a Burstein-Moss or a Stark shift. Since there was no kinetic data to suggest these states are less mobile than the absorbing states, and hence may or may not be ‘trapped,’ we term them ‘phantom electrons,’ to simply represent electrons that have a negligible extinction coefficient in the visible region.

The presence of multiple types of states within SnO<sub>2</sub> thin films was perhaps most clearly evident in the charge extraction measurements. In these experiments, the charge density in the mesoporous thin films was compared to the color change. Plots of the absorbance at 900 nm as a function of charge density displayed the expected linear response for TiO<sub>2</sub> thin films, but were nonlinear for SnO<sub>2</sub> thin films, particularly at low potentials (-800 mV) where very small absorbances were observed yet significant charge was extracted.

At potentials between -1000 mV and -1300 mV, corresponding to charge densities of 1-3.5 mC cm<sup>-2</sup>, the data became linear and an extinction coefficient of 910 M<sup>-1</sup>cm<sup>-1</sup> at 900 nm was abstracted from the slope. If it is assumed that only one type of state was responsible for this absorption as the PAS suggests, then at early potentials approximately 80% of the measured charge exists as phantom electrons. This value decreases to approximately 20% at -1100 mV at which point all remaining charge appears to occupy light-absorbing states. Under normal operating conditions, we estimate that 20-50 % of the charge within the thin film resides as 'phantom electrons.' At potentials negative of -1300 mV (charge density greater than 3.5 mC cm<sup>-2</sup>, not shown), deviations from linearity were again observed due to irreversible chemistry changes that occurred under these more highly reducing conditions. The details of the irreversible chemistry remain unknown, however theoretical calculations suggest that formation of partially reduced SnO<sub>2</sub> (SnO<sub>x</sub>, where x<2) results in a material with a lower bandgap. Extrapolation of the high-energy portion of PAS 3 resulted in an estimated bandgap of 2.8 eV, corresponding to Sn<sub>2</sub>O<sub>3</sub> or Sn<sub>3</sub>O<sub>4</sub>.<sup>50</sup>

Comparison of the absorbance (Table 6.1) and current (Table 6.2) onset potentials also support the existence of phantom electrons in SnO<sub>2</sub> thin films. A current response was observed at potentials 200 mV more positive than the absorbance onset in Li<sup>+</sup> containing electrolytes. Of note, this discrepancy between current and absorbance onset potentials was not observed in TiO<sub>2</sub>. Furthermore, if the current onset potential measured by cyclic voltammetry corresponded to the SnO<sub>2</sub> acceptor states, then one would conclude SnO<sub>2</sub> has a 425 mV more positive acceptor state distribution than TiO<sub>2</sub>, in good agreement with many literature reports of a more positive conduction band edge for SnO<sub>2</sub>.<sup>25,51</sup>

We note that spectroscopic evidence for more than one type of  $\text{TiO}_2(e^-)$  has been reported in aqueous electrolyte.<sup>52</sup> Boschloo and Fitzmaurice observed a very weak absorbance centered at 400 nm that appeared at more positive potentials than did the characteristic spectrum that is also reported here. This absorption feature was attributed to surface trapped electronic states.<sup>16</sup> Curiously these states are not observed in  $\text{CH}_3\text{CN}$  electrolytes.

Similar spectroelectrochemical studies on highly doped nanostructured  $\text{SnO}_2:\text{Sb}$  have been performed where no evidence for phantom electrons was reported.<sup>53</sup> The  $\text{SnO}_2:\text{Sb}$  bandgap is only 2.8 eV, compared to 3.6 eV for un-doped  $\text{SnO}_2$ . Antimony, as an n-type dopant, would be expected to introduce states below the conduction band. Therefore, if any 'phantom electron' states were present in their material, they would likely overlap with the phantom states and this could obscure their detection. In addition, the extinction coefficient calculated for the  $\text{SnO}_2:\text{Sb}$  material ( $2400 \text{ M}^{-1}\text{cm}^{-1}$  at 700 nm) are a factor of 4-5 times higher than that measured here, suggesting phantom electrons were not present at all with these highly doped materials.

The lack of a significant color change upon moderate reduction is important for applications of these materials as transparent conductive oxide electrodes. Wide bandgap semiconductors, such as  $\text{SnO}_2$ , are known to behave as conductive oxides following electron injection. Indeed, Bard has shown that under such forward bias conditions, rutile  $\text{TiO}_2$  single crystals behave much like a Pt electrode in cyclic voltammetry experiments.<sup>14</sup> Generally, in all transparent conductive oxide (TCO) materials, a trade-off exists between conductivity and transparency in the visible region. Highly conductive TCOs have lower transmission efficiencies than do less conductive materials. If these 'phantom electrons' do in fact

promote conductivity, the results indicate that doping can be achieved without significant color change.

**Cation effects on energetic distribution of acceptor states:** Spectroelectrochemistry has been utilized previously to quantify the energetic position and density of acceptor states in TiO<sub>2</sub> thin films and a similar approach was utilized herein for SnO<sub>2</sub> thin films.<sup>43,21</sup> For TiO<sub>2</sub> thin films, the measured absorbance change was directly related to the charge within the thin film through Beer's Law, allowing the chemical capacitance to be readily calculated. This process was complicated in SnO<sub>2</sub> thin films by the presence of phantom electrons that caused deviations from Beer's Law. Instead, complete spectral deconvolution was required by the PAS method. This allowed the chemical capacitance of each state to be uniquely estimated from the magnitude of the PAS. For example, the concentration of phantom electrons could be estimated from the magnitude of PAS2. We note that although the presence of phantom electrons was inferred from changes to the fundamental absorption, they do not appreciably absorb light in the 400-1100 nm region. Figure 6.06 compares the electronic distributions for TiO<sub>2</sub> and SnO<sub>2</sub> thin films immersed in all the electrolytes studied.

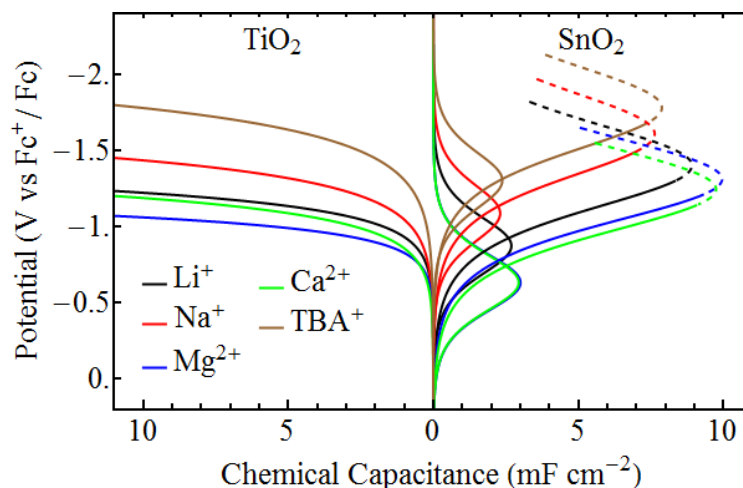


Figure 6.06. A) Chemical capacitance for TiO<sub>2</sub> (left) and SnO<sub>2</sub> (right) thin films in 100 mM metal perchlorate acetonitrile solutions of Li<sup>+</sup> (black), Na<sup>+</sup> (red), Mg<sup>2+</sup> (blue), Ca<sup>2+</sup> (green), and TBA<sup>+</sup> (brown). For SnO<sub>2</sub> thin films, the smaller distributions represent phantom electrons and the larger optically-active electrons.

Figure 6.06 clearly shows the energetic distribution of both SnO<sub>2</sub> and TiO<sub>2</sub> electrons were sensitive to the nature of the electrolyte cation. The distributions follow the trend  $TBA^+ < Na^+ < Li^+ < Mg^{2+} \approx Ca^{2+}$  consistent with the cation size-to-charge ratio and suggests Lewis acidity may be an important determining parameter for how cations affect the electronic distributions of metal oxide semiconductors. While this behavior is well documented for mesoporous TiO<sub>2</sub> thin films,<sup>20,24</sup> to our knowledge this is the first time SnO<sub>2</sub> thin films have been shown to be sensitive to the electrolyte cation.

The phantom electron distribution in SnO<sub>2</sub> thin films was more positive than the non-phantom distribution on an electrochemical scale and did not monotonically increase but rather reached a maximum. The shape of this distribution more closely resembled a localized transition than an extended band, where 95 % of the total phantom distribution resided within 500 mV of the peak. The fact that these states resided at more positive potentials than the

states that absorb visible light suggests that electrons injected through dye-sensitization may relax into them which could complicate kinetic analysis.

Interestingly, the absorbance change as a function of applied bias did not increase exponentially in the SnO<sub>2</sub> thin films but appeared to reach a plateau. Therefore, the chemical capacitance, which is proportional to the derivative of the absorbance change, was non-exponential and displayed a maximum. This maximum chemical capacitance for non-phantom electrons should be viewed with caution as irreversible spectral changes occurred when the charge density in SnO<sub>2</sub> exceeded about 8 mF/cm<sup>2</sup>; subsequent measurements made on films that had stored such high charge resulted in different capacitances.

Larger chemical capacitances were measured for TiO<sub>2</sub> thin films relative to SnO<sub>2</sub>. This may be due to the effective mass,  $m_e$ , of electrons in each semiconductor. In a simplified conduction band model the density of states is proportional to  $m_e^{3/2}$ . A wide range of effective masses for TiO<sub>2</sub> electrons has been reported, most ranging from 1-10, while SnO<sub>2</sub> electrons have an effective mass of 0.2  $m_e$ .<sup>54-58</sup> These values predict that the TiO<sub>2</sub> conduction band will have an 10-350 times greater density of states than does SnO<sub>2</sub> depending on the choice of TiO<sub>2</sub> electron effective mass. The chemical capacitances calculated here support the higher density of states for TiO<sub>2</sub>, but the exact value is difficult to determine experimentally. Since the conduction band position is ill-defined and is certainly not the same for the two metal oxides, a direct comparison at a given potential was not possible. Furthermore, the shape of the electronic distributions were different which prevented a simple offset adjustment. Larger chemical capacitances indicate a higher density of states. Therefore, the change in capacitance for a given potential step was used to estimate the relative density of states for the two thin films. Using this method, the experimentally

determined density of states in SnO<sub>2</sub> is ~2-3 times smaller than in TiO<sub>2</sub>. This suggests that the effective mass of an electron in TiO<sub>2</sub> is closer to 1 m<sub>e</sub>, as measured by Tang et.al.<sup>54</sup>

An alternative, and perhaps more intuitive, explanation for the disparate density of states in these materials is based on their dielectric constants. Anatase TiO<sub>2</sub> has a large dielectric constant reported to be between 30 and 60,<sup>59-61</sup> while SnO<sub>2</sub> has a smaller value of 9-14.<sup>36</sup> Therefore, electrons injected into SnO<sub>2</sub> nanocrystallites are less effectively screened from one another and repel each other more strongly than do electrons in TiO<sub>2</sub>. In other words, there is a larger Coulombic penalty for each additional electron in SnO<sub>2</sub> which decreases the number of states within a given energy range. The ratio of dielectric constants is between 3 and 4 and this value is surprisingly close to the density of states ratio measured near -1.1 V vs Fc<sup>+</sup>/Fc. The data measured for these nanocrystalline thin films is more consistent with localized electronic states instead of a conventional conduction band.

The lower density of SnO<sub>2</sub> states measured herein is consistent with previous observations that excited-state injection into TiO<sub>2</sub> is faster than SnO<sub>2</sub>.<sup>62,63</sup> Such transient data could not be rationalized by the more positive conduction band edge of SnO<sub>2</sub>. Instead, a smaller density of acceptor states provides less overlap with the dye excited states resulting in slower electron injection as predicted by Gerischer theory.<sup>6</sup>

## 6.5 Conclusions

The distribution of acceptor states in nanocrystalline SnO<sub>2</sub> thin films was studied by spectroelectrochemical and electrochemical methods. Simultaneous analysis of potential dependent data resulted in the identification of three unique 'potential associated spectra' for reduced SnO<sub>2</sub> while only one was identified for TiO<sub>2</sub>. Reduction of SnO<sub>2</sub> resulted in the appearance of: 1) a broad absorption that spans across the visible and near IR regions; 2) a

blue-shifted fundamental absorption; and 3) an absorption band in the blue region. The absorption onsets were dependent on the electrolyte cation, present as the perchlorate salt of  $\text{Li}^+$ ,  $\text{Na}^+$ ,  $\text{Mg}^{2+}$ ,  $\text{Ca}^{2+}$  and  $\text{TBA}^+$ . Correlations of the thin film charge with the absorbance intensity revealed that significant charge was transferred to  $\text{SnO}_2$  films without a measureable color change. This suggests presence of electrons within the  $\text{SnO}_2$  thin films that do not absorb visible light and are termed ‘phantom electrons.’ The density of acceptor states in  $\text{SnO}_2$  was found to be significantly lower than that measured for  $\text{TiO}_2$  which represents behavior consistent with previous reports of more rapid excited state injection into  $\text{TiO}_2$ .

### **Author Information**

Corresponding Author

\*Gerald J. Meyer. Email: [gjmeyer@email.unc.edu](mailto:gjmeyer@email.unc.edu). Phone: 919-962-6320.

### **Acknowledgements**

The authors acknowledge support by a grant from the Division of Chemical Sciences, Office of Basic Energy Sciences, Office of Energy Research, U.S. Department of Energy (Grant DE-SC0013461).

### **Supporting Information:**

A modified Beer-Lambert law is derived to correlate the absorbance to charge within the film.

## REFERENCES

- (1) O'Regan, B.; Grätzel, M. A Low-Cost, High-Efficiency Solar Cell Based on Dye-Sensitized Colloidal TiO<sub>2</sub> Films. *Nature* **1991**, *353*, 737–740.
- (2) Frank, S. N.; Bard, A. J. Heterogeneous Photocatalytic Oxidation of Cyanide and Sulfite in Aqueous Solutions at Semiconductor Powders. *J. Phys. Chem.* **1977**, *81*, 1484–1488.
- (3) Ohko, Y.; Tatsuma, T.; Fujii, T.; Naoi, K.; Niwa, C.; Kubota, Y.; Fujishima, A. Multicolour Photochromism of TiO<sub>2</sub> Films Loaded with Silver Nanoparticles. *Nat. Mater.* **2003**, *2*, 29–31.
- (4) Colbow, K. M.; Dahn, J. R.; Haering, R. R. Structure and Electrochemistry of the Spinel Oxides LiTi<sub>2</sub>O<sub>4</sub> and Li<sub>4/3</sub>Ti<sub>5/3</sub>O<sub>4</sub>. *J. Power Sources* **1989**, *26*, 397–402.
- (5) Idota, Y.; Kubota, T.; Matsufuji, A.; Maekawa, Y.; Miyasaka, T. Tin-Based Amorphous Oxide: A High-Capacity Lithium-Ion-Storage Material. *Science* **1997**, *276*, 1395–1397.
- (6) Gerischer, H. Electrochemical Techniques for the Study of Photosensitization. *Photochem. Photobiol.* **1972**, *16*, 243–260.
- (7) Pomykal, K. E.; Fajardo, A. M.; Lewis, N. S. Stability of N-Si/CH<sub>3</sub>OH Contacts as a Function of the Reorganization Energy of the Electron Donor. *J. Phys. Chem.* **1995**, *99*, 8302–8310.
- (8) Idígoras, J.; Pellejà, L.; Palomares, E.; Anta, J. a. The Redox Pair Chemical Environment Influence on the Recombination Loss in Dye-Sensitized Solar Cells. *J. Phys. Chem. C* **2014**, *118*, 3878–3889.
- (9) Farnum, B. H.; Morseth, Z. A.; Brennaman, M. K.; Papanikolas, J. M.; Meyer, T. J. Driving Force Dependent, Photoinduced Electron Transfer at Degenerately Doped, Optically Transparent Semiconductor Nanoparticle Interfaces. *J. Am. Chem. Soc.* **2014**, *136*, 15869–15872.
- (10) Zigler, D. F.; Morseth, Z. A.; Wang, L.; Ashford, D. L.; Brennaman, M. K.; Grumstrup, E. M.; Brigham, E. C.; Gish, M. K.; Dillon, R. J.; Alibabaei, L.; et al. Disentangling the Physical Processes Responsible for the Kinetic Complexity in Interfacial Electron Transfer of Excited Ru(II) Polypyridyl Dyes on TiO<sub>2</sub>. *J. Am. Chem. Soc.* **2016**, *138*, 4426–4438.
- (11) Green, A. N. M.; Palomares, E.; Haque, S. A.; Kroon, J. M.; Durrant, J. R. Charge Transport versus Recombination in Dye-Sensitized Solar Cells Employing Nanocrystalline TiO<sub>2</sub> and SnO<sub>2</sub> Films. *J. Phys. Chem. B* **2005**, *109*, 12525–12533.
- (12) Jarzebski, Z. M.; Marton, J. P. Physical Properties of SnO<sub>2</sub> Materials. *J. Electrochem. Soc.* **1976**, *123*, 299C-310C.
- (13) Bolts, J. M.; Wrighton, M. S. Correlation of Photocurrent-Voltage Curves with Flat-Band Potential for Stable Photoelectrodes for the Photoelectrolysis of Water. *J. Phys. Chem.* **1976**, *80*, 2641–2645.
- (14) Frank, S. N.; Bard, A. J. Semiconductor Electrodes. II. Electrochemistry at N-Type Titanium Dioxide Electrodes in Acetonitrile Solutions. *J. Am. Chem. Soc.* **1975**, *97*, 7427–

7433.

- (15) Bisquert, J.; Zaban, A.; Salvador, P. Analysis of the Mechanisms of Electron Recombination in Nanoporous TiO<sub>2</sub> Dye-Sensitized Solar Cells. Nonequilibrium Steady-State Statistics and Interfacial Electron Transfer via Surface States. *J. Phys. Chem. B* **2002**, *106*, 8774–8782.
- (16) Nguyen, T. T. O.; Peter, L. M.; Wang, H. Characterization of Electron Trapping in Dye-Sensitized Solar Cells by Near-IR Transmittance Measurements. *J. Phys. Chem. C* **2009**, *113*, 8532–8536.
- (17) Swierk, J. R.; McCool, N. S.; Nemes, C. T.; Mallouk, T. E.; Schmittenmaer, C. A. Ultrafast Electron Injection Dynamics of Photoanodes for Water-Splitting Dye-Sensitized Photoelectrochemical Cells. *J. Phys. Chem. C* **2016**, *120*, 5940–5948.
- (18) Prasittichai, C.; Avila, J. R.; Farha, O. K.; Hupp, J. T. Systematic Modulation of Quantum (Electron) Tunneling Behavior by Atomic Layer Deposition on Nanoparticulate SnO<sub>2</sub> and TiO<sub>2</sub> Photoanodes. *J. Am. Chem. Soc.* **2013**, *135*, 16328–16331.
- (19) McCool, N. S.; Swierk, J. R.; Nemes, C. T.; Schmittenmaer, C. A.; Mallouk, T. E. Dynamics of Electron Injection in SnO<sub>2</sub>/TiO<sub>2</sub> Core/Shell Electrodes for Water-Splitting Dye-Sensitized Photoelectrochemical Cells. *J. Phys. Chem. Lett.* **2016**, *7*, 2930–2934.
- (20) Rothenberger, G.; Fitzmaurice, D.; Graetzel, M. Spectroscopy of Conduction Band Electrons in Transparent Metal Oxide Semiconductor Films: Optical Determination of the Flatband Potential of Colloidal Titanium Dioxide Films. *J. Phys. Chem.* **1992**, *96*, 5983–5986.
- (21) Redmond, G.; Fitzmaurice, D. Spectroscopic Determination of Flatband Potentials for Polycrystalline Titania Electrodes in Nonaqueous Solvents. *J. Phys. Chem.* **1993**, *97*, 1426–1430.
- (22) O'Regan, B.; Grätzel, M.; Fitzmaurice, D. Optical Electrochemistry I: Steady-State Spectroscopy of Conduction-Band Electrons in a Metal Oxide Semiconductor Electrode. *Chem. Phys. Lett.* **1991**, *183*, 89–93.
- (23) Berger, T.; Anta, J. A.; Morales-Flórez, V. Electrons in the Band Gap: Spectroscopic Characterization of Anatase TiO<sub>2</sub> Nanocrystal Electrodes under Fermi Level Control. *J. Phys. Chem. C* **2012**, *116*, 11444–11455.
- (24) O'Donnell, R. M.; Sampaio, R. N.; Barr, T. J.; Meyer, G. J. Electric Fields and Charge Screening in Dye Sensitized Mesoporous Nanocrystalline TiO<sub>2</sub> Thin Films. *J. Phys. Chem. C* **2014**, *118*, 16976–16986.
- (25) Bedja, I.; Hotchandani, S.; Kamat, P. V. Preparation and Photoelectrochemical Characterization of Thin SnO<sub>2</sub> Nanocrystalline Semiconductor Films and Their Sensitization with Bis(2,2'-bipyridine)(2,2'-bipyridine-4,4'-dicarboxylic acid)ruthenium(II) Complex. *J. Phys. Chem.* **1994**, *98*, 4133–4140.
- (26) Matsumoto, Y.; Yoshikawa, T.; Sato, E. Dependence of the Band Bending of the Oxide Semiconductors on pH. *J. Electrochem. Soc.* **1989**, *136*, 1389–1391.

- (27) Knauf, R. R.; Brennaman, M. K.; Alibabaei, L.; Norris, M. R.; Dempsey, J. L. Revealing the Relationship between Semiconductor Electronic Structure and Electron Transfer Dynamics at Metal Oxide–Chromophore Interfaces. *J. Phys. Chem. C* **2013**, *117*, 25259–25268.
- (28) Watson, D. F.; Meyer, G. J. Cation Effects in Nanocrystalline Solar Cells. *Coord. Chem. Rev.* **2004**, *248*, 1391–1406.
- (29) Chappel, S.; Zaban, A. Nanoporous SnO<sub>2</sub> Electrodes for Dye-Sensitized Solar Cells: Improved Cell Performance by the Synthesis of 18nm SnO<sub>2</sub> Colloids. *Sol. Energy Mater. Sol. Cells* **2002**, *71*, 141–152.
- (30) Heimer, T. A.; D’Arcangelis, S. T.; Farzad, F.; Stipkala, J. M.; Meyer, G. J. An Acetylacetonate-Based Semiconductor–Sensitizer Linkage. *Inorg. Chem.* **1996**, *35*, 5319–5324.
- (31) Pavlishchuk, V. V.; Addison, A. W. Conversion Constants for Redox Potentials Measured versus Different Reference Electrodes in Acetonitrile Solutions at 25°C. *Inorganica Chim. Acta* **2000**, *298*, 97–102.
- (32) Cava, R. J.; Murphy, D. W.; Zahurak, S.; Santoro, A.; Roth, R. S. The Crystal Structures of the Lithium-Inserted Metal Oxides Li<sub>0.5</sub>TiO<sub>2</sub> Anatase, LiTi<sub>2</sub>O<sub>4</sub> Spinel, and Li<sub>2</sub>Ti<sub>2</sub>O<sub>4</sub>. *J. Solid State Chem.* **1984**, *53*, 64–75.
- (33) van de Krol, R.; Goossens, A.; Meulenkamp, E. A. Electrical and Optical Properties of TiO<sub>2</sub> in Accumulation and of Lithium Titanate Li<sub>0.5</sub>TiO<sub>2</sub>. *J. Appl. Phys.* **2001**, *90*, 2235–2242.
- (34) Barr, T. J.; Morris, A. J.; Taheri, A.; Meyer, G. J. Charge Rectification at Molecular Nanocrystalline TiO<sub>2</sub> Interfaces: Overlap Optimization To Promote Vectorial Electron Transfer. *J. Phys. Chem. C* **2016**, *120*, 27173–27181.
- (35) Ardo, S.; Achey, D.; Morris, A. J.; Abrahamsson, M.; Meyer, G. J. Non-Nernstian Two-Electron Transfer Photocatalysis at Metalloporphyrin-TiO<sub>2</sub> Interfaces. *J. Am. Chem. Soc.* **2011**, *133*, 16572–16580.
- (36) *CRC Handbook of Chemistry and Physics*, 97th (Inte.; Haynes, W. M., Ed.; CRC Press/Taylor & Francis: Boca Raton, 2016.
- (37) Koelle, U.; Moser, J.; Graetzel, M. Dynamics of Interfacial Charge-Transfer Reactions in Semiconductor Dispersions. Reduction of Cobaltoceniumdicarboxylate in Colloidal Titania. *Inorg. Chem.* **1985**, *24*, 2253–2258.
- (38) Kay, A.; Humphry-Baker, R.; Graetzel, M. Artificial Photosynthesis. 2. Investigations on the Mechanism of Photosensitization of Nanocrystalline TiO<sub>2</sub> Solar Cells by Chlorophyll Derivatives. *J. Phys. Chem.* **1994**, *98*, 952–959.
- (39) Ward, C. L.; O’Donnell, R. M.; DiMarco, B. N.; Meyer, G. J. Kinetic Resolution of Charge Recombination and Electric Fields at the Sensitized TiO<sub>2</sub> Interface. *J. Phys. Chem. C* **2015**, *119*, 25273–25281.
- (40) Lofroth, J.-E. Multivariate Fitting and the Error Matrix in Global Analysis of Data.

*Phys. Rev. D* **1986**, *90*, 1160–1168.

(41) van de Krol, R.; Goossens, A.; Meulenkamp, E. A. In Situ X-Ray Diffraction of Lithium Intercalation in Nanostructured and Thin Film Anatase TiO<sub>2</sub>. *J. Electrochem. Soc.* **1999**, *146*, 3150-3154.

(42) Boschloo, G.; Fitzmaurice, D. Electron Accumulation in Nanostructured TiO<sub>2</sub> (Anatase) Electrodes. *J. Electrochem. Soc.* **2000**, *147*, 7860-7868.

(43) O'Donnell, R. M.; Sampaio, R. N.; Barr, T. J.; Meyer, G. J. Electric Fields and Charge Screening in Dye Sensitized Mesoporous Nanocrystalline TiO<sub>2</sub> Thin Films. *J. Phys. Chem. C* **2014**, *118*, 16976–16986.

(44) Kamat, P. V.; Patrick, B. Photophysics and Photochemistry of Quantized ZnO Colloids. *J. Phys. Chem.* **1992**, *96*, 6829–6834.

(45) Bedja, I.; Hotchandani, S.; Kamat, P. V. Photoelectrochemistry of Quantized Tungsten Trioxide Colloids: Electron Storage, Electrochromic, and Photoelectrochromic Effects. *J. Phys. Chem.* **1993**, *97*, 11064–11070.

(46) Moss, T. S. The Interpretation of the Properties of Indium Antimonide. *Proc. Phys. Soc. Sect. B* **1954**, *67*, 775–782.

(47) Burstein, E. Anomalous Optical Absorption Limit in InSb. *Phys. Rev.* **1954**, *93*, 632–633.

(48) Szczepankiewicz, S. H.; Moss, J. A.; Hoffmann, M. R. Electron Traps and the Stark Effect on Hydroxylated Titania Photocatalysts. *J. Phys. Chem. B* **2002**, *106*, 7654–7658.

(49) Norris, D. J.; Sacra, A.; Murray, C. B.; Bawendi, M. G. Measurement of the Size Dependent Hole Spectrum in CdSe Quantum Dots. *Phys. Rev. Lett.* **1994**, *72*, 2612–2615.

(50) Wang, J.; Umezawa, N.; Hosono, H. Mixed Valence Tin Oxides as Novel van Der Waals Materials: Theoretical Predictions and Potential Applications. *Adv. Energy Mater.* **2016**, *6*, 1501190.

(51) Nozik, A. J. Photoelectrochemistry: Applications to Solar Energy Conversion. *Ann. Rev. Phys. Chem.* **1978**, *29*, 189–222.

(52) Boschloo, G.; Fitzmaurice, D. Spectroelectrochemical Investigation of Surface States in Nanostructured TiO<sub>2</sub> Electrodes. *J. Phys. Chem. B* **1999**, *103*, 2228–2231.

(53) Boschloo, G.; Fitzmaurice, D. Spectroelectrochemistry of Highly Doped Nanostructured Tin Dioxide Electrodes. *J. Phys. Chem. B* **1999**, *103*, 3093–3098.

(54) Tang, H.; Prasad, K.; Sanjinès, R.; Schmid, P. E.; Lévy, F. Electrical and Optical Properties of TiO<sub>2</sub> Anatase Thin Films. *J. Appl. Phys.* **1994**, *75*, 2042–2047.

(55) Pascual, J.; Camassel, J.; Mathieu, H. Fine Structure in the Intrinsic Absorption Edge of TiO<sub>2</sub>. *Phys. Rev. B* **1978**, *18*, 5606–5614.

(56) Kormann, C.; Bahnemann, D. W.; Hoffmann, M. R. Preparation and Characterization of Quantum-Size Titanium Dioxide. *J. Phys. Chem.* **1988**, *92*, 5196–5201.

- (57) Enright, B.; Fitzmaurice, D. Spectroscopic Determination of Electron and Hole Effective Masses in a Nanocrystalline Semiconductor Film. *J. Phys. Chem.* **1996**, *100*, 1027–1035.
- (58) Jarzebski, Z. M.; Marton, J. P. Physical Properties of SnO<sub>2</sub> Materials. *J. Electrochem. Soc.* **1976**, *123*, 299C–310C.
- (59) Tang, H.; Prasad, K.; Sanjinès, R.; Schmid, P. E.; Lévy, F. Electrical and Optical Properties of TiO<sub>2</sub> Anatase Thin Films. *J. Appl. Phys.* **1994**, *75*, 2042-2047.
- (60) Roberts, S. Dielectric Constants and Polarizabilities of Ions in Simple Crystals and Barium Titanate. *Phys. Rev.* **1949**, *76*, 1215–1220.
- (61) van der Krol, R.; Goossens, A.; Schoonman, J. Mott-Schottky Analysis of Nanometer-Scale Thin-Film Anatase TiO<sub>2</sub>. *J. Electrochem. Soc.* **1997**, *144*, 1723-1727.
- (62) Bauer, C.; Boschloo, G.; Mukhtar, E.; Hagfeldt, A. Ultrafast studies of electron injection in Ru dye sensitized SnO<sub>2</sub> nanocrystalline thin film. *Int. J. Photoenergy* **2002**, *4*, 17–20.
- (63) Asbury, J. B.; Hao, E.; Wang, Y.; Ghosh, H. N.; Lian, T. Ultrafast Electron Transfer Dynamics from Molecular Adsorbates to Semiconductor Nanocrystalline Thin Films. *J. Phys. Chem. B* **2001**, *105*, 4545–4557.

## CHAPTER 7: STRiVE DESCRIPTION AND OPERATION

### 7.1 Introduction

The STRiVE is an apparatus designed to measure charge density, charge transport, and recombination in dye-sensitized solar cells. The hardware consists of two LED arrays, one white and one colored, which provide constant and pulsed illumination, respectively. Solar cells are held at open or short-circuit by fast solid state switches, with switching times  $\sim 250$  ns. STRiVE is an acronym for “**S**equential **T**ime-**R**esolved current(**i**)-**V**oltage **E**xperiments.” The STRiVE monitors electrical signals and is capable of measuring the voltage and current simultaneously with  $\sim \mu\text{s}$  time resolution. As described below, the experiments and their analysis are generally divided into either large or small perturbation regimes.

For large perturbation experiments, cells equilibrate in the presence of an external perturbation, either light or an applied potential. The perturbation is then removed and, depending on the experiment, the cell may be switched between open and short circuit. An example of such an experiment is charge extraction from open circuit. In this experiment, the solar cell equilibrates at open circuit under steady state white light illumination. After equilibration is reached, the light is turned off and the cell is short-circuited. The current that flows through the circuit is integrated and represents the charge present in the cell under illumination.

The small perturbation techniques monitor kinetic responses of the solar cells as they return to steady state conditions following an external perturbation. Steady-state conditions are typically under illumination by an array of white LEDs at either open or short-circuit. A short ( $\mu\text{s}$ -ms) pulse from a separate array of colored LEDs then acts a small perturbation from the steady state (white light) conditions. Because the response is monitored as the cell returns to steady state (pre pulse) conditions, the cell is always kept at either open or short circuit conditions. A common example of a small perturbation technique is transient photovoltage decay. The voltage response is monitored and the decay is fit to a single exponential to obtain the electron lifetime.

This STRiVE is generally based on Brian O'Regan's 'TRACER' (**TR**Ansient and **Ch**arge **Ex**traction **R**obot),<sup>1,2</sup> however the hardware and software have been substantially modified. The STRiVE was developed at Johns Hopkins University and UNC Chapel Hill between 2013-2016. The design team was led by Tim Barr, who wrote the LabVIEW based software and led the mechanical and electrical engineering aspects of the instrument. C. Tilden Hagan IV also assisted with the overall circuit design that improved signal to noise ratios. Matthew Verber built and arranged the circuit board and assisted with troubleshooting.

This chapter is intended to be a physical description and brief summary of the experiments the STRiVE can perform, but not an exhaustive review of the underlying theory. Comprehensive reviews have been published focusing on the background theory and interpretation of measurements.<sup>3,1,4,5</sup> A brief summary of small perturbation theory and its applications in DSSCs was presented in Chapter 1.

## 7.2 Hardware Description

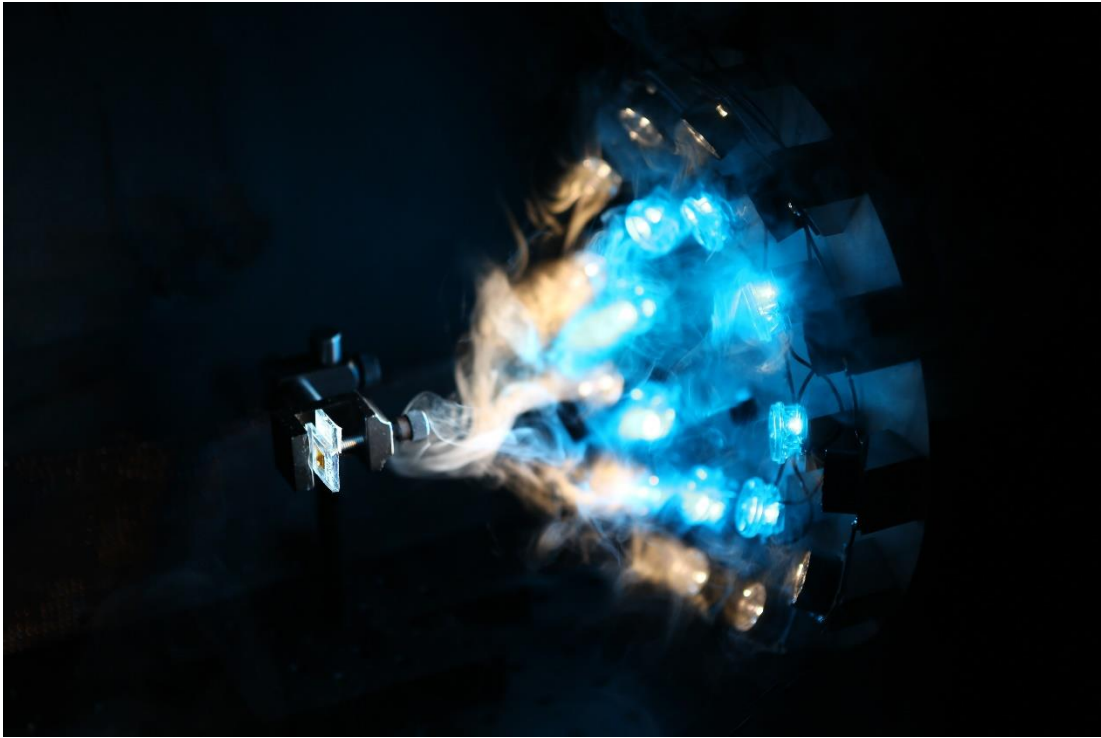


Figure 7.01. White and blue LED arrays illuminating a typical DSSC inside the STRiVE apparatus. Fog was generated from liquid nitrogen carefully poured between the LED array and the cell. Picture taken by Lars Sahl.

**Light Sources and Power Supplies:** Cells can be illuminated by two different circular LED arrays, Figure 7.01. The outer array consists of 12 white LEDs (Luxeon SR-12-WN300). These LEDs come equipped with a lens to focus the light at a  $9^\circ$  beam angle onto the solar cell. The output irradiance, given in Figure 7.02, is white to the eye but is not precisely calibrated to the AM1.5 solar spectrum. The LEDs are connected in series, each requiring  $\sim 3$  V to produce light. Therefore, the total voltage applied by a Kepco Bipolar Operational Power Supply/Amplifier to the LEDs is set to 36-37 V at all times. Illumination intensity is controlled by the current, which is typically defined by the user or the STRiVE

automatically. Typical operating currents are less than 500 mA, however the LEDs are rated to 1A.

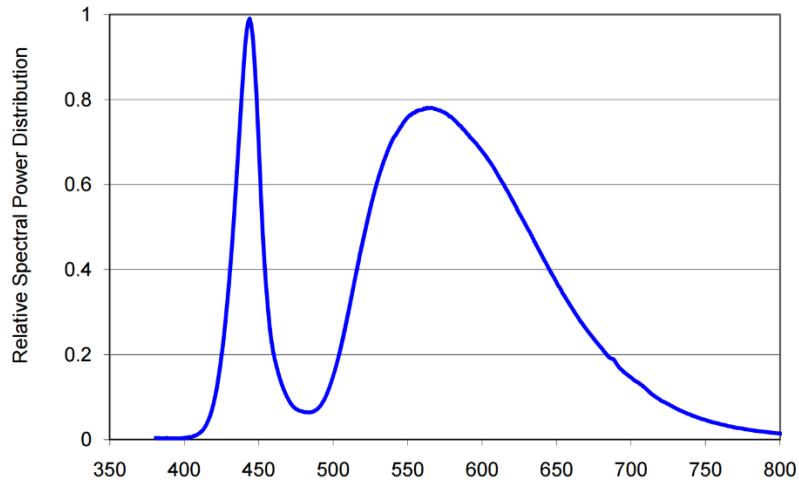


Figure 7.02. Relative spectral power distribution of the white LEDs.<sup>6</sup>

The inner array consists of 8 RGB tri-colored LEDs (Luxeon SP-03; Red: LXM2-PD01-0050,  $\lambda_{\max}=627\pm 20$  nm, FWHM=20 nm; Green: LXML-PM01-0090,  $\lambda_{\max}=530\pm 10$  nm, FWHM=30 nm; Blue: LXML-PB01-0040,  $\lambda_{\max}=470\pm 15$  nm, FWHM=20 nm), where an individual color is used for a given experiment. The spectral distribution is shown in Figure 7.03 for all available colored LEDs. The installed LEDs are Blue, Green, and Red. Each color is independently connected in series to allow for a single color to be used at a time. The minimum voltage required to produce light is variable (variable photon energy), but a constant voltage of  $\sim 38$  V is applied by a MASTECH HY5003D DC Power Supply to the array for all colors. The colored LEDs are typically used for short ( $\mu$ s-ms) pulses for the transient experiments.

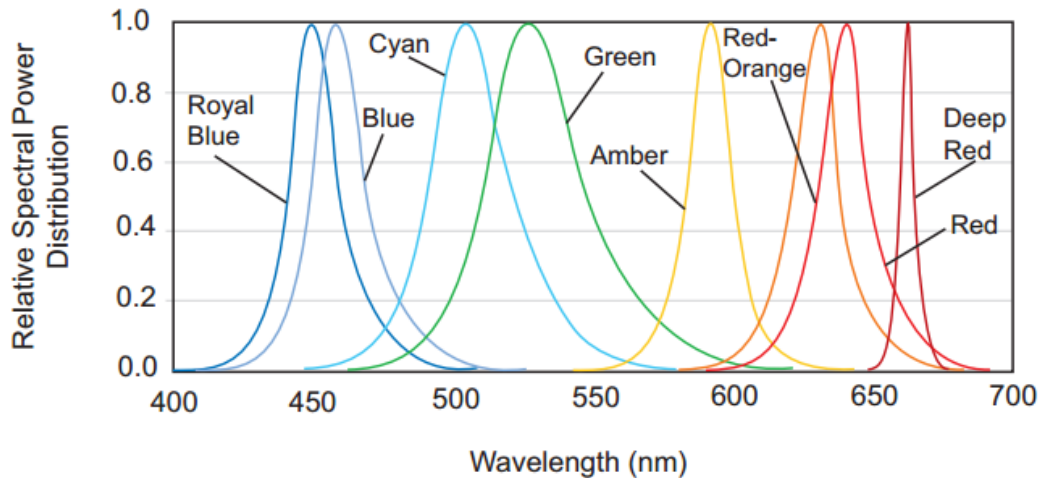


Figure 7.03. Relative spectral distribution of colored LEDs. Blue, Green, and Red are installed on the STRiVE.

These power supplies are set to run in controlled current mode. The user sets a maximum voltage limit, which is applied when there is no current flow. When the lights are turned on, the voltage is adjusted within the allowed range to provide the desired current.

**DAQ Board:** Communication between the computer and each instrument is managed by a NI-6251-BNC data acquisition (DAQ) board. It converts computer commands into voltage outputs which control essentially all functions (open/short circuit, applied potential, illumination intensity etc.) and converts analog voltage signals into digitized values that are stored on a computer. The maximum sampling rate is 1.25 MHz, which corresponds to 0.8  $\mu$ s. This sampling rate can only be realized when a single input/output is used. Using multiple channels divides the maximum sampling rate by the number of channels used.

The act of measuring a voltage requires some current to flow. Our solar cells typically have very small active areas ( $<1 \text{ cm}^2$ ) and provide low current (typically  $<3 \text{ mA}$ ). For these devices, measuring a voltage can, in some cases, draw enough current to make an open

circuit measurement not be truly at ‘open circuit.’ We empirically found that the amount of current drawn by the act of measuring was related to the sampling rate. Reducing the sampling rate to 100 kHz (as opposed to 1.25 MHz) was sufficient to prevent the act of measuring from influencing the results. Therefore, the maximum sampling rate has been fixed at 100 kHz (10  $\mu$ s/sample).

**Integrated Circuit:** The integrated circuit used is shown schematically in Figure 7.04A and pictorially in 7.04B. The cell electrical connections (open/short circuit) are controlled by metal-oxide semiconductor field effect transistors (MOSFETs) shown on the left. MOSFETs operate by allowing current to pass between the ‘source’ and ‘drain’ if a voltage is applied to a ‘gate’ (relative to source). The original design by Brian O’Regan connected two MOSFETs ‘drain to drain,’ which was replicated here.<sup>7</sup> This was done because some MOSFETs are better rectifiers in one direction (i.e. source to drain) versus the opposite (drain to source).<sup>8</sup> Therefore, connecting two MOSFETs drain-to-drain prevents essentially all current when the gate is off. There are two pairs of two MOSFETs. One pair controls if the cell is at open/short circuit, the other allows the external potentiostat (PAR 362) to be in electrical communication with the DSSC. Both pairs should never be ‘closed’ at the same time because it would effectively short the potentiostat.

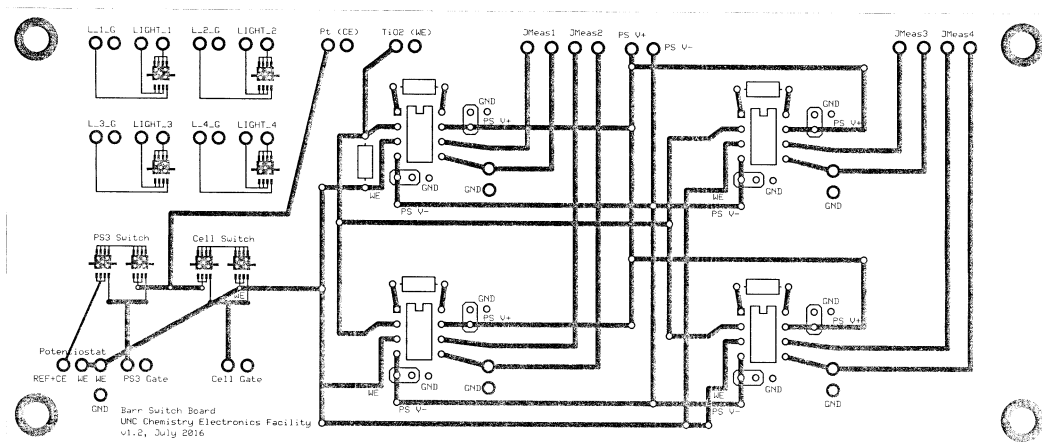
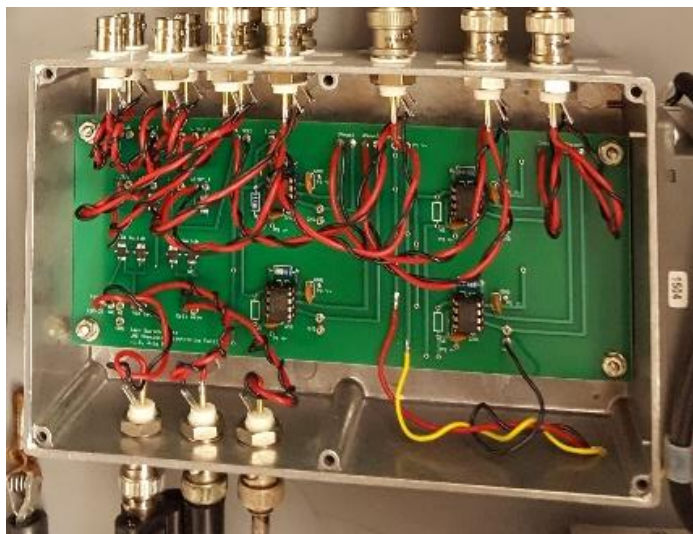


Figure 7.04. Picture (Top) of the integrated circuit used in the STRiVE shown schematically on the Bottom. On the left are MOSFETs used to hold the cell at open/short circuit or allow the potentiostat to be connected to the circuit. On the right are the amplifiers to accurately measure the current.

Under open circuit conditions, all the MOSFETs are ‘open’ and no current flows. Under short-circuit, the pair of MOSFETs that allow open/short circuit are ‘closed’ and current flows from the  $\text{TiO}_2$  working electrode, across a 1 Ohm resistor to measure the current, and then to the counter electrode. Since less than 5 mA are typically output, the

voltage drop across the resistor is in the  $10^{-6}$  to  $10^{-3}$  V range. The DAQ board cannot accurately measure voltages this small, so the signal is amplified (INA 128P) by a factor of 100-5000. The amplification amount is controlled by the resistance of what has been termed an ‘amplifying resistor,’ which is fixed and not easily changed. Since measurements are taken over a wide range of operating conditions, the current varies from  $10^{-6}$ - $10^{-3}$  A. Therefore, the same amplification ratio is not ideal under all operating conditions. To ensure the user does not have to manually adjust this parameter, four separate amplifiers are used, each with a different amplification ratio (100, 500, 1000, 5000). Every output is measured by the DAQ, where the software calculates the optimal amplification ratio and uses only that data.

**Faraday Cage:** The sample and LEDs are enclosed in a copper Faraday cage to minimize environmental (line) noise. The decrease in the noise was actually small, but the cage was still used as a ‘black box’ to prevent unwanted light from illuminating the cell.

**Potentiostat:** Although the DAQ board is capable of outputting a voltage, it can only output ~10 mA current. Therefore, if high efficiency cells were used it would not be able to supply enough current to reach the desired voltage. To overcome this obstacle, an external potentiostat was used. A PAR Model 362 Scanning Potentiostat was utilized for this work, however any potentiostat with an external input can be used. The external potentiostat is set to apply the voltage specified by the DAQ board, but is capable of providing up to amps of current as needed and can therefore easily apply any potential of interest. The potentiostat is connected to the circuit through the a pair of MOSFETs. The potentiostat is not in electrical contact unless the MOSFETs are closed. When closed, the reference and counter electrodes

are connected to the counter electrode of the DSSC and the working electrode is connected to the TiO<sub>2</sub> electrode in the DSSC.

### **7.3 Software Description and Typical Operation**

The software that controls the STRiVE is written in LabVIEW and is designed to make device analysis fast, robust, and hands-off. This is accomplished by ‘grouping’ parameters (light intensity, pulse time, open-circuit voltage/short-circuit current) for sequential experiments. Grouping experiments are automatically performed under matched operating conditions without the user having to manually enter parameters. Key cell parameters (electron concentration, lifetime, diffusion coefficient) are a function of incident light intensity. Therefore, experiments are repeated under a wide range of light intensities and compared at matched electron concentrations. Typical operation starts by measuring the steady-state current-voltage curve of the cell and then using the results as guidelines for time-dependent experiments. For example, a cell with an open-circuit voltage,  $V_{OC}$ , of 600 mV would be analyzed under light intensities that produce  $V_{OC}$ ’s ranging from ~300-650 mV. These bounds are empirically set by the feasible reasonable range of incident light intensities that can be accurately output without introducing neutral density filters (on the low side) or lenses to focus the light (on the high side).

When investigating DSSCs, the parameters of interest are typically the electron lifetime, diffusion coefficient, and charge within the TiO<sub>2</sub> thin film. Electron lifetime is typically measured by the transient photovoltage decay (TVD) technique from open circuit, but could also be measured by the large perturbation technique open-circuit photovoltage decay. The diffusion coefficient is measured by transient photocurrent decay (TCD) from short circuit, although could be performed under an applied bias (see Transient Photocurrent

Decay below). The electron lifetime,  $\tau_n$ , and diffusion coefficient,  $D_n$ , are often used to calculate the diffusion length,  $L_n$ , according to Equation 7.01:

$$L_n = \sqrt{\tau_n D_n} \quad 7.01$$

where the  $n$ 's in Equation 7.01 represent that the lifetime and diffusion coefficient used must be compared at the same TiO<sub>2</sub> electron concentration. Since TVD is at open circuit and TCD is at short circuit, the electron concentration is much different at the same light intensity. Therefore, charge extraction is performed to estimate the charge within the film under both open and short circuit, which allows the lifetime and diffusion coefficient to be accurately compared at matched electron concentrations.

**General User Interface:** The experiment(s) to be performed are selected from the list of dropdown boxes titled 'Select Experiments.' The individual experiments will be discussed in detail below. Experiments can be grouped together by selecting 'yes' for the group parameter. When grouped, the first experiment acts as a 'master' experiment and all parameters set during that experiment (light intensity, cell current/voltage, pulse time) will be shared with subsequent experiments where relevant. If 'grouped' is not yet to 'yes,' each experiment will be performed as defined without modifying the parameters from the 'master' experiment. Once an experiment is selected, clicking 'Set Parameters' bring up a dialog where the user can set parameters for the experiment. Execution of all selected experiments is begun by clicking the 'Run' button at the bottom. The 'Stop' button stops experiments in progress (although not instantly) and stops execution of the STRiVE software. All data collected is automatically saved in the selected folder. The file name always begins with the

experiment name, i.e. “Transient Photovoltage Decay...” followed by an extension, defined in the Parameters dialog.

Common parameters that are independent of the experiment are input, such as the user name, a cell description, cell area, etc. are defined in the general user interface and saved into every data file. Email options are setup, where the STRiVE computer has its own Gmail account. The user can select the option to send all data as it is collected (through email) or a single message that informs the user when data collection is complete. This latter method is more common and very useful because the user does not need to constantly check when the STRiVE is done. Below, an overview, user-defined parameters, and automatic data workup are discussed for each experiment.

**Jsc and Voc:** *Overview:* The experiment Jsc and Voc is the simplest experiment the STRiVE performs. The cell is placed at open circuit by the MOSFETs and illuminated. The voltage is monitored and displayed in real-time until it is constant (under 2 % variability) for 2 seconds or the maximum time is reached. Next, the cell is placed at short circuit and the current is monitored, again until it remains constant (within 0.1 mV) for 1 seconds or until the maximum time is reached.

*User-defined Parameters:* (See Figure 7.05) The user simply sets the maximum amount of time and the LED current, which determines the illumination intensity.

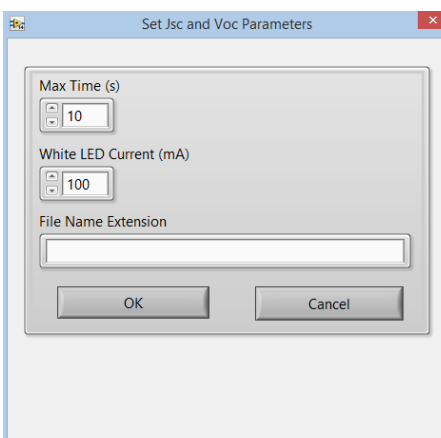


Figure 7.05: The “Set Jsc and Voc Parameters” dialog box with typical values shown.

*Data Workup:* The  $V_{OC}$  and  $J_{SC}$  values will be displayed along with the standard deviation for the last ~1 second during the measurement.

**Current-Voltage (iV) Curve: Overview:** The overall solar cells performance is evaluated by a current-voltage (iV) curve. Cell current is monitored as the voltage applied between the working and counter electrode is varied. This is typically done in the dark and under illumination. The voltage applied by the STRiVE is not applied directly to the electrodes as would be done with a stand-alone potentiostat. Instead, the voltage is applied to two points inside the circuit. When voltage is applied from the potentiostat, voltage drop occurs across all resistive elements in the circuit. In this case, the significant resistive elements are the MOSFETs, the DSSC, and the measuring resistor. Practically, this means that the total applied voltage must be greater than the desired voltage drop across the cell. However, the resistance in the DSSC is a function of the applied voltage. Therefore, the amount of ‘extra voltage’ needed to apply the correct voltage is not constant. The STRiVE empirically corrects for this in a point-by-point fashion, but does not apply the exact desired voltage. It

should be noted that the voltage directly across the DSSC is measured independently and reported in the output.

*User-Defined Parameters:* The input parameters are displayed in Figure 7.06. Basic parameters are the scan direction positive (higher photovoltages) or negative, the initial potential, high and low potentials, the voltage step between points, the light intensity, and number of scans (one scan is a complete cycle, going forward and reverse). The ‘Voltage Bounds (+/-)’ option is total voltage applied by the potentiostat. Due to the need to apply ‘extra’ potential to the circuit to achieve the desired voltage drop across the DSSC, the correction will, in rare cases, fail and try to apply huge voltages (this used to happen if the working and counter electrodes were switched; the STRiVE would try to correct the wrong way and the error would get progressively larger). The ‘Voltage Bounds’ button serves to protect the cell from huge voltage in the case of this error.

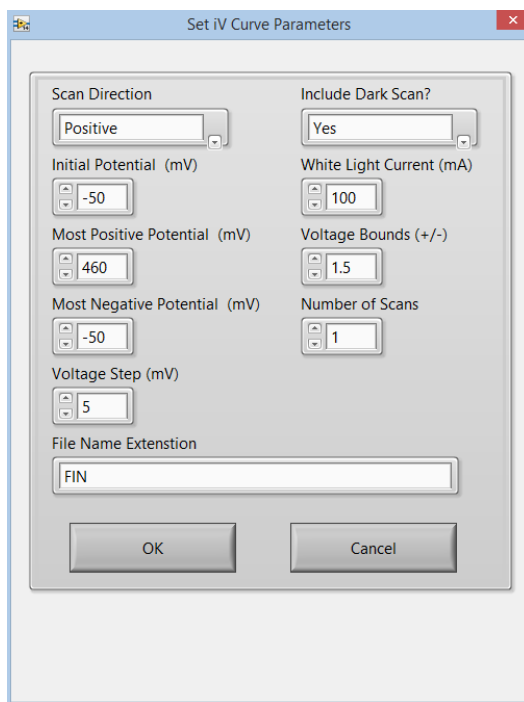


Figure 7.06: The “Set iV Curve Parameters” dialog box showing typical experimental conditions for a DSSC with a  $V_{OC}$  near 440 mV.

*Data Workup:* The STRiVE will output the raw data for the light on and light off scans in addition to the light-on power scan (voltage x current). The software will also automatically workup the data and calculate short circuit current ( $J_{SC}$ ), open circuit voltage ( $V_{OC}$ ), the maximum power, and the fill factor ( $FF$ ). The results are typically quite accurate as long as there are sufficient data points. The  $J_{SC}$  is calculated by fitting a line through all the points within 50 mV of zero voltage and calculating the intercept. Deciding which points to take to calculate  $V_{OC}$  is more complicated because the cell current varies depending on the composition and the light intensity so a similar fixed range, i.e. +/- 0.1 mA, does not always contain points. Therefore, points are taken that are below 20 % of the  $J_{SC}$  value. The maximum power is easily calculated by the maximum value of the power curve. The fill

factor is calculated using the current and voltage at the power point ( $pp$ ) relative to  $J_{sc}$  and  $V_{oc}$  according to Equation 7.02:

$$FF = \frac{J_{pp}V_{pp}}{J_{sc}V_{oc}} \quad 7.02$$

**Transient Photovoltage Decay (TVD): Overview:** Transient photovoltage decay is one of the most common techniques used to measure the electron lifetime in dye-sensitized solar cells. The cell is illuminated under open-circuit conditions and then a short pulse is superimposed on the background illumination. The cell voltage is monitored before, during, and after the pulse. The decay is well-fit to a single exponential decay, where the “decay lifetime” is the lifetime of the injected electrons. The number of extra electrons injected by the pulse is related to the magnitude of the voltage response by the chemical capacitance. In the small perturbation regime, the chemical capacitance can be approximated as a constant so that at a given  $V_{oc}$ , a pulse with 2x the intensity results in a 2x larger voltage. The term of ‘short pulse’ has a precise meaning here: it means that the decay lifetime is independent of the pulse intensity; conditions that are achieved by injecting so few electrons that the total electron concentration in the  $TiO_2$  thin films is essentially unchanged (< 5 %). Experimentally, this is achieved by having a small voltage perturbation, usually about 4 mV.

The number of injected electron can be controlled by the duration of the pulse when the intensity is fixed. Since the chemical capacitance increases exponentially with cell voltage, the same pulse time does not result in the same peak at all  $V_{oc}$ 's. At higher  $V_{oc}$ 's, the pulse time must be increased so that enough electrons are injected to produce a 4 mV voltage spike. The STRiVE software is coded to automatically find the correct pulse duration to give a voltage spike of a set magnitude.

One detail to keep in mind for STRiVE experiments is that the response is measured from the FTO substrate that supports the mesoporous TiO<sub>2</sub> thin film. Therefore, the electron concentration profile as a function of distance from the FTO substrate impacts the results. In TVD experiments, the voltage response at early times is dependent on how the cell is illuminated, either through the TiO<sub>2</sub> or through the counter electrode, and how strongly the light is absorbed. If the cell is illuminated through the TiO<sub>2</sub> electrode, the highest light intensity, and therefore number of injected electrons, is at the FTO/TiO<sub>2</sub> interface (due to absorption). This results in a short transient voltage that may briefly flatten out before following an exponential decay. Alternatively, if illuminated through the counter electrode, the highest electron concentration is generated at the TiO<sub>2</sub> electrolyte interface. If the light is strongly absorbed, this creates a time-of-flight type measurement where the response at the FTO contact is delayed due to the time it takes the electrons to diffuse through the film and be collected. Illuminating through the counter electrode is preferred because it is experimentally easier to determine where the decay begins. Another benefit of illuminating through the counter electrode is that the rise time can be used to determine the electron diffusion coefficient.<sup>9,10</sup> However, the rise time is influenced by the capacitance of the substrate and in our experience does not provide results that are as robust as transient photocurrent decay.

*User-Defined Parameters:* The TVD parameter dialog is shown in Figure 7.07. The user has the option to choose how the cell voltage is controlled in the ‘Experiment Type’ menu. Normal operation is with a desired V<sub>OC</sub> that allows the STRiVE to find the light intensity that gives the desired V<sub>OC</sub>. Alternatively, the user can set a light intensity that the STRiVE will not adjust, or set the voltage using a potentiostat. An examination of the left columns of

Figure 7.07 shows the equilibration time, pre-pulse collection time, pulse duration, and post pulse collection times. The user can choose to set the pulse time manually (Pulse Control Method-Time) or allow the STRiVE to find a pulse that produced a voltage spike of given magnitude (Pulse Control Method-Voltage Spike and Red LED Pulse Spike (mV) ). If this option is selected, the STRiVE will use the defined pulse time as a first ‘guess’ and adjust the pulse time from there until the desired spike is achieved. Adjusting the pulse duration to produce a given voltage spike is the normal operating procedure as this method allows the total charge injected to be kept as a small fraction of the total electron concentration.

Since the electron concentration is a function of light intensity ( $V_{OC}$ ) it is common to perform a number of TVD experiments at varying light intensities. The right hand side of the parameters in Figure 7.07 allow the user to set the number of TVD experiments performed (Number of  $V_{OC}$  Steps), how many pulses are averaged at a single  $V_{OC}$  (Number of Scans per  $V_{OC}$ ), and the voltage step between experiments (Voc Step (mV) ). The x-spacing (dx) in the data collected can be selected (Time Step (aka dx, us) ) menu. This option is included for two reasons: (1) Some responses are very slow and this can prevent excess data from being taken and (2) to increase the signal-to-noise ratio. The signal-to-noise is not improved on the DAQ board by measuring slower, but the STRiVE software will always measure at the fastest possible rate (100 kHz) and can average the data into user-defined segments. Therefore, a larger ‘dx’ results in higher signal-to-noise ratio.

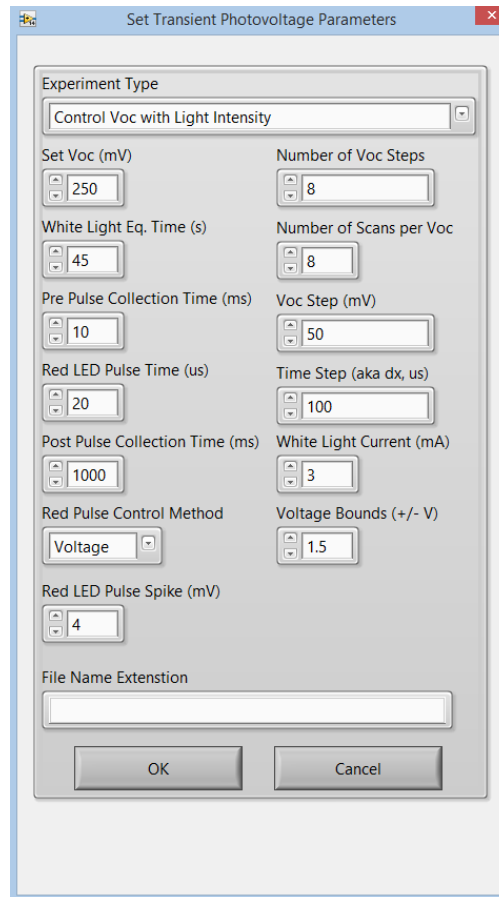


Figure 7.07. The “Set Transient Photovoltage Parameters” dialog box showing typical values when employed as the first grouped experiment.

*Data Workup:* The STRiVE will automatically calculate  $V_{OC}$  by the voltage recorded in the pre-pulse period. It will also attempt to calculate the electron lifetime, although this number can sometimes be calculated more rigorously in Mathematica or Origin. The electron lifetime is easily calculated by fitting the decay to a single exponential decay, however the trick for accurately calculating the electron is in defining where to start and stop the fit. The STRiVE defines the start time as the first data point that is past the peak and has a value below 80 % the peak value. The Stop time is the first data point after the peak whose magnitude is within

the noise of the pre-peak data collection. Once the data is selected, the decay is fit to a single exponential function, Equation 7.03:

$$V(t) = \Delta V_0 e^{-t/\tau_n} \quad 7.03$$

where the initial amplitude,  $\Delta V_0$ , and electron lifetime,  $\tau_n$ , are readily calculated. The initial amplitude is not typically used for anything other than the fit, but it can provide an alternative method to calculate the chemical capacitance (usually calculated via charge extraction) according to Equation 7.04:

$$\text{Chemical capacitance} = \frac{\Delta V_0}{\Delta Q} \quad 7.04$$

where  $\Delta Q$  is the charge injected from the pulse, that can be calculated by integrating a transient photocurrent experiment with an identical pulse.

**Transient Photocurrent Decay (TCD):** *Overview:* Transient photocurrent decay is used to measure the electron diffusion coefficient in dye-sensitized solar cells. The cell is illuminated under (typically) short-circuit conditions and then a short pulse is superimposed on the background illumination. The cell current is monitored before, during, and after the pulse. The decay is well-fit to a single exponential decay, where the decay lifetime is related to the diffusion coefficient of the injected electrons. It is often assumed that recombination is negligible during TCD, i.e. all injected electrons are collected. Models to account for recombination during TCD have been proposed where the decay lifetime is related to both the electron (recombination) lifetime and the photocurrent lifetime.<sup>1</sup> The number of electrons injected by the pulse can be estimated by integrating the current response. The term ‘short pulse’ again has a precise meaning: conditions where that the decay lifetime is independent

of the pulse intensity, which is achieved by injecting few enough electrons that the total electron concentration in the TiO<sub>2</sub> thin films is essentially unchanged (< 5 %).

Experimentally, this is achieved by having a small current response, about 25 μA.

The illumination direction (though the TiO<sub>2</sub> or through the counter electrode) again influences the current response. In theory, the same shape should be observed as in TVD: illumination through the TiO<sub>2</sub> would give a voltage spike then decay while through the counter electrode would give a slower rise then decay. However, a voltage spike is often observed in our lab when illuminated from either illumination direction. The absence of the delayed rise when illuminating through the counter electrode may result from the photocurrent response of the FTO (very small), scattered light, or some other unknown reason. In any case, the decay is typically well-fit to a single exponential from which the diffusion coefficient can be calculated.

In addition to performing TCD from short circuit, the current transient can monitored at any applied potential.<sup>9</sup> This is rarely done, but has the potential to be very useful. In this experiment, the cell voltage is controlled by the external potentiostat and the current is monitored during an otherwise normal TCD experiment. The advantage of this technique is that the electron concentration in the TiO<sub>2</sub> thin film is equal to the electron concentration for the TVD experiment, so the two lifetimes can be directly compared. However, data obtained in this dissertation research often provides RC limited lifetimes that appear (as has been reported<sup>9</sup>) and do not vary as expected with light intensity. It is unclear where the limitation comes from, but the potentiostat, MOSFETs, and the DSSC itself may play roles.

*User-Defined Parameters:* The parameter dialog for TCD is shown in Figure 7.08. The user can define how the experiment is performed in the Experiment Type box. When run as

individual experiment, this is typically 'Set Jsc,' where the STRiVE will adjust the light intensity to a desired  $J_{SC}$  value. When TCD is run after a TVD experiment in a series of grouped experiments, the user should select 'No Jsc Control' to use the light intensity from the TVD experiment. The other option less commonly used is 'Set voltage and monitor current' as discussed above. The pre-pulse, pulse, and post-pulse times can be set in the appropriate boxes. As with TVD, there are two options on how to define the pulse duration set by the 'Pulse Control Method' box. The options are to manually set the time or to define a current spike and allow the STRiVE calculate the pulse time needed. I have found that a current spike of  $\sim 25 \mu A$  has sufficient signal-to-noise but is small enough to not appear to influence the results. On the right hand side of Figure 7.08, the Number of Scans, which defines how many experiments are averaged at a single  $J_{SC}$ , and the time spacing are set.

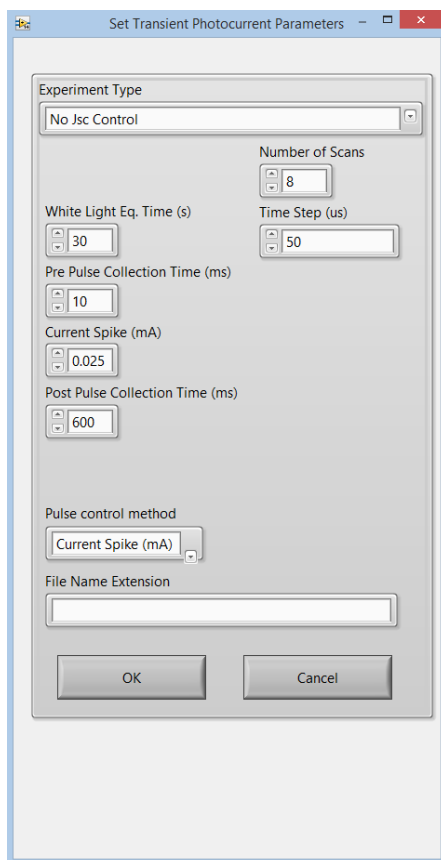


Figure 7.08. The “Set Transient Photocurrent Parameters” dialog box displaying typical values when TCD is run as part of a series of grouped experiments (not the first).

*Data Workup:* The STRiVE will automatically calculate  $J_{SC}$  by the current recorded in the pre-pulse period. It will also attempt to calculate the photocurrent lifetime, although, as with TVD, this number can sometimes be calculated more rigorously in Mathematica or Origin. The photocurrent lifetime is calculated by fitting the decay to a single exponential function. As with TVD, the STRiVE defines the start time as the first data point that is past the peak and has a value below 80 % the peak value. The Stop time is the first data point after the peak whose magnitude is within the noise of the pre-peak data collection. Once the data is selected, the decay is fit to a single exponential function, Equation 7.05:

$$J(t) = \Delta J_0 e^{-t/\tau_c} \quad 7.05$$

where the initial amplitude,  $\Delta J_0$ , and photocurrent decay lifetime,  $\tau_c$ , are readily calculated.

The photocurrent lifetime is used to calculate the diffusion coefficient,  $D_n$ , (at electron concentration  $n$ ) of films with known thickness,  $d$ , according to Equation 7.06:

$$D_n = \frac{d^2}{2.77\tau_c} \quad 7.06$$

The factor of 2.77 is an empirical number that corresponds to the time it takes half the electron to diffuse through half the film and converting from natural log (in the lifetime fit).<sup>11</sup> Other values (2.35<sup>12</sup>, 2.47<sup>1</sup>) have been reported in the literature, which slightly impact the magnitude of the diffusion coefficient, but not any reported trends.

**Charge Extraction: Overview:** It is now well established that the electron lifetime and diffusion coefficient of one DSSC to another should be compared at matched electron concentrations. One method to estimate the charge within the TiO<sub>2</sub> thin film is charge extraction. Charge extraction is typically performed at open-circuit while the cell is illuminated, but can be done from any starting condition (short-circuit or under applied bias). After the DSSC equilibrates, any external perturbation (light or applied potential) is removed while the cell is short-circuited. The current that flows is recorded and integrated to give the charge.

*User-Defined Parameters:* The parameters dialog for charge extraction is shown in Figure 7.09. The user can select the Experiment, which can be from the open-circuit (OC) condition, the short-circuit (SC) condition, or under potentiostatic control. When not under potentiostatic control, the light intensity can be pre-defined (No Voc Control or No Jsc control) or adjust by the STRiVE to achieve a desired V<sub>OC</sub> or J<sub>SC</sub> (Set Voc/Jsc with light

intensity). When under potentiostatic control, the light intensity is pre-defined. Depending on the type of experiment chosen, the user can select a given light intensity,  $V_{OC}$ , or applied current. Next, the user defines the collection time window. Typically, equilibration is performed for 45 seconds, followed by a 10 ms pre-short circuit collection window (used to calculate  $V_{OC}$  or  $J_{SC}$ ), and finally a ~4 s window where the cell is short circuited and data is recorded. The amount of time required to collect all the carriers is light intensity dependent, but 4 seconds is usually long enough. Extra time does not significantly influence the measurement as essentially no current flows after all the charge is extracted. Like the other experiments, there is an option to repeat the charge extraction measurement a number of times at a given  $V_{OC}$  (Number of Scans per Step) as well as repeating the measurement over a wide range of  $V_{OC}$ s (Number of Steps). Due to the high signal-to-noise ratio of this measurement, only one scan is typically needed for accurate data.

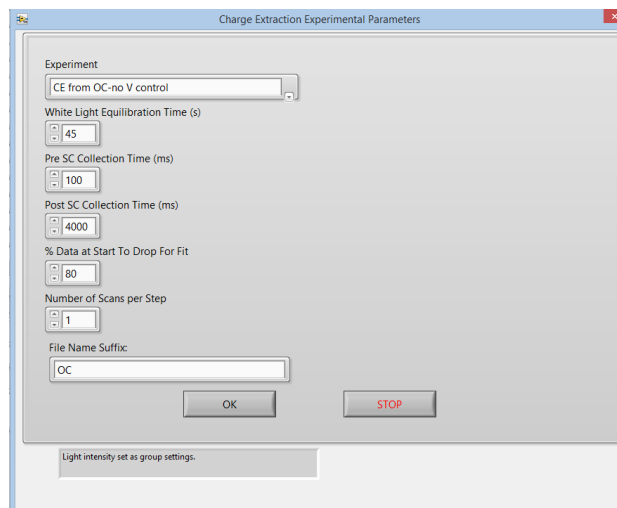


Figure 7.09. The “Charge Extraction Experimental Parameters” dialog box showing typical values when performed as ‘grouped’ and not the first experiment.

*Data Workup:* The charge extracted is automatically calculated and output by the STRiVE. Assuming that there is no non-Faradaic current, a plot of charge as a function of time will plateau at long times. In some cases, especially when there is very low total charge, the charge will appear to increase or decrease due to minor zero-offsets in the current measurement (presumably due to non-Faradaic current). Therefore, the STRiVE calculates the final charge extracted by fitting a line to the last 20 % of the data, where the y-intercept in the fit represents the total charge extracted. This method corrects for minor current flow that may cause the charge to artificially appear to indefinitely increase or decrease.

**Current Interrupt Voltage:** *Overview:* Electron transport in the TiO<sub>2</sub> thin film is well-defined by Fick's Law of diffusion, where electrons are driven towards the collecting substrate by a concentration gradient that increases with distance from the substrate. Therefore, charge must exist in the thin film under short circuit conditions to drive the electrons towards the FTO substrate. Current interrupt voltage is an alternative technique to charge extraction that estimates the charge in the TiO<sub>2</sub> thin film under short-circuit conditions. The experiment is performed by allowing the DSSC to reach a steady-state condition, typically under illumination at short circuit. The perturbation (light or current) is then removed as the cell is switched to open-circuit. The voltage is monitored where the peak value has been shown to give a reasonable value of the average quasi-Fermi level of the electrons in the thin film. This value, sometimes called  $V_{sc}$  or  $V_{int}$ , represents the average internal voltage in the TiO<sub>2</sub> thin film at short circuit.

*User-Defined Parameters:* The user can define the equilibrium starting conditions by the 'Variable to control' box shown in Figure 7.10. The user can choose to set the light intensity or the current. If the user chooses to set the current, the 'White Light Current (mA)' box

serves as a starting point when the STRiVE attempts to find the light intensity that results in the requested current. Equilibration time (again ~45 seconds), pre-open circuit, and post open-circuit collection times are easily defined. The user can define how many times the measurement is repeated at a given light intensity/current in the ‘Number of scans’ box. The time spacing between x-data points is defined, where typical values are around 0.5-2 ms. Finally, the number of experiments performed at different starting conditions and the magnitude of the light intensity or current step between experiments are set.

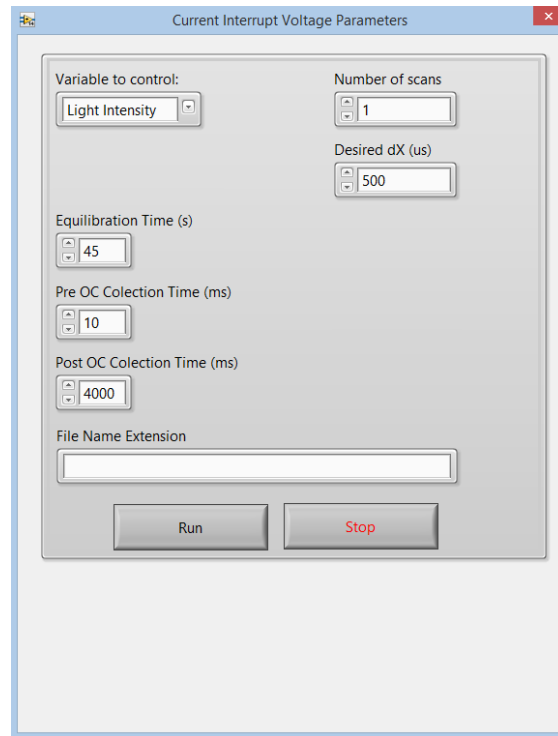


Figure 7.10. The “Current Interrupt Voltage Parameters” dialog box with values for typical operation when performed as a ‘grouped’ (not the first) experiment.

*Data Workup:* The STRiVE will automatically report the maximum voltage measured as the internal voltage,  $V_{int}$ , as well as an approximate open circuit voltage,  $V_{oc}$ , under identical operating conditions. The accuracy of  $V_{int}$  can be tested by comparing the internal voltage

and charge at short circuit to the open circuit equivalents. It is often found that the charge extracted at short circuit versus the internal voltage (from current interrupt voltage) often lies on the line for the open circuit charge versus  $V_{OC}$ , as shown in Figure 7.11. Therefore,  $V_{int}$  often does not need to be calculated more carefully, however if electron collection is less than unity, recombination may need to be considered.

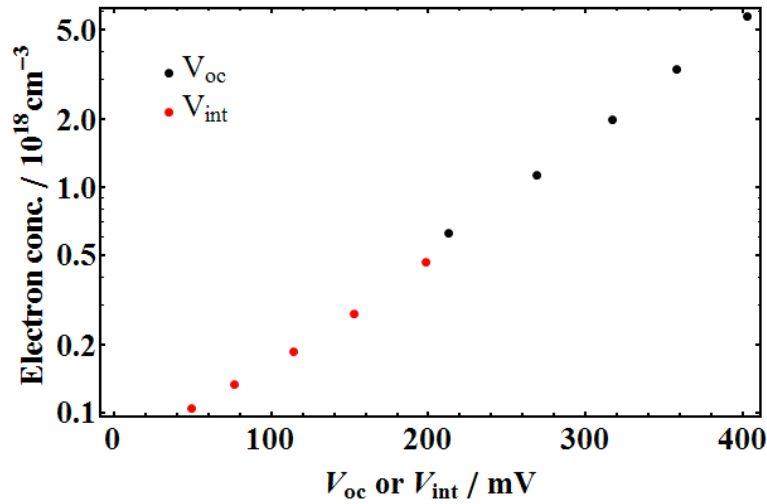


Figure 7.11. Comparison of charge extracted from open-circuit and  $V_{oc}$  to the charge extracted at short-circuit and  $V_{int}$ , the internal voltage calculated from current interrupt voltage.

**Open Circuit Photovoltage Decay: Overview:** Open circuit photovoltage decay is a common large perturbation technique to estimate the electron lifetime. The experiment is simply performed by perturbing the DSSC with light or an applied bias and then removing the perturbation while monitoring the cell voltage from open circuit. The derivative of the voltage change as a function of time,  $\frac{dV_{oc}}{dt}$ , is related to the electron lifetime by Equation

7.07:<sup>3</sup>

$$\tau_n = \frac{k_B T}{e} \left( \frac{dV_{oc}}{dt} \right)^{-1} \quad 7.07$$

where  $k_B$  is Boltzmann's constant,  $T$  is the absolute temperature, and  $e$  is the elementary charge. This method provides similar (although not identical) values for the electron lifetime as does transient photovoltage decay.<sup>1</sup>

It can take a long time for the voltage to reach zero (due to the increasing electron lifetime as voltage decreases). This can make it difficult for the user to know how long to let the experiment run. New software was developed that allows the user to choose an end condition (time, absolute, or relative voltage) by monitoring the voltage in real time (normal STRiVE data collection is defined by a preset number of points that are all collected before they can be analyzed). Essentially, a fast measurement is taken, checked to see if the end condition is satisfied, and then the experiment stops or takes another measurement. This limits the minimum time spacing between data points to 35 ms when an end condition other than time is specified. The code must collect the data and analyze it before the next data point. If the user tries to take data spaced more closely than 35 ms, time is the default end condition.

*User-Defined Parameters:* The selectable parameters are shown in Figure 7.11. The user can choose to control the light intensity or  $V_{OC}$  in the 'Variable to control' box. The 'End Condition' (described above) defines when the experiment will stop. Options are time, absolute, or relative (to the initial voltage) voltage. The user can again select the time spacing between data points. If the time spacing is less than 35 ms, the 'time' end condition is automatically used. If relative or absolute voltage is used as the end condition, the stop time still represents the maximum amount of time the experiment will run. A small, ~10 ms, amount of data is typically collected before the perturbation (light or bias) is removed. Again,

the experiment can be repeated over a range of light intensities or applied biases by the ‘Number of Steps’ button.

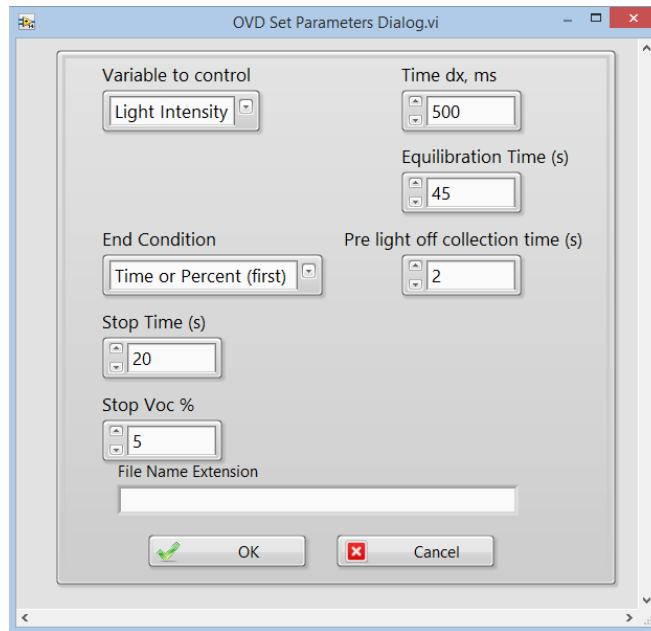


Figure 7.12. The “[Open Circuit Photovoltage Decay] Set Parameters Dialog” box for typical values when performed in a series of ‘grouped’ experiments (not the first).

*Data Workup:* Open circuit photovoltage decay was rarely used in this dissertation work, so very effort was set to automate this. The program will output the  $V_{OC}$  and experimental conditions, but will not automatically differentiate the data or calculate the lifetime.

## REFERENCES

- (1) Barnes, P. R. F.; Miettunen, K.; Li, X.; Anderson, A. Y.; Bessho, T.; Gratzel, M.; O'Regan, B. C. Interpretation of Optoelectronic Transient and Charge Extraction Measurements in Dye-Sensitized Solar Cells. *Adv. Mater.* **2013**, *25*, 1881–1922.
- (2) O'Regan, B. C. Use of the TRACER instrument in solar cell research. [https://workspace.imperial.ac.uk/people/Public/chemistry/Brian O'Regan/What the TRACER measures.pdf](https://workspace.imperial.ac.uk/people/Public/chemistry/Brian%20O'Regan/What%20the%20TRACER%20measures.pdf) (accessed Mar 30, 2017).
- (3) Zaban, A.; Greenshtein, M.; Bisquert, J. Determination of the Electron Lifetime in Nanocrystalline Dye Solar Cells by Open-Circuit Voltage Decay Measurements. *ChemPhysChem* **2003**, *4*, 859–864.
- (4) Li, L.-L.; Chang, Y.-C.; Wu, H.-P.; Diao, E. W.-G. Characterisation of Electron Transport and Charge Recombination Using Temporally Resolved and Frequency-Domain Techniques for Dye-Sensitized Solar Cells. *Int. Rev. Phys. Chem.* **2012**, *31*, 420–467.
- (5) Bisquert, J.; Fabregat-santiago, F. Electron Lifetime in Dye-Sensitized Solar Cells: Theory and Interpretation of Measurements. *J. Phys. Chem. C* **2009**, *113*, 17278–17290.
- (6) LUXEON Rebel ES <http://www.luxeonstar.com/assets/downloads/ds61.pdf> (accessed Mar 26, 2017).
- (7) O'Regan, B. C. TRACER Hardware [https://workspace.imperial.ac.uk/people/Public/Forms/AllItems.aspx?RootFolder=%2Fpeople%2FPublic%2Fchemistry%2FBrian O'Regan](https://workspace.imperial.ac.uk/people/Public/Forms/AllItems.aspx?RootFolder=%2Fpeople%2FPublic%2Fchemistry%2FBrian%20O'Regan) (accessed Mar 31, 2017).
- (8) Source vs Drain polarity for MOSFETS <http://electronics.stackexchange.com/questions/15106/source-vs-drain-polarity-for-mosfets> (accessed Mar 31, 2017).
- (9) O'Regan, B. C.; Bakker, K.; Kroeze, J.; Smit, H.; Sommeling, P.; Durrant, J. R. Measuring Charge Transport from Transient Photovoltage Rise Times. A New Tool To Investigate Electron Transport in Nanoparticle Films. *J. Phys. Chem. B* **2006**, *110*, 17155–17160.
- (10) Dunn, H. K.; Peter, L. M. How Efficient Is Electron Collection in Dye-Sensitized Solar Cells? Comparison of Different Dynamic Methods for the Determination of the Electron Diffusion Length. *J. Phys. Chem. C* **2009**, *113*, 4726–4731.
- (11) Nakade, S.; Kanzaki, T.; Wada, Y.; Yanagida, S. Stepped Light-Induced Transient Measurements of Photocurrent and Voltage in Dye-Sensitized Solar Cells: Application for Highly Viscous Electrolyte Systems. *Langmuir* **2005**, *21*, 10803–10807.
- (12) van de Lagemaat, J.; Frank, A. J. Nonthermalized Electron Transport in Dye-Sensitized Nanocrystalline TiO<sub>2</sub> Films: Transient Photocurrent and Random-Walk Modeling Studies. *J. Phys. Chem. B* **2001**, *105*, 11194–11205.

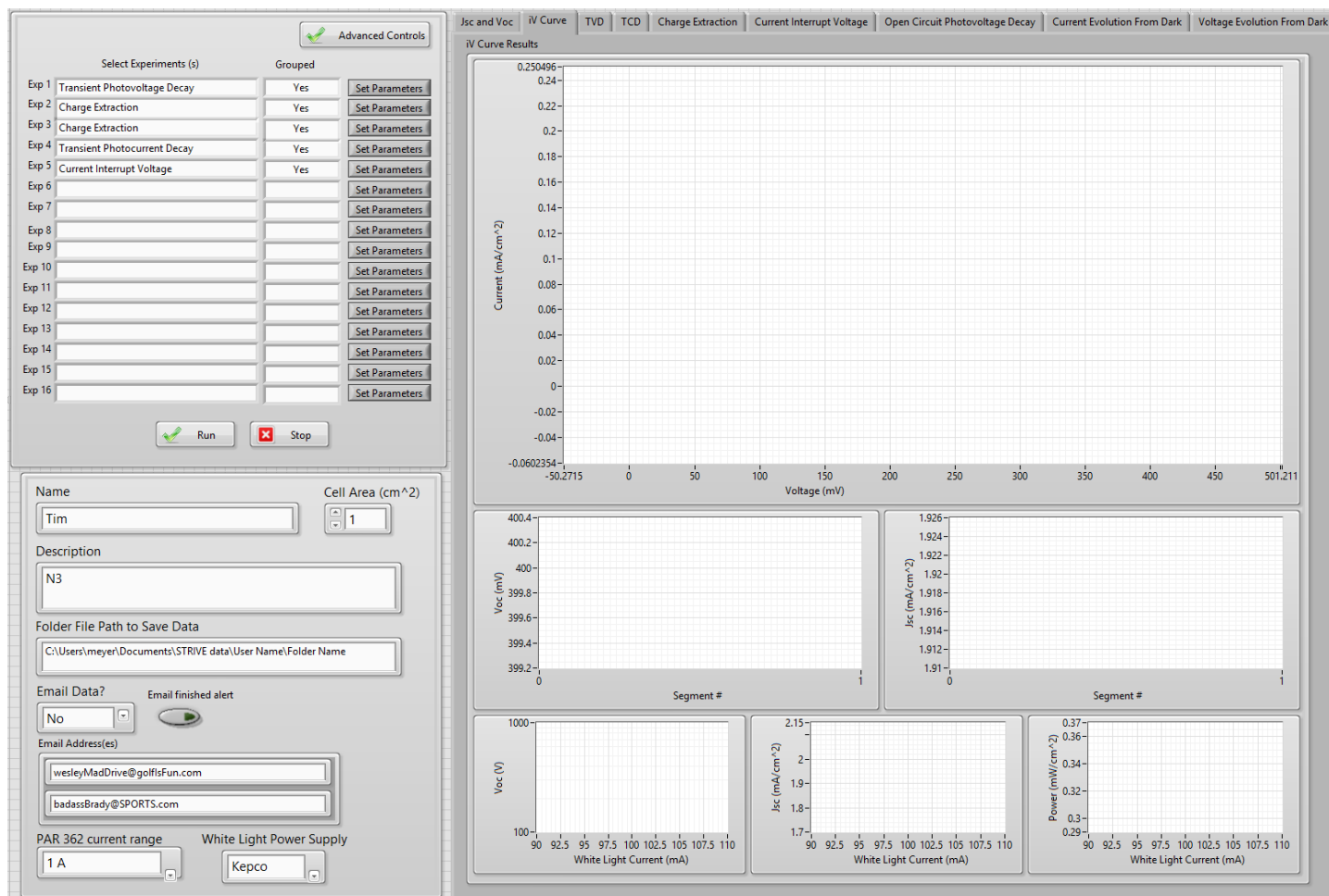


Figure A.01. STRiVE 5.0 user interface 'Front Panel' where the experiments selected reflect normal operating procedure.

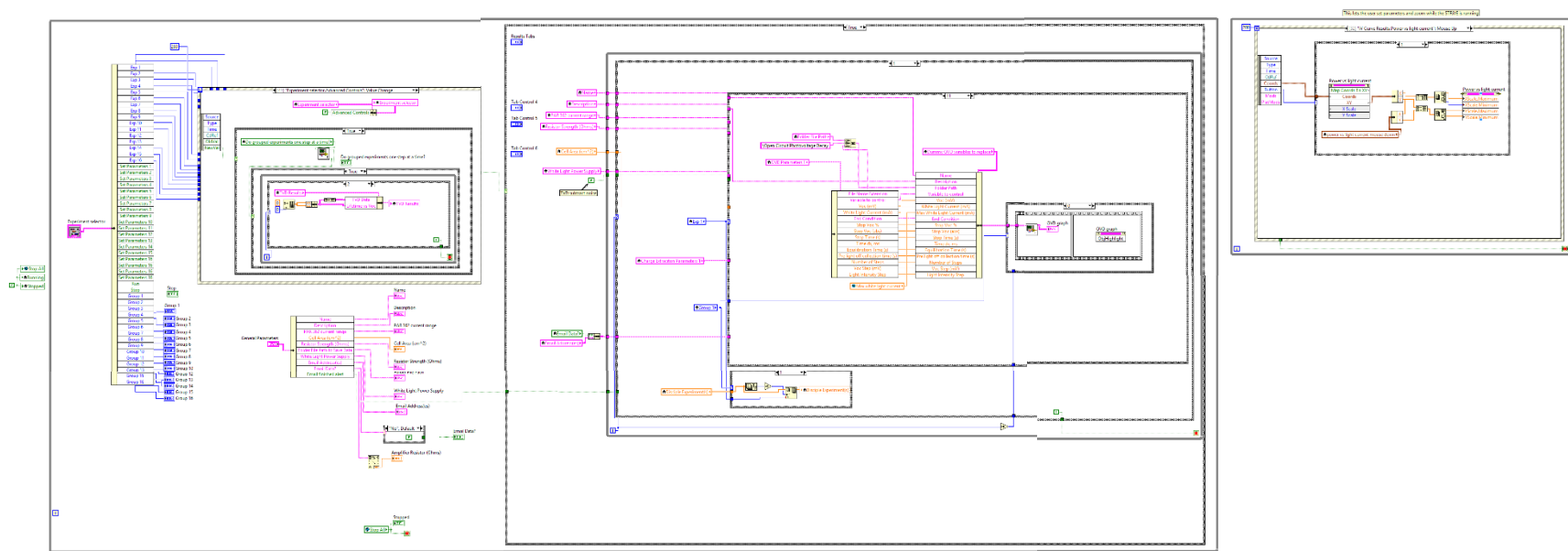


Figure A.02. STRiVE user interface ‘Block Diagram.’ The left and right rectangles are event structures, which execute only for a user-defined event, such as selecting an experiment or zooming on a graph. In the center is a loop that executes all selected (ungrouped) experiments and then performs grouped experiments.

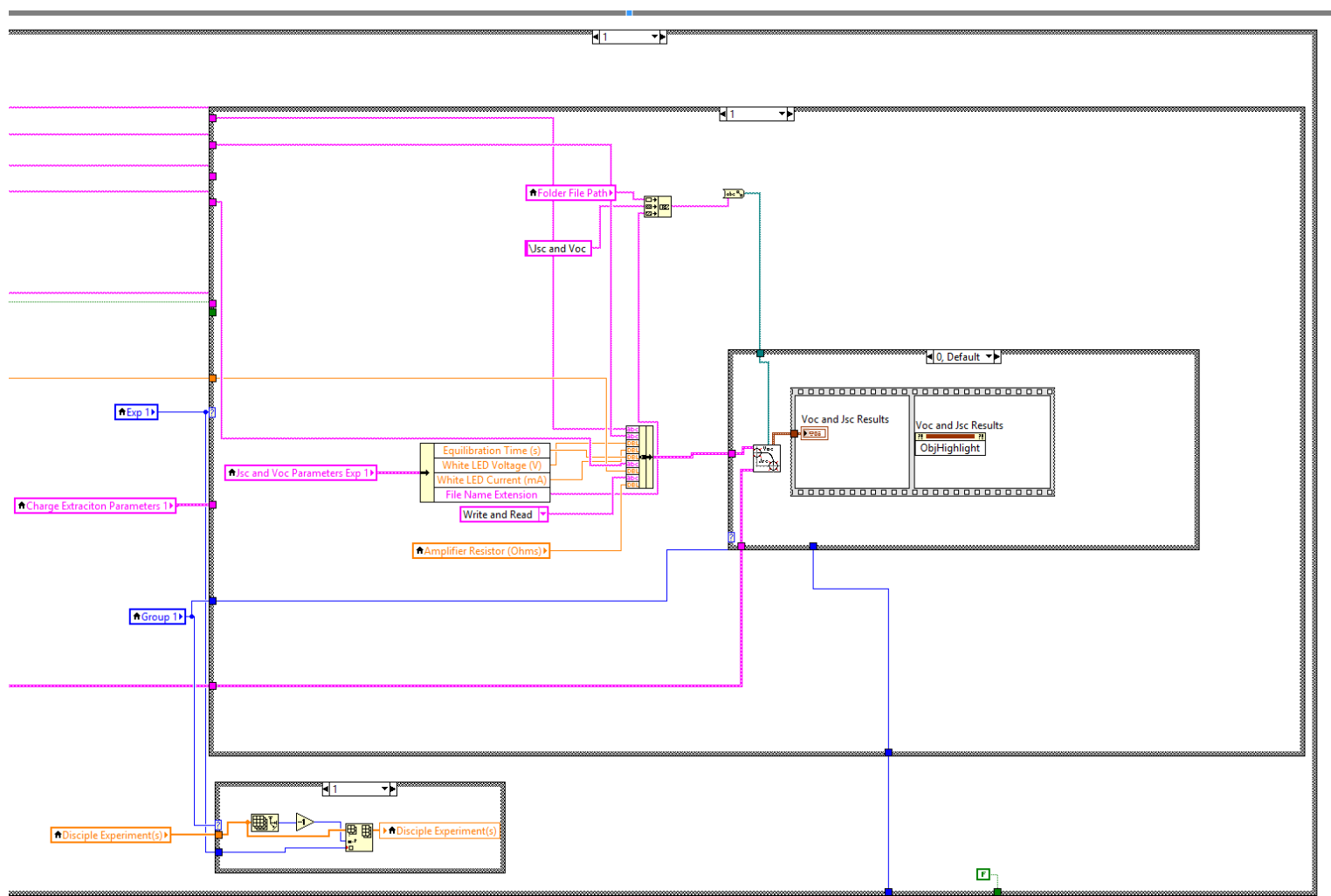
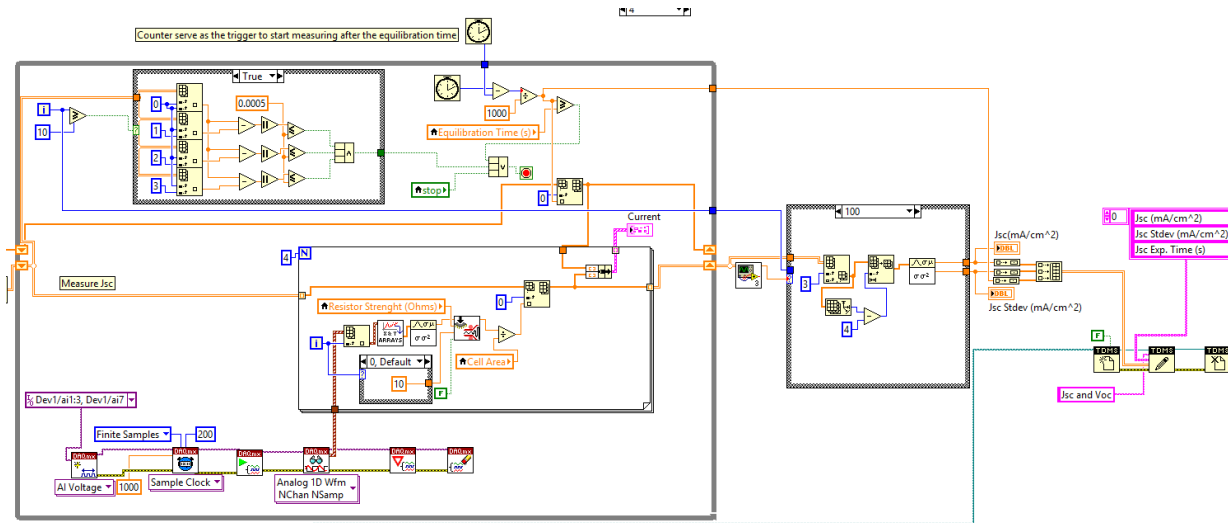
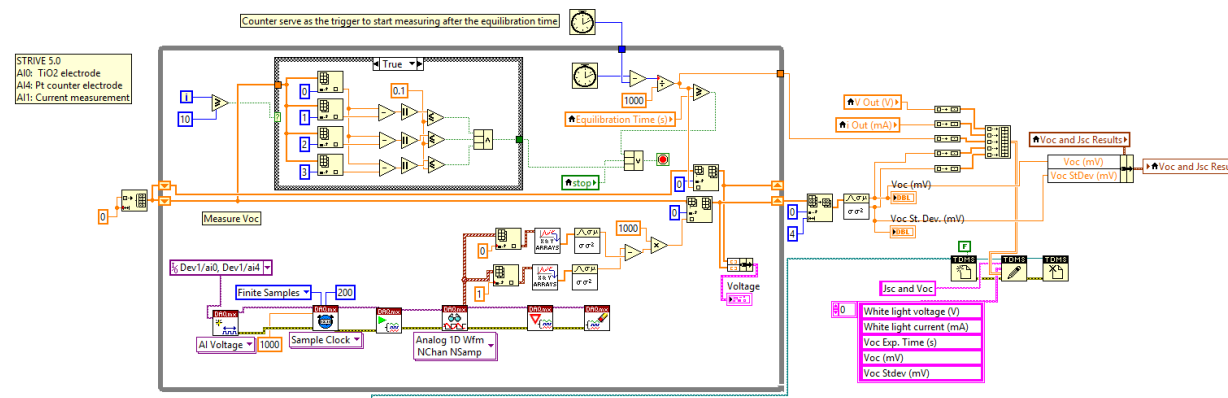


Figure A.03. STRiVE user interface 'Block Diagram' selecting the first experiment, Jsc and Voc.

Figure A.04. Measure Jsc and Voc 'Block Diagram' depicting how  $V_{OC}$  is measured.Figure A.05. Measure Jsc and Voc 'Block Diagram' depicting how  $J_{SC}$  is measured.

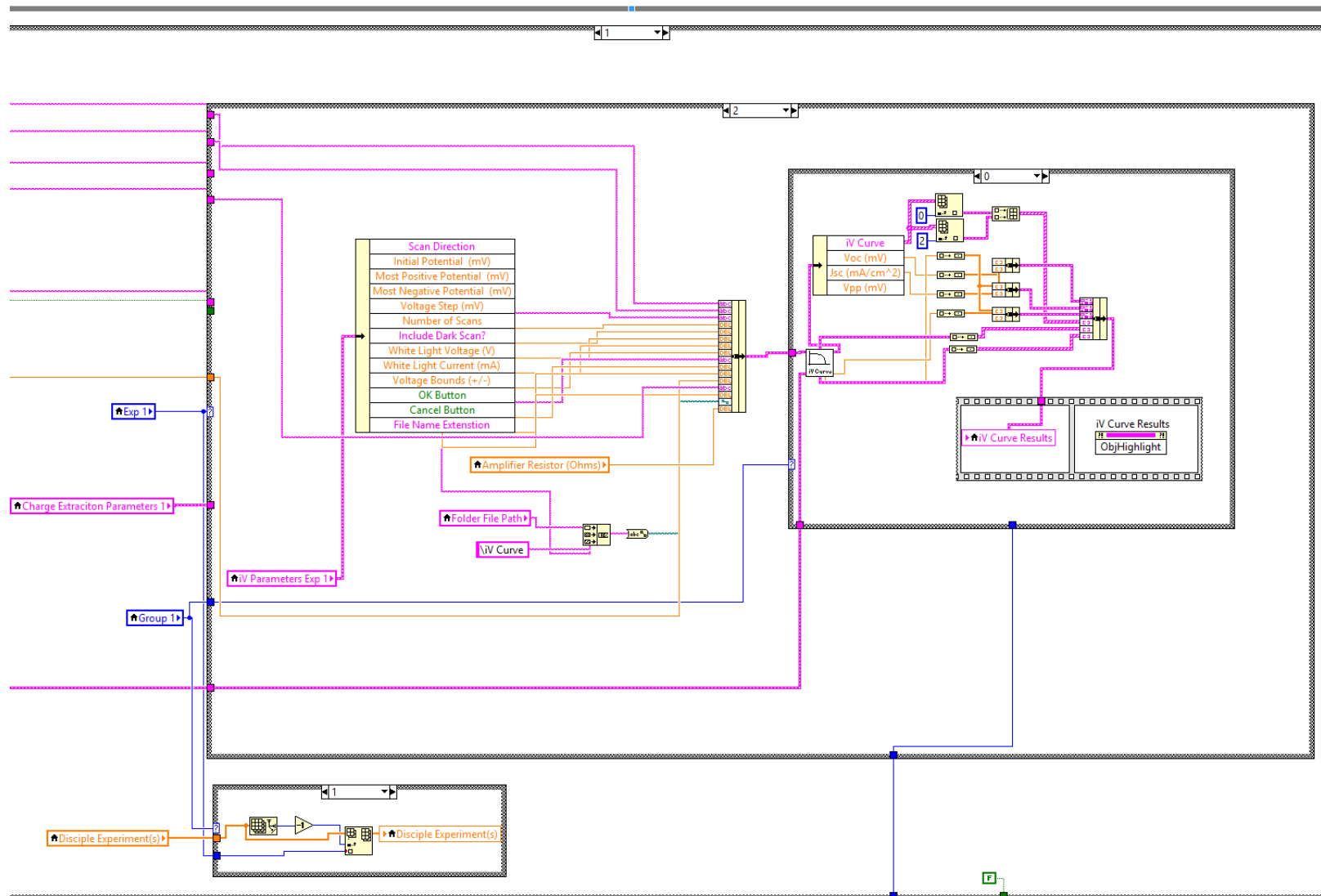


Figure A.06. STRiVE user interface 'Block Diagram' selecting the second experiment, iV Curve.

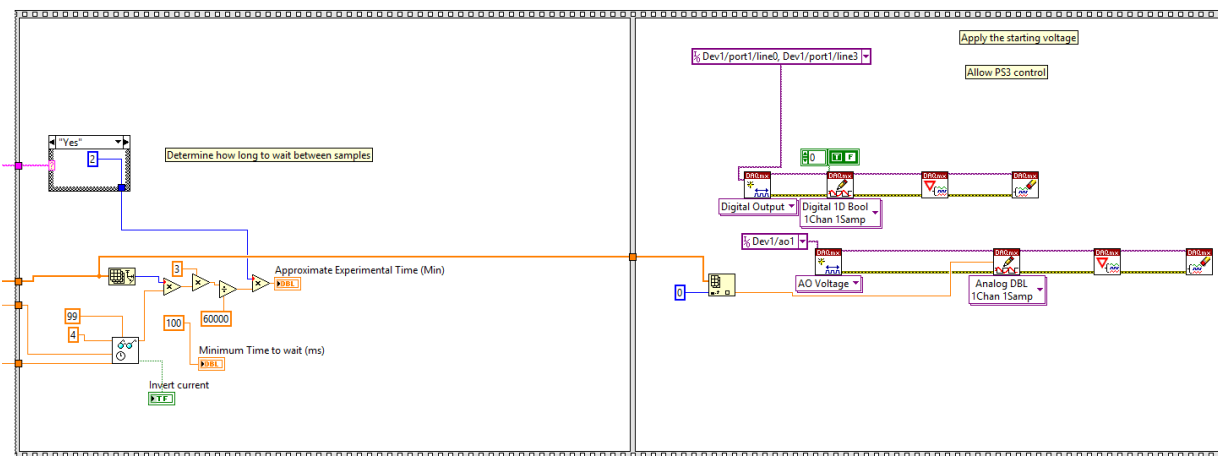


Figure A.07. iV Curve 'Block Diagram' Step 1: determine the time to wait between data points on the curve and connect the potentiostat.

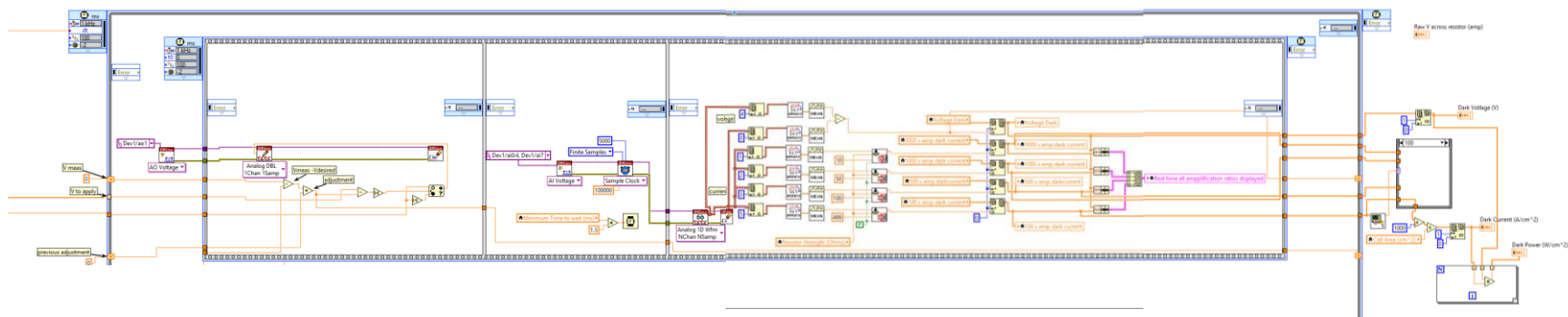


Figure A.08 iV Curve 'Block Diagram' Step 2: run the dark iV curve. This code is essentially the same as the light-on iV curve.

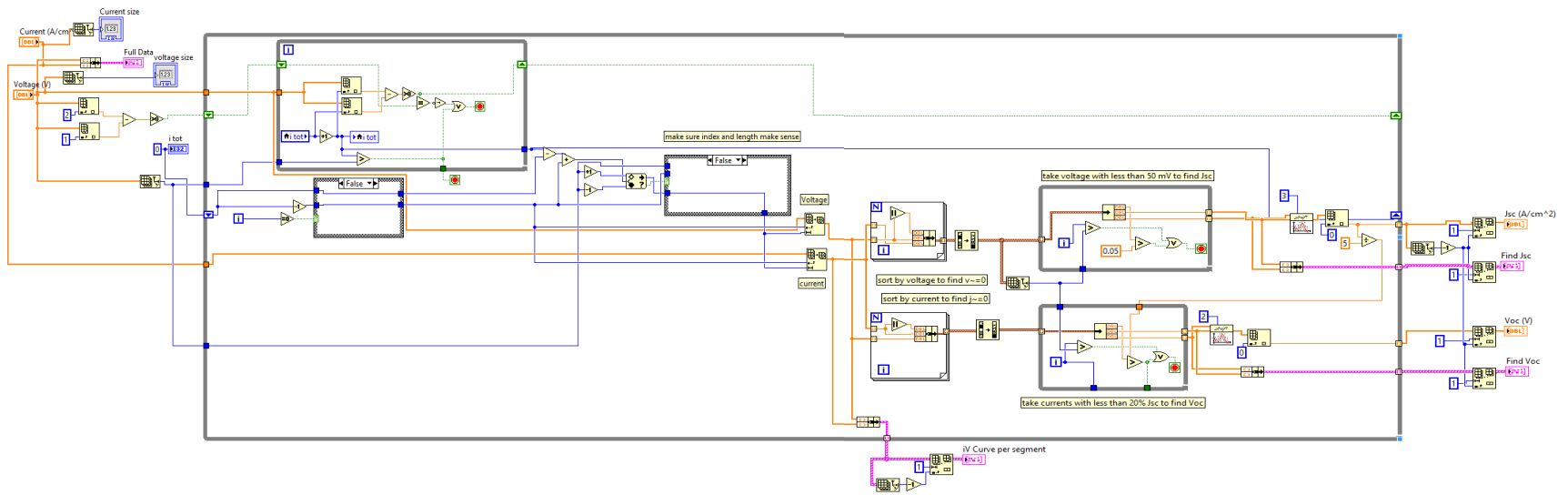


Figure A.09 iV Curve 'Block Diagram' Step 3: calculate  $J_{sc}$  and then  $V_{oc}$  and display the results.

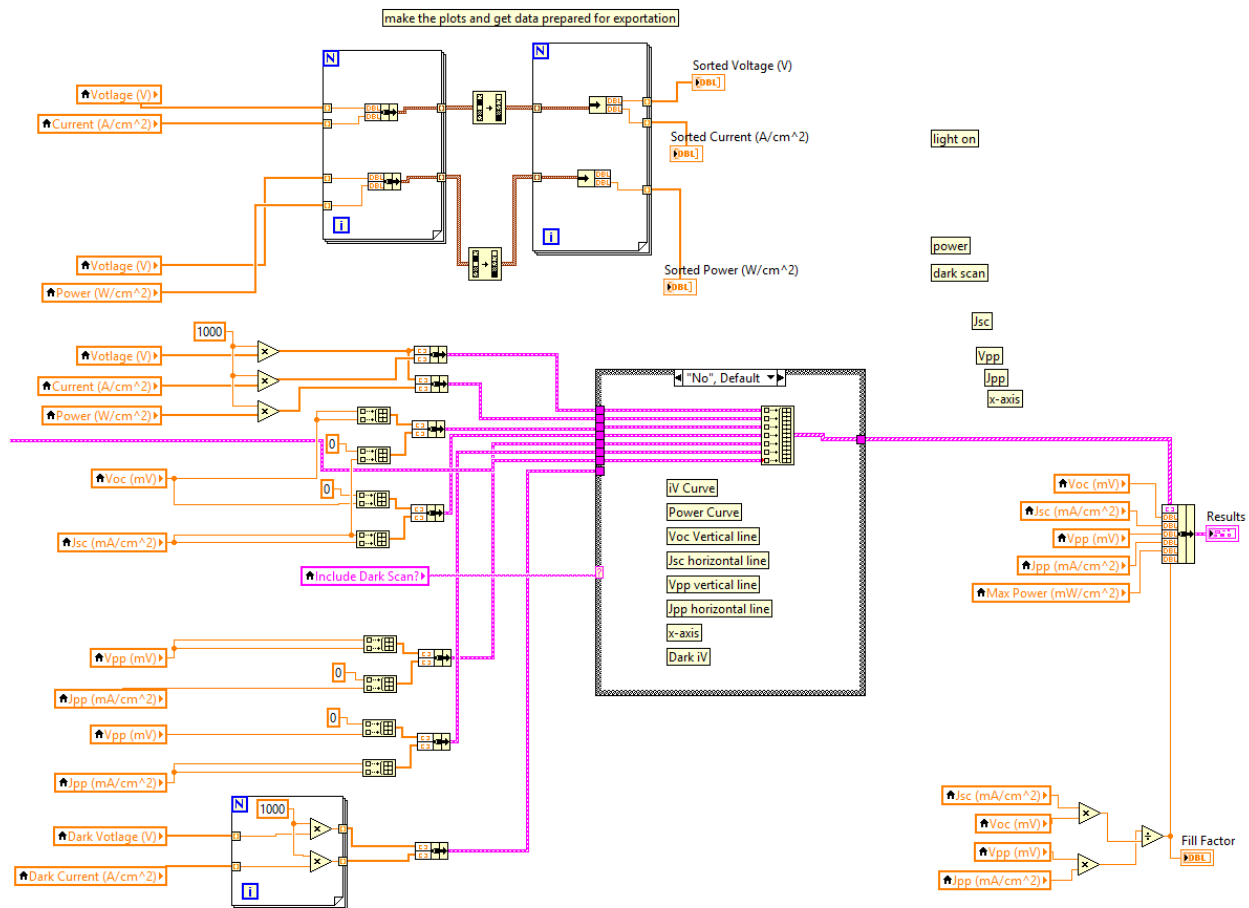


Figure A.10 iV Curve 'Block Diagram' Step 4: plot the dark, light, and power curves.

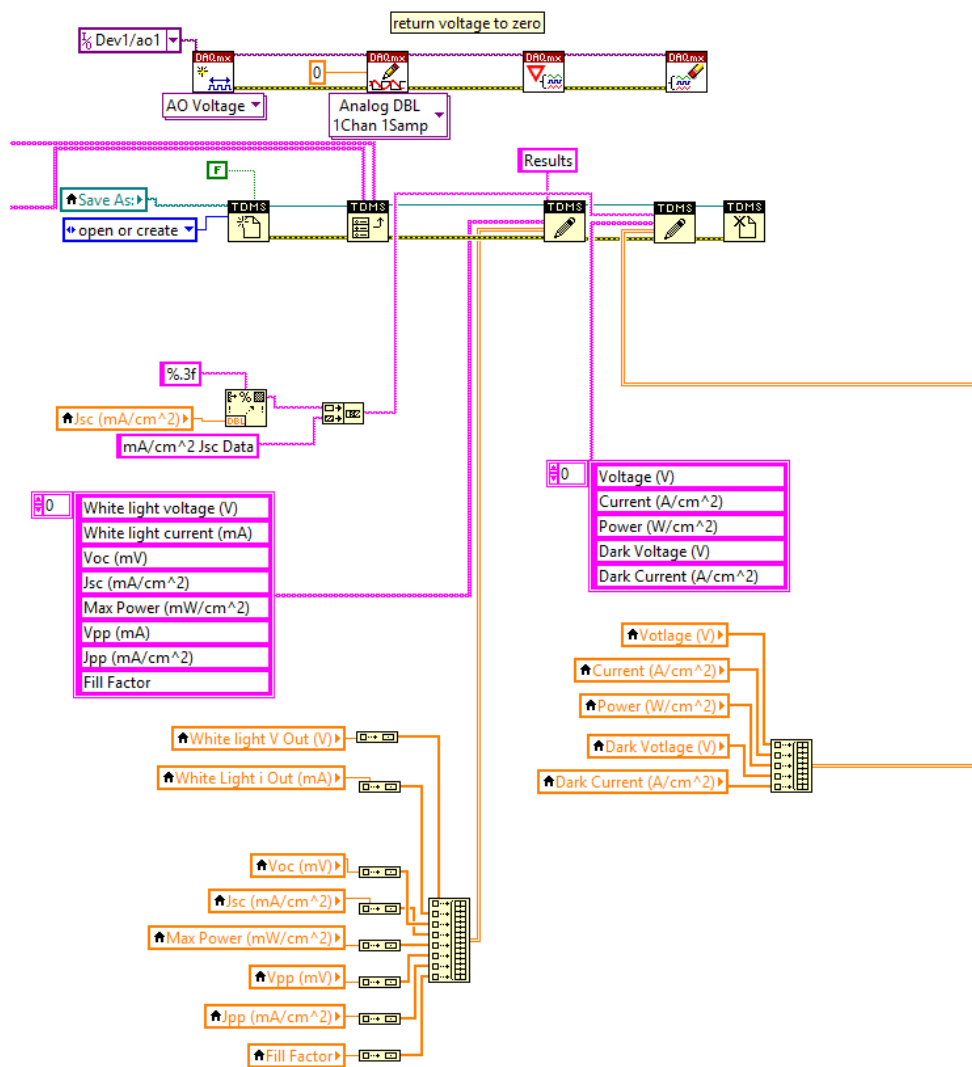


Figure A.11 iV Curve 'Block Diagram' Step 5: export the iV data as a .TDMS file and ensure the potentiostat is set to zero V.

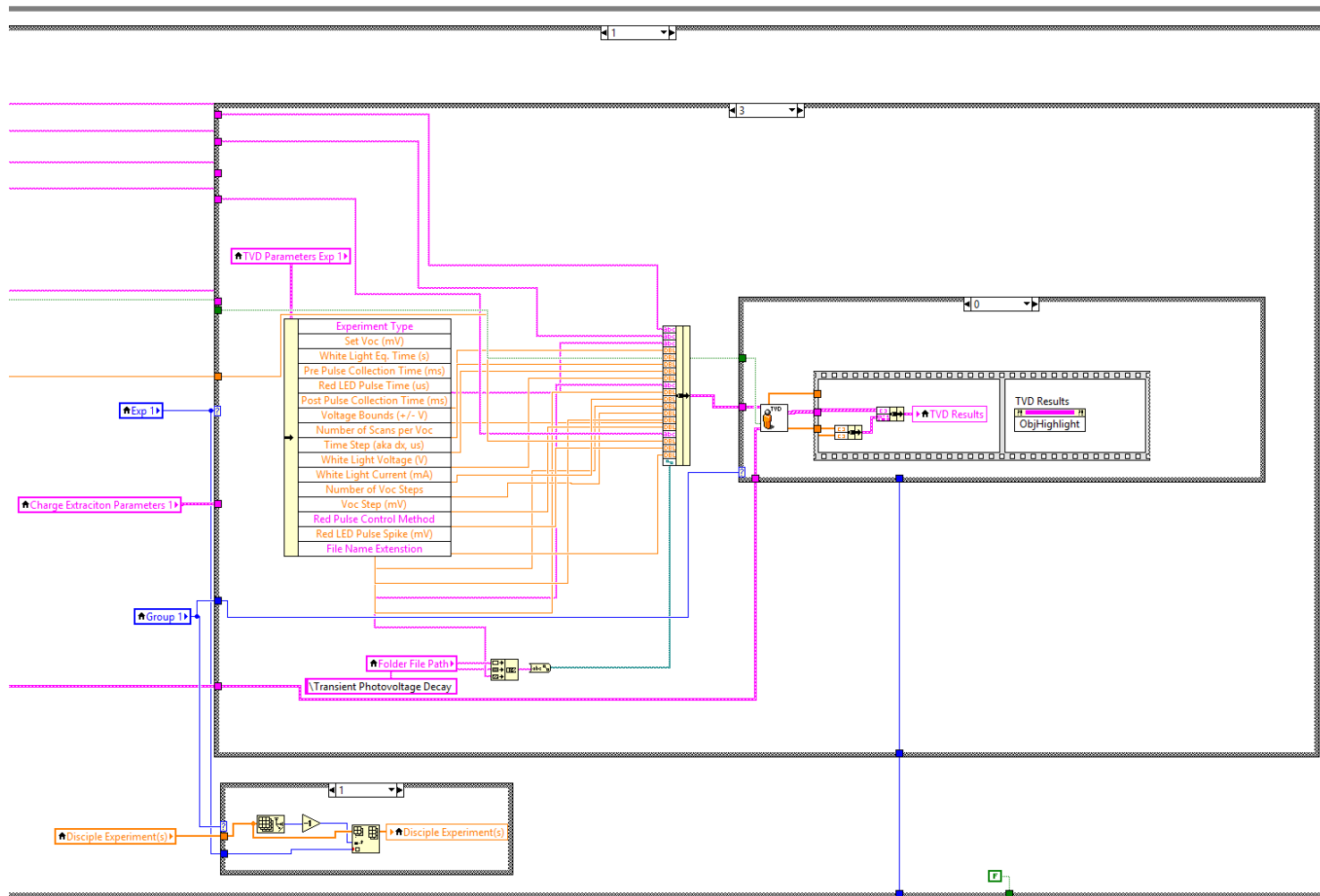


Figure A.12. STRiVE 5.0 user interface 'Block Diagram' selecting the third experiment, transient photovoltage decay.

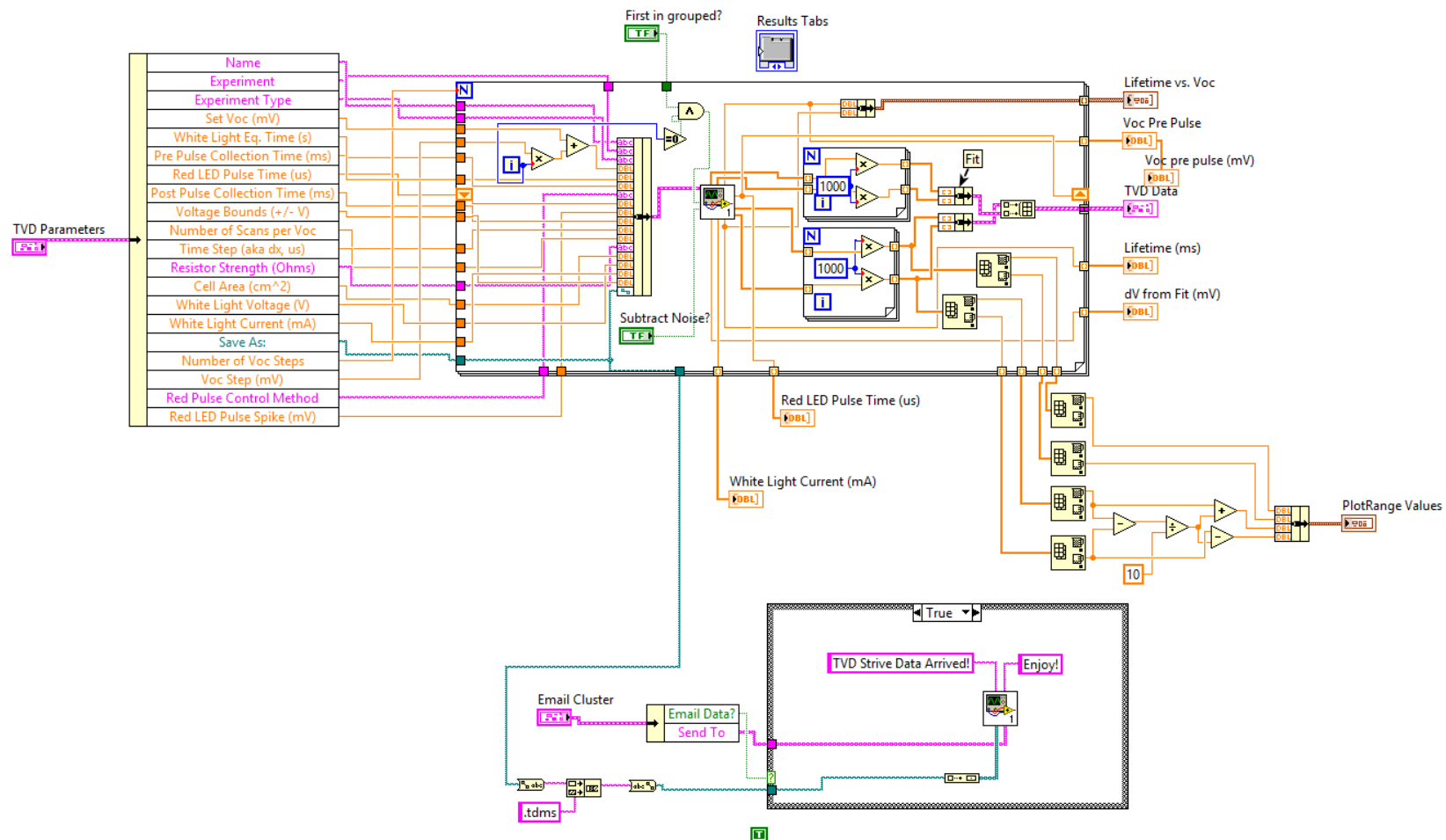


Figure A.13. Transient photovoltage decay 'Block Diagram' where multiple experiments are performed and then the results are collected and plotted.

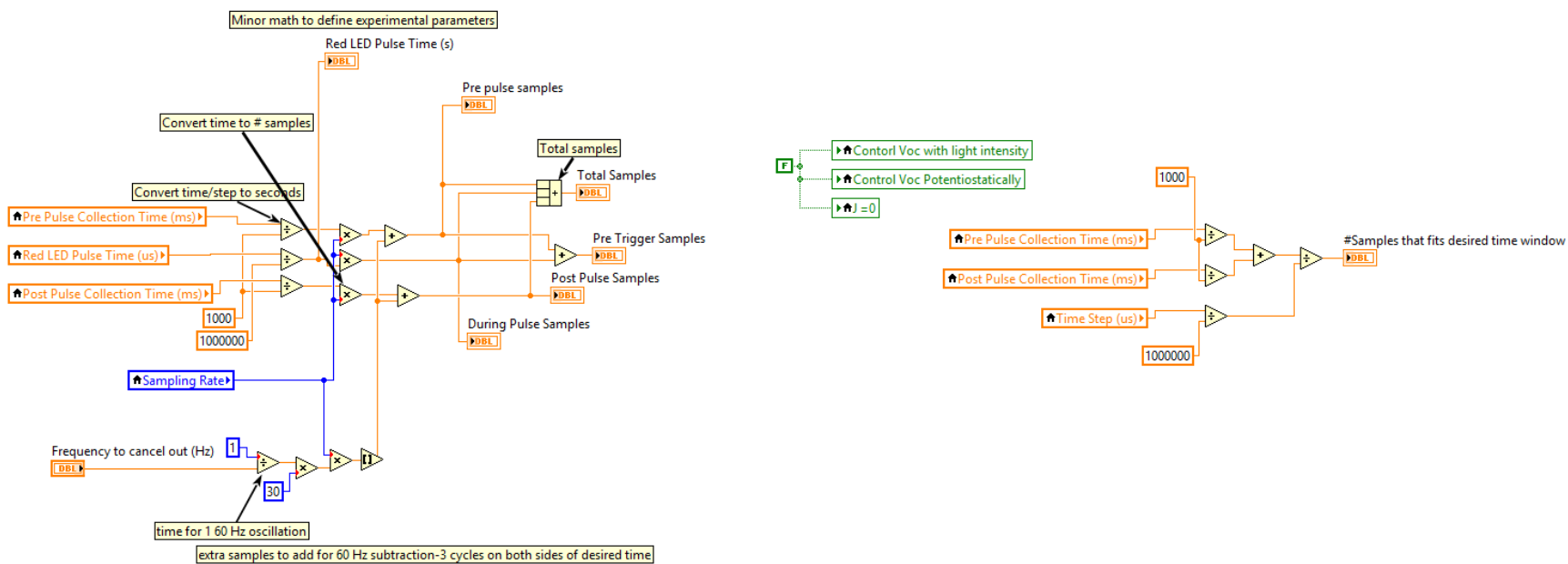


Figure A.14. Transient photovoltage decay experimental 'Block Diagram' step 1: calculate the sampling parameters.

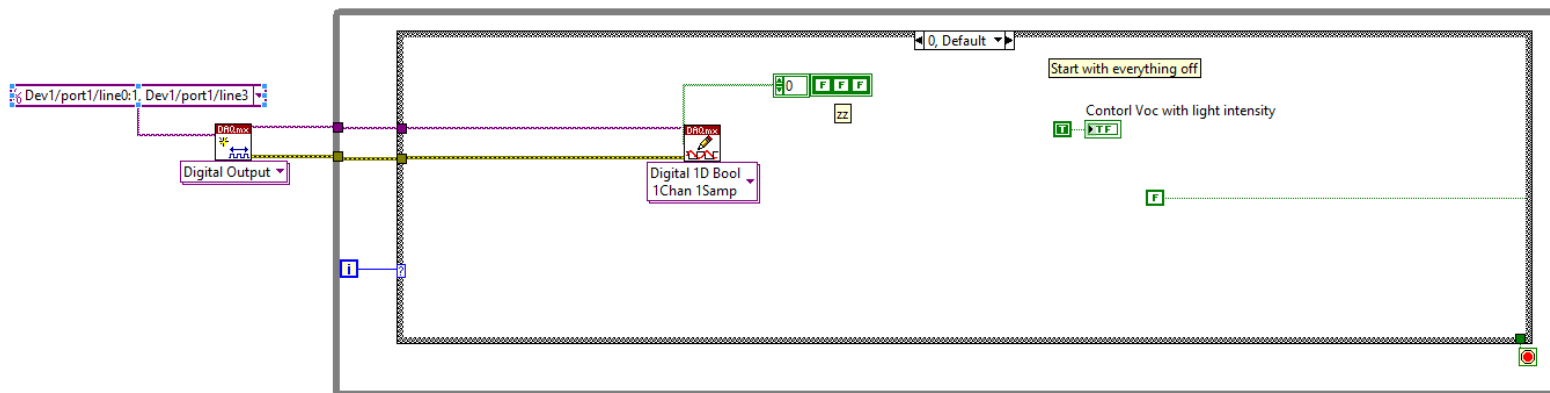


Figure A.15. Transient photovoltage decay experimental 'Block Diagram' step 2: start with the lights and potentiostat off.

209

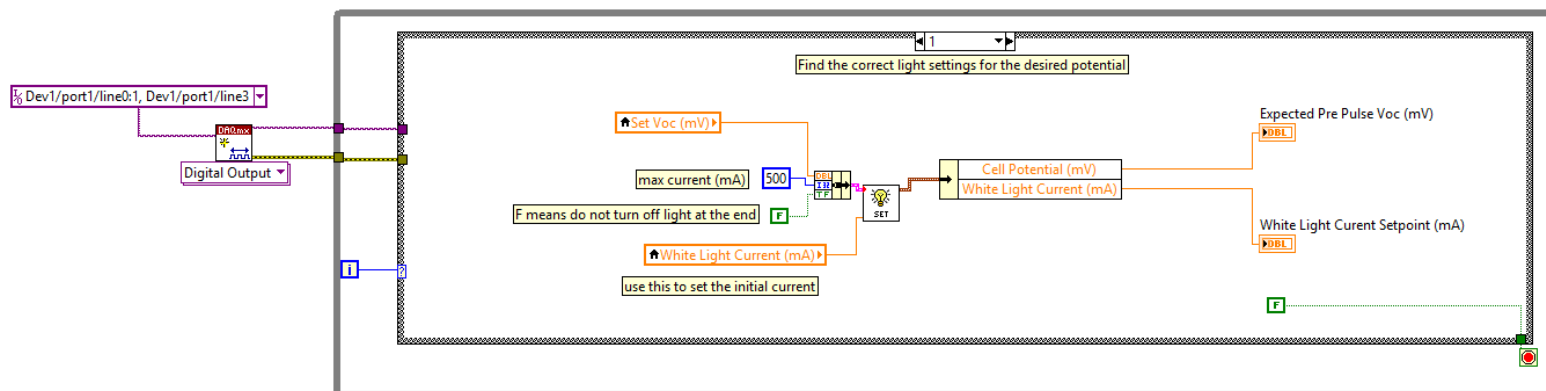


Figure A.16. Transient photovoltage decay experimental 'Block Diagram' step 3: set the light intensity. As shown, a subVI is selected where the STRiVE finds the light intensity to give a desired  $V_{OC}$ . This code is displayed in Figures A.24-A.27

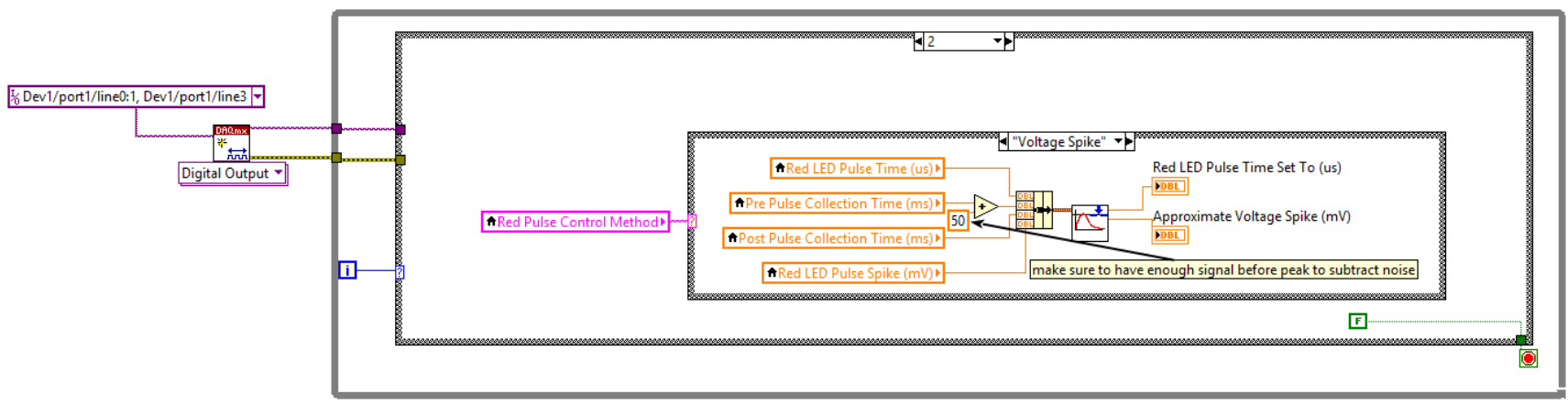


Figure A.17. Transient photovoltage decay experimental 'Block Diagram' step 4: set the pulse LED duration. As shown, the STRiVE will find the duration to give a desired 'Voltage Spike.' This code is displayed in Figure A.30.

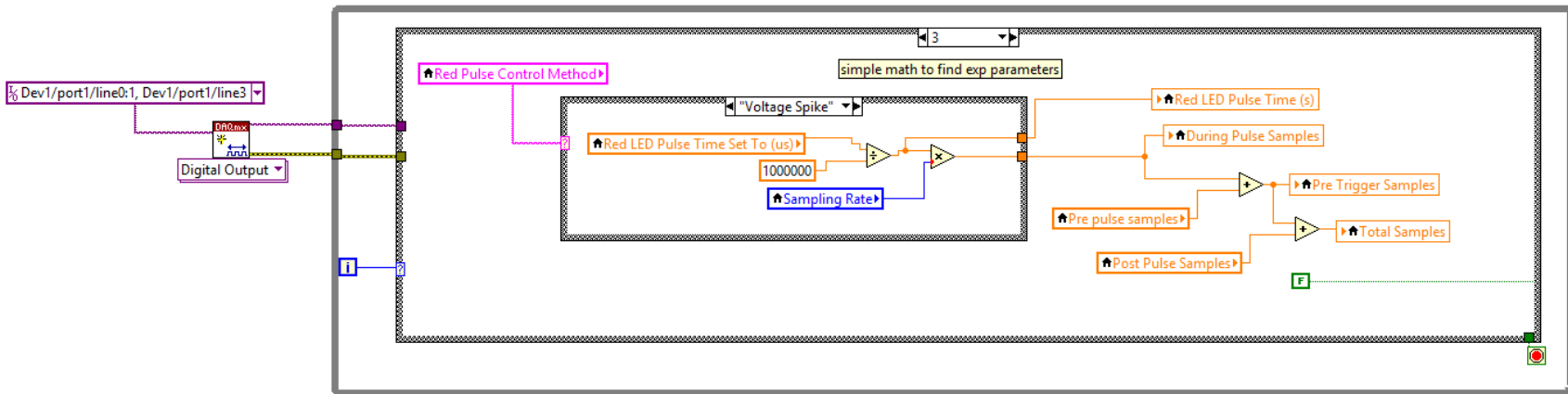


Figure A.18. Transient photovoltage decay experimental 'Block Diagram' step 5: finalize sampling parameters using the LED pulse time defined in step 4.

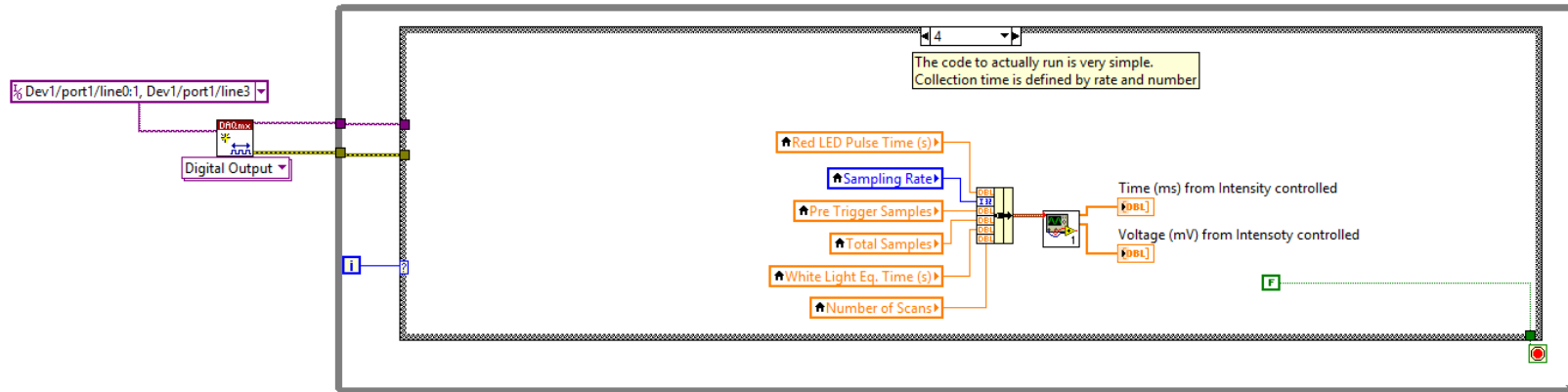


Figure A.19. Transient photovoltage decay experimental 'Block Diagram' step 6: collect the data. This code is found in Figures A.28-

212

29.

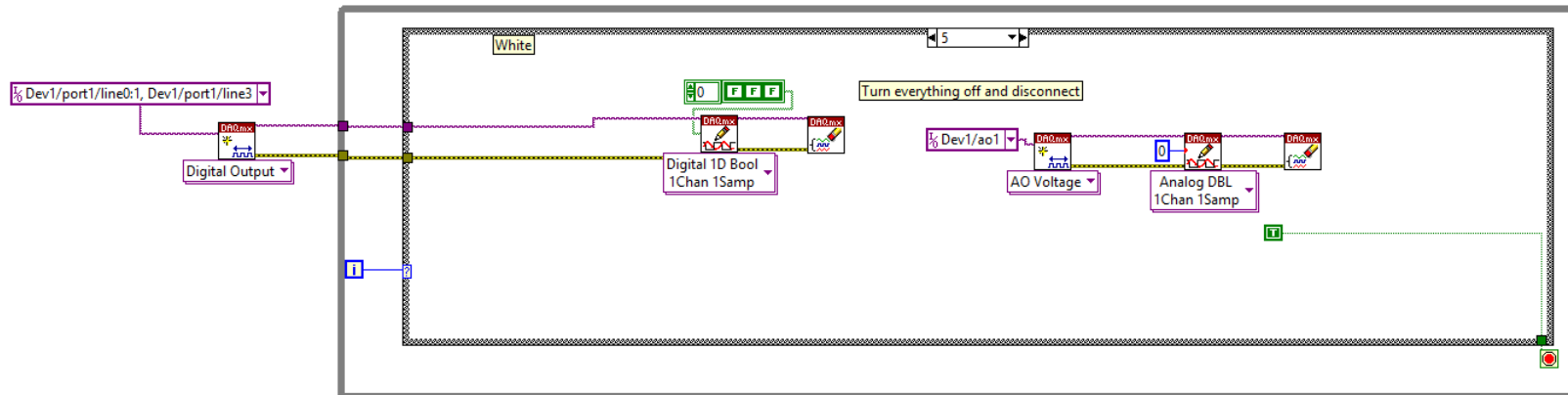


Figure A.20. Transient photovoltage decay experimental 'Block Diagram' step 7: turn everything off.

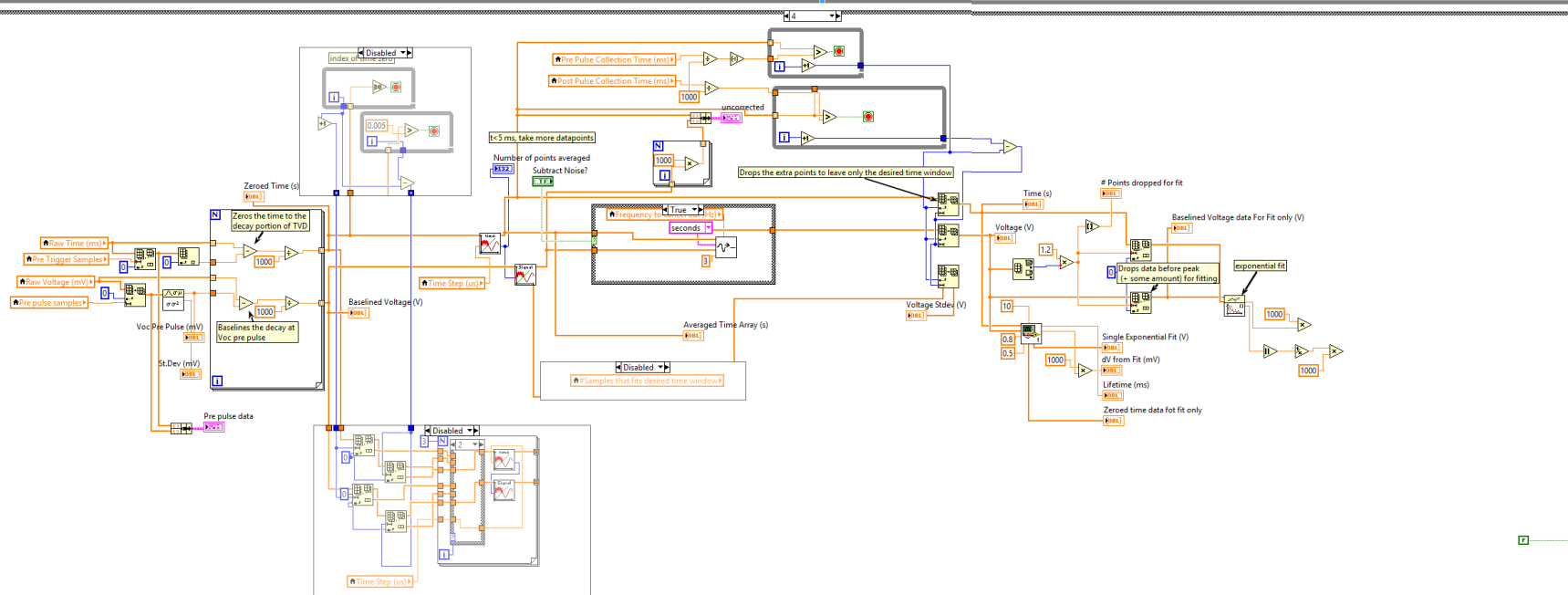


Figure A.21. Transient photovoltage decay experimental 'Block Diagram' step 8: baseline the data and calculate the electron lifetime.

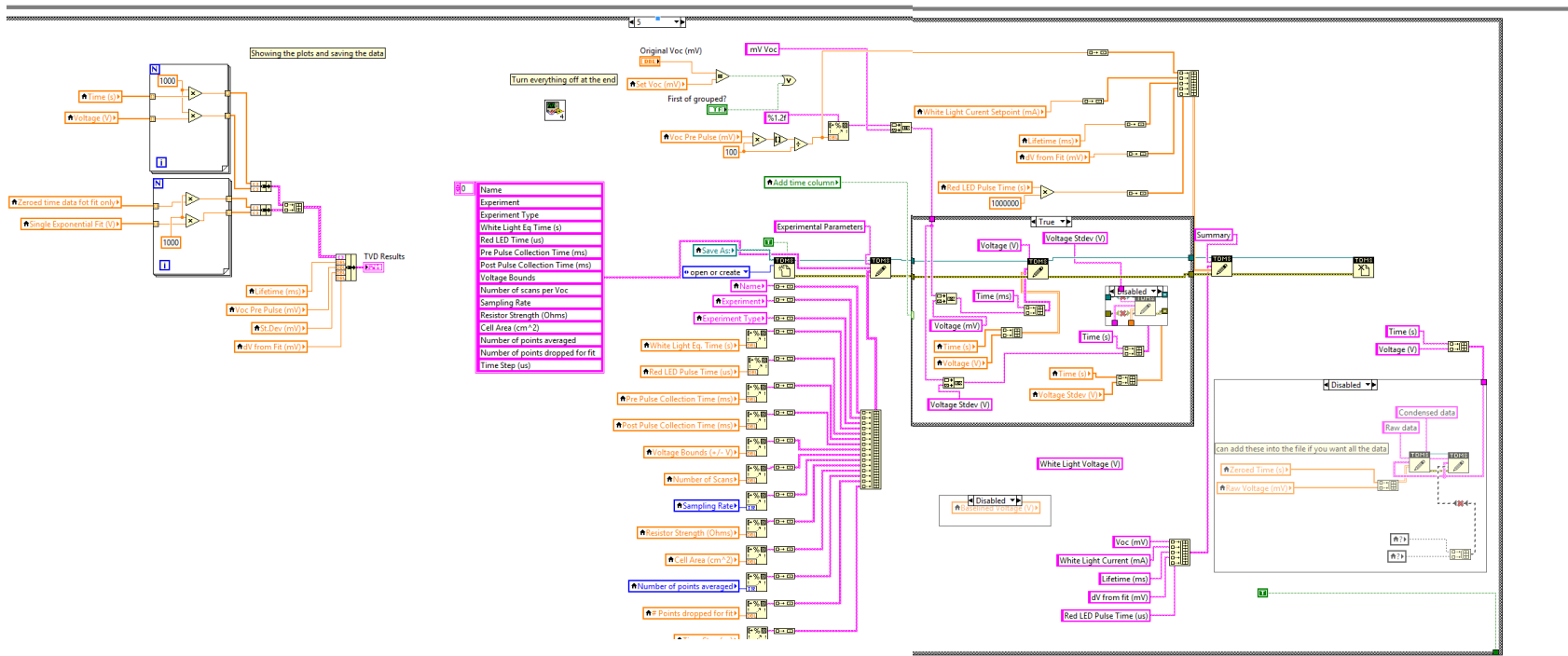


Figure A.22. Transient photovoltage decay experimental 'Block Diagram' step 9: display the results and export the data as a .TDMS file.

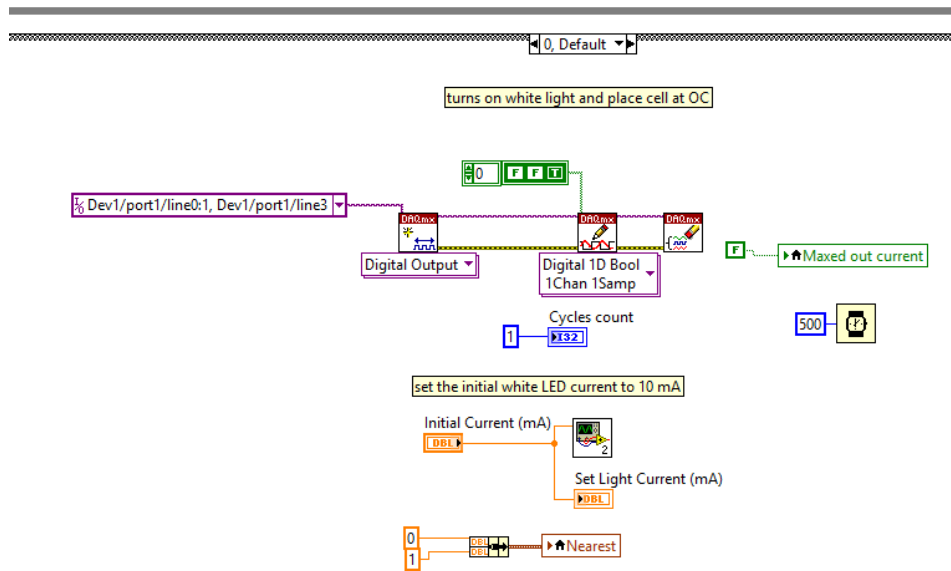


Figure A.23. Set light intensity step 0: begin with the user defined current.

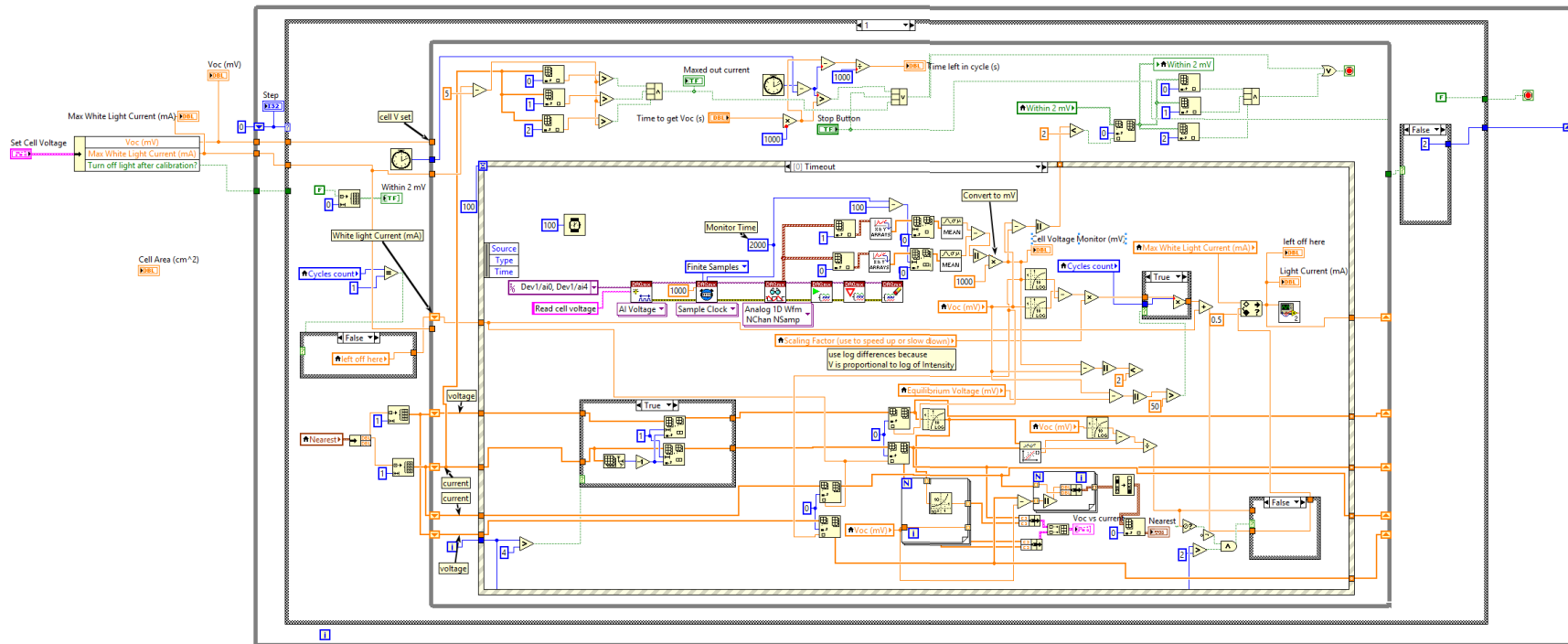


Figure A.24. Set light intensity step 1: monitor the voltage as the light intensity is adjusted. The most 3 recent data points are used in a fit to better approximate the next light intensity output.

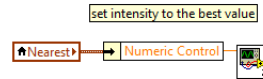
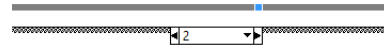


Figure A.25. Set light intensity step 2: set light intensity as the one that was produced the nearest  $V_{OC}$  to the target.

217

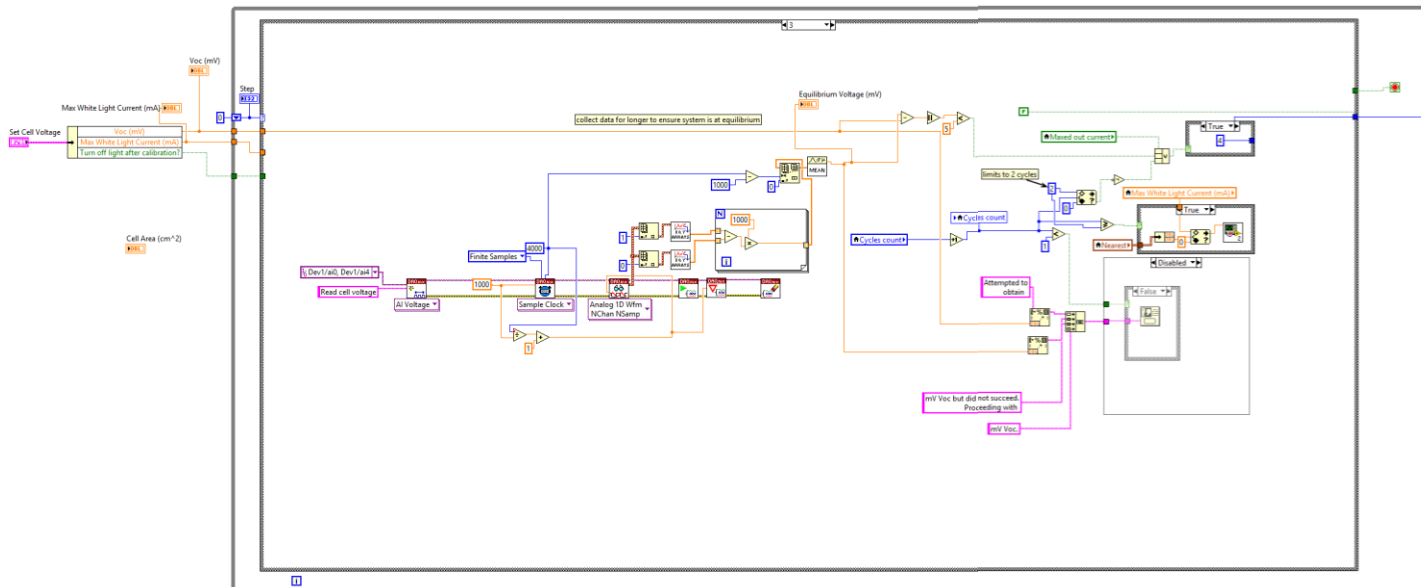


Figure A.26. Set light intensity step 3: Monitor the voltage for 5 seconds and check if the equilibrium value is within 5 mV of the target  $V_{OC}$ .

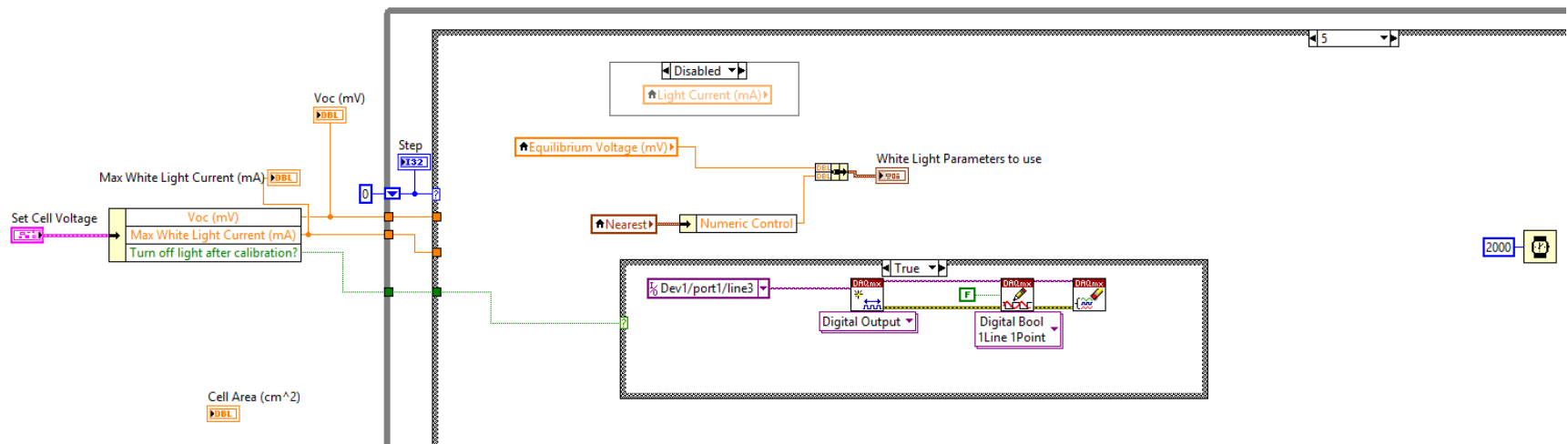


Figure A.27. Set light intensity step 4: Output the light intensity.



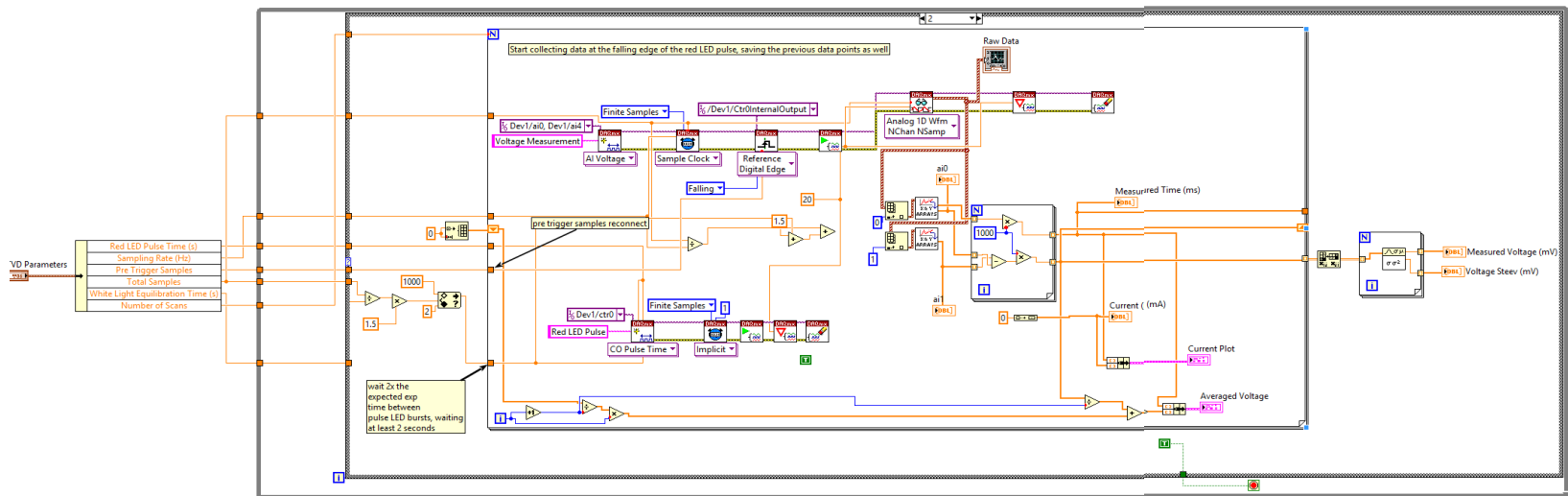


Figure A.29. Transient photovoltage decay Collect Data step 2: use an internal time ‘counter’ to control the pulse LED and trigger data collection (Reference Digital Edge) that monitors the cell voltage. This process is repeated and averaged.

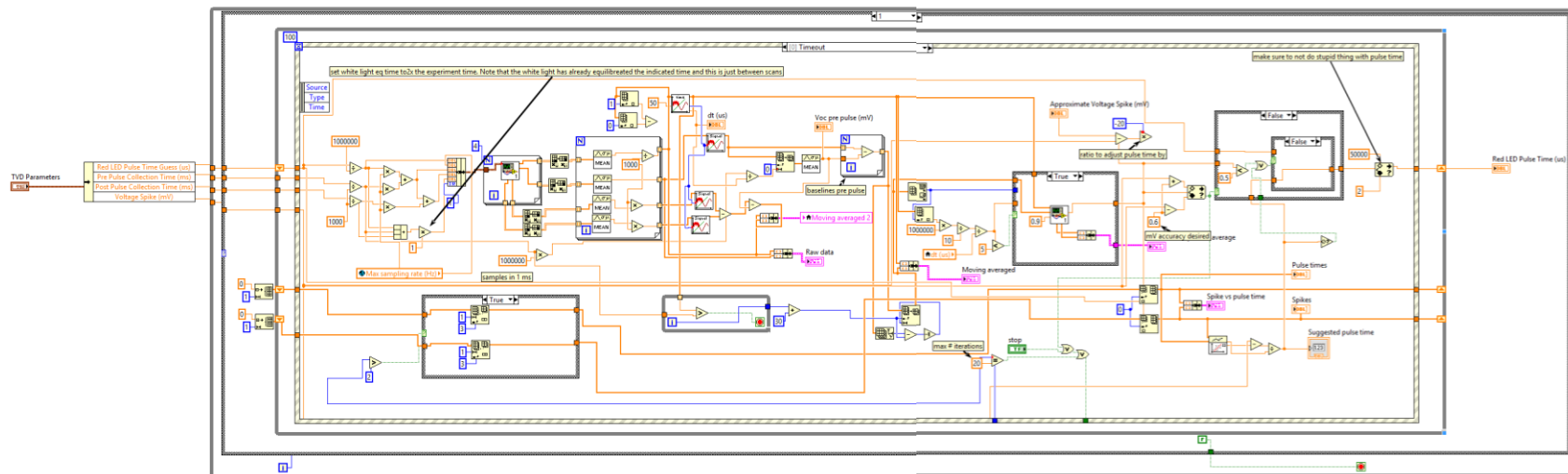


Figure A.30. Transient photovoltage decay ‘Set Voltage Spike’ key code. The pulse time is adjusted and the transient photovoltage peak is calculated. The most 3 recent pulses are used to fit and better estimate the required pulse time.

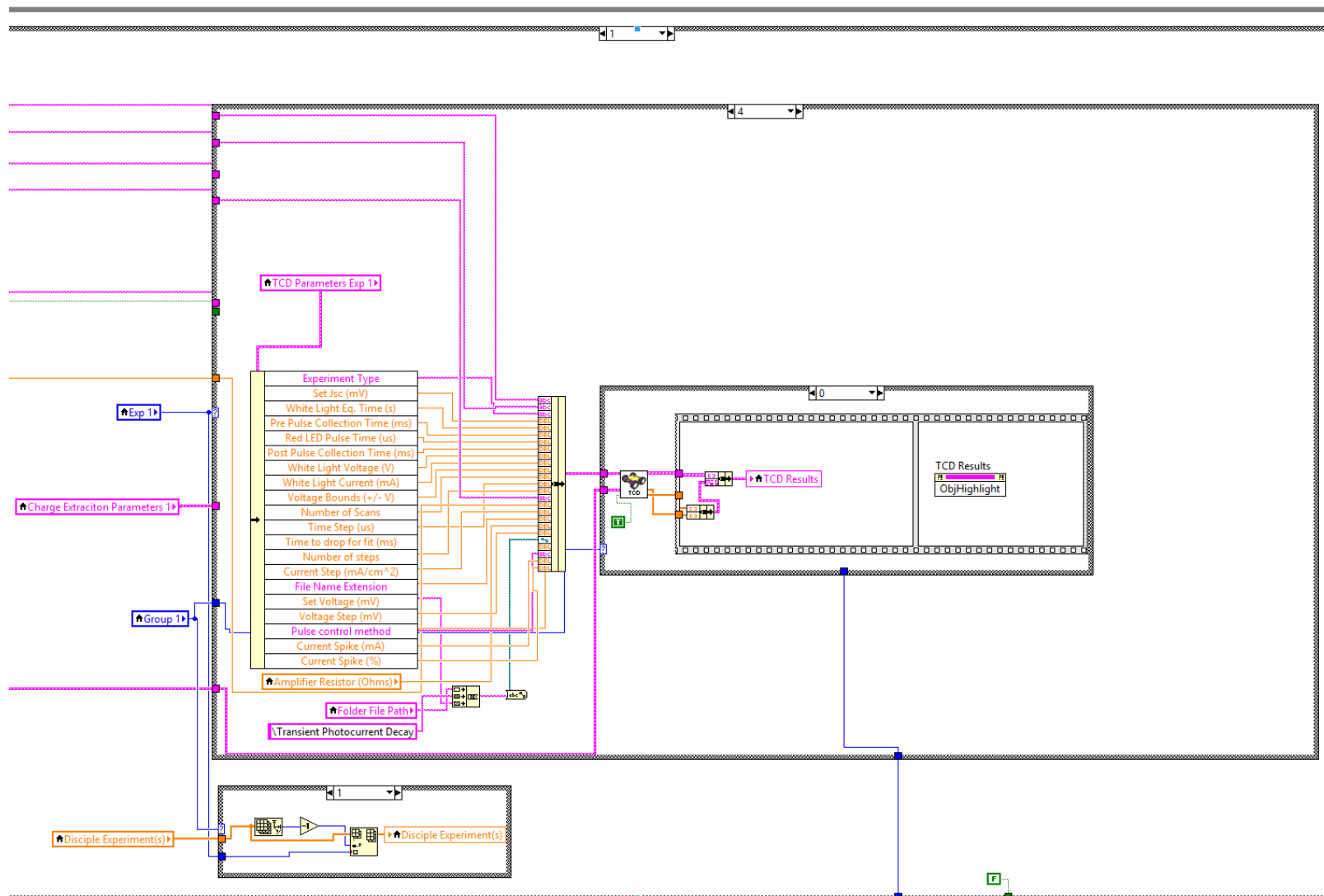


Figure A.31. STRiVE 5.0 user interface 'Block Diagram' selecting the fourth experiment, transient photocurrent decay.

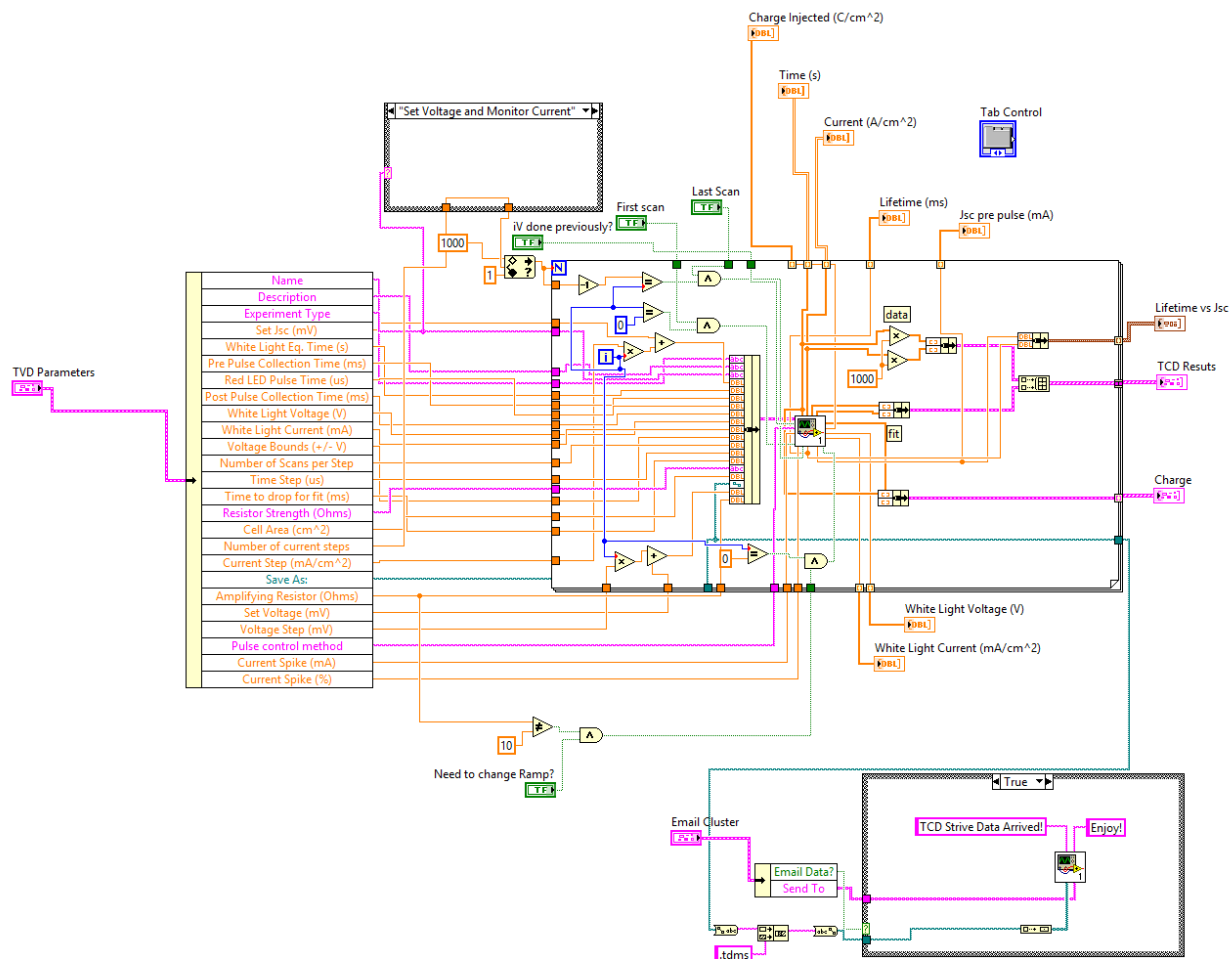


Figure A.32. Transient photocurrent decay 'Block Diagram' where multiple experiments are performed and then the results are collected and plotted.

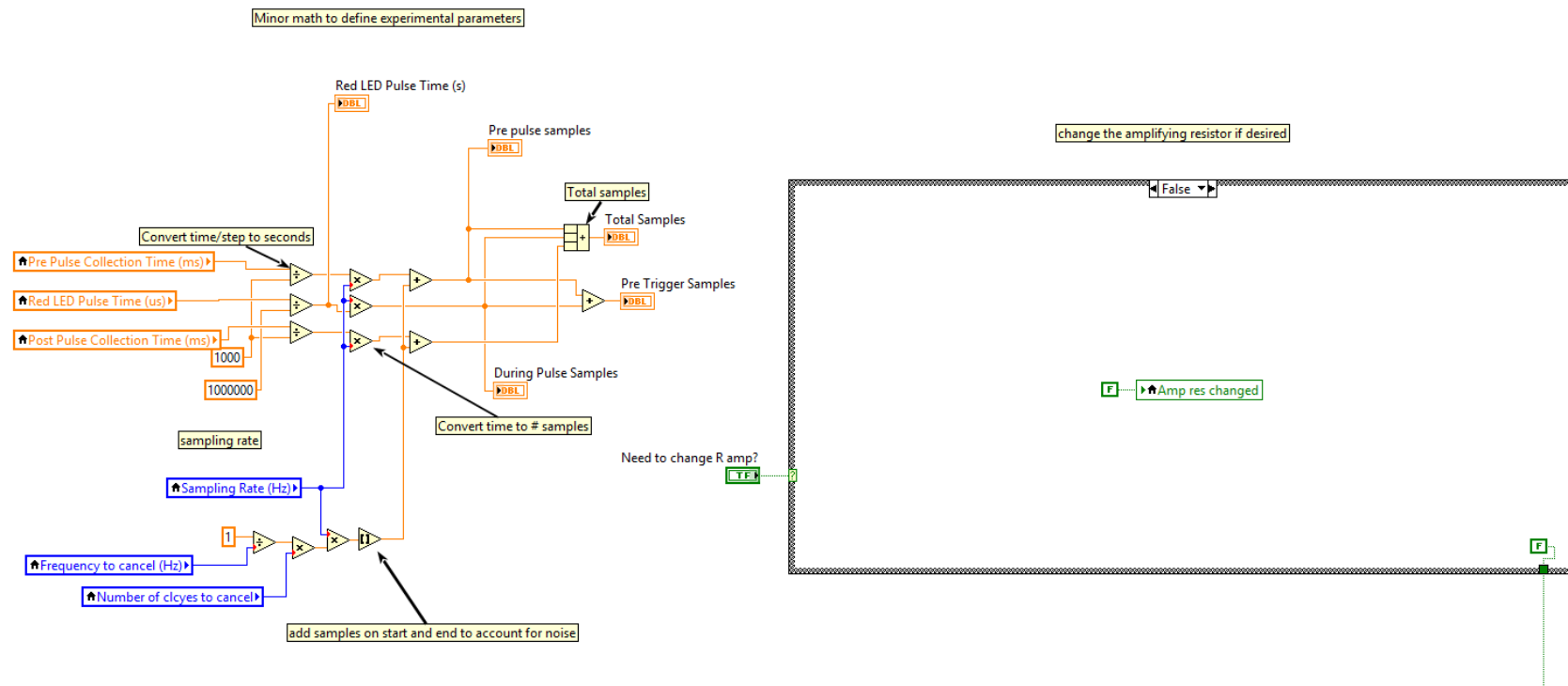


Figure A.33. Transient photocurrent decay experimental ‘Block Diagram’ step 1: calculate the sampling parameters.



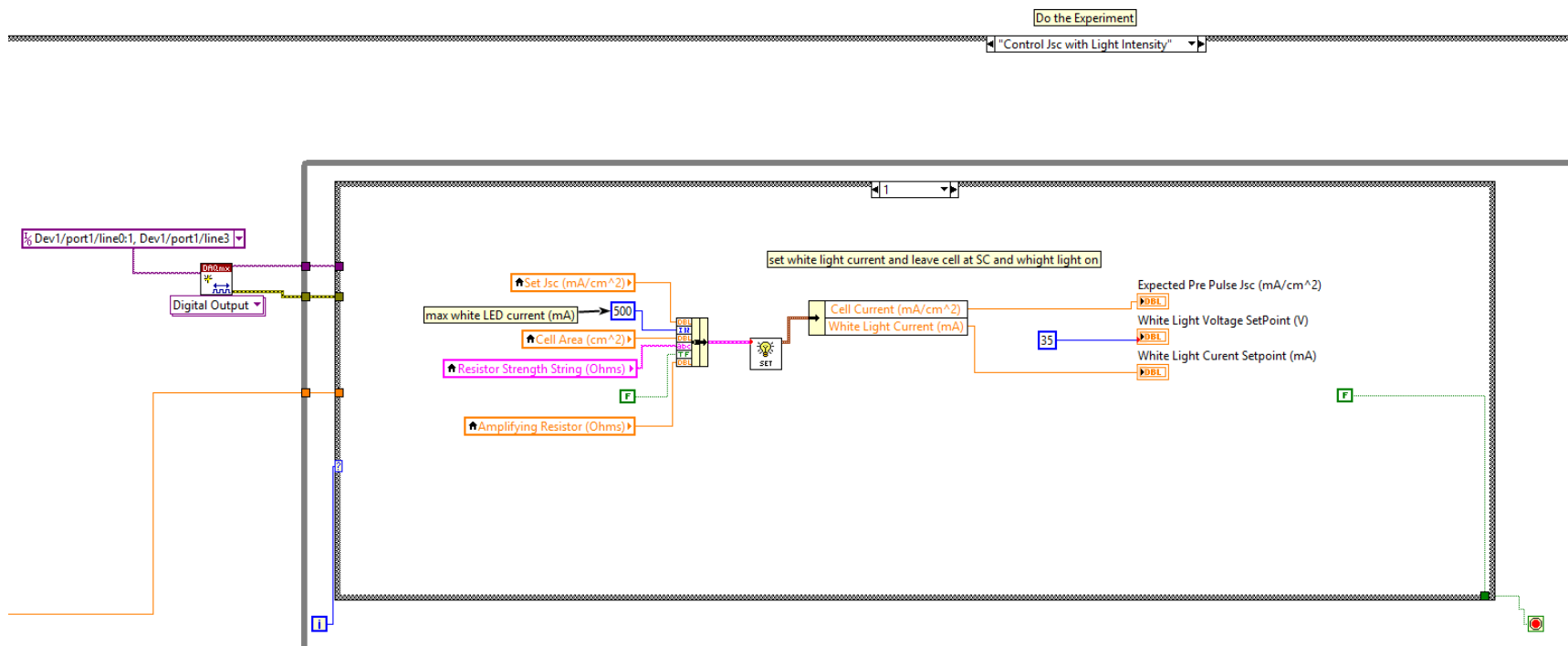


Figure A.35. Transient photocurrent decay experimental 'Block Diagram' step 3: set the light intensity. As shown the STRiVE will adjust the light intensity to get a defined  $J_{sc}$ . This code is very similar to adjusting the light intensity to set the  $V_{oc}$ , Figures A.24-27.



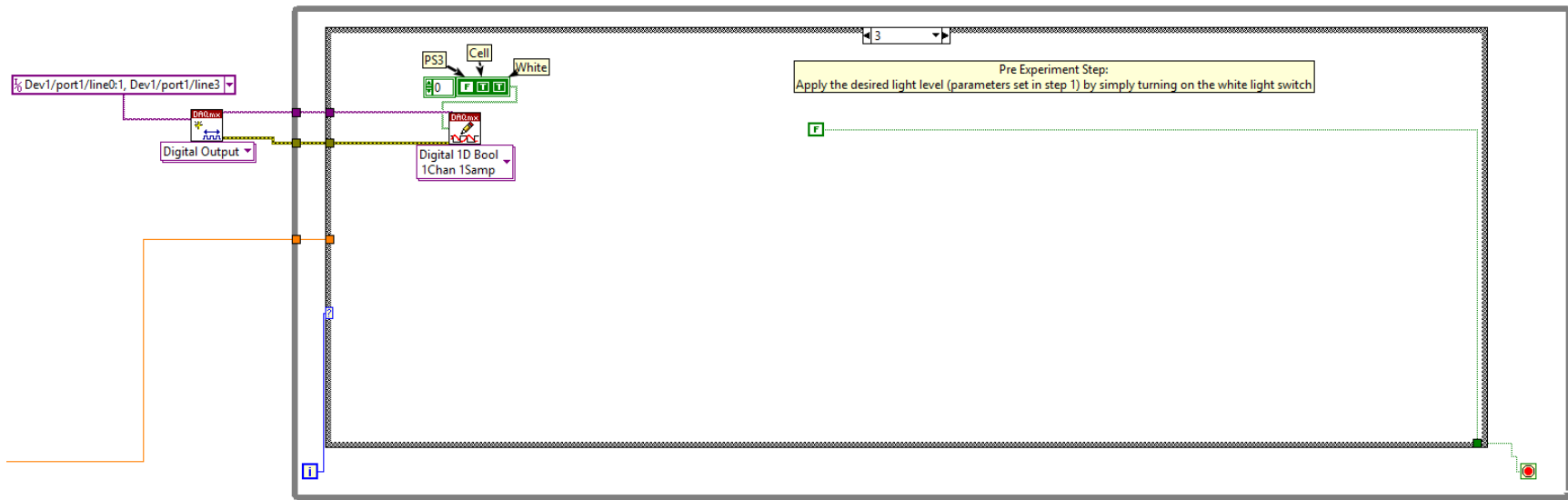


Figure A.37. Transient photocurrent decay experimental 'Block Diagram' step 5: Apply the set parameters.

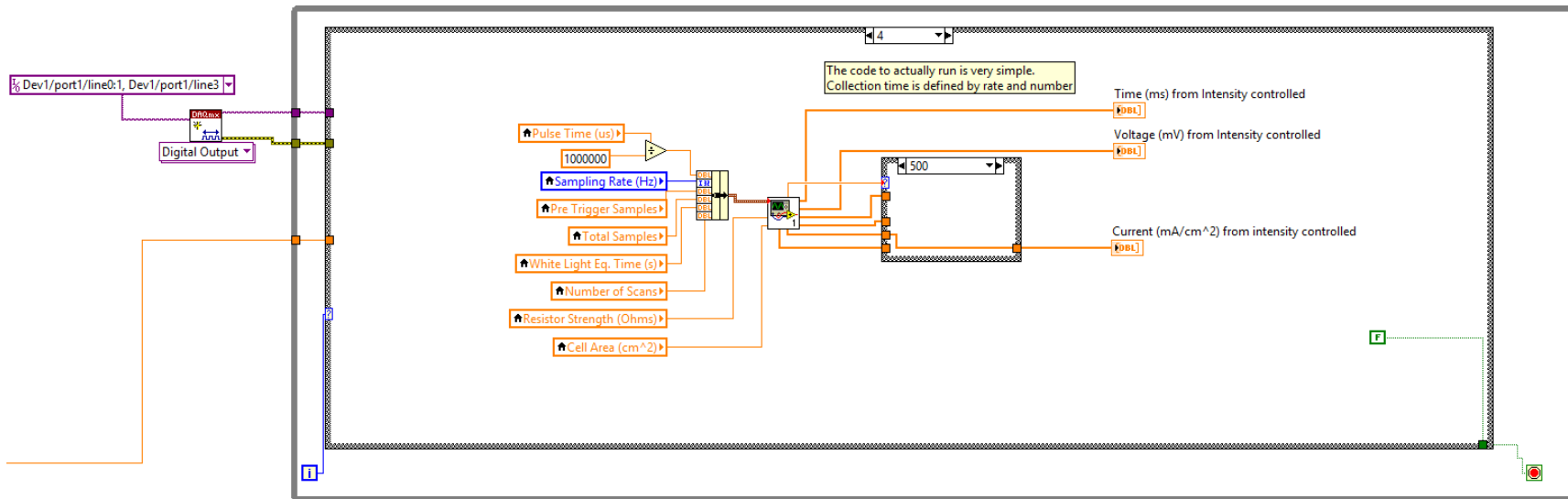


Figure A.38. Transient photocurrent decay experimental 'Block Diagram' step 6: collect the data. This code can be found in Figure A.42.

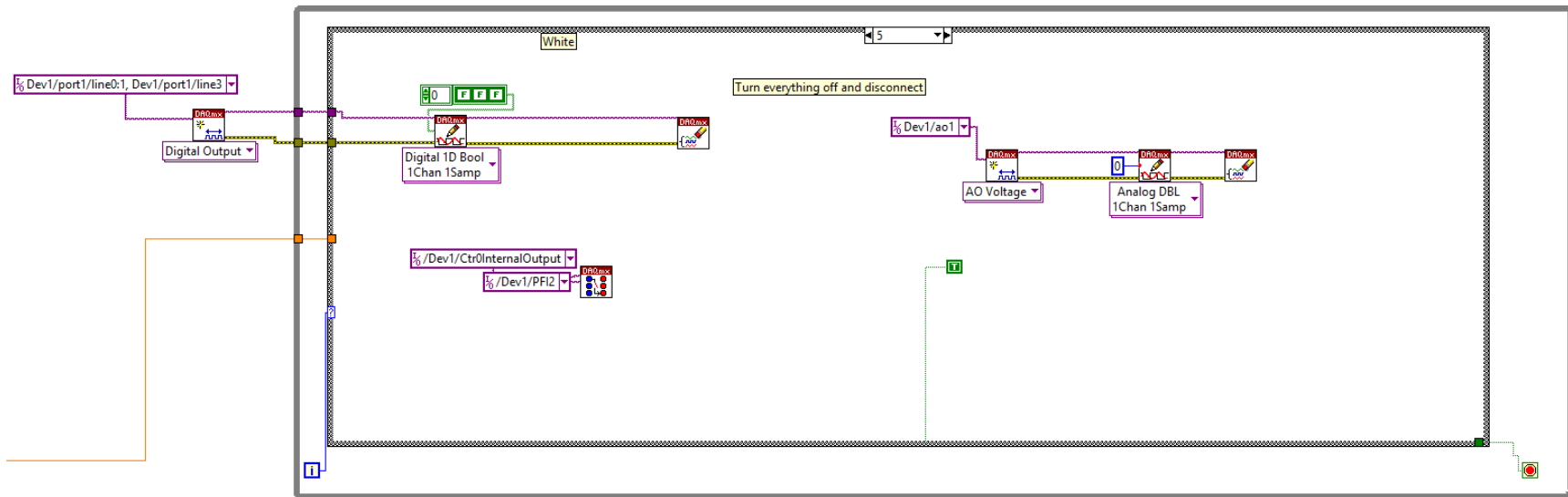


Figure A.39. Transient photocurrent decay experimental 'Block Diagram' step 7: turn everything off and disconnect the potentiostat.

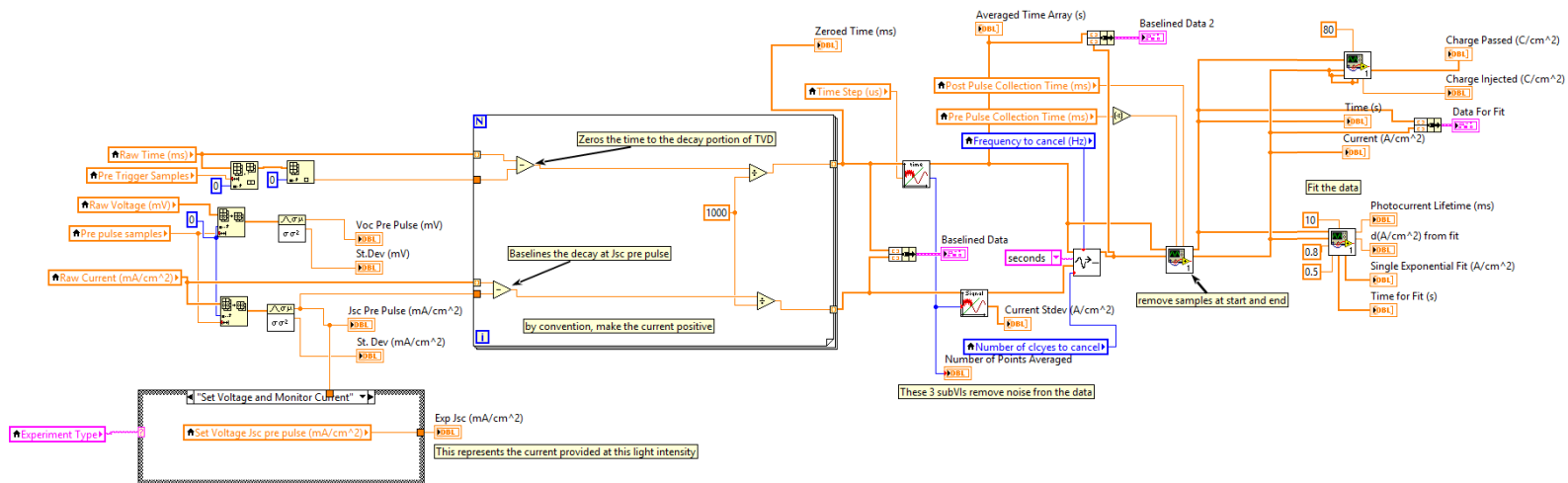


Figure A.40. Transient photocurrent decay experimental 'Block Diagram' step 8: baseline the data and calculated the photocurrent lifetime.

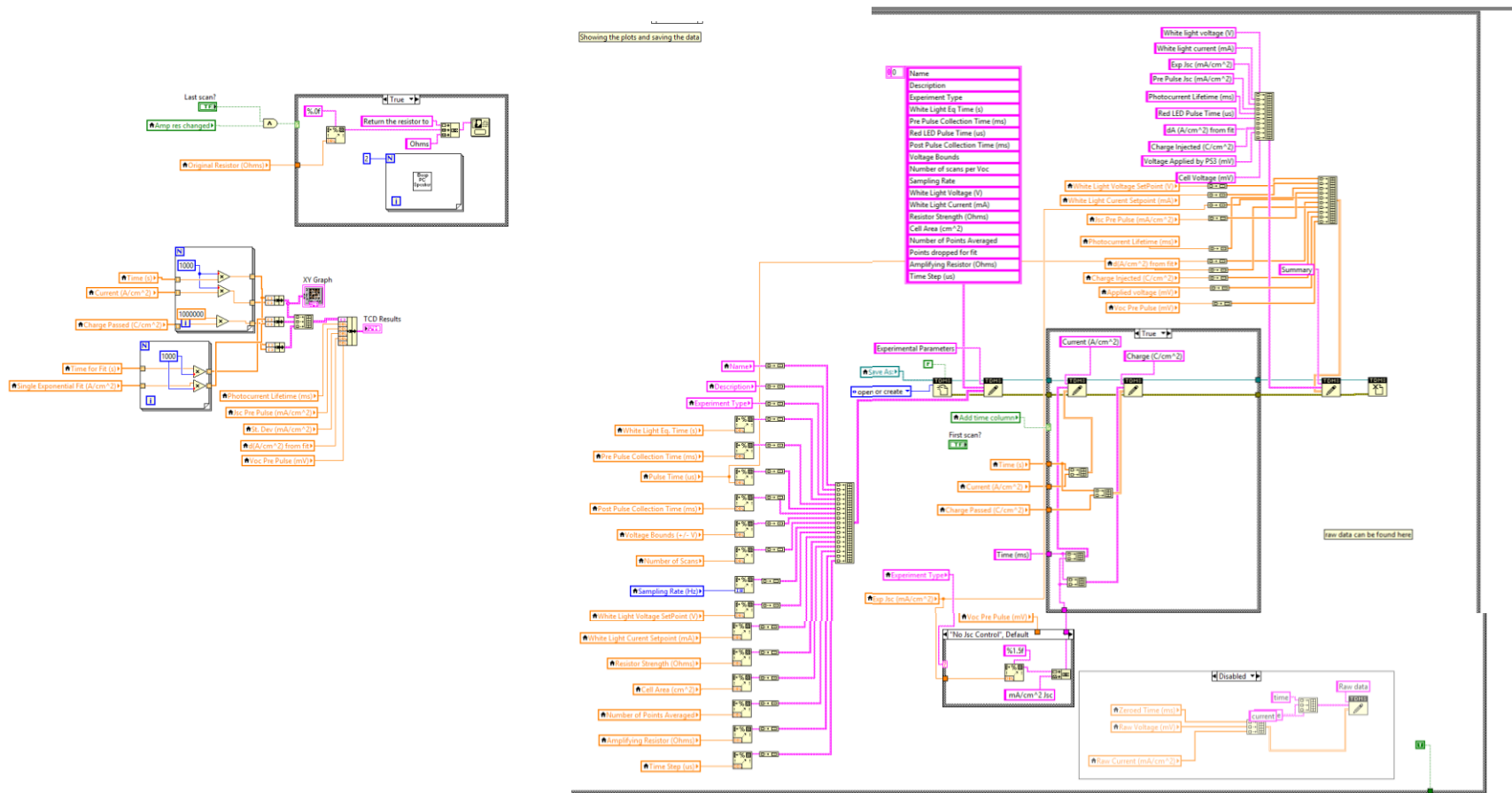


Figure A.41. Transient photocurrent decay experimental 'Block Diagram' step 9: plot the data and export the results as a .TDMS file.

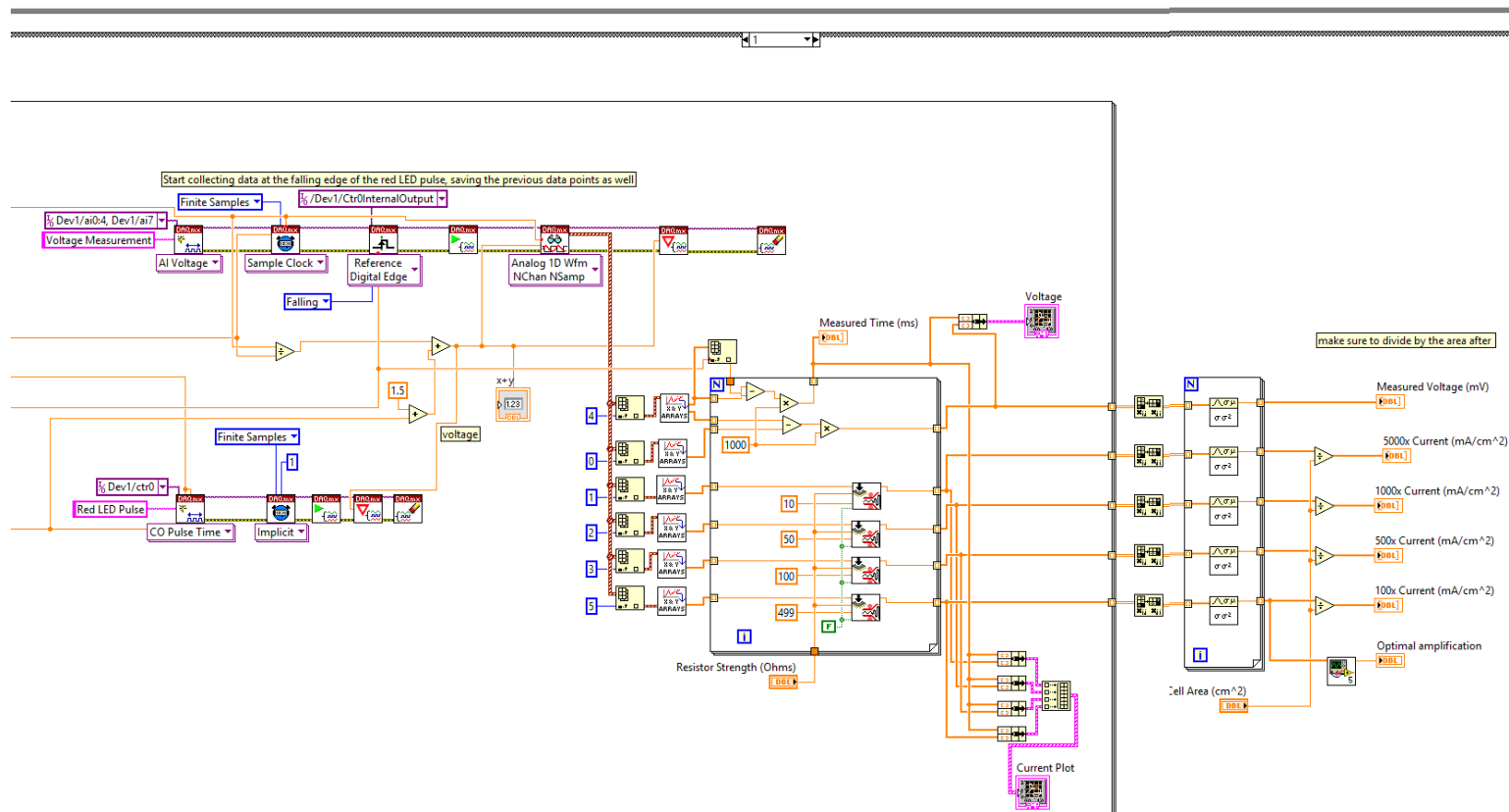


Figure A.42. Transient photocurrent decay Collect Data 'Block Diagram.' An internal time counter is used to define the pulse time and trigger the start of data acquisition. This process is repeated a defined number of times and averaged.

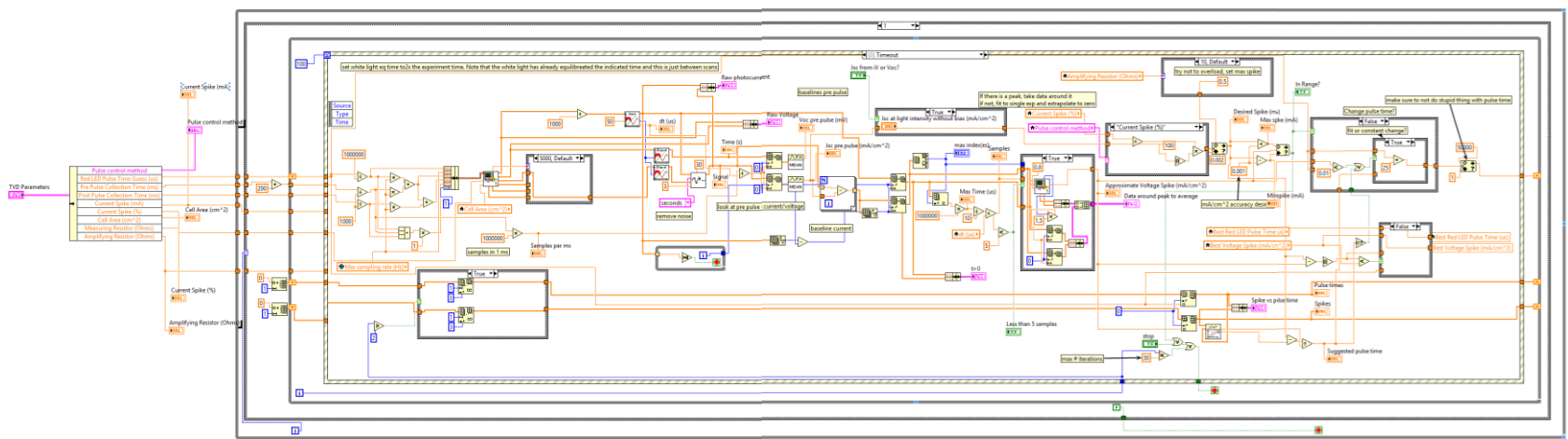


Figure A.43. Transient photocurrent decay Set Current Spike ‘Block Diagram.’ The STRiVE adjusts the pulse time and monitors the current spike. The 3 most recent spikes are fit to more accurately determine the next pulse time.

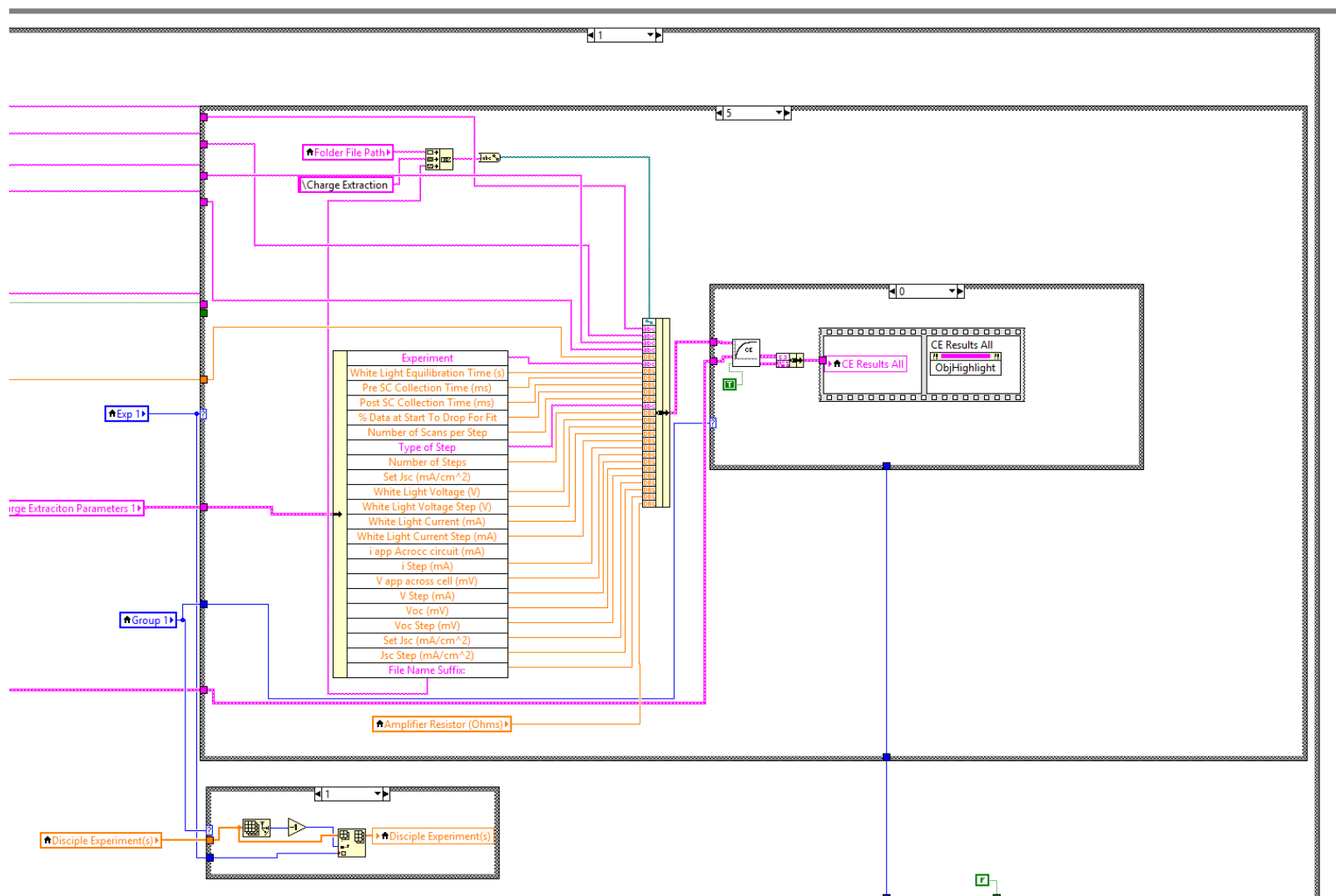


Figure A.44. STRiVE 5.0 user interface 'Block Diagram' selecting the fifth experiment, charge extraction.

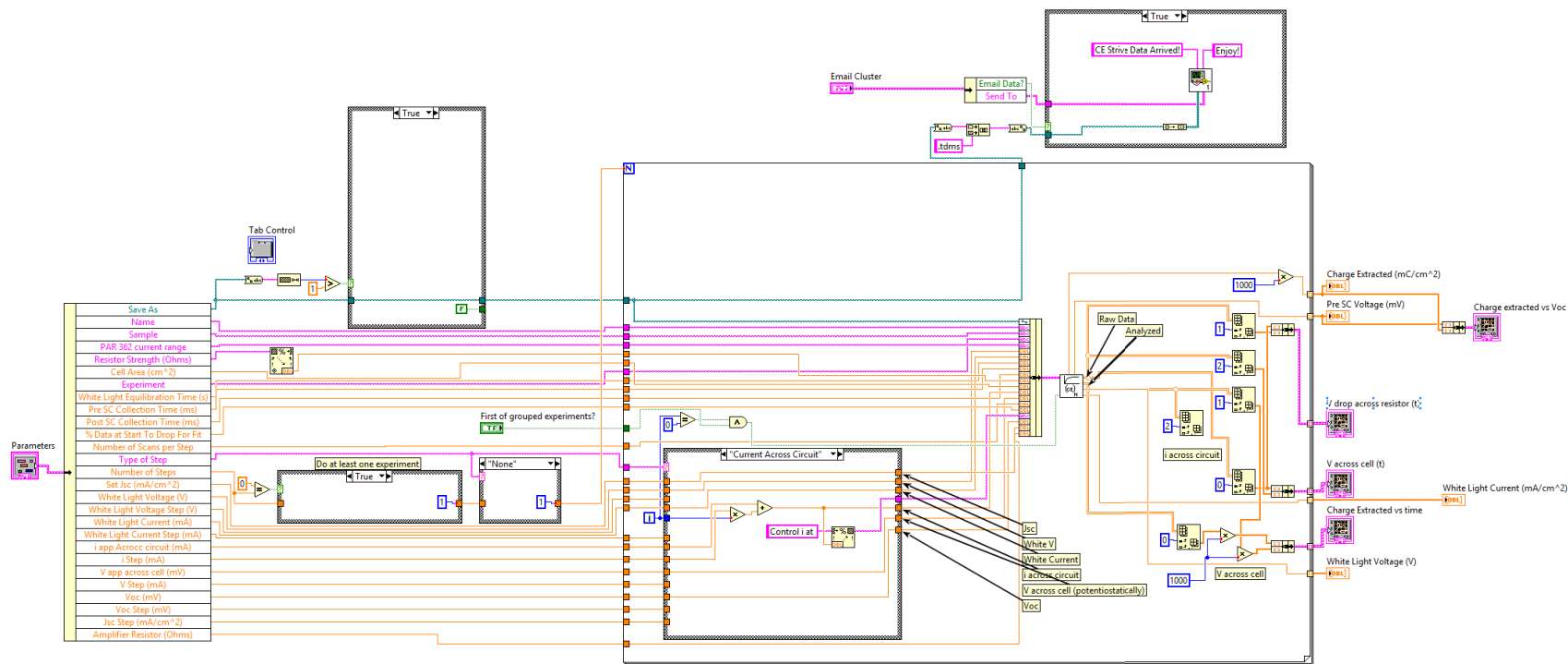


Figure A.45. Charge extraction 'Block Diagram' displaying how multiple experiments are performed and displayed.

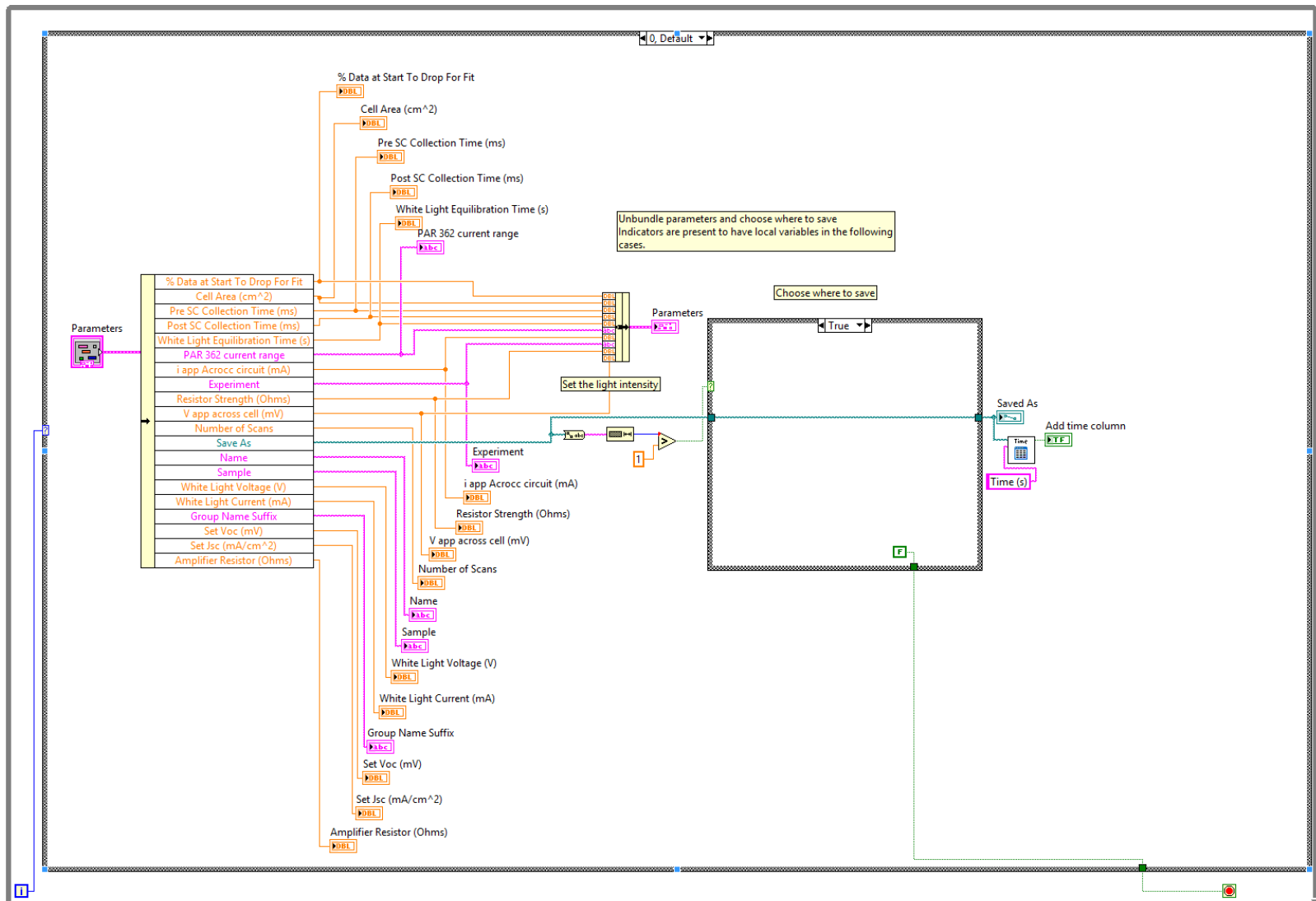


Figure A.46. Charge extraction experimental 'Block Diagram' step 1: define the experimental parameters.

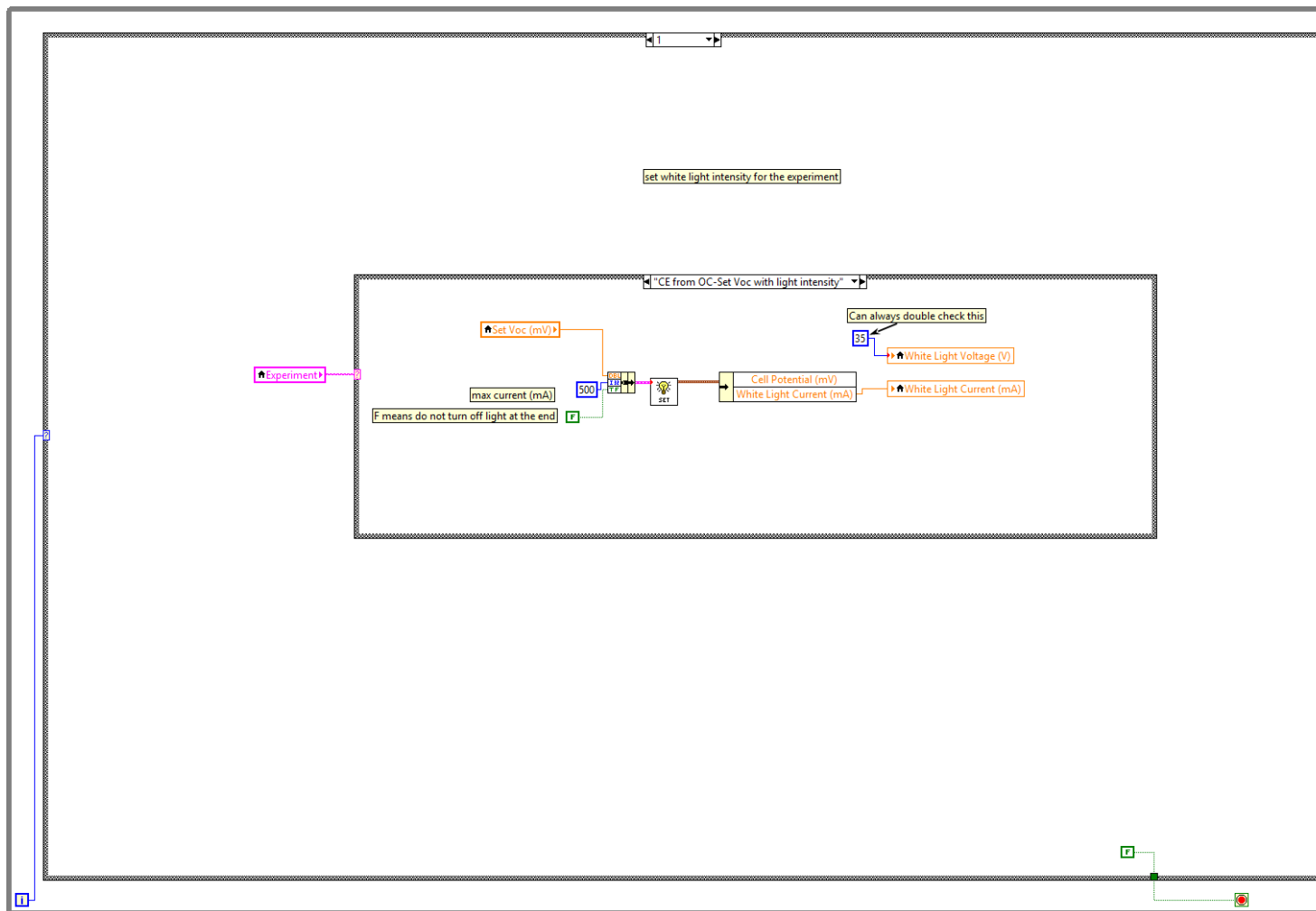


Figure A.47. Charge extraction experimental 'Block Diagram' step 2: set the light intensity. As shown the STRiVE will find the light intensity for a given  $V_{oc}$ . This code can be found in Figure A24-27.

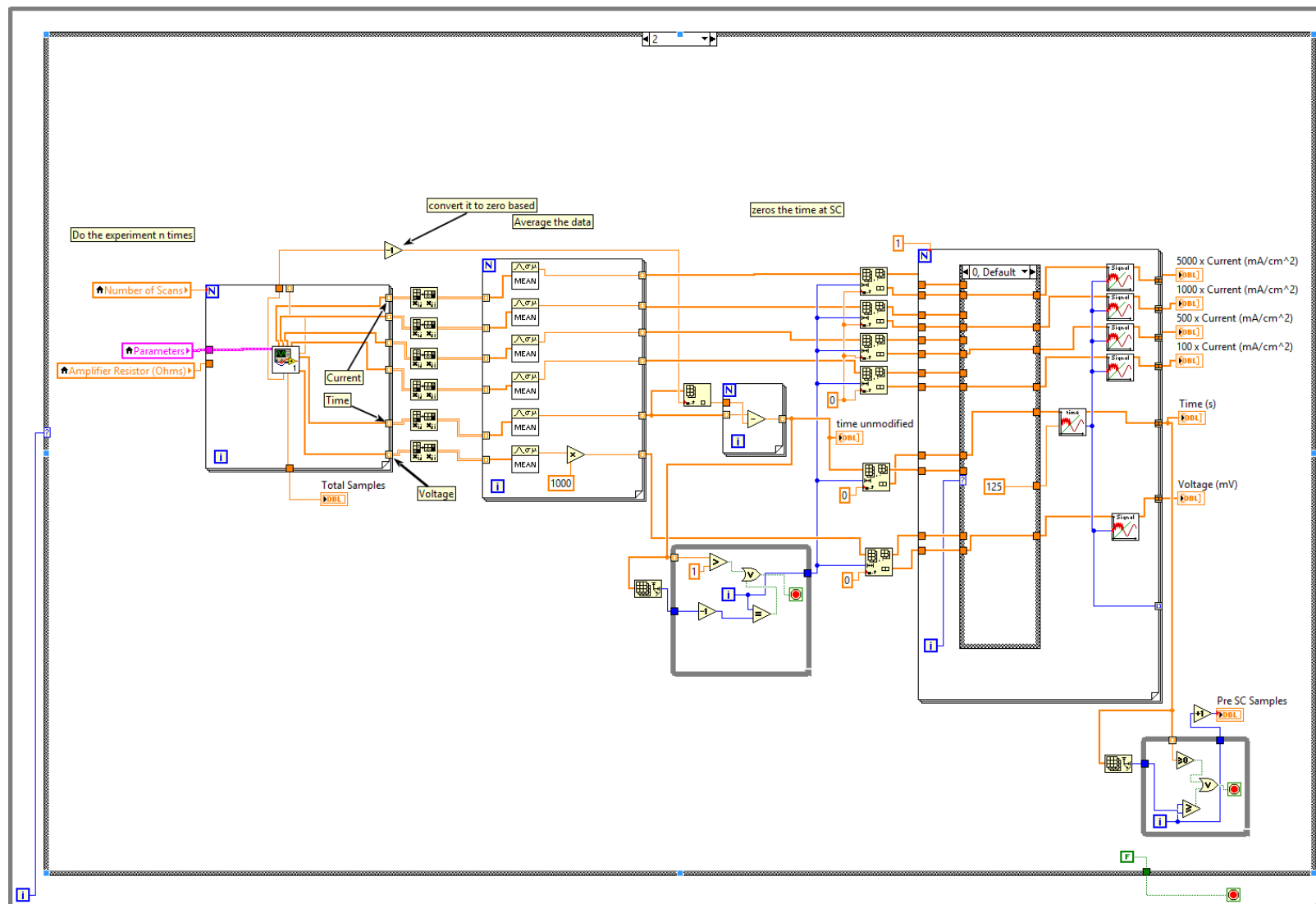


Figure A.48. Charge extraction experimental 'Block Diagram' step 3: perform the experiment and average the data.



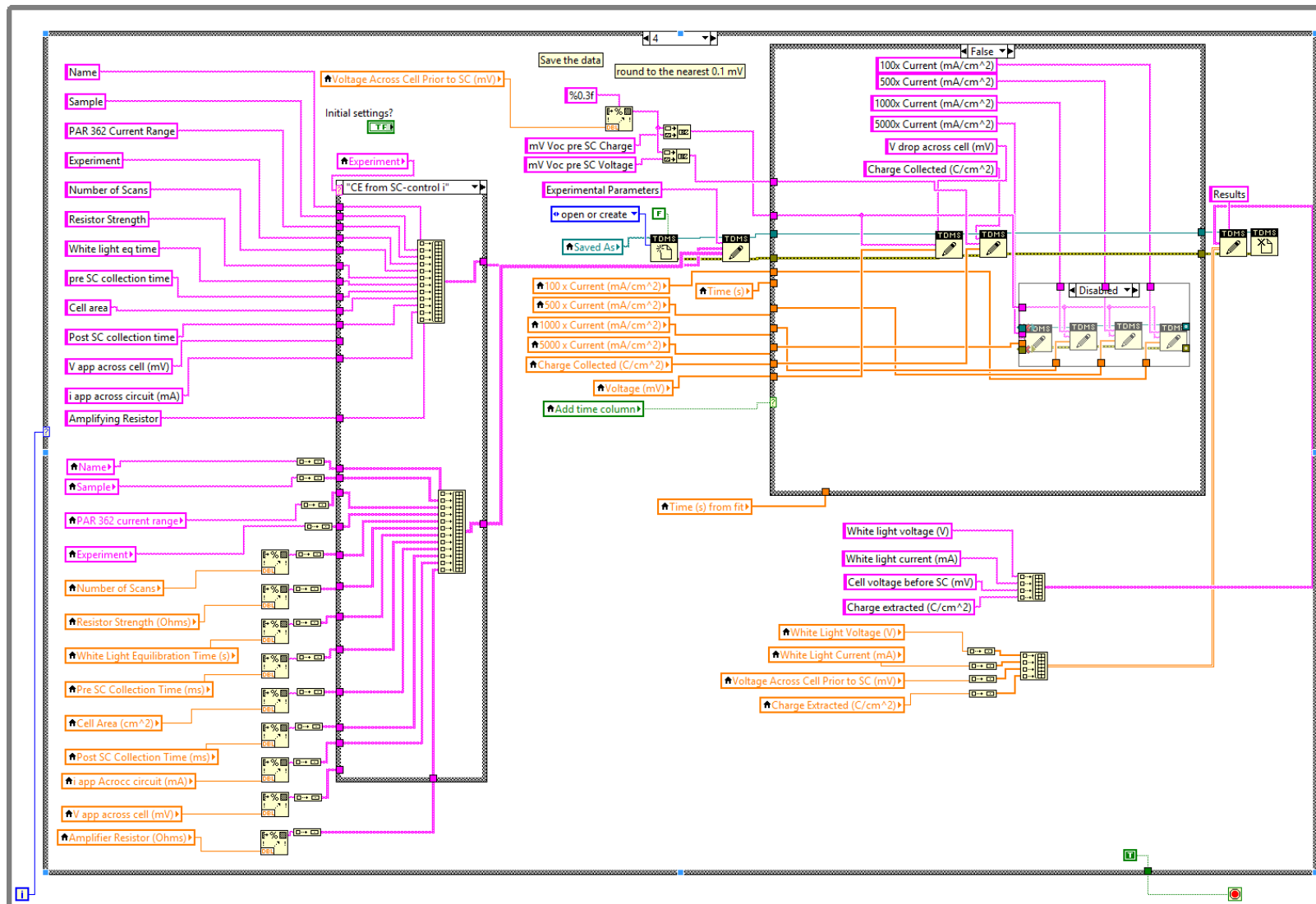


Figure A.50. Charge extraction experimental 'Block Diagram' step 5: display the results and export the data as a .TDMS file.

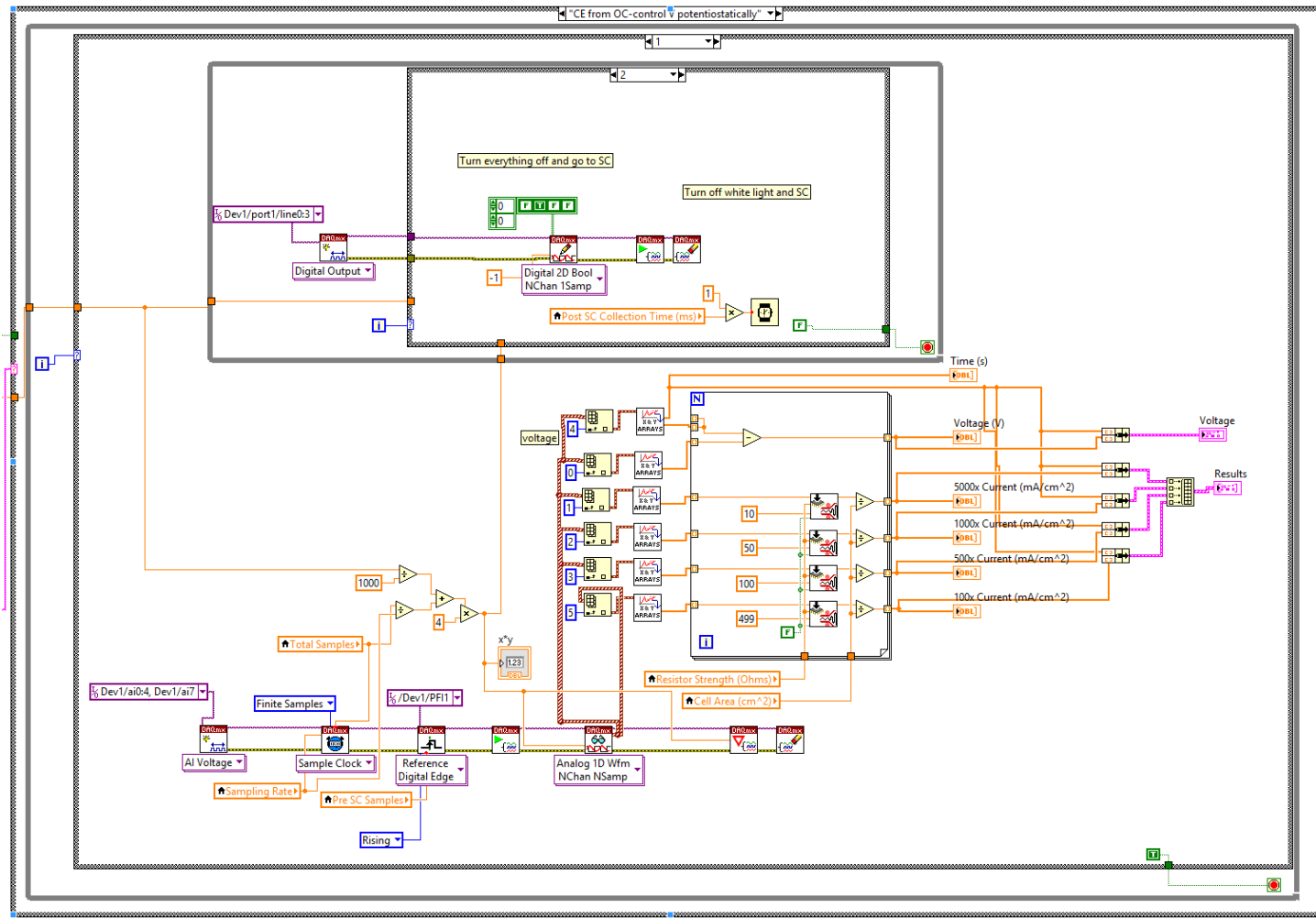


Figure A.51. Charge extraction collect data 'Block Diagram.' Use the digital output to switch between open and short-circuit and trigger acquisition.

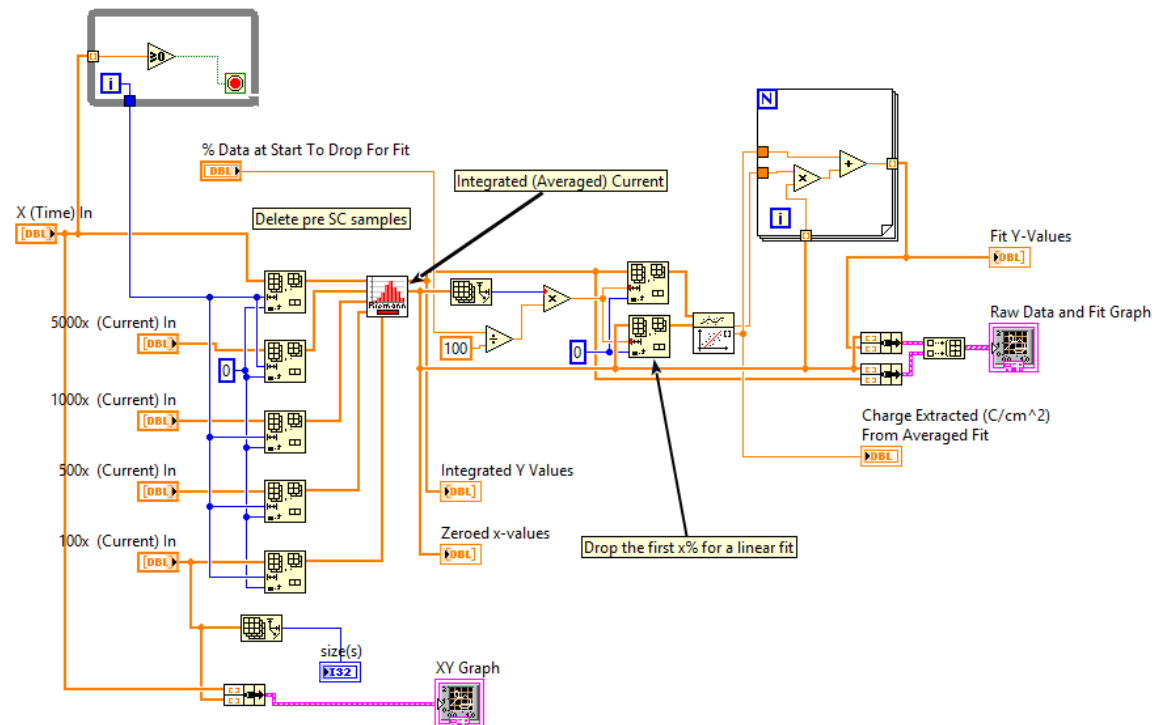


Figure A.52. Charge extraction integrate current and calculate charge extracted 'Block Diagram.'



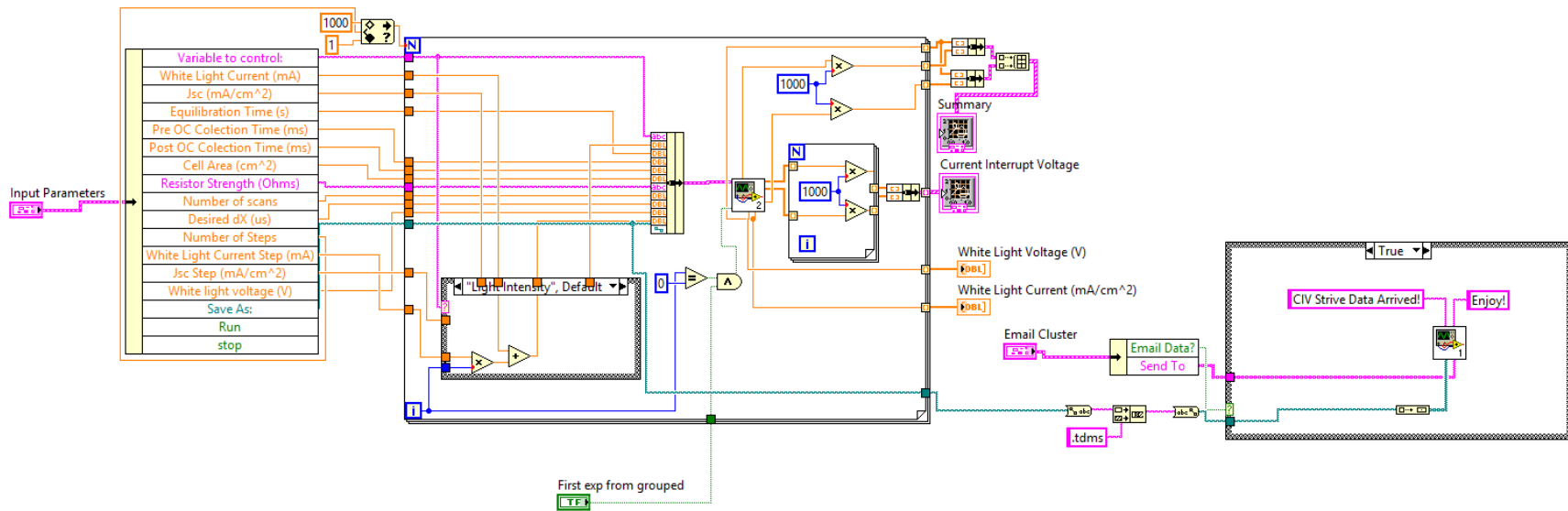


Figure A.54. Current interrupt voltage 'Block Diagram' where multiple experiments are performed and then the results are collected and displayed.

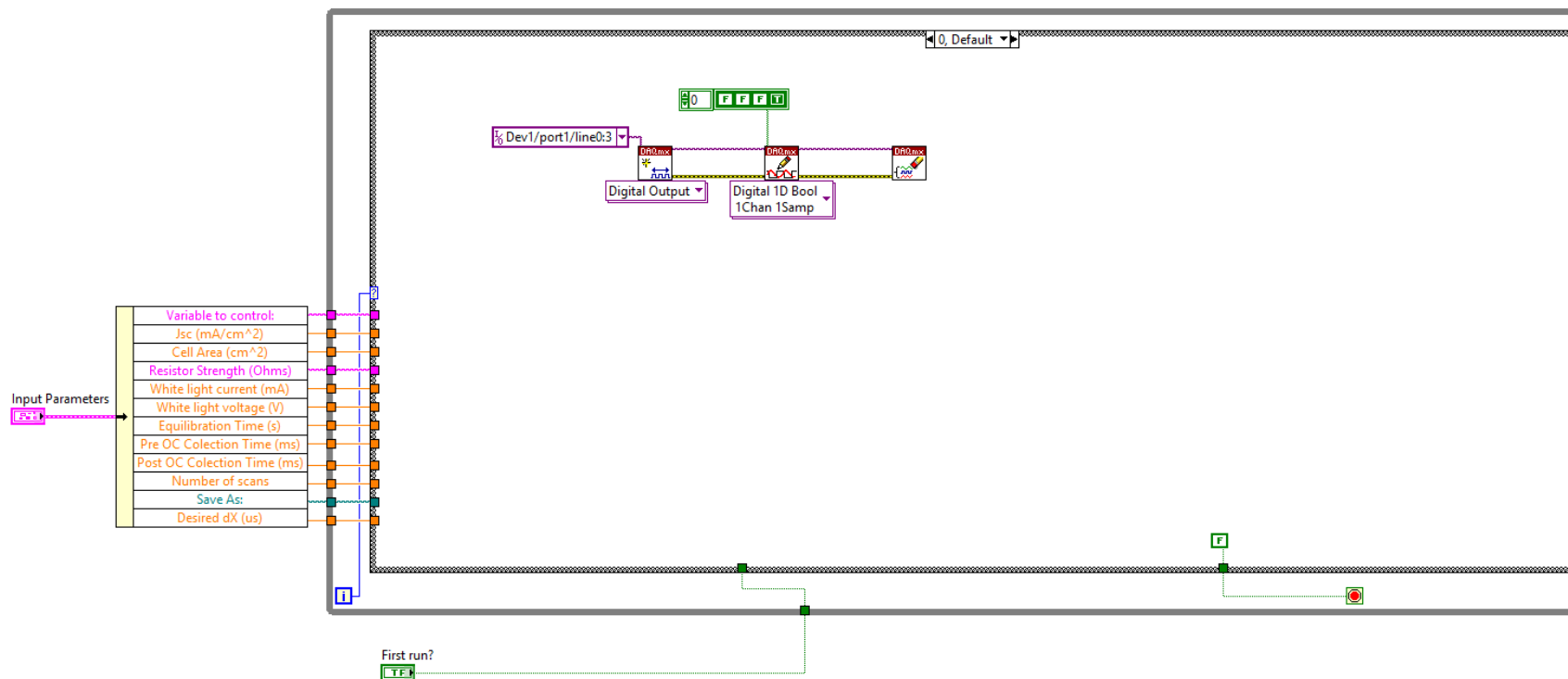


Figure A.55. Current interrupt voltage experimental 'Block Diagram' step 0: start at open-circuit with the light only the light on.

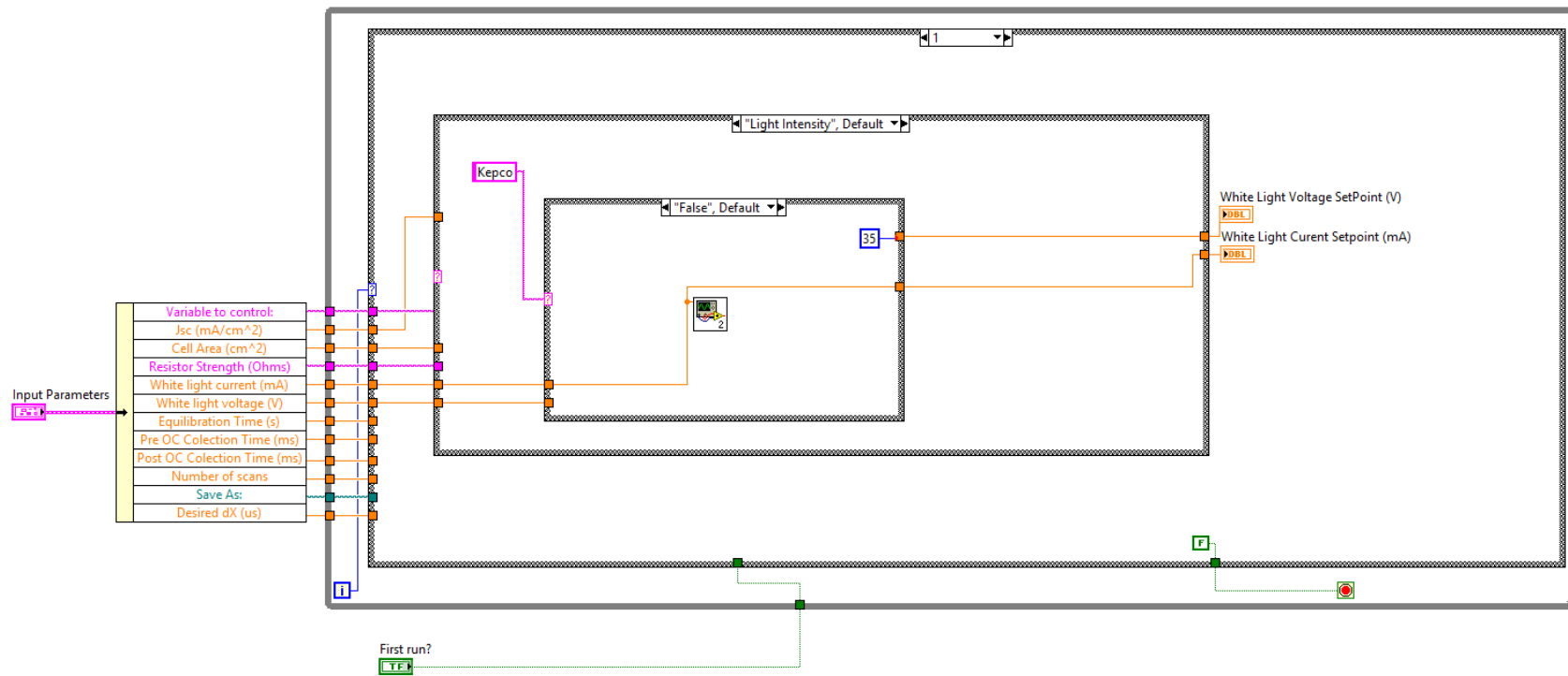


Figure A.56. Current interrupt voltage experimental 'Block Diagram' step 1: set the light intensity.

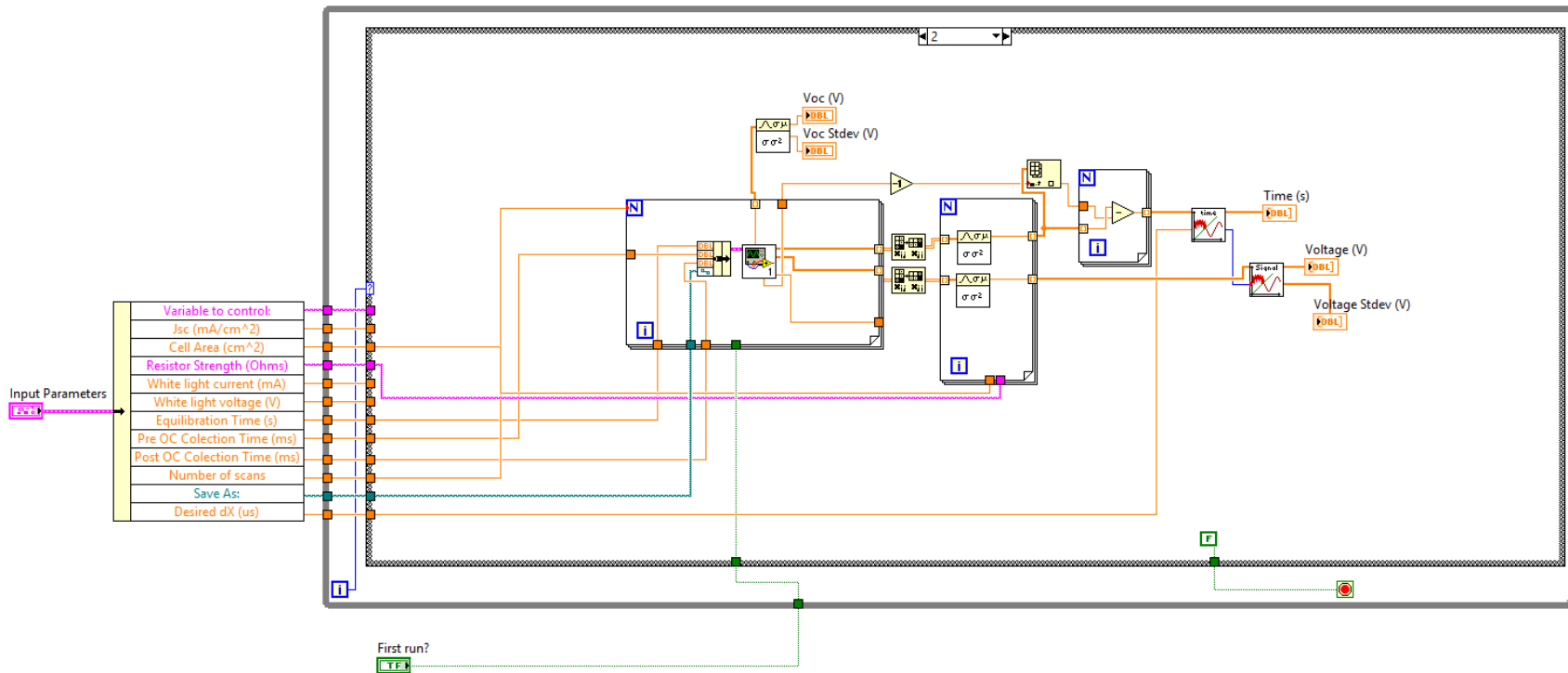


Figure A.57. Current interrupt voltage experimental 'Block Diagram' step 2: perform the experiment a defined number of times and average the results. The code to collect the data can be found in Figure A.61.

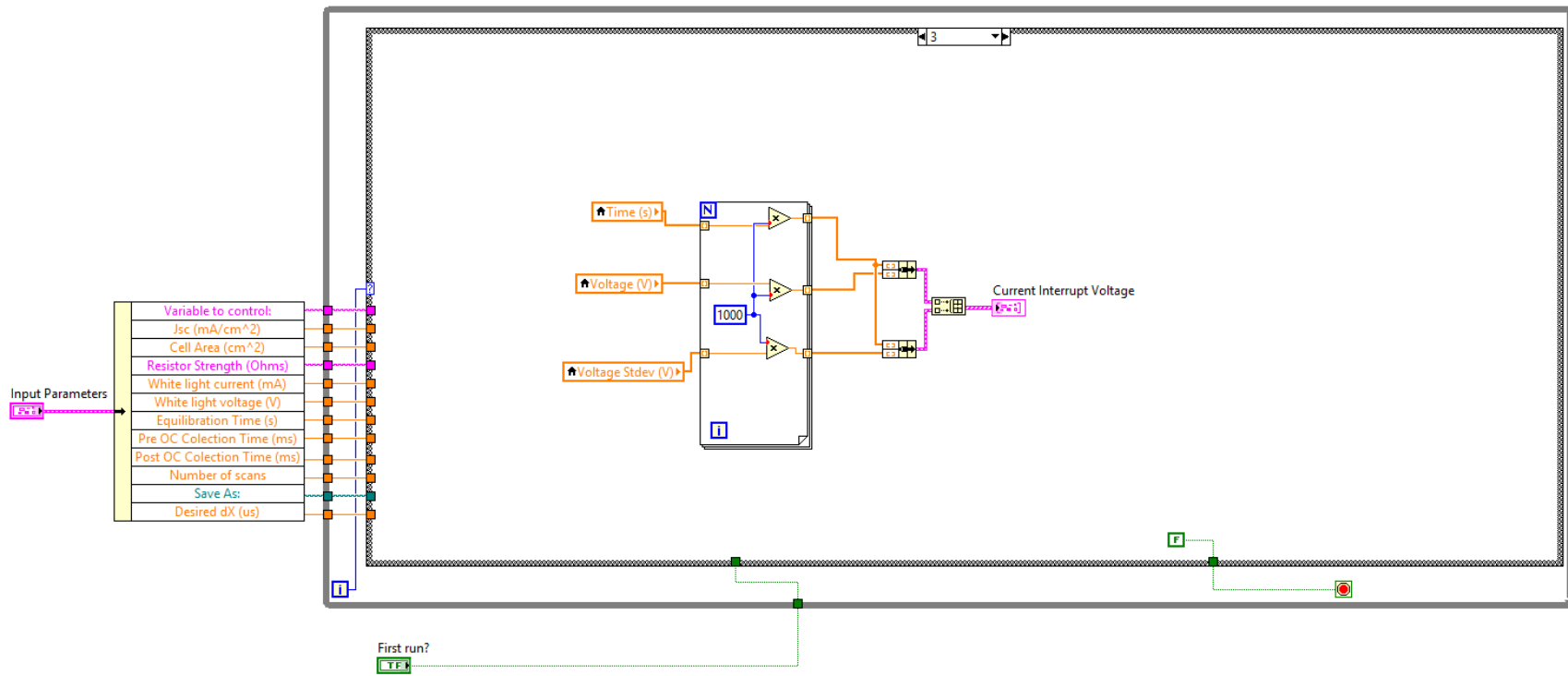


Figure A.58. Current interrupt voltage experimental 'Block Diagram' step 3: display the data.

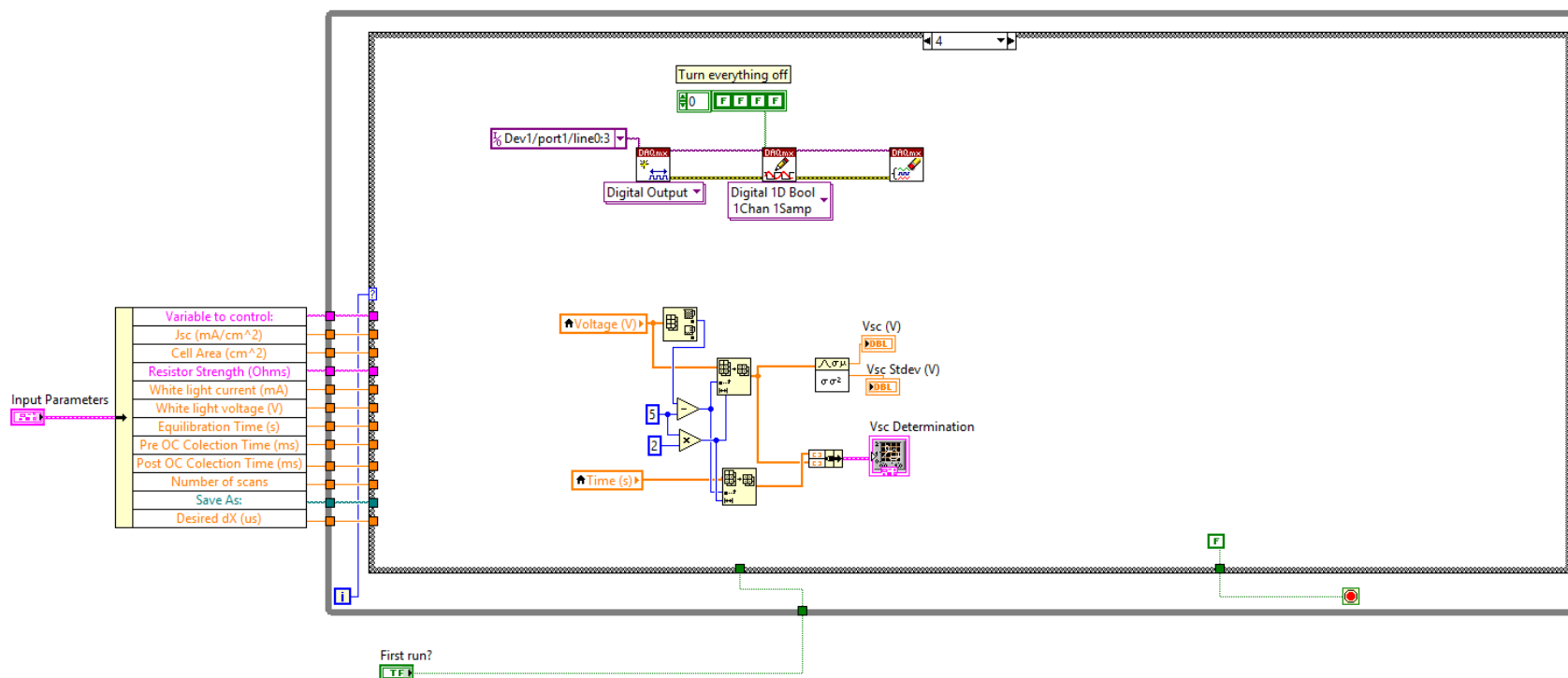


Figure A.59. Current interrupt voltage experimental 'Block Diagram' step 4: turn off the potentiostat, lights, and leave cell at open-circuit.

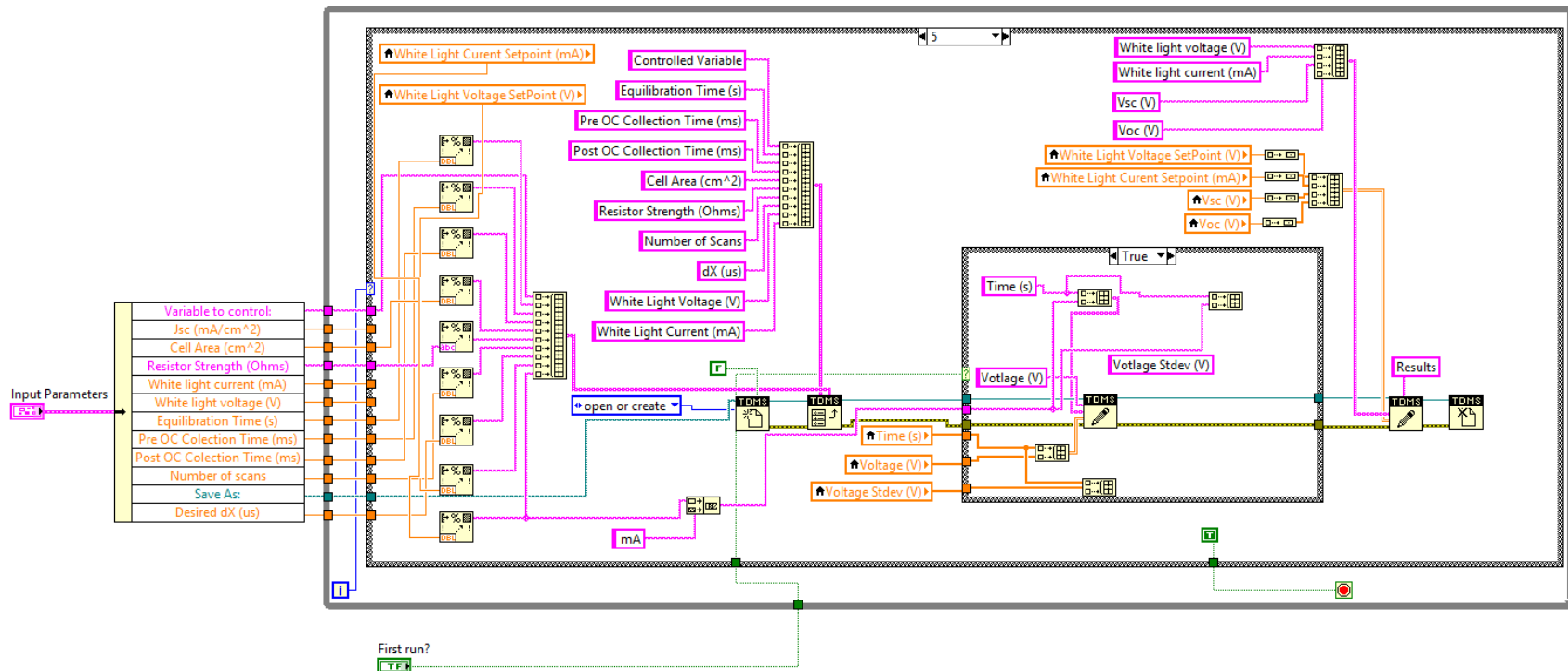


Figure A.60. Current interrupt voltage experimental 'Block Diagram' step 5: export the data as a .TDMS file.

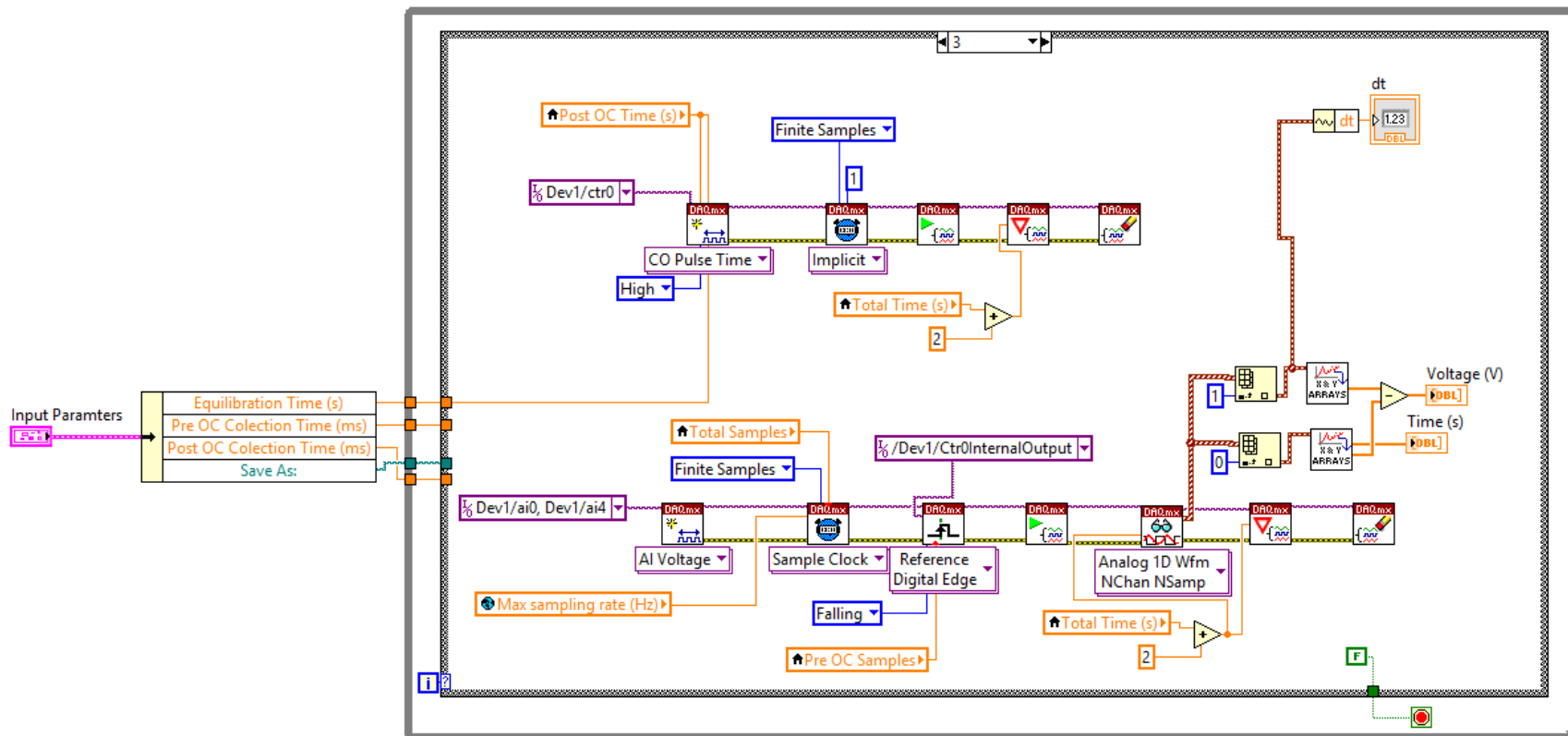


Figure A.61. Current interrupt voltage Collect Data ‘Block Diagram.’ An internal time counter is used to switch between short and open-circuit and trigger the start of data acquisition.

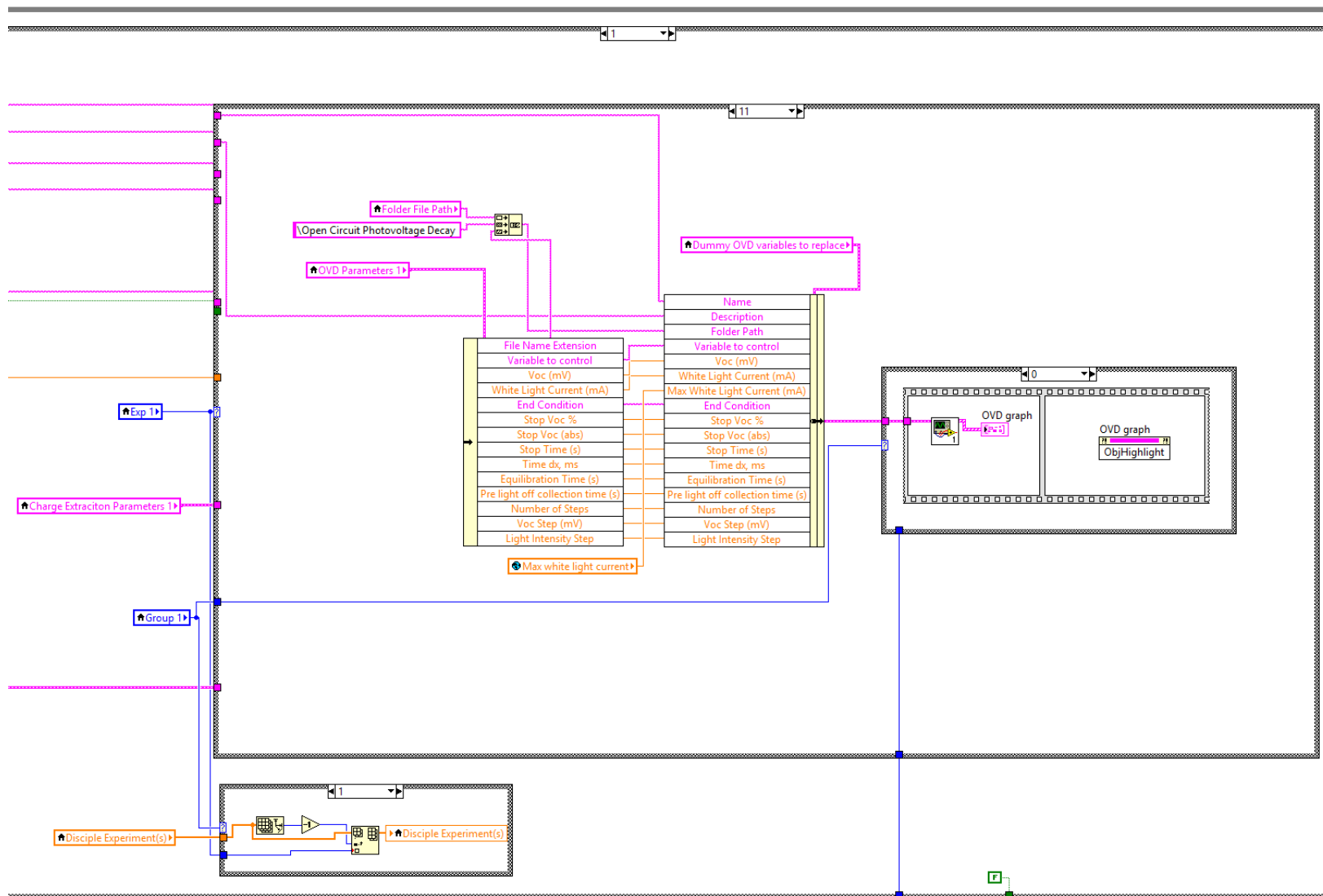


Figure A.62. STRiVE 5.0 user interface 'Block Diagram' selecting the seventh experiment, open-circuit photovoltage decay.

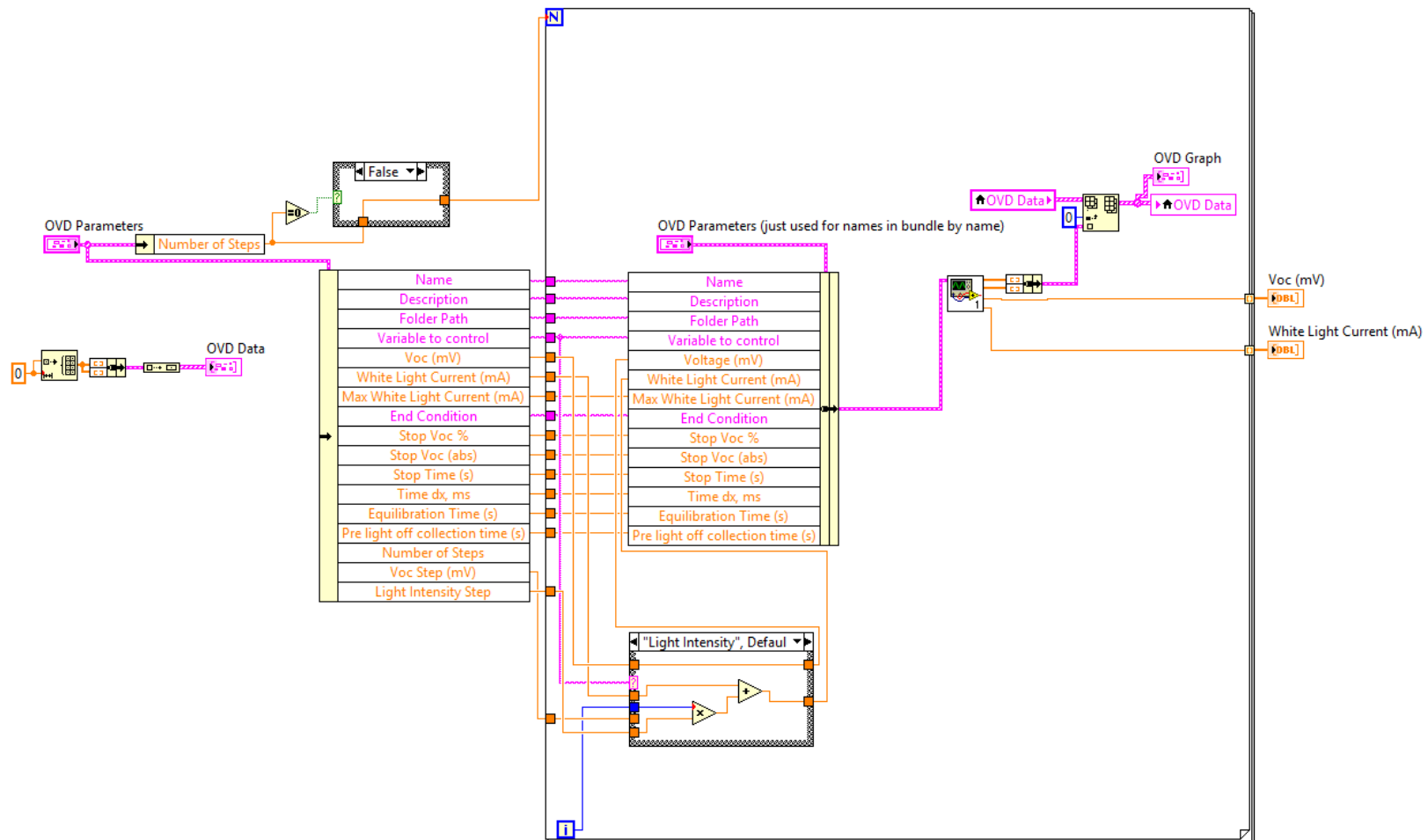


Figure A.63. Open-circuit photovoltage decay 'Block Diagram' where multiple experiments are performed and then the results are collected and displayed.





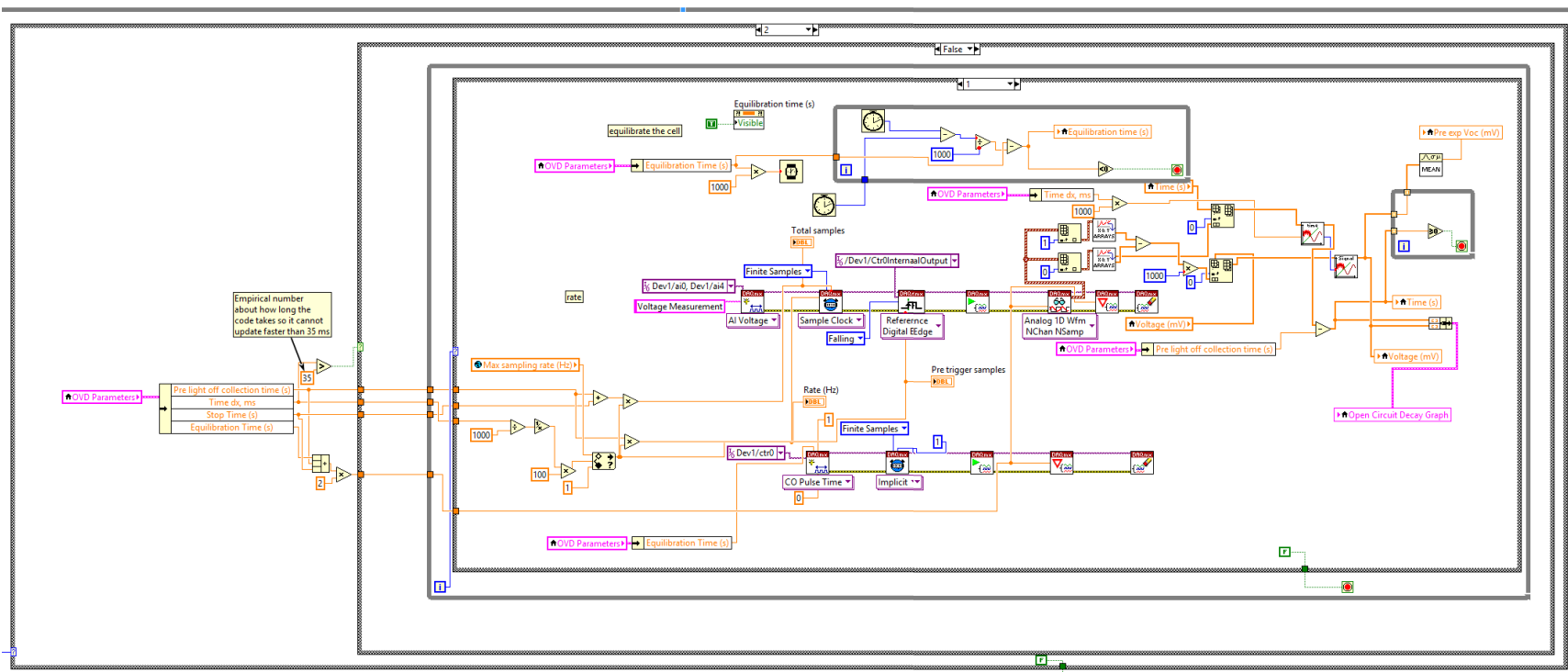


Figure A.67. Open-circuit photovoltage decay experimental ‘Block Diagram’ step 2b: collect data when the spacing between data points is less than 35 ms. In this case, the end condition cannot be monitored and the experiment will stop when the time is reached.

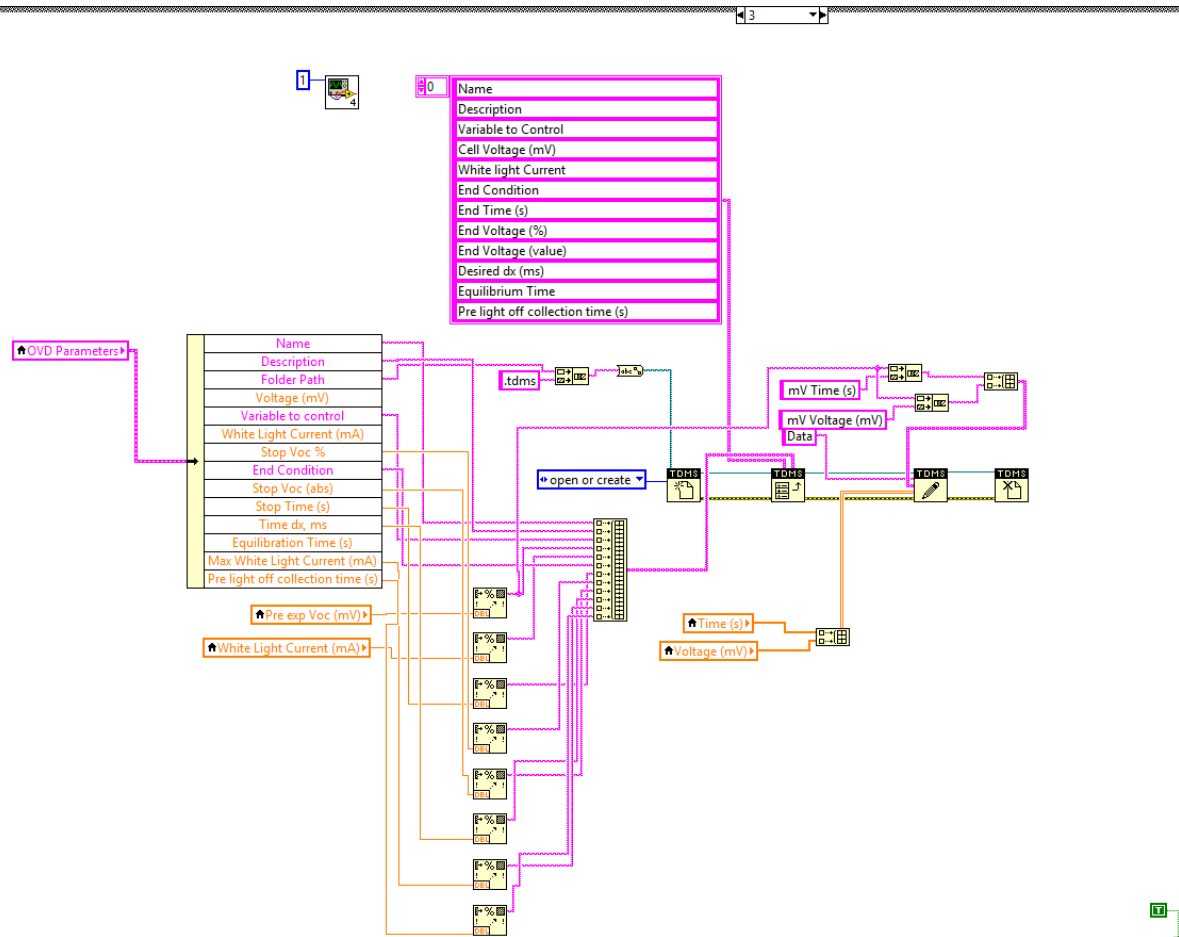


Figure A.68. Open-circuit photovoltage decay experimental 'Block Diagram' step 3: export the data as a .TDMS file.

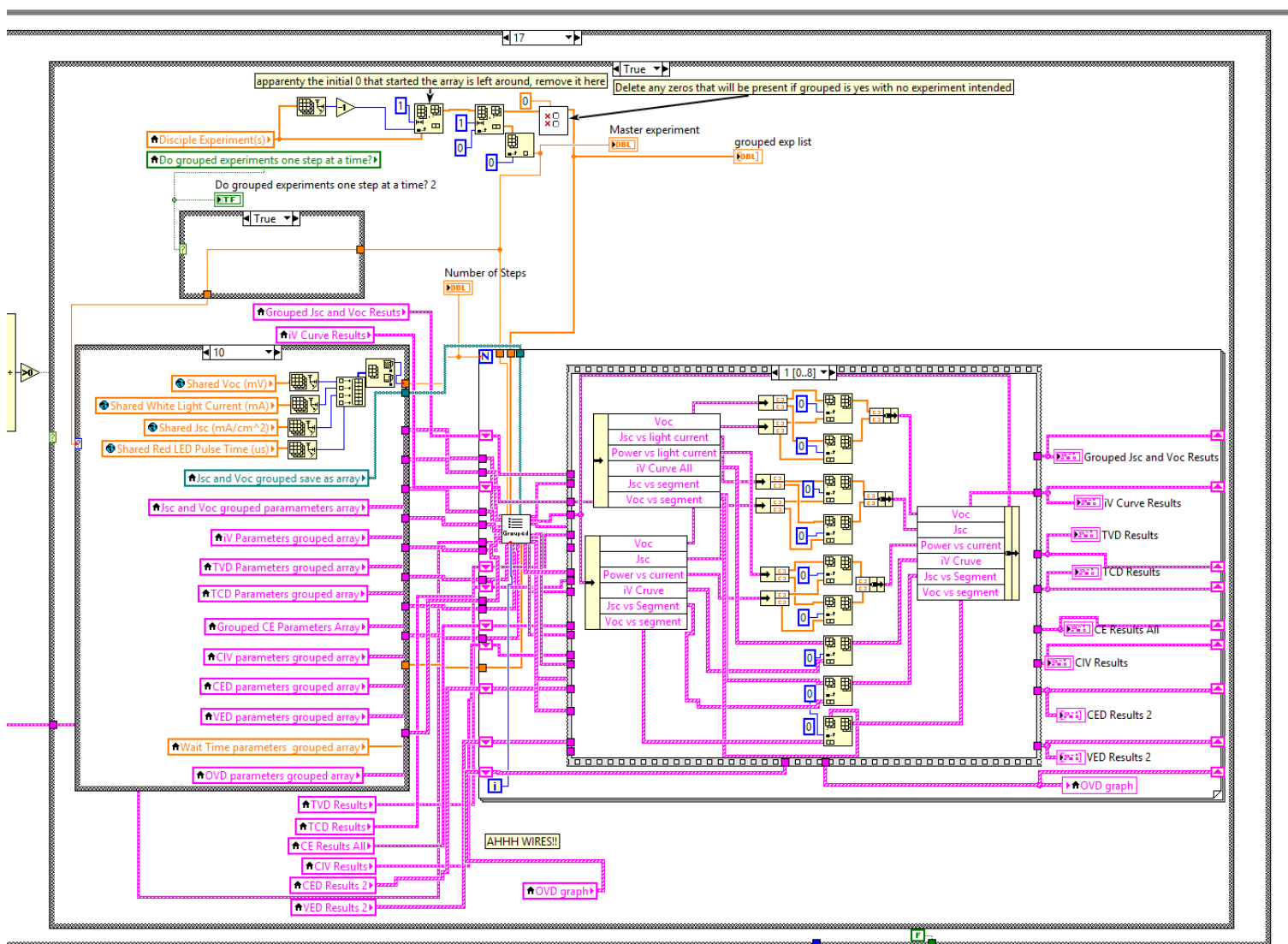


Figure A.69. STRiVE 5.0 user interface 'Block Diagram' selecting the grouped experiment.

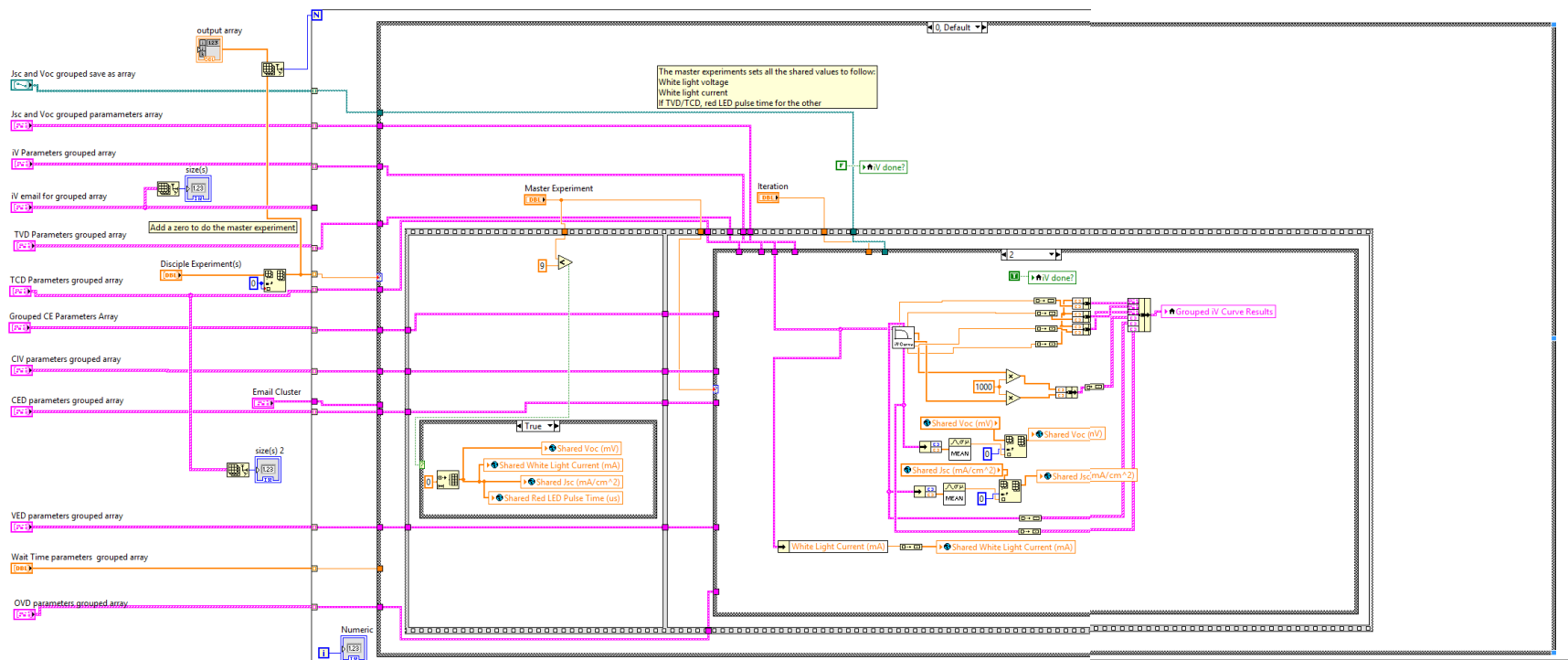


Figure A.70. Grouped experiments 'Block Diagram' showing how shared parameters are set. The rest of the code runs through the experiments similar to the STRiVE 5.0 as shown above.